

**Notice 1**

Under the Copyright Act 1968, this thesis must be used only under the normal conditions of scholarly fair dealing. In particular no results or conclusions should be extracted from it, nor should it be copied or closely paraphrased in whole or in part without the written consent of the author. Proper written acknowledgement should be made for any assistance obtained from this thesis.

**Notice 2**

I certify that I have made all reasonable efforts to secure copyright permissions for third-party content included in this thesis and have not knowingly added copyright content to my work without the owner's permission.

# Back Contact Dye-sensitized Solar Cells

**Dongchuan Fu**

B.Eng (Hons) (Materials Engineering)

Submitted for the degree of Doctor of Philosophy

Department of Materials Engineering

Monash University

Australia

January 2012

## Abstract

The objective of this work was to develop back-contact dye-sensitized solar cells (back-contact DSCs). These solar cells comprise working and counter electrodes on the same side of the dye-sensitized  $\text{TiO}_2$  film, in either an interdigitated or a coplanar configuration. In the novel solar cell architectures, transparent conductive electrodes can be replaced by metal-based electrodes. This facilitates the use of cheaper and more conductive electrode materials in dye-sensitized solar cells.

We presented in Chapter 1 an introduction to solar energy and solar cells including dye-sensitized solar cell, followed by a literature review on relevant research.

In Chapter 2, we summarized experimental details, including materials, reagents, general DSC fabrication methods, and DSC characterization techniques.

In Chapter 3, we described the first step in the fabrication of interdigitated back-contact DSCs (IBCDSCs) - the laser ablation process to produce interdigitated electrodes. Successfully patterned electrodes are essentially required to produce working IBCDSCs.

In Chapter 4, we developed a pulsed-current electrochemical deposition method for producing Pt catalytic coatings in IBCDSCs. The method was found also suitable for platinizing counter electrodes for conventional DSCs.

In Chapter 5 and chapter 6, we discussed the fabrication of interdigitated and coplanar back-contact DSCs (IBCDSCs and CBCDSCs). We achieved the highest conversion efficiencies of 3.6 % and 4.6 % on the two devices measured under simulated AM1.5G sunlight. All the results were compared to the performance of conventional DSCs using identical  $\text{TiO}_2$ , dyes and electrolytes.

In Chapter 7, we described three-terminal tandem DSCs comprising conventional  $\text{TiO}_2$  photoelectrodes and IBCDSCs. Nearly 10 % improvements in the photocurrent and conversion efficiencies were shown by using the IBCDSCs as back subcells.

The final chapter drew general conclusions and proposed outlook of the future work for the present research.



## Acknowledgements

Along with the preparation of the thesis, I eventually realized that every single piece of the work conducted during my PhD study was associated with the supports from my supervisors, colleagues, friends and family. Within a short passage, I would not be able express my sincerely appreciation to all these people.

At first, I would like to thank my supervisor Associate Professor Udo Bach for his kind and patient supervision. He is the person who introduced me to the research of dye-sensitized solar cells, and led me to all the accomplishments during my PhD study. His passion and preciseness on research guided me through all the difficulties and will light the way in my career.

Many thanks to Professor Yibing Cheng who helped me to build up the connection with the researchers from the Wuhan National Laboratory for Optoelectronics (WNLO). I would also appreciate Professor Jun Duan, PhD student Mr. Huan Yang and master student Mr. Shan Huang from WNLO for their great assistances with my laser ablation experiments. The collaboration with these colleagues has contributed a lot to my work. Special thanks would be given to Mr. Huan Yang who devoted a lot of his time to the fabrication of interdigitated electrodes.

I would also like to thank previous and current members of our research group, especially Dr. Andrew Nattestad, Dr. Cecilia Lalander, Dr. Fuzhi Huang, Dr. Hongwei Han, Dr. Naomi Lewcenko, Mr. Patrick Lay, Ms. Peipei Huang, Dr. Peter Chen, Mr. Philipp Reineck, Dr. Simon Thompson, Mr. Torben Daeneke, Dr. Vanessa Armel, Dr. Xiaoli Zhang, Dr. Yong Peng, and Mr. Yuanhui Zheng (in an alphabetic sequence) for their generous helps to my research. Special thanks would also be given to Associate Professor Nick Birbilis from the department of materials engineering for the help with optical profilometry, Dr Orawan Winther-Jensen and Dr. Patrick Howlett from the ARC center for electromaterials science (ACES) for the help with electrochemical experiments, Dr. Flame Burgmann, Dr. Tim Williams and Dr Xiya Fang from the Monash center for electron microscopy (MCEM) for the assistance with electron microscopy, John Grace from Raymax for the comprehensive demonstration of his excimer laser system, and Inga Tegtmeier (Advanced Design and Communication) for the help with graphical design.

Further, I appreciate Ms. Tamara Wright, Ms. Sandra Pedersen, Ms. Edna Tan, and Ms. Michelle Laing from the department of materials engineering for their patient assistance with all the administrative work.

I would also like to thank my parents and family for bringing up and supporting my oversea study. Last but not least, my sincerely thank and my love to my wife Yueting, for her continuous support and consideration during my study.

## **Declaration**

This thesis contains no material which has been accepted for the award of any other degree or diploma in any university or other institution. To the best of my knowledge, the thesis contains no material previously published or written by any other person, except where due reference is made in the text of thesis.

Dongchuan Fu  
December 2011





## Table of Contents

<b>Abstract</b>	<b>i</b>
<b>Acknowledgements</b>	<b>iii</b>
<b>Declaration</b>	<b>v</b>
<b>1 Introduction</b>	<b>1</b>
<i>1.1 A brief history of photovoltaic</i>	<i>1</i>
<i>1.2 Recent advances in dye-sensitized solar cells (DSCs)</i>	<i>4</i>
<i>1.3 Principle of p-n junction photovoltaic</i>	<i>4</i>
<i>1.4 Principle of dye-sensitized solar cell</i>	<i>6</i>
1.4.1 An overview of charge transfer kinetics in DSC	8
1.4.2 Electron transport in TiO <sub>2</sub> nanocrystalline network and charge recombination process	9
<i>1.5 Materials for dye-sensitized solar cells</i>	<i>12</i>
1.5.1 Substrate materials	12
1.5.2 Semiconductor materials	13
1.5.3 Dyes	14
1.5.4 Electrolyte	19
1.5.5 Catalytic materials	20
<i>1.6 DSCs with modified architectures</i>	<i>22</i>
1.6.1 Monolithic DSCs based on carbon counter electrodes	22
1.6.2 Sharp's Back-contact DSCs	24
1.6.3 Electron transport in back-contact DSCs	26
<i>1.7 Objective of the current work</i>	<i>28</i>

1.8	<i>References to Chapter 1</i>	28
<b>2</b>	<b>Experimental methodology</b>	<b>37</b>
2.1	<i>Materials and detergents</i>	37
2.1.1	Materials	37
2.1.2	Chemicals and reagents	38
2.2	<i>Standardized DSC fabrication procedures</i>	39
2.2.1	The preparation of FTO working electrode substrates	39
2.2.2	The deposition of dense TiO <sub>2</sub> blocking layer	39
2.2.3	The preparation of dye-sensitized TiO <sub>2</sub> working electrodes	40
2.2.4	The reparation of counter electrodes	41
2.2.5	Cell construction	41
2.3	<i>Characterization techniques</i>	42
2.3.1	Current-voltage (IV) test	42
2.3.2	Incident Photon-to-Electron Conversion Efficiency (IPCE)	46
2.3.3	Electrochemical Impedance Spectroscopy (EIS)	48
2.4	<i>References to chapter 2</i>	54
<b>3</b>	<b>Laser ablation to produce interdigitated electrodes</b>	<b>57</b>
3.1	<i>Background information</i>	57
3.2	<i>Mask-delivered process using KrF excimer laser</i>	60
3.2.1	Evaluation of processing parameters	60
3.2.2	Processing of full-size patterns	63
3.3	<i>Direct-write process using ND:YV04 solid-state laser</i>	67
3.3.1	Evaluation of parameters for the processing of FTO glass	68

3.3.2	Evaluation of parameters for the processing of Ti coated glass and PI	73
3.3.1	Comparison of ablation on different materials	75
3.3.2	Processing of full-size patterns	78
3.4	<i>Conclusion</i>	80
3.5	<i>References to chapter 3</i>	81
<b>4</b>	<b>Pulsed-current electrochemical deposition of Pt catalytic coatings</b>	<b>83</b>
4.1	<i>Experimental methods</i>	84
4.1.1	Materials and reagents	84
4.1.2	Pulsed-current electrochemical deposition (PED)	84
4.1.3	Charge transfer resistance ( $R_{ct}$ )	85
4.1.4	Cyclic voltammetry	86
4.1.5	Scanning electron microscopy	86
4.1.6	UV-Vis spectroscopy	86
4.1.7	DSC fabrication	86
4.1.8	Photocurrent-voltage characterization	86
4.2	<i>Results and discussion</i>	87
4.2.1	Coating morphology	87
4.2.2	Charge transfer resistance	90
4.2.3	Optical transparency	91
4.2.4	Cyclic voltammetry	92
4.2.5	Photovoltaic performances of DSCs	94
4.3	<i>Conclusions</i>	96
4.4	<i>References to chapter 4</i>	96

<b>5</b>	<b>Interdigitated back-contact DSCs</b>	<b>99</b>
5.1	<i>The structure of interdigitated back-contact DSC</i>	99
5.2	<i>The fabrication of interdigitated back-contact DSCs</i>	103
5.2.1	The laser ablation process	103
5.2.2	The electrochemical deposition of platinum black	104
5.2.3	Electrochemical characterization	106
5.2.4	Electrophoretic deposition (EPD) of $\text{ZrO}_2$ nanoparticles	107
5.2.5	Cell assembly	107
5.3	<i>Devices on the MiniFAB FTO backplates</i>	108
5.3.1	The microstructure of backplates	108
5.3.2	Photovoltaic characteristic	109
5.3.3	Photocurrent mapping	114
5.4	<i>Interdigitated back-contact DSCs on WNLO FTO backplates</i>	118
5.5	<i>Interdigitated back-contact DSCs on WNLO Ti backplates</i>	120
5.6	<i>Conclusion</i>	121
5.7	<i>References to chapter 5</i>	122
<b>6</b>	<b>Coplanar back-contact DSCs</b>	<b>123</b>
6.1	<i>Configurations of coplanar back-contact DSCs</i>	123
6.2	<i>Materials selection</i>	125
6.3	<i>Experimental procedures</i>	127
6.3.1	Fabrication of insulating spacer	127
6.3.2	Fabrication of top electrodes by magnetron sputtering	129
6.3.3	Laser ablation for configuration 1	129

6.3.4	Measurement of diffusion resistance	129
6.3.5	Cell fabrication	130
<b>6.4</b>	<b><i>Results and discussion</i></b>	<b>131</b>
6.4.1	Configuration 2 - dense ceramic spacer layer	131
6.4.2	Configuration 2 - dense polyimide spacer layer	132
6.4.3	Configuration 2 - Preliminary laser ablation tests	132
6.4.4	Configuration 3 - magnetron sputtering of Ti porous electrodes	133
6.4.5	Configuration 3 - electrochemical activity of covered Pt catalytic coatings	135
6.4.6	Configuration 3 - Characterization of fully assembled cells	137
6.4.7	Preliminary results of coplanar back-contact DSCs on Ti substrates	142
<b>6.5</b>	<b><i>Conclusion</i></b>	<b>143</b>
<b>6.6</b>	<b><i>References to chapter 6</i></b>	<b>144</b>
<b>7</b>	<b>Three-terminal tandem DSCs</b>	<b>147</b>
7.1	<i>Introduction</i>	147
7.2	<i>Three-terminal tandem DSCs using N719 and N749 dyes</i>	150
7.2.1	The effects of mixing light scattering particles in TiO <sub>2</sub> films	150
7.2.2	The effects of using coadsorbent in the N749 dye solution	151
7.2.3	The assembly of tandem devices	155
7.3	<i>Tandem DSCs using N719 and SQ2 dyes</i>	157
7.4	<i>Conclusion</i>	159
7.5	<i>References to chapter 7</i>	160
<b>8</b>	<b>General conclusions and outlook</b>	<b>163</b>

<b>8.1</b>	<b><i>General conclusions</i></b>	<b>163</b>
<b>8.2</b>	<b><i>Outlook</i></b>	<b>164</b>
<b>Appendix: Curriculum Vitae</b>		<b>167</b>

# 1 Introduction

Energy is the basis for the development of human society. The rapid development of the contemporary world is associated with an intensive growth in the demand of energy. In 2005, the annual global energy consumption was  $4.1 \times 10^{20}$  J, and this figure is projected to double by the year 2050 and to triple by the end of this century.<sup>1</sup> The rapidly increasing energy consumption urgently requires the emerging of advanced energy technology.

The present worldwide energy supply is mainly based on the combustion of fossil fuels. However, the natural reserve of fossil energy is projected to be exhausted within the century. What also raises worldwide concern is the emission of CO<sub>2</sub> and other greenhouse gases that have caused severe climate change over the past decades. Various issues relating to the dependency on fossil fuels have urged mankind to seek for alternative energy sources for a more sustainable future.

Fortunately, the sun that has irradiated earth for billions of years provides us with an unlimited energy source. In fact most of the energy forms including fossil fuels and wind power are indirectly converted from the energy of the sun. Compared to the potential risks of using nuclear power and the deficient supply of other renewable energy sources such as wind power, solar energy is absolutely clean and abundant. On a year average, sunlight delivers  $1.2 \times 10^5$  TW irradiation to the earth surface,  $10^4$  times more than the present global energy consumption. This means that the present energy demand could be satisfied by covering only 0.13 % of the earth surface with photovoltaic cells with 10 % conversion efficiency.<sup>2</sup> On the other hand, photovoltaic devices exhibit quiet operation, good mobility and low maintenance requirements. As such, in recent years great interest has been attracted to the conversion of sunlight into electric power by solar cells.

## 1.1 *A brief history of photovoltaic*

In fact, the photovoltaic effect has been recognized by mankind over a long period. Back to the 19<sup>th</sup> century, in 1839 French physicist Alexandre Edmond Becquerel conducted pioneer works on the photovoltaic effect.<sup>3, 4</sup> He observed the generation of an electric current when illuminating a silver chloride coated platinum electrode in contact with an electrolyte solution.

In 1873, Willoughby Smith observed that the resistivity of a selenium conducting bar was reduced when it was transferred from dark to light condition.<sup>5</sup> Four years later, W.G. Adams and R.E followed Smith's work and published a paper entitled 'The action of light on selenium' in the Proceeding of the Royal Society.<sup>6</sup> In 1883, an American inventor named Charles Fritts developed the first prototype of a solar cell. The device, comprising gold coated selenium, exhibited a conversion efficiency of less than 1%. Charles believed that his 'photoelectric plate' would soon become comparable to coal fire power plants.<sup>7</sup> However he seemed to be too optimistic about his solar cells, as even up to now solar cells have not been able to replace significant fractions of fossil power plants for electricity generation.

In the 'science's miracle year of 1905' the great scientist Albert Einstein, who was still a patent clerk at that time, published five papers which 'changed the face of physics'.<sup>8</sup> In one paper entitled 'On a Heuristic Point of View Concerning the Production and Transformation of Light', Einstein explained the theory of the photoelectric effect. The great work led him to the Nobel Prize in Physics in 1921.<sup>9</sup> This is the first theoretical explanation of the photoelectric effect, and is now the basis of semiconductor physics and photovoltaic devices.

In the mid 20<sup>th</sup> century, the research on solar cells was benefited from the rapid development in the semiconductor industry. The breakthrough work in solar cells was published by Chaplin et al. from the Bell Laboratory in 1954.<sup>10</sup> In this brief communication, they described a single crystal silicon p-n junction 'photocell' with a conversion efficiency of 6%,<sup>10</sup> before which the direct conversion from solar irradiation to electricity has never reached over 1 % efficiency.<sup>11</sup> However, the cost of a solar cell at that time was quite high. This limited the application of solar cells in consumer market. For many years, solar cells were only used for military and space engineering purpose.

At the same time, work was also conducted on 'second generation' solar cell using ternary compound semiconductors, such as  $\text{CuInSe}_2$ ,  $\text{CuGaSe}_2$ ,  $\text{CuInS}_2$  and  $\text{Cu(In,Ga)(S,Se)}_2$  (CIGS), achieving efficiencies of around 5%.<sup>12, 13</sup> Simpler processing technology made these thin-film solar cells competitive in cost to efficiency ratios at that time.<sup>14</sup>

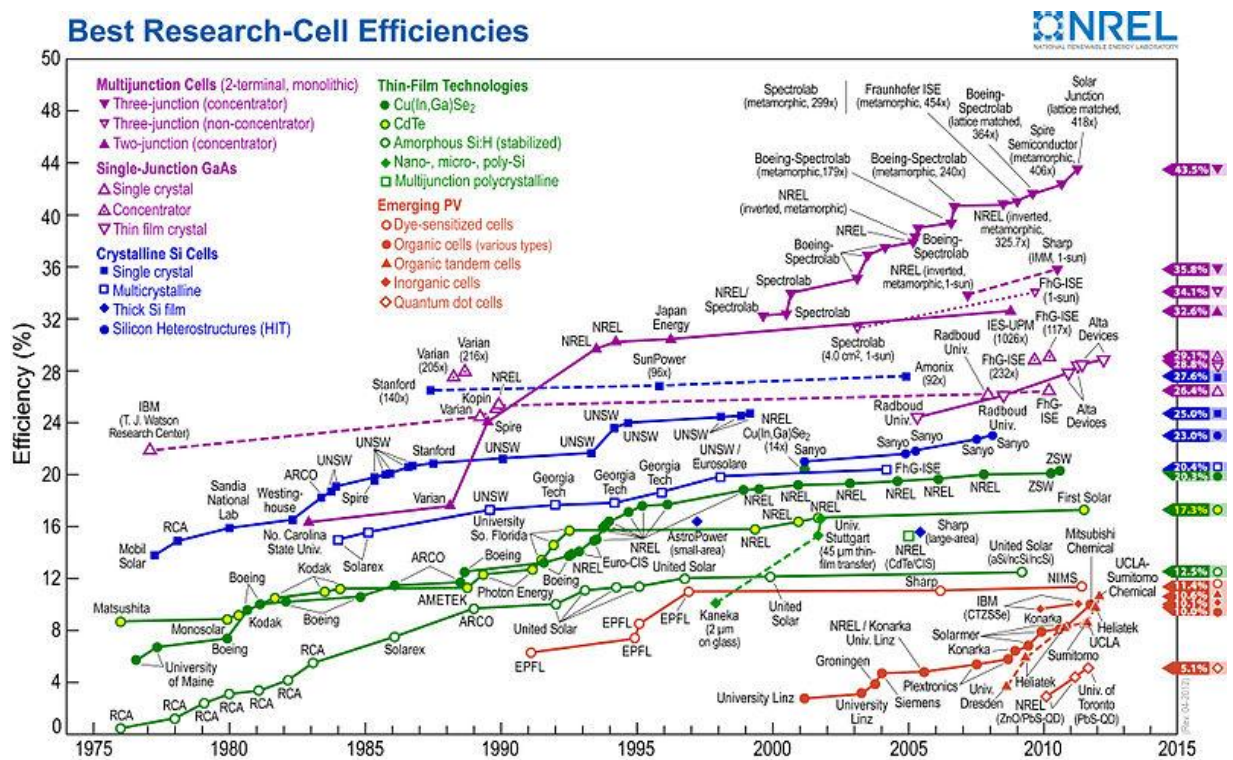
Several decades after the emergence of the first and second generation solar cells, first examples of emerging solar cells were successfully developed. In 1991, O'Regan and Grätzel published their milestone work in *Nature*, describing the Dye-sensitized Solar Cells (DSCs) based on a photo-electrochemical system. Four years after that, the organic photovoltaic (OPV)



based on a polymer/polymer heterojunction were developed by Yu et al..<sup>15</sup> These novel solar cells exhibit low cost and promising conversion efficiencies, and are expected to take a considerable share in the future photovoltaic market.

The first decade in the 21<sup>st</sup> century is a golden period for the development of the photovoltaic technology. With over half a century of development, now people could achieve an conversion efficiency of 42.3 % using a InGaP/GaAs/InGaAs tandem solar cell under concentrated sunlight.<sup>16</sup> Modules efficiencies of over 20 % have been achieved on crystalline Si-based devices.<sup>16</sup> The up-to-date solar cell efficiency data are shown in Figure 1.1. The figure also shows the evolution of solar cell efficiencies from 1975 to 2012.

In 2008, the global solar capacity was increased by 70 %, although slowed down by global economy recession, the increment still reached as much as 47 % in 2009.<sup>17</sup> The growth rate recovered to 73 % in the later year. At the end of 2010, solar capacity reached a record of 40 GW.<sup>17</sup> Though solar industry is still at an early age of development, this new market is expected to grow rapidly in the new century.



**Figure 1.1** The evolution of solar cell efficiencies from 1975 to 2012.<sup>18</sup> Produced by National Renewable Energy Research Laboratory (NREL) USA.

## 1.2 *Recent advances in dye-sensitized solar cells (DSCs)*

With over two decades of development, various new materials and fabrication techniques have been developed to boost the efficiency and enhance the long term stability of DSCs. Researchers aim at the large-scale commercialization of novel photovoltaic device in the close future.

By far the most efficient DSC system has been the one based on the nanocrystalline  $\text{TiO}_2$  sensitized by ruthenium complexes and supported by an iodine/triiodide electrolyte. Following well developed fabrication procedures, DSCs using the well-know N179 or N3 sensitizer could achieve a consistent efficiency of over 10 %.<sup>19, 20</sup> By far the highest certified conversion efficiency for the DSCs employing liquid electrolytes is  $11.4 \pm 0.3$  %, reported by NIMS in 2009.<sup>21</sup> The cell produced a high photocurrent of  $20.9 \text{ mA/cm}^2$  under one sun illumination, attributing to the panchromatic N749 dye (black dye) with a extended light absorption threshold to around 920 nm.<sup>22</sup> Detailed discussion of dyes will be presented in section 1.5.3. In parallel, work have been conducted on the replacement of the volatile solvent-based electrolyte with quasi solid state electrolyte systems, and this has lead to great improvements in the long-term stability of DSCs devices.<sup>23-25</sup> Under the outdoor working condition as well as the accelerated aging condition (AM1.5 irradiation, 60 °C, 1000 hr), remarkable stability has been demonstrate at various institutes.<sup>23, 24, 26-28</sup>

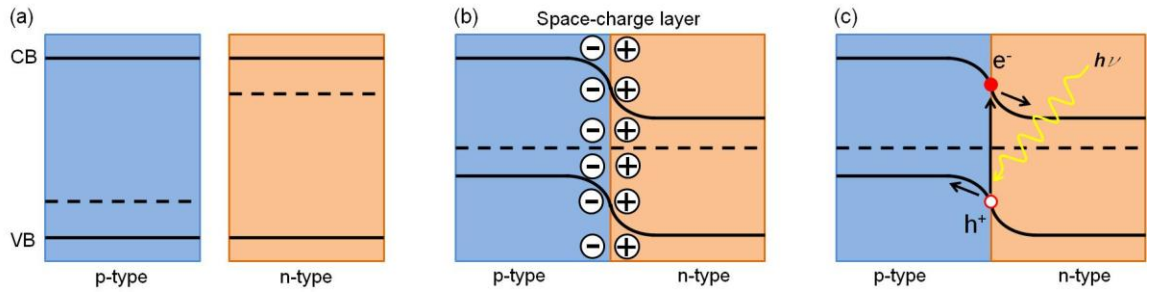
In the industrialization sector, the scale-up and commercialization of DSCs has attracted worldwide interest. DSC modules have been produced by industry giants as well as smaller players, including Sony, Mitsubhishi, Peccell, G24 Innovation and Dyesol.<sup>29</sup> Commercial products have been released, although in small quantity at the current stage. Given the recent advance in research and development, a rapid growth in this market can be foreseen.

## 1.3 *Principle of p-n junction photovoltaic*

Before the emergence of 'third generation' solar cells, conversion of sunlight into electricity was mainly accomplished by inorganic p-n junction solar cells. These photovoltaic devices are constructed using p- and n- type semiconductors that are differed in the form of doping. In p-type semiconductors doping results in excess holes and the shift of Fermi level towards the valence band, whereas in n-type semiconductors doping leads to excess electrons and the shift of the Fermi level towards the conduction band (Figure 1.2(a)). When the two semiconductors

are in close contact, a p-n heterojunction is formed where electrons on the n side and holes on the p side are driven by concentration difference to diffuse towards opposite directions, generating a space charge layer (or depletion layer) and accordingly a build-in electric field close to the interface (Figure 1.2(b)). According to the classical semiconductor physics theory, the formation of a p-n junction results in the leveling of Fermi levels of the two semiconductors, as well as the bending of conduction and valence bands.<sup>30</sup>

When illuminating the solar cell with light (Figure 1.2(c)), excitons (i.e. electron-hole pairs bound by columbic forces) are generated due to the excitation of electrons by incident photons. The excitons then diffuse to the junction where the paired electrons and holes are separated by the build-in electric field. An electric current is formed upon the collective diffusion of these charges.

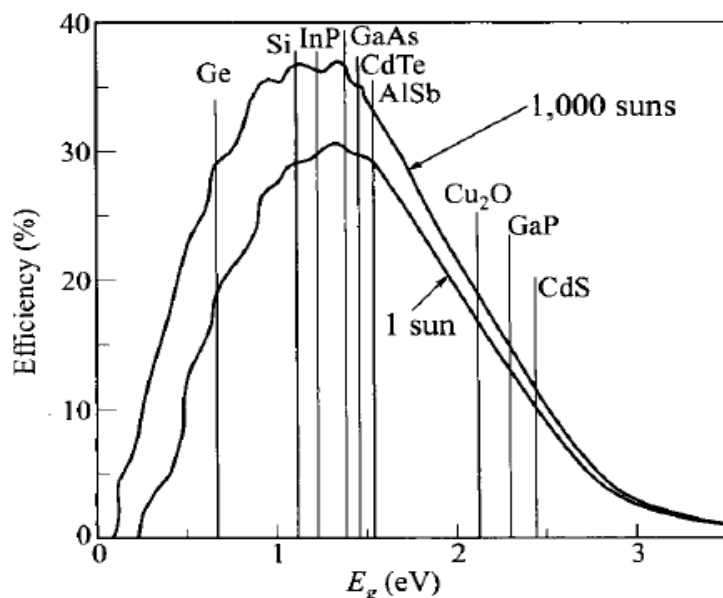


**Figure 1.2** (a) Band diagram of a p- and a n- type semiconductors. (b) Scheme of a p-n junction in dark condition and the generation of a space-charge layer. The forming of a p-n junction results in the leveling of Fermi levels and bending of the conduction and valence band. (c) Under light irradiation, excitons are formed and diffuse to the p-n junction. Electrons and holes are separated by the build-in electric field resulting in electric current.

The wavelength of light harvested by a p-n junction solar cell is correlated to the band gap ( $E_g$ ) of the semiconductor materials (Equation 1.1). A semiconductor with a moderate band gap is essential for an efficient solar energy conversion. A semiconductor with a wide band gap would only absorb ultraviolet light and omit most light in visible and infrared region. On the other hand, a semiconductor with a too narrow band gap would absorb light with a wide range of wavelength, however dissipating a significant fraction of the energy of most injected electrons by thermalization.

$$\lambda_g(nm) = 1240/E_g(eV) \quad 1.1$$

Figure 1.3 shows the maximum theoretical efficiency as a function of  $E_g$  of semiconductor materials.<sup>31</sup> Under one sun (AM1.5  $100 \text{ mW/cm}^2$ ) illumination, single junction solar cells have a theoretical efficiency maximum of 33 %.<sup>32</sup> Si and GaAs are the two semiconductors whose band gaps are within the ideal range of 0.8-1.4 eV, and therefore have theoretical efficiencies close to the theoretical maximum.<sup>30</sup>

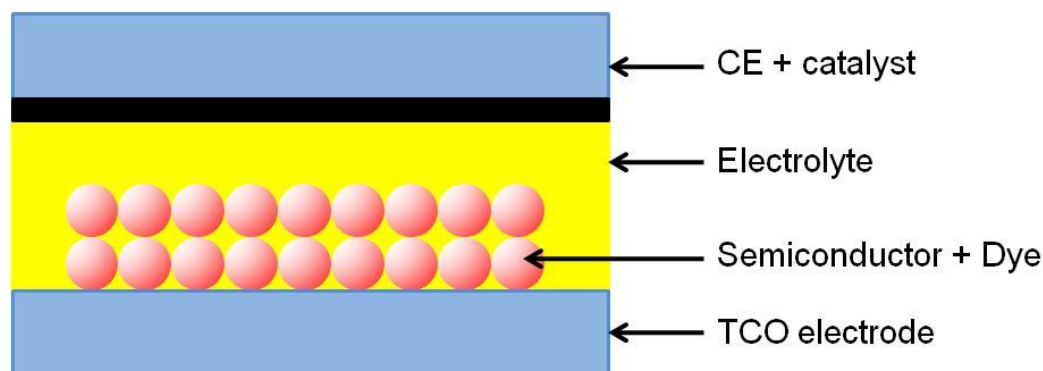


**Figure 1.3** Theoretical efficiency maximum of several semiconductor materials illuminated under 1 sun (AM1.5,  $100 \text{ mW/cm}^2$ ) and 1000 sun, taken from Sze S. and Ng K. Physics of semiconductor devices.<sup>30</sup>

#### 1.4 Principle of dye-sensitized solar cell

In contrast to solid state p-n junction solar cells, DSCs are based on an electrochemical system where charge separation occurs at a solid/electrolyte interface. The absorption of sun light by DSCs also follows Equation 1.1. However, the most widely used semiconductor  $\text{TiO}_2$  has a band gap of 3.2 eV, which makes it only response to ultraviolet light up to a wavelength of around 390 nm. The use of dye, however, greatly enhances the absorption of light. The absorption spectrum of DSCs could be modified through the use of different dyes. The commonly used N719 or N3 dyes, for example, have an absorption threshold of around 750 nm. Under standard AM1.5 illumination, a high quality 10 % DSC made with these dyes would have a photocurrent of around  $18 \text{ mA/cm}^2$ .<sup>20</sup> Better engineered panchromatic dyes, such

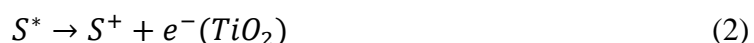
as the N749 dye, have an extended absorption onset of around 920 nm, leading to improved photocurrent to above 20 mA/cm<sup>2</sup>.<sup>21</sup> Merely from the point of light harvesting, the ultimate goal is to use a dye converting all light below a wavelength of 900 nm, yielding a photocurrent of 28 mA/cm<sup>2</sup> and an overall conversion efficiency of 15 %.<sup>33</sup> This would make the optical feature of DSCs similar to that of GaAs solar cells.<sup>34</sup>



**Figure 1.4** A cross-sectional scheme of a typical dye-sensitized solar cell.

A cross-sectional scheme of a DSC is shown in Figure 1.4. A DSC typically consists of a dye-sensitized mesoporous semiconductor layer deposited onto a Transparent Conductive Oxides (TCO) electrode, a counter electrode with a catalytic coating and an electrolyte filled between the two electrodes.

The following paragraph describes the fundamental steps involved in the charge generation and collection processes in DSCs using the N3 or N719 dyes (see section 1.5.3 for chemical structures) and I<sup>-</sup>/I<sub>3</sub><sup>-</sup> electrolyte.<sup>35</sup> Upon light irradiation a dye molecule is promoted from the ground state ( $S^0$ ) to the excited state ( $S^*$ ) (reaction 1). It then inject an electron into the conduction band of TiO<sub>2</sub>, leaving behind an oxidized dye cation ( $S^+$ ) (reaction 2). The electron diffuses within the TiO<sub>2</sub> nanocrystalline network to the TCO electrode. On the other hand, the dye cation forms a ( $S - I$ ) complex with a  $I^-$ <sup>36</sup> (reaction 3), which then react with an additional  $I^-$  and dissociate into a regenerated dye molecule and an intermediate radical  $I_2^{\bullet -}$  (reaction 4). Two  $I_2^{\bullet -}$  react to release an  $I_3^-$  and an  $I^-$  (reaction 5). The  $I_3^-$  then diffuses towards CEs, at which it is reduced by the catalytic material (reaction 6).<sup>35</sup>





Parallel to the charge generation and collection, free electrons are lost through various recombination and back reaction routes. The excited dye molecule could return to its ground state by relaxation (reaction 7). The injected electrons could recombine with dye cations (reaction 8), alternatively they could backreact with acceptors in the electrolyte (reaction 9). While electrons in FTO (mainly  $SnO_2$ ) could also backreact with the acceptors in the electrolyte, such a process is considered to be negligible for iodine/triiodide electrolyte system<sup>37</sup>, especially when the FTO surface is covered by a dense  $TiO_2$  blocking layer<sup>38, 39</sup>.

#### 1.4.1 An overview of charge transfer kinetics in DSC

A DSC is an electrochemical system where the overall charge transfer efficiency is determined by the kinetics of various charge transfer processes. It is therefore important to understand the rate constants of these processes. Taking the classical liquid-state DSC employing the ruthenium sensitizer and the iodide/triiodide electrolyte as an example, the time scales of various charge transfer processes are summarized in Figure 1.5.<sup>35, 40, 41</sup> Under one sun illumination ( $AM1.5$ ,  $100mW/cm^2$ ), the excitation of dye molecules by incident photons occurs in a few femtosecond range, after which electrons are injected into  $TiO_2$  with an ultrafast rate (on the 100 femtosecond timescale)<sup>42</sup>. The injected electrons are then thermalized to the conduction band edge of  $TiO_2$  in a picosecond timescale, followed by the slow transit via the  $TiO_2$  nanocrystalline network accompanied by multiple trapping and detrapping processes. In the meantime, the dye cations are regenerated by iodide ions within a few microseconds.<sup>41</sup> On the contrary, the dye molecules in their excited states could thermalize into the ground states in a few tens of nanoseconds, which is much slower than the ultrafast electron injection process.<sup>40</sup> The recapture of injected electrons by dye cations is much slower than the dye regeneration process, and the back-reaction of injected electrons with triiodide



Recent publications suggest that the transport of electrons in TiO<sub>2</sub> occurs by diffusion, driven by the gradient in electron concentration or the gradient of the quasi-Fermi level.<sup>43, 44</sup> After photo-excitation and injection, electrons undertake random walks in the TiO<sub>2</sub> network, during which they experience multiple trapping-detrapping events.<sup>45, 46</sup> Electrons easily fall into traps, from which they can escape by thermal activation.

Trapping of conduction band electrons in nanocrystalline TiO<sub>2</sub> is physically due to bulk defects, grain boundaries, and cations in the electrolyte.<sup>41</sup> Depending on the physical location in nanocrystalline TiO<sub>2</sub>, traps can generally be classified into bulk traps and surface traps.<sup>47</sup>

Thermodynamically, trap states are distributed within the band gap. According to the model described by Bisquert et al., the distribution of these trap states, or the Density of States (DOS), follows an exponential dependence on the trap energy  $E$ , as shown in Equation. 1.2.<sup>44</sup>

$$g(E) = \frac{N_L}{k_B T_0} \exp[(E - E_c)/k_B T_0] \quad 1.2$$

Where  $N_L$  is the total density of trap states,  $E_c$  is the energy level of lower conduction band edge,  $k_B$  is the Boltzmann constant with a value of  $1.38 \times 10^{-23}$  and  $T_0$  is a parameter determining the depth of the distribution.

Similar to the occupancy of energy states by fermions in other semiconductor materials, the occupancy of both bulk and surface trap states by electrons follows the Fermi-Dirac distribution, as shown in Equation. 1.3.<sup>47</sup>

$$f(E) = \frac{1}{1 + e^{(E - E_f)/k_B T}} \quad 1.3$$

Where  $E_f$  is the quasi Fermi level potential,  $k_B$  is the Boltzmann constant and  $T$  is the absolute temperature. The concentration of electrons at a given energy level can then be estimated by  $g(E)f(E)$ .

Under illumination, most free electrons are in trap states.<sup>45, 48, 49</sup> The concentration of conduction band electrons  $n_c$  is much lower than the concentration of trapped electrons  $n_L$  in the localized trap states. With increasing light intensity or increasing bias voltage applied to a DSC, the rise in the quasi-Fermi level eventually results in increased filling of deep trap states.<sup>44</sup> It has been commonly agreed that trapping of conduction band electrons results in a significant reduction in electron diffusion as well as in recombination processes.<sup>44, 48-51</sup>

The diffusion coefficient of the conduction band electrons can be expressed by Equation 1.3.<sup>44</sup>

$$D_n = \left(1 + \frac{\partial n_L}{\partial n_c}\right)^{-1} D_0 \quad 1.3$$



Since  $n_c \ll n_L$ , the diffusion coefficient of conduction electrons is usually around  $10^{-8}$  to  $10^{-4}$   $\text{cm}^2/\text{s}$ , much lower than a typical value of  $D_0$  ( $0.4 \text{ cm}^2 \text{ s}^{-1}$ ).<sup>43, 52</sup>

According to the model proposed by Bisquert et al., the recombination in DSCs is delayed by the trapping events in  $\text{TiO}_2$ .<sup>44</sup> This model is explained in the following section. The major recombination mechanism in a DSC is the electron transfer from the conduction band of  $\text{TiO}_2$  to triiodide. This process can be express by Equation 1.4.



According to Bisquert's model, trap states in  $\text{TiO}_2$  can be classified into bulk traps and surface traps. While the electrons in the conduction band and surface traps of  $\text{TiO}_2$  are directly transferred to triiodide, the electrons in bulk traps would need to be thermally activated into the conduction band before they recombine.

Based on the above assumptions, the recombination of electrons constitutes two major processes, namely the direct transfer and the transfer from bulk traps. As such, the time constant  $\tau_f$  for the direct recombination of free electrons is only a portion of the measured time constant  $\tau_n$  for the recombination at the  $\text{TiO}_2/\text{dye}/\text{electrolyte}$  interface (Equation 1.4). The delay of recombination can be expressed by Equation 1.5.

$$\tau_n = \left(1 + \frac{\partial n_L}{\partial n_c}\right) \tau_f \quad 1.5$$

Equation 1.3 and 1.5 described the dependence of the electron diffusion coefficient and lifetime on the free electron concentration, and accordingly on the trapping events. The prefactors for both equations quantitatively define the delay of diffusion and recombination by trapping.

For a DSC system, it is important to determine the diffusion length  $L_n$  of free electrons combining the diffusion and recombination terms (Equation 1.6).

$$L_n = \sqrt{D_n \tau_n} \quad 1.6$$

The term describes the distance that electrons can travel in mesoporous  $\text{TiO}_2$  before they annihilate through recombination. An  $L_n$  value higher than the film thickness  $L$  of  $\text{TiO}_2$  film is essential for an efficient charge collection. Due to the use of the same prefactor in Equation 1.3 and 1.5,  $L_n$  can then be converted into a form containing  $D_0$  and  $\tau_f$  (Equation 1.7).

$$L_n = \sqrt{D_0 \tau_f} \quad 1.7$$

Since  $D_0$  is a constant,  $L_n$  should merely be dependent on the free electron lifetime  $\tau_f$  which is a variable on the free electron density. However, such a dependency is still under debate.<sup>48, 53,</sup>

<sup>54</sup> The interpretation of the electron diffusion in  $\text{TiO}_2$  and the back reaction still requires a better understanding of the trapping-detrapping process.

## 1.5 *Materials for dye-sensitized solar cells*

### 1.5.1 Substrate materials

Glass sheets with TCO coatings are commonly used as the charge collection electrodes as well as the supporting substrates for thin film semiconductor photoelectrodes. The commercially available TCO materials are mostly In-doped  $\text{SnO}_2$  primarily developed for flat panel displays and F-doped  $\text{SnO}_2$  widely applied to solar cells. The present commercial available FTO electrodes usually have around  $10 \Omega/\square$  sheet resistance and 80 % transparency, which are of acceptable standards for laboratory scale DSCs. Larger scale modules, however, require the use of conductive grids or alternatively complex interconnection solutions to reduce Ohmic losses within devices. The use of FTO instead of ITO in DSCs is due to its superior thermal stability. The conductivity of ITO drops significantly upon annealing at elevated temperatures. For flexible DSCs ITO/PEN flexible electrodes are usually used.<sup>55-62</sup> This is due to their relative ease of fabrication on polymer substrates when compared to FTO. There are other types of TCO materials such as Aluminum Zinc Oxide (AZO),<sup>63-68</sup> single-wall carbon nanotube<sup>69</sup> and conductive polymers<sup>70-72</sup>, however they are either less chemically stable or less conductive and therefore can not compete FTO and ITO for TCO electrode applications.

Metal foils have also been used as DSC electrodes. There are investigations showing the use of stainless steel as CEs and Ti as WEs.<sup>73-77</sup> However, the major concern with the use of metals in DSCs is their chemical stability in an electrochemical system in the presence of iodine. Metal compounds, especially iron ions, released into DSC system could deteriorate the cell performance by encouraging recombination.<sup>20, 78, 79</sup> Ti is probably the most ideal material for DSC WEs as the intrinsic surface oxide makes perfect Ohmic contact with  $\text{TiO}_2$  nanoparticles. It is chemically inert, and would not be harmful even dissolved into the DSC electrolyte. Although with a higher resistivity ( $420 \text{ n}\Omega\cdot\text{m}$ ) than many other metals, a sheet resistance of much less than  $1 \Omega/\square$  could be easily achieved on a Ti substrate with  $100 \mu\text{m}$

thickness. However, the construction of DSCs using Ti as WEs would still require the use of transparent CEs.<sup>77</sup> Alternatively, metal electrodes could be used in DSCs with modified architecture which will be discussed in section 1.6 of this thesis.

### 1.5.2 Semiconductor materials

There are two major functions for the semiconductor materials in conventional p-n junction solar cells. These materials harvest light to generate excitons, and thereafter separate electrons from holes and transport them to the external circuit to form electric current. In contrast, semiconductor materials in DSCs are mainly responsible for charge transportation and for dye molecules adsorption.

In general, semiconductor photoelectrodes for DSCs should have a large surface area for enhanced dye loading as well as strong inter-particle connection to enable efficient charge extraction. The semiconductor materials used for DSCs are usually metal oxides. They are made into nanoparticles and sintered to form a mesoporous network with large surface area. Dye molecules are bonded to the surface by carboxylate groups. Strong binding could be formed using two carboxylate groups, such as the adsorption of N719 dye onto TiO<sub>2</sub> surface.<sup>78</sup> In an ideal condition, dye molecules would form a monolayer on the surface of semiconductors. The vertical stacking of dye molecules would result in filtering and quenching effect which makes charge generation less efficient. The close packing of dye molecules would also block the access of redox species to semiconductor surface, so that back reaction of electrons could be suppressed. However, it is always difficult to obtain a perfect coverage of the semiconductor surface by dye molecules. In some cases, dye coverage could only achieve around 70 % or even less.<sup>80</sup> Coadsorbents can be used to reduce dye aggregation and passivate semiconductor surface, in order to suppress the back reaction.<sup>81-86</sup>

Most commonly, photoelectrodes for DSCs are made of 20 nm nanocrystalline TiO<sub>2</sub>. The use of a mesoporous TiO<sub>2</sub> network instead of a TiO<sub>2</sub> single crystal on a 10  $\mu$ m film resulted in a 1000 fold increase in the TiO<sub>2</sub> surface area and therefore a much higher dye loading for an efficient light harvesting.<sup>87</sup> The nanocrystalline TiO<sub>2</sub> was firstly introduced by O'Regan and Grätzel in their Nature paper, and forms the basis for most DSCs developed since then.<sup>20, 21, 23, 33, 34, 88-102</sup> Prior to O'Regan, fractal TiO<sub>2</sub> film was used in the first laboratory embodiment of the dye-sensitized solar cells.<sup>103</sup>

TiO<sub>2</sub> is an abundant natural resource which, in its natural form, is present in three mineral forms, namely rutile, anatase and brookite. It is a common industrial raw material widely used to make white pigments, cosmetic products, toothpaste, self-cleaning coatings, etc. It is also a key material used in the research of photocatalysis and photoelectrochemical cells. Anatase has a higher photocatalytic activity than rutile due to its indirect band-gap.<sup>104</sup> TiO<sub>2</sub> used for DSCs are mostly anatase due to its wider band gap (3.2 eV) as well as the higher conduction band edge compared to the rutile form.<sup>105</sup> This leads to a better cell performance due to a higher open-circuit voltage caused by a higher Fermi level at the same concentration of conduction band electrons.<sup>41</sup>

Anatase TiO<sub>2</sub> nanoparticles could be produced by combined hydrolysis and hydrothermal techniques.<sup>98, 106-109</sup> The change of hydrothermal conditions, such as temperature, pressure, additives could effectively modify the morphology of nanostructures. Alternatively, TiO<sub>2</sub> nanostructures could be produced by techniques such as sol-gel methods<sup>57, 110</sup>, chemical vapor deposition<sup>111</sup> and anodic oxidation<sup>55, 112-114</sup>. These result in the production of various TiO<sub>2</sub> nanostructures, such as nanorods<sup>115, 116</sup>, nanowires<sup>117-119</sup>, and sub-micron beads comprising nanoparticles<sup>120</sup>. These novel nanostructures are designed to achieve improved electron diffusion coefficients, higher surface area for improved dye loading, and enhanced light scattering effects.

Work has also been done to investigate alternative n-type semiconductors such as ZnO<sup>121, 122</sup>, SnO<sub>2</sub><sup>123-125</sup>, and Nb<sub>2</sub>O<sub>5</sub><sup>126, 127</sup>. However, these materials generally produce lower solar cell efficiencies, and therefore could not compete with TiO<sub>2</sub> for DSC applications.

### 1.5.3 Dyes

The dye adsorbed onto the semiconductors is a major component responsible for the light harvesting and charge injection in a DSC system. An efficient dye should generally follow the properties as listed below:

- The dye should absorb over a wide range of the solar spectrum to convert a considerable portion of solar energy.
- The molar extinction coefficient of the dye should be as high as possible to enable the use of thinner semiconductor films. This could reduce the mean pathway for electron diffusion before reaching charge collecting electrodes.

- In n-type DSCs, the dye should have higher Lowest Unoccupied Molecular Orbital (LUMO) level than the conduction band of the semiconductor to facilitate electron injection. On the other hand, the Highest Occupied Molecular Orbital (HOMO) of the dye should be more positive than the electrochemical potential of redox mediator to facilitate dye regeneration. On the contrary, in p-type DSCs, the HOMO level should be more positive than the valence band, whilst the LUMO level should be more negative than the redox potential to enable efficient transfer of holes.
- The dye should strongly anchor to the semiconductor surface, and should be thermally and chemically stable over a long term.
- The positive charge on the dye after injection should be further away from the surface of  $\text{TiO}_2$  to suppress recombination.<sup>128</sup>
- The dye should have a minimum level of undesired aggregation.

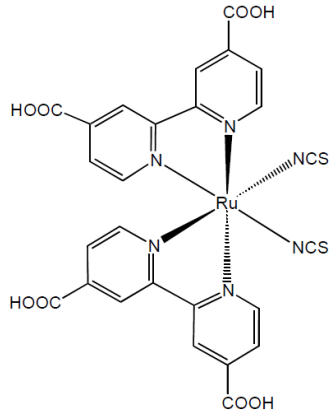
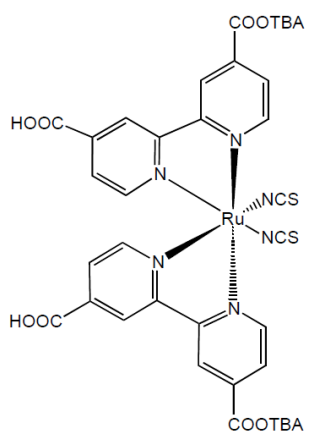
Ever since the development of efficient DSCs in 1991, the efficiency record has been lead by metal complex dyes comprising Ru center and polypyridyl ligand, such as the well-know N3<sup>19</sup> dye and recently developed C101 (11.9 %)<sup>129-131</sup>, C106 (11.4 %)<sup>132</sup> and Z991 (12.2%)<sup>133</sup> dyes. These dyes usually have broad light absorption over the visible range, due to the strong Metal-to-Ligand Charge Transfer (LMCT) transition.<sup>19</sup> Some of these complexes, such as the Z907 dye, show promising stability in accelerated lifetime measurements.<sup>134-136</sup> However, the molar extinction coefficients of the ruthenium dyes are usually less than  $20,000 \text{ M}^{-1} \text{ cm}^{-1}$ . DSCs comprising these dyes generally requires a thick ( $>12 \text{ }\mu\text{m}$ ) semiconductor film to absorb a large portion of incident light. On the other hand, there is also the concern about the limited natural reserve of ruthenium. As such, great efforts have been devoted to the development of alternative dyes to achieve similar or potentially higher cell efficiencies.

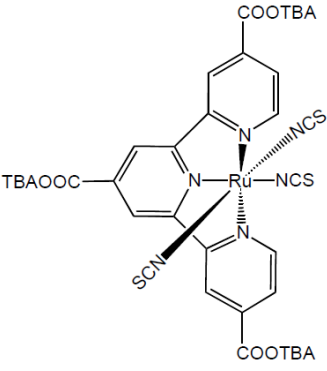
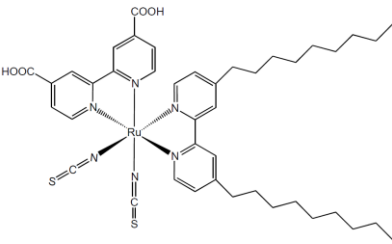
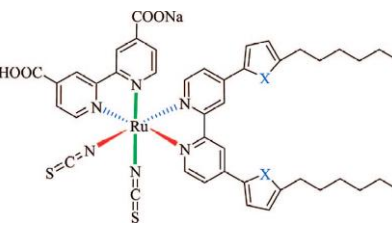
Remarkable efficiencies of over 9 % have been achieved using an organic indoline dye D149.<sup>137, 138</sup> The organic dyes exhibit the advantage that dye properties, including energy levels and absorption spectra, are fully tunable through the use of properly designed dye structures. High extinction coefficients could be realized with these dyes, making them attractive for DSCs requiring thin semiconductor films.

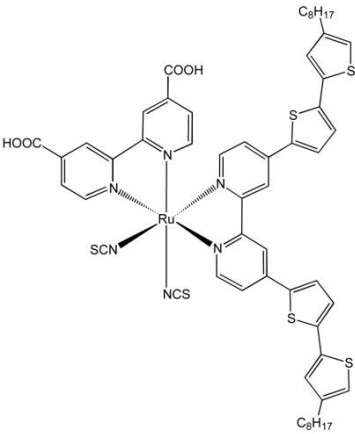
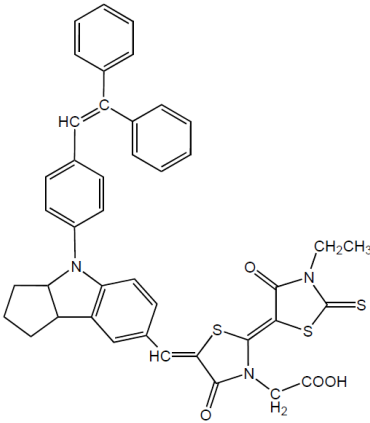
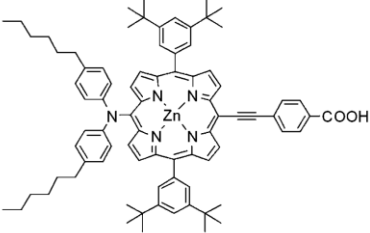
Organic dyes usually exhibit a structure incorporating a donor and an acceptor units conjugated by a  $\pi$ -bridge (a D- $\pi$ -A structure).<sup>128</sup> For n-type DSCs, the dye molecules are attached onto the  $\text{TiO}_2$  surface by the anchoring groups on the acceptors. Typically, the donor,

acceptor, and  $\pi$ -bridge units would incorporate aryl amine units, cyanoacrylic acid group and thiophene units respectively.<sup>128</sup> Promising results have also been shown on porphyrins, such as the YD2 dye<sup>139, 140</sup> and metal complexes using metal centers other than Ru<sup>141-143</sup>. Research into these dyes has opened an era of correlating structure and property using advanced design principles.

**Table 1.1** The chemical structure and molar extinction coefficient of selected dyes.

Name	IUPAC name	Chemical structure	$\epsilon$ ( $M^{-1} cm^{-1}$ ) & $\lambda_{max}$ (nm)
N3 <sup>19</sup>	cis-di(thiocyanato)-bis(2,2'-bipyridyl-4,4'-dicarboxylic acid)-ruthenium(II)		14,200 (in ethanol) at 534
N719	bis(tetrabutylammonium)[cis-di(thiocyanato)-bis(2,2'-bipyridyl-4-carboxylate-4'-carboxylic acid)-ruthenium(II)]	 (TBA=tetrabutylammonium)	13,600 (in ethanol) at 535

N749 <sup>22</sup>	(2,2':6',2'-terpyridine-4,4',4'-tricarboxylate)ruthenium(I) tris(tetrabutylammonium) tris(isothiocyanate)	 <p>(TBA=tetrabutylammonium)</p>	7,480 (in ethanol) at 609
Z907 <sup>134-136</sup>	cis-di(thiocyanato)-(2,2'-bipyridyl-4,4'-dicarboxylic acid)(4,4'-dinonyl-2,2'-bipyridyl)-ruthenium(II)		12,200 (in ethanol) at 528
C101 <sup>129</sup>			17,500 (in dimethyl-formamide) at 547

Z991 <sup>133</sup> , 144			44,600 (in dimethyl- formamide) at 400 nm
D149 <sup>137</sup> , 138			68700 (in tert- butanol/ acetonitrile (1/1)) at 526 nm
YD2 <sup>139</sup> , 140			31,200 at 644 nm



### 1.5.4 Electrolyte

The redox mediator in an electrolyte is responsible for the regeneration of dye cations. The redox potential together with the quasi Fermi level of  $\text{TiO}_2$  defines the  $V_{oc}$  of DSCs. In an electrolyte system containing a certain amount of reduced and oxidized species, the redox potential  $E_{redox}$  could be calculated by the Nernst equation (Equation 1.7)

$$E_{redox} = E^0 - \frac{RT}{nF} \ln \frac{[Red]}{[Ox]} \quad 1.7$$

Where  $E^0$  is the standard reduction potential of a redox couple,  $R$  is the gas constant that equals to  $8.314 \text{ J K}^{-1} \text{ mol}^{-1}$ ,  $T$  is the absolute temperature of the system,  $n$  is the number of electrons transferred in the reaction,  $F$  is the Faraday constant that is equal to  $9.648 \times 10^4 \text{ C/mol}$ , and  $[Red]$  and  $[Ox]$  are the concentration of reduction and oxidation species respectively.

A record efficiency of over 12 % was recently achieved using a Co(II/III)tris(bipyridyl)-based redox electrolyte.<sup>145</sup> Most of other high-efficiency DSCs have employed the liquid state electrolyte containing  $\text{I}^-/\text{I}_3^-$  redox mediator. The electrolyte used in high-efficiency DSCs usually contains 0.03 M  $\text{I}_2$ , 0.6 M butylmethylimidazolium iodide<sup>146</sup>, 0.10 M guanidinium thiocyanate and 0.5 M 4-tert-butylpyridine in the mixture of acetonitrile and valeronitrile (volume ratio 85:15). Lithium iodide is not commonly used at present due to the band shift effect and adverse lattice intercalation phenomena of the lithium ion.<sup>147-149</sup> The addition of guanidinium thiocyanate results in the passivation of the  $\text{TiO}_2$  surface and hence the suppression of interfacial recombination.<sup>150</sup>

The high-efficiency acetonitrile based  $\text{I}^-/\text{I}_3^-$  electrolyte system exhibits several advantages. It is low in viscosity, and shows very fast ionic diffusion. The two-electron charge transfer process also results in slow recombination of  $\text{TiO}_2$  electrons.<sup>35</sup> Yet, there are substantial driving forces for the replacement of  $\text{I}^-/\text{I}_3^-$  electrolyte. Iodine is a strong oxidation agent which causes the corrosion of metal charge-collection grids in DSC modules. The use of iodine also leads to various environmental issues once it leaks out off the devices. It has also been argued that the two-electron system involves complex charge transfer processes. According to the model proposed by Boschloo et al., immediate after dye regeneration, an intermediate species  $\text{I}_2^{\bullet -}$  is formed. It then requires an driving force to convert  $\text{I}_2^{\bullet -}$  to  $\text{I}_3^-$ , which accounts for a several hundred millivolts potential loss in the DSC system.<sup>35</sup>

Due to these reasons, intensive works has been conducted to develop non-volatile, non-corrosive electrolyte systems. Alternative redox mediators have been developed, including  $\text{Br}^-/\text{Br}_3^{-151}$ , ferrocene/ferrocenium ( $\text{Fc}/\text{Fc}^+$ )<sup>152</sup>, 2,2,6,6-tetramethyl-1-piperidinloxy (TEMPO)/TEMPO<sup>+</sup><sup>153</sup>,  $\text{SeCN}^-/(\text{SeCN})_3^-$ <sup>154</sup>, and  $\text{Co}^{2+}/\text{Co}^{3+}$ <sup>155, 156</sup>. Some of these redox mediators perform similar to iodine/iodide under certain measurement conditions. Promising results were reported by Daeneke et al., using an organic dye and the  $\text{Fc}/\text{Fc}^+$  redox mediator.<sup>152</sup> The more positive redox potential of the  $\text{Fc}/\text{Fc}^+$  mediator results in a high  $V_{\text{oc}}$  and accordingly a high efficiency of 7.5 %, despite the fact that ferrocenium is inherently instable in the presence of oxygen. More stable organic mediator TEMPO/TEMPO<sup>+</sup> developed by Zhang et al. also shows a high efficiency of 5.4 %.<sup>153</sup> However, shorter electron lifetime was measured for TEMPO-based devices, due to the much faster recapture of conduction band electrons by TEMPO<sup>+</sup> than by triiodide. In general, the faster recombination seems to be a common problem for all one-electron redox systems.<sup>41</sup>

Aimed at better device stability, a great variety of ionic liquid electrolytes and polymer gel electrolytes have been developed<sup>157-164</sup>. However, none of these systems could compete with the performance of iodine/iodide system, mostly owing to their lower charge mobility. Recently, the mass transport limits seems to be overcome by Wang and coworkers.<sup>24, 25</sup> A high efficiency of over 8 % was achieved using an eutectic mixtures with a reduced melting point.

### 1.5.5 Catalytic materials

The catalytic coating on the CE is responsible for the reduction of oxidized redox species. Previous investigations mostly focus on four types of catalytic materials for the reduction of triiodide, including noble metals<sup>91</sup>, carbon based materials<sup>165-169</sup>, conductive polymers<sup>170</sup>, and hybrid materials<sup>171, 172</sup>.

CEs with Pt coating have been a standard component for most DSCs employing iodine/iodide electrolytes.<sup>2, 21, 40, 87, 93, 173</sup> They are easy to prepare in laboratory condition, and show fast charge transfer kinetics towards the triiodide reduction. Very low charge transfer resistances of less than  $1 \Omega \cdot \text{cm}^2$  have been demonstrated.<sup>91, 174</sup> Platinized CEs have been well recognized to be 'expensive' due to the nobility of Pt. However, when thinking of the cost of Pt catalytic coatings, one has to consider the actual amount of Pt that has been used. In fact, the mass loading of Pt required for an efficient DSC is quite low, usually being around 0.1 g for  $1 \text{ m}^2$ .

With optimized fabrication conditions, this could be further reduced to much lower values.<sup>175</sup> From this point, the actual cost of Pt in DSCs could even be lower than some other components such as the TCO electrodes.

Most commonly, Pt catalytic coatings are produced by Thermal Decomposition (TD) of Pt precursors, such as hexachloroplatinic acid ( $\text{H}_2\text{PtCl}_6$ ).<sup>91</sup> The method results in highly active Pt coatings that are employed for most high efficiency DSCs.<sup>21, 139</sup> However, the method offers poor control of coating morphology, and the involved sintering process at around 400 °C restricts its application to flexible plastic TCO electrodes. It was also reported that  $\text{H}_2\text{PtCl}_6$  would only be completely decomposed by sintering at a temperature over 580 °C. The commonly used 400 °C would leave over 20 % Pt in its 2+ and 4+ form.<sup>176</sup>

Alternatively, Pt CEs could be produced by room-temperature processes such as magnetron sputtering<sup>174, 177-179</sup>, electrochemical deposition<sup>175, 180-186</sup> and chemical reduction<sup>176</sup>. Electrochemical deposition is a low-cost non-vacuum method that has been intensively studied in recent years.<sup>77, 175, 179, 181, 182, 185</sup> Detailed studies have been carried out on constant potential electrodeposition,<sup>180, 185</sup> pulsed-current electrodeposition,<sup>182</sup> effects of additives,<sup>175</sup> etc. Many of these have shown enhanced electrochemical activity compared to Pt coatings produced by thermal decomposition and magnetron sputtering.

Carbon based materials are particularly attractive for their much lower cost compared to other catalytic materials. They are, however, less electrochemically active than Pt in terms of triiodide reduction. Efficient DSCs usually require a carbon catalytic coating with tens of micrometers thickness to ensure acceptable fill factors.<sup>165</sup> It is also difficult to fabricate carbon catalytic coatings with a low sheet resistance, which is particularly important when making monolithic DSCs using the carbon based counter electrodes. Possible approaches to improve the conductivity include mixing with graphite<sup>89</sup> and doping with Pt<sup>187</sup>.

With the recent advances in novel functional materials, novel catalysts such as poly(3,4-ethylenedioxythiophene) (PEDOT)<sup>170, 188-192</sup> have been used to fabricate DSC CEs with enhanced electrochemical performance. PEDOT was firstly synthesized by Jonas et al. in late 1980s<sup>193</sup>, and has now been widely applied to commercial products in the electronics and display industry. In its doped form, PEDOT shows good conductivity and catalytic activity towards the reduction of triiodide.<sup>194, 195</sup> Catalytic coatings for DSCs could be produced by electrochemical polymerization,<sup>195, 196</sup> which is typically performed in organic electrolyte

containing  $\text{LiClO}_4$ .<sup>197</sup> The process results in the doping of PEDOT with  $\text{ClO}_4$  and therefore an enhanced conductivity. Research has also been conducted to further improve the electrochemical activity of PEDOT coatings using porous carrier bodies such as  $\text{TiO}_2$ .<sup>198</sup> The rapid development in PEDOT-based DSC CEs provides us with an alternative solution to low-cost polymer-based DSC CEs.

Until now, high conversion efficiencies have been achieved with DSCs using various catalytic coatings. It seems like once a threshold of the catalytic performance is achieved, the overall solar cell efficiency is unlikely to significantly vary depending on the type of catalytic coating. A major focus for the future research can be on the fabrication of catalytic coatings using continuous processes.

## 1.6 *DSCs with modified architectures*

Sandwich devices constructed on FTO glass electrodes are by far the most commonly adapted device architecture for DSCs. Standardized device fabrication procedures have been summarized leading to consistent high performance.<sup>20</sup> However, work has been conducted to modify DSC architectures. The aim is to achieve further reduced production cost and the feasibility of continuous production. Most previous works on alternative device architecture focus on reducing the use of FTO glass which accounts for a major part of the DSC fabrication cost.<sup>199</sup>

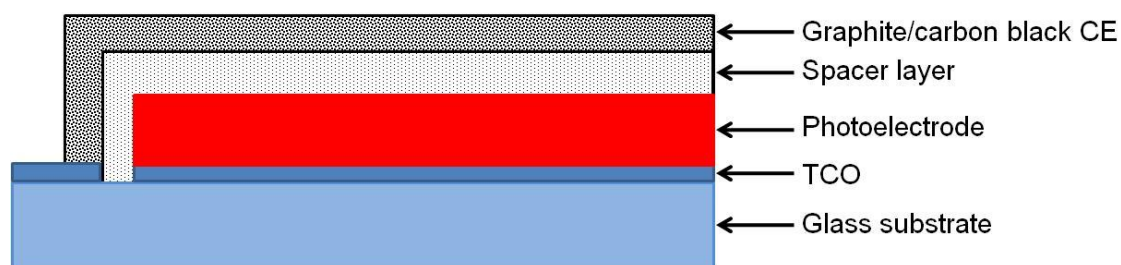
### 1.6.1 **Monolithic DSCs based on carbon counter electrodes**

Monolithic DSCs represent an alternative architecture to the conventional sandwich devices.<sup>89</sup> The device architecture was firstly reported by Kay et al in 1996.<sup>89</sup> Prototypes of monolithic DSCs were fabricated with a certified conversion efficiency of 6.67 %. The structure details of the cell are schematically shown in Figure 1.6. The cell employs only one piece of TCO glass, with an insulating track etched through the TCO layer to form two separated electrodes on the same substrate. A CE made of a mixture of carbon black and graphite is used to replace platinized CEs as used in sandwiched DSCs. A porous rutile  $\text{TiO}_2$  spacer layer is printed between  $\text{TiO}_2$  photoelectrode and CEs to achieve electrical insulation while allowing for free ionic diffusion of redox mediators. Additionally the spacer layer functions as a light reflector to enhance light absorption, especially in the red light region. As proposed in Kay's paper,

series connected monolithic DSC modules could be fabricated by continuous laser scribing and printing technique. Even device sealing could be eliminated in quasi or fully solid state monolithic DSCs employing polymer electrolyte or polymer hole-conductors.<sup>187, 200</sup> Monolithic DSC architecture is therefore considered as a low cost photovoltaic device configuration suitable for high throughput non-vacuum production.

Other than properly selected sensitizer and electrolyte system, performances of monolithic DSCs are substantially affected by the properties of spacer layer and carbon-based CEs. A highly porous spacer is required to allow for efficient ionic diffusion. In solid state devices, this is even important as the infiltration of polymer electrolyte or polymer hole-conductors into porous layers is much more difficult than the filling of liquid electrolyte.<sup>201</sup> Thompson et al. investigated the role of the spacer layer in monolithic DSCs.<sup>202</sup> In their study, a high porosity was achieved through adding polymeric binders as well as using a high percentage of large particles with sizes of 300~400 nm. The study also compared the monolithic DSCs with  $\text{ZrO}_2$  spacer to those with rutile  $\text{TiO}_2$  spacer and those without spacer, and found  $\text{ZrO}_2$  a better insulator to achieve a better cell performance.

On the other hand, the carbon based CE is responsible for both electric conduction and redox mediator regeneration. The use of graphite is to facilitate sufficient electrical conduction, while high surface area carbon black is to enhance the catalytic activity.<sup>41, 89</sup> The performance of the graphite/carbon black CEs could be further improved by doping with Pt, which enhances the catalytic activity and the conductivity of the CE layer.<sup>187</sup> However, this would increase the complexity and therefore the cost of the device fabrication process.



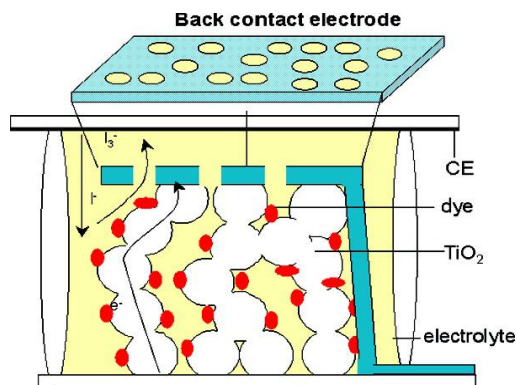
**Figure 1.6** Schematic configuration of a typical monolithic DSC. From the bottom to the top, the device comprises of TCO glass with an etched insulating track, a nanocrystalline  $\text{TiO}_2$  (anatase) photoelectrode layer, an insulating light reflecting porous  $\text{TiO}_2$  (rutile) layer and a CE layer comprising a mixture of graphite and carbon black powders.<sup>89</sup>

### 1.6.2 Sharp's Back-contact DSCs

The concept of back-contact pn junction solar cells was introduced by Schwartz et al. in 1977.<sup>203</sup> In these solar cells, both p and n contacting electrodes are located on the rear side of the silicon, resulting in reduced shadowing by the front contact fingers and reduced Ohmic loss using more conductive back-contact electrodes. When making solar cells with high current, such as large-scale modules and the cells used in concentrated sunlight, the back-contact concept is especially promising as the advantage of the reduced optical and Ohmic losses become more pronounced.

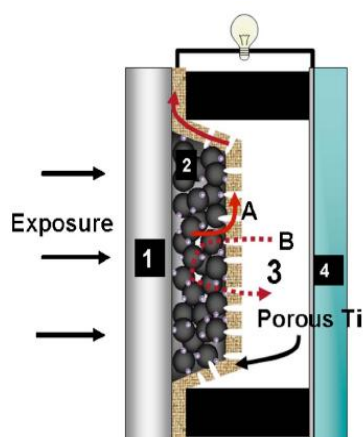
Yet, this classical back-contact design has not been applied to DSC devices. Although alternative device concepts such as the architecture shown in Figure 1.7 and Figure 1.8 were described as '*back contact DSCs*',<sup>204-207</sup> the use of this term is ambiguous. The classical back-contact architecture designed for silicon solar cells are of monolithic structure with both contacting electrodes located on the same substrate. The designs shown in Figure 1.7 and Figure 1.8 still require a secondary substrate working as a CE and are therefore not monolithic. These devices exhibit the advantage that light can reach the dye-sensitized TiO<sub>2</sub> layer without having to pass through a conducting transparent electrode, therefore avoiding transmission losses that typically occur in this layer.

BCDSC design shown in Figure 1.7 was reported by Fuke et al. in 2007<sup>204</sup>. They described in detail the fabrication of a TCO-less BCDSC with a conversion efficiency of 7.1 %. In their cell a vacuum deposited Ti metal layer covering the rear side of the TiO<sub>2</sub> film was employed as the WE. A Pt-coated glass was used as a CE. The Ti WE was thick enough to achieve sufficient conductivity and was also sufficiently porous to allow free diffusion of I<sup>-</sup>/I<sub>3</sub><sup>-</sup>



**Figure 1.7** Schematic illustration of a TCO less back contact DSC, taken from reference [204].<sup>204</sup> A vacuum deposited Ti metal layer covering the reverse side of the  $\text{TiO}_2$  film is used as the WE, while a Pt-coated glass is used as the CE.

Yohei Kashiwa et al. reported an all-metal-electrode-type DSC (Figure 1.8).<sup>207</sup> Their design is similar to the BCDSC reported by Fuke et al.. However a Pt coated Ti metal foil rather than a glass piece was used as the CE. A novel method was used to improve the porosity of the Ti WE. Tetrapod shaped ZnO whiskers were deposited above the  $\text{TiO}_2$  film, and were subsequently dissolved by 0.1 M HCl after the Ti deposition. This results in straight channels on the Ti WE which facilitate the diffusion of redox mediators. With the improved fabrication technique, a higher efficiency of 7.43 % was measured compared to a conventional DSC with an efficiency of 8.44 %.



**Figure 1.8** All-metal-electrode-type DSC constructed with (1) a glass slide, (2) a  $\text{TiO}_2$  semiconductor film, (3) a porous titanium film and (4) a platinum coated titanium foil, taken from reference [207].<sup>207</sup>

### 1.6.3 Electron transport in back-contact DSCs

Due to the difference in electrode configuration, the direction of electron transport in Sharp's BCDSCs is differed from that in the sandwiched DSCs (Figure 1.9). This may results in the difference in charge collection efficiencies of the two systems. A detailed study comparing electron transport in a DSC and a BCDSC was carried out by Fuke et al.<sup>205</sup> They compared the change of  $J_{sc}$  of the two devices with increasing  $\text{TiO}_2$  film thickness, and found that the increase in  $J_{sc}$  is less pronounced in the BCDSC than in the DSC. They also noticed a drop in  $J_{sc}$  when the  $\text{TiO}_2$  film is over 15  $\mu\text{m}$  thick.

The  $J_{sc}$  of a solar cell depends on the incident photon flux  $I_0$ , Light Harvesting Efficiency (*LHE*), electron injection efficiency  $\Phi_{inj}$  and charge collection efficiency  $\Phi_{coll}$  (Equation 1.8)

$$J_{sc} = I_0 \cdot LHE \cdot \Phi_{inj} \cdot \Phi_{coll} \quad 1.8$$

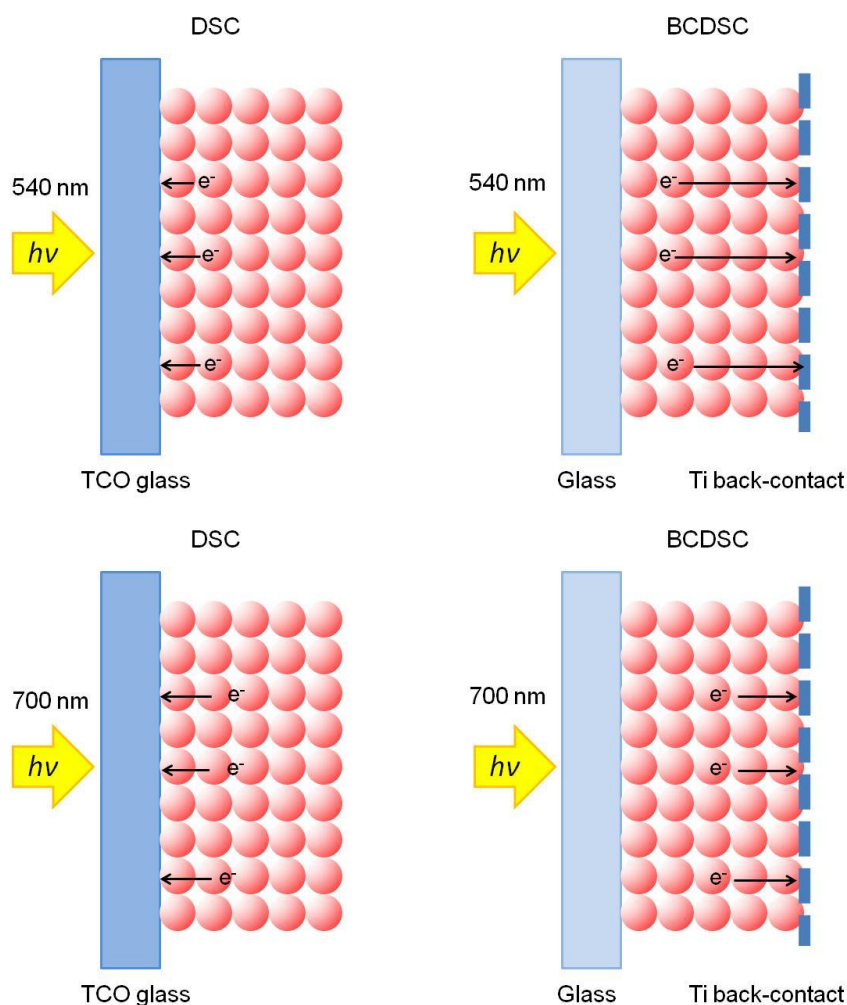
Due to the use of a transparent front window glass, more light is transmitted into the BCDSC than in the DSC that uses TCO glass. As such,  $I_0$  is higher in the BCDSC than in the DSC.  $\Phi_{inj}$  are also similar for the two cells due to the use of the same  $\text{TiO}_2$ , dye and electrolyte. The lower  $J_{sc}$  measured for the BCDSC is hence due to the lower  $\Phi_{coll}$  in the cell.

Further studies were conducted to investigate the origin for the lower  $\Phi_{coll}$  in the BCDSC.  $\Phi_{coll}$  of a cell depends mainly on four factors, namely the redox reaction at the Pt CE, the redox transport in the electrolyte, the electron transfer at the interface between the Ti back-contact electrode and the  $\text{TiO}_2$  film, and the electron transport in the mesoporous  $\text{TiO}_2$  film. The redox reaction is considered to be similar for the two cells due to the use of the same Pt CE and the same electrolyte composition. On the other hand, similar  $\text{I}_3^-$  concentrations were measured near the front windows of the two cells using Raman scattering measurement, meaning a smooth redox couple diffusion in both cells. Besides, the electron transfer at the Ti/ $\text{TiO}_2$  interface is considered to be efficient, as the two materials make a perfect Ohmic contact. The lower  $\Phi_{coll}$  is therefore believed to be mostly due to the inefficient electron transport in the  $\text{TiO}_2$  film.

The authors then calculated the Average Electron Transport Lengths (AETLs) of the two cells under 540 nm and 700 nm light illumination. According to the authors, the AETL refers to the average lengths that electrons need to travel before they are collected by electrodes. Since the N719 dye has an absorption maximum near 540 nm, in both devices electrons are generated at an average distance of around 3  $\mu\text{m}$  away from the front windows under 540 nm illumination.



However, due to the difference in the direction of electron diffusion in the two devices, the AETL is much longer in the BCDSC than in the DSC when using  $\text{TiO}_2$  films thicker than  $10\ \mu\text{m}$ . The charge collection in the BCDSC is therefore less efficient, and this explains the less increment of  $J_{sc}$  in the BCDSC than in the DSC when using thick  $\text{TiO}_2$  films. When using  $700\ \text{nm}$  light, the AETL in the BCDSC is also larger than that in the DSC. However, the difference is smaller due to the lower extinction coefficient of the N719 dye at this wavelength.



**Figure 1.9** Scheme of the electron diffusion in a conventional DSC photoelectrode and a 'Sharp' back-contact DSC photoelectrode under  $540\ \text{nm}$  and  $700\ \text{nm}$  illumination. Note that under  $540\ \text{nm}$  illumination, electrons are generated close to the front window, results in longer diffusion pathway for electrons to be collected in BCDSCs.

### 1.7 *Objective of the current work*

The objective of the current work is to develop two back-contact DSC architectures, one with interdigitated finger electrodes and the other with coplanar electrodes. The two types of DSCs both feature the WE and the CE on the rear side of the dye-sensitized TiO<sub>2</sub> photoelectrodes. The two types of back-contact DSCs proposed in this project are differed from the back-contact DSCs in literature. To the best of our knowledge, it is the first time that classical back-contact architectures are adopted to fabricate DSCs.

There are at least four advantages of these back-contact designs. Firstly, the usage of TCO electrodes could be reduced or even omitted. Secondly, cheaper and more conductive metal electrode materials can be used. Thirdly, the devices can be sealed by transparent cover slides, therefore avoiding optical transmission losses typically occurred on TCO glass. Fourthly, the back-contact DSCs could be assembled with conventional TiO<sub>2</sub> WEs to construct tandem DSCs.

The thesis is divided into four parts. Chapter 2 describes DSC fabrication procedures and characterization techniques. Relevant theoretical and practical issues are discussed. Chapter 3, 4 and 5 present the fabrication of interdigitated electrodes, electrochemical deposition of catalytic coating and thereafter the construction of back-contact DSCs based on coated electrodes. Chapter 6 presents the works on back-contact DSCs based on coplanar electrodes. Chapter 7 investigates the use of back-contact DSCs in three-terminal tandem DSCs. Chapter 8 draws general conclusions of the present work and proposes the future perspectives of our back-contact DSCs.

### 1.8 *References to Chapter 1*

- [1] A. J. Nozik, "BASIC RESEARCH NEEDS FOR SOLAR ENERGY UTILIZATION", presented at *Basic Energy Sciences Workshop on Solar Energy Utilization*, Bethesda North Marriott Hotel and Conference Center Bethesda, Maryland, **2005**.
- [2] M. Grätzel, *Nature* **2001**, 414, 338.
- [3] R. Williams, *J. Chem. Phys.* **1960**, 32, 1505.
- [4] A. E. Becquerel, *Compt. Rend. Acad. Sci.* **1839**, 9, 145.
- [5] W. Smith, *Nature* **1873**, 303.
- [6] W. G. Adams, R. E. Day, *Philos. T. R. Soc. Lond.* **1877**, 167, 313.
- [7] C. E. Fritts, *Van Nostrand's Engineering Magazine* **1885**, 32, 392.

- [8] J. J. S. Albert Einstein, *Einstein's Miraculous Year: Five Papers that Changed the Face of Physics*, Princeton University Press, Princeton, NJ 2005.
- [9] A. Einstein, *Ann. Phys.* **1905**, 17, 132.
- [10] D. Chapin, *J. Appl. Phys.* **1954**, 25, 676.
- [11] M. Telkes, *J. Appl. Phys.* **1947**, 18, 1116.
- [12] S. Wagner, *Appl. Phys. Lett.* **1974**, 25, 434.
- [13] L. Kazmerski, *Appl. Phys. Lett.* **1976**, 29, 268.
- [14] A. Goetzberger, C. Hebling, H.-W. Schock, *Mat. Sci. Eng. R-Rept.* **2003**, 40, 1.
- [15] G. Yu, J. Gao, J. C. Hummelen, F. Wudl, A. J. Heeger, *Science* **1995**, 270, 1789.
- [16] M. A. Green, K. Emery, Y. Hishikawa, W. Warta, *Prog. Photovoltaics*. **2011**, 19, 84.
- [17] BP, 2011.
- [18] National Renewable Energy Laboratory (NREL) USA.
- [19] M. Nazeeruddin, A. Kay, I. Rodicio, R. Humphrybaker, E. Muller, P. Liska, *J. Am. Chem. Soc.* **1993**, 115, 6382.
- [20] S. Ito, T. N. Murakami, P. Comte, P. Liska, C. Grätzel, M. K. Nazeeruddin, M. Grätzel, *Thin Solid Films* **2008**, 516, 4613.
- [21] M. A. Green, K. Emery, Y. Hishikawa, W. Warta and E. D. Dunlop, *Prog. Photovoltaics*. **2012**, 20, 12.
- [22] M. Nazeeruddin, P. Pechy, T. Renouard, S. Zakeeruddin, R. Humphry-Baker, P. Comte, *J. Am. Chem. Soc.* **2001**, 123, 1613.
- [23] P. Wang, S. M. Zakeeruddin, J. E. Moser, M. K. Nazeeruddin, T. Sekiguchi, M. Grätzel, *Nat. Mater.* **2003**, 2, 402.
- [24] Y. Bai, Y. Cao, J. Zhang, M. Wang, R. Li, P. Wang, S. M. Zakeeruddin, M. Grätzel, *Nat. Mater.* **2008**, 7, 626.
- [25] Y. Cao, J. Zhang, Y. Bai, R. Li, S. M. Zakeeruddin, M. Grätzel, P. Wang, *J. Phys. Chem. C* **2008**, 112, 13775.
- [26] N. Kato, Y. Takeda, K. Higuchi, A. Takeichi, E. Sudo, H. Tanaka, T. Motohiro, T. Sano, T. Toyoda, *Sol. Energ. Mat. Sol. C* **2009**, 93, 893.
- [27] P. M. Sommeling, M. Späth, H. J. P. Smit, N. J. Bakker, J. M. Kroon, *J. Photoch. Photobio. A* **2004**, 164, 137.
- [28] H. Pettersson, T. Gruszecki, L. Johansson, P. Johander, *Sol. Energ. Mat. Sol. C* **2003**, 77, 405.
- [29] K. Kalyanasundaram, Ed. *Dye-sensitized Solar Cells*, EPFL Press, Lausanne, Switzerland 2010.
- [30] K. K. N. Simon M. Sze, *PHYSICS OF SEMICONDUCTOR DEVICES*, John Wiley & Sons, Inc., Hoboken 2006.
- [31] H. Ehrenreich, Ed. *Principal Conclusions of the American Physical Society Study Group on Solar Photovoltaic Energy Conversion*, 1979.
- [32] P. Baruch, *J. Appl. Phys.* **1985**, 57, 1347.
- [33] M. Grätzel, *J. Photoch. Photobio. C* **2003**, 4, 145.
- [34] M. Grätzel, *Prog. Photovoltaics*. **2000**, 8, 171.
- [35] G. Boschloo, A. Hagfeldt, *Accounts. Chem. Res.* **2009**, 42, 1819.
- [36] J. N. Clifford, E. Palomares, M. K. Nazeeruddin, M. Grätzel, J. R. Durrant, *J. Phys. Chem. C* **2007**, 111, 6561.
- [37] S. Huang, G. Schlichthorl, A. Nozik, M. Grätzel, A. Frank, *J. Phys. Chem. B* **1997**, 101, 2576.

- [38] P. J. P. Cameron, L. M. & Hore, S., *J. Phys. Chem. B* **2005**, 109, 930.
- [39] P. J. Cameron, L. M. Peter, *J. Phys. Chem. B* **2003**, 107, 14394.
- [40] A. Hagfeldt, M. Graetzel, *Chem. Rev.* **1995**, 95, 49.
- [41] G. B. A. Hagfeldt, L. Sun, L. Kloo, H. Pettersson, *Chem. Rev.* **2010**, 110, 6595.
- [42] Y. Tachibana, J. Moser, M. Grätzel, D. Klug, J. Durrant, *J. Phys. Chem. US* **1996**, 100, 20056.
- [43] J. Bisquert, I. n. Mora-Seró, *J. Phys. Chem. Lett.* **2009**, 1, 450.
- [44] F. Fabregat-Santiago, I. Mora-Sero, G. Garcia-Belmonte, S. Gimenez, J. Bisquert, *J. Phys. Chem. C* **2009**, 113, 17278.
- [45] J. Nelson, *Phys. Rev. B* **1999**, 59, 15374.
- [46] J. Gonzalez-Vazquez, J. Anta, J. Bisquert, *J. Phys. Chem. C* **2010**, 114, 8552.
- [47] I. Mora Sero, J. Bisquert, *Nano Lett.* **2003**, 3, 945.
- [48] A. C. Fisher, L. M. Peter, E. A. Ponomarev, A. B. Walker, K. G. U. Wijayantha, *J. Phys. Chem. B* **2000**, 104, 949.
- [49] A. J. Frank, N. Kopidakis, J. van de Lagemaat, *Coordin. Chem. Rev.* **2004**, 248, 1165.
- [50] P. E. de Jongh, D. Vanmaekelbergh, *Phys. Rev. Lett.* **1996**, 77, 3427.
- [51] J. Nelson, S. A. Haque, D. R. Klug, J. R. Durrant, *Phys. Rev. B* **2001**, 63.
- [52] Q. Wang, S. Ito, M. Grätzel, F. Fabregat-Santiago, I. Mora-Sero, J. Bisquert, *J. Phys. Chem. B* **2006**, 110, 25210.
- [53] J. Krüger, R. Plass, M. Grätzel, P. J. Cameron, L. M. Peter, *J. Phys. Chem. B* **2003**, 107, 7536.
- [54] T. Nguyen, L. Peter, H. Wang, *J. Phys. Chem. C* **2009**, 113, 8532.
- [55] D. Kuang, J. Brillet, P. Chen, M. Takata, S. Uchida, H. Miura, K. Sumioka, S. M. Zakeeruddin, M. Grätzel, *Acs Nano* **2008**, 2, 1113.
- [56] M. Durr, A. Schmid, M. Obermaier, S. Rosselli, A. Yasuda, G. Nelles, *Nat. Chem.* **2005**, 4, 607.
- [57] F. Pichot, J. R. Pitts, B. A. Gregg, *Langmuir* **2000**, 16, 5626.
- [58] G. Boschloo, J. Lindstrom, E. Magnusson, A. Holmberg, A. Hagfeldt, *J. Photoch. Photobio. A* **2002**, 148, 11.
- [59] S. A. Haque, E. Palomares, H. M. Upadhyaya, L. Otley, R. J. Potter, A. B. Holmes, J. R. Durrant, *Chem. Commun.* **2003**, 3008.
- [60] S. Ito, N. L. C. Ha, G. Rothenberger, P. Liska, P. Comte, S. M. Zakeeruddin, P. Pechy, M. K. Nazeeruddin, M. Grätzel, *Chem. Commun.* **2006**, 4004.
- [61] C. Longo, J. Freitas, M. A. De Paoli, *J. Photoch. Photobio. A* **2003**, 159, 33.
- [62] D. S. Zhang, T. Yoshida, T. Oekermann, K. Furuta, H. Minoura, *Adv. Funct. Mater.* **2006**, 16, 1228.
- [63] X. Jiang, F. Wong, M. Fung, S. Lee, *Appl. Phys. Lett.* **2003**, 83, 1875.
- [64] C. Agashe, O. Kluth, G. Schope, H. Siekmann, J. Hupkes, B. Rech, *Thin Solid Films* **2003**, 442, 167.
- [65] Y. Igasaki, H. Saito, *J. Appl. Phys.* **1991**, 70, 3613.
- [66] H. Kim, J. S. Horwitz, W. H. Kim, A. J. Makinen, Z. H. Kafafi, D. B. Chrisey, *Thin Solid Films* **2002**, 420, 539.
- [67] J. Nishino, S. Ohshio, K. Kamata, *J. Am. Chem. Soc.* **1992**, 75, 3469.
- [68] J. Yoo, J. Lee, S. Kim, K. Yoon, I. J. Park, S. K. Dhungel, B. Karunagaran, D. Mangalaraj, J. S. Yi, *Thin Solid Films* **2005**, 480, 213.

- [69] M. W. Rowell, M. A. Topinka, M. D. McGehee, H. J. Prall, G. Dennler, N. S. Sariciftci, L. B. Hu, G. Gruner, *Appl. Phys. Lett.* **2006**, 88.
- [70] Y. Cao, G. M. Treacy, P. Smith, A. J. Heeger, *Appl. Phys. Lett.* **1992**, 60, 2711.
- [71] Y. Cao, G. Yu, C. Zhang, R. Menon, A. J. Heeger, *Synthetic Met.* **1997**, 87, 171.
- [72] S. A. Carter, M. Angelopoulos, S. Karg, P. J. Brock, J. C. Scott, *Appl. Phys. Lett.* **1997**, 70, 2067.
- [73] J. J. Yun, T. Y. Kim, S. Y. Cho, K. J. Hwang, J. W. Lee, H. B. Gu, K. H. Park, in *J. Sci. Conf. P.*, Vol. 1 (Ed: H. S. Nalwa), **2009**, 6.
- [74] J. J. Yun, T. Y. Kim, S. Y. Cho, E. M. Jin, H. B. Gu, K. H. Park, *J. Chem. Eng. Jpn.* **2008**, 41, 639.
- [75] K. Miettunen, J. Halme, M. Toivola, P. Lund, *J. Phys. Chem. C* **2008**, 112, 4011.
- [76] Q. Qin, J. Tao, Y. Yang, *Synthetic Met.* **2010**, 160, 1167.
- [77] S. Ito, N.-L. C. Ha, G. Rothenberger, P. Liska, P. Comte, S. M. Zakeeruddin, P. Pechy, M. K. Nazeeruddin, M. Grätzel, *Chem. Commun.* **2006**, 4004.
- [78] A. Kay, Vol. PhD, Ecole Polytechnique Fédérale de Lausanne, Lausanne, Switzerland 1994.
- [79] B. A. Gregg, F. Pichot, S. Ferrere, C. L. Fields, *J. Phys. Chem. B* **2001**, 105, 1422.
- [80] M. Ikeda, N. Koide, L. Han, A. Sasahara, H. Onishi, *Langmuir* **2008**, 24, 8056.
- [81] P. Wang, S. Zakeeruddin, P. Comte, R. Charvet, R. Humphry Baker, M. Grätzel, *J. Phys. Chem. B* **2003**, 107, 14336.
- [82] N. R. Neale, N. Kopidakis, J. van de Lagemaat, M. Grätzel, A. J. Frank, *J. Phys. Chem. B* **2005**, 109, 23183.
- [83] Z. P. Zhang, S. M. Zakeeruddin, B. C. O'Regan, R. Humphry-Baker, M. Grätzel, *J. Phys. Chem. B* **2005**, 109, 21818.
- [84] G. Boschloo, L. Hagelman, A. Hagfeldt, *J. Phys. Chem. B* **2006**, 110, 13144.
- [85] N. Kopidakis, N. R. Neale, A. J. Frank, *J. Phys. Chem. B* **2006**, 110, 12485.
- [86] J. Yum, S. Moon, R. Humphry-Baker, P. Walter, T. Geiger, F. Nuesch, *Nanotechnology* **2008**, 19.
- [87] B. O'Regan, M. Grätzel, *Nature* **1991**, 353, 737.
- [88] M. Wang, S. Moon, D. Zhou, F. Le Formal, N. Cevey Ha, R. Humphry Baker, *Adv. Funct. Mater.* **2010**, 20, 1821.
- [89] A. Kay, *Sol. Energ. Mat. Sol. C.* **1996**, 44, 99.
- [90] U. Bach, D. Lupo, P. Comte, M. J. E., F. Weissörtel, J. Salbeck, J. Spreitzer, M. Grätzel, *Nature* **1998**, 395, 583.
- [91] N. Papageorgiou, W. Maier, M. Grätzel, *J. Electrochem. Soc.* **1997**, 144, 876.
- [92] J. Bisquert, *J. Phys. Chem. B* **2002**, 106, 8774.
- [93] M. Grätzel, *J. Photoch. Photobio. A* **2004**, 164, 3.
- [94] M. K. Nazeeruddin, F. De Angelis, S. Fantacci, A. Selloni, G. Viscardi, P. Liska, S. Ito, T. Bessho, M. Grätzel, *J. Am. Chem. Soc.* **2005**, 127, 16835.
- [95] M. K. Nazeeruddin, A. Kay, I. Rodicio, R. Humphrybaker, E. Muller, P. Liska, N. Vlachopoulos, M. Grätzel, *J. Am. Chem. Soc.* **1993**, 115, 6382.
- [96] M. Grätzel, *J. Photoch. Photobio. A* **2004**, 164, 3.
- [97] B. Oregan, M. Grätzel, *Nature* **1991**, 353, 737.
- [98] C. J. Barbe, F. Arendse, P. Comte, M. Jirousek, F. Lenzmann, V. Shklover, M. Grätzel, *J. Am. Chem. Soc.* **1997**, 80, 3157.

- [99] U. Bach, D. Lupo, P. Comte, J. E. Moser, F. Weissortel, J. Salbeck, H. Spreitzer, M. Grätzel, *Nature* **1998**, 395, 583.
- [100] S. Y. Huang, G. Schlichthorl, A. J. Nozik, M. Grätzel, A. J. Frank, *J. Phys. Chem. B* **1997**, 101, 2576.
- [101] N. G. Park, J. van de Lagemaat, A. J. Frank, *J. Phys. Chem. B* **2000**, 104, 8989.
- [102] A. Kay, M. Grätzel, *Sol. Energ. Mat. Sol. C* **1996**, 44, 99.
- [103] N. Vlachopoulos, P. Liska, J. Augustynski, M. Grätzel, *J. Am. Chem. Soc.* **1988**, 110, 1216.
- [104] Y. R. Park, K. J. Kim, *Thin Solid Films* **2005**, 484, 34.
- [105] H. Tang, H. Berger, P. E. Schmid, F. Lévy, G. Burri, *Solid State Commun.* **1993**, 87, 847.
- [106] H. M. Cheng, J. M. Ma, Z. G. Zhao, L. M. Qi, *Chem. Mater.* **1995**, 7, 663.
- [107] R. L. Penn, J. F. Banfield, *Geochim. Cosmochim. AC.* **1999**, 63, 1549.
- [108] D. V. Bavykin, J. M. Friedrich, F. C. Walsh, *Adv. Mater.* **2006**, 18, 2807.
- [109] C. C. Wang, J. Y. Ying, *Chem. Mater.* **1999**, 11, 3113.
- [110] M. Grätzel, *J. Sol-gel. Sci. Techn.* **2001**, 22, 7.
- [111] P. S. Shinde, C. H. Bhosale, *Anal. Appl. Pyrol.* **2008**, 82, 83.
- [112] J. M. Macak, H. Tsuchiya, A. Ghicov, P. Schmuki, *Electrochem. Commun.* **2005**, 7, 1133.
- [113] M. Paulose, K. Shankar, O. K. Varghese, G. K. Mor, C. A. Grimes, *J. Phys. D Appl. Phys.* **2006**, 39, 2498.
- [114] K. Shankar, G. K. Mor, H. E. Prakasam, S. Yoriya, M. Paulose, O. K. Varghese, C. A. Grimes, *Nanotechnology* **2007**, 18.
- [115] J. T. Jiu, S. Isoda, F. M. Wang, M. Adachi, *J. Phys. Chem. B* **2006**, 110, 2087.
- [116] B. Liu, E. S. Aydil, *J. Am. Chem. Soc.* **2009**, 131, 3985.
- [117] X. J. Feng, K. Shankar, O. K. Varghese, M. Paulose, T. J. Latempa, C. A. Grimes, *Nano Lett.* **2008**, 8, 3781.
- [118] M. Law, L. E. Greene, J. C. Johnson, R. Saykally, P. D. Yang, *Nat. Chem.* **2005**, 4, 455.
- [119] M. Law, L. E. Greene, A. Radenovic, T. Kuykendall, J. Liphardt, P. D. Yang, *J. Phys. Chem. B* **2006**, 110, 22652.
- [120] D. Chen, F. Huang, Y. B. Cheng, R. A. Caruso, *Adv. Mater.* **2009**, 21, 2206.
- [121] A. B. F. Martinson, J. W. Elam, J. T. Hupp, M. J. Pellin, *Nano Lett.* **2007**, 7, 2183.
- [122] E. Galoppini, J. Rochford, H. H. Chen, G. Saraf, Y. C. Lu, A. Hagfeldt, G. Boschloo, *J. Phys. Chem. B* **2006**, 110, 16159.
- [123] K. Tennakone, J. Bandara, P. K. M. Bandaranayake, G. R. A. Kumara, A. Konno, *Jpn. J. Appl. Phys.* **2001**, 40, L732.
- [124] S. Chappel, A. Zaban, *Sol. Energ. Mat. Sol. C* **2002**, 71, 141.
- [125] S. Chappel, S. G. Chen, A. Zaban, *Langmuir* **2002**, 18, 3336.
- [126] A. Le Viet, R. Jose, M. V. Reddy, B. V. R. Chowdari, S. Ramakrishna, *J. Phys. Chem. C* **2010**, 114, 21795.
- [127] K. Eguchi, H. Koga, K. Sekizawa, K. Sasaki, *J. Ceram. Soc. Jpn.* **2000**, 108, 1067.
- [128] A. Mishra, M. Fischer, P. Bauerle, *Angew. Chem. Int. Edit.* **2009**, 48, 2474.
- [129] F. Gao, Y. Wang, D. Shi, J. Zhang, M. Wang, X. Jing, R. Humphry-Baker, P. Wang, S. M. Zakeeruddin, M. Grätzel, *J. Am. Chem. Soc.* **2008**, 130, 10720.
- [130] F. Gao, Y. Wang, J. Zhang, D. Shi, M. Wang, R. Humphry-Baker, P. Wang, S. M. Zakeeruddin, M. Grätzel, *Chem. Commun.* **2008**, 2635.

- [131] M. Grätzel, in *International Symposium on Solar cells and Solar Fuels*, Dalian, China **2008**.
- [132] Y. Cao, Y. Bai, Q. Yu, Y. Cheng, S. Liu, D. Shi, F. Gao, P. Wang, *J. Phys. Chem. C* **2009**, 113, 6290.
- [133] M. Grätzel, presented at *MRS Fall Meeting*, Boston, USA, **2009**.
- [134] S. M. Zakeeruddin, M. K. Nazeeruddin, R. Humphry-Baker, P. Péchy, P. Quagliotto, C. Barolo, G. Viscardi, M. Grätzel, *Langmuir* **2002**, 18, 952.
- [135] P. Wang, S. M. Zakeeruddin, J. E. Moser, M. K. Nazeeruddin, T. Sekiguchi, M. Grätzel, *Nat. Mater.* **2003**, 2, 402.
- [136] P. Wang, S. M. Zakeeruddin, R. Humphry-Baker, J. E. Moser, M. Grätzel, *Adv. Mater.* **2003**, 15, 2101.
- [137] S. Ito, S. M. Zakeeruddin, R. Humphry-Baker, P. Liska, R. Charvet, P. Comte, M. K. Nazeeruddin, P. Pechy, M. Takata, H. Miura, S. Uchida, M. Grätzel, *Adv. Mater.* **2006**, 18, 1202.
- [138] T. Horiuchi, H. Miura, K. Sumioka, S. Uchida, *J. Am. Chem. Soc.* **2004**, 126, 12218.
- [139] T. Bessho, S. M. Zakeeruddin, C. Yeh, E. Diau, M. Grätzel, *Angew. Chem. Int. Edit.* **2010**, 49, 6646.
- [140] H.-P. Lu, C.-Y. Tsai, W.-N. Yen, C.-P. Hsieh, C.-W. Lee, C.-Y. Yeh, E. W.-G. Diau, *J. Phys. Chem. C* **2009**, 113, 20990.
- [141] D. Kuciauskas, M. S. Freund, H. B. Gray, J. R. Winkler, N. S. Lewis, *J. Phys. Chem. B* **2001**, 105, 392.
- [142] G. Sauve, M. E. Cass, G. Coia, S. J. Doig, I. Lauermann, K. E. Pomykal, N. S. Lewis, *J. Phys. Chem. B* **2000**, 104, 6821.
- [143] G. Sauve, M. E. Cass, S. J. Doig, I. Lauermann, K. Pomykal, N. S. Lewis, *J. Phys. Chem. B* **2000**, 104, 3488.
- [144] C.-Y. Chen, S.-J. Wu, C.-G. Wu, J.-G. Chen, K.-C. Ho, *Angew. Chem. Int. Edit.* **2006**, 45, 5822.
- [145] A. Yella, H.-W. Lee, H. Tsao, C. Yi, A. Chandiran, M. K. Nazeeruddin, E. W.-G. Diau, C.-Y. Yeh, S. M. Zakeeruddin, M. Grätzel, *Science* **2011**, 334, 629.
- [146] P. Bonhôte, A.-P. Dias, N. Papageorgiou, K. Kalyanasundaram, M. Grätzel, *Inorg. Chem.* **1996**, 35, 1168.
- [147] B. Enright, G. Redmond, D. Fitzmaurice, *J. Phys. Chem. US* **1994**, 98, 6195.
- [148] J. van de Lagemaat, N. G. Park, A. J. Frank, *J. Phys. Chem. B* **2000**, 104, 2044.
- [149] N. Kopidakis, K. D. Benkstein, J. van de Lagemaat, A. J. Frank, *J. Phys. Chem. B* **2003**, 107, 11307.
- [150] C. Zhang, Y. Huang, Z. Huo, S. Chen, S. Dai, *J. Phys. Chem. C* **2009**, 113, 21779.
- [151] Z. S. Wang, K. Sayama, H. Sugihara, *J. Phys. Chem. B* **2005**, 109, 22449.
- [152] T. Daeneke, T. Kwon, A. Holmes, N. Duffy, U. Bach, L. Spiccia, *Nat. Chem.* **2011**, 3, 211.
- [153] Z. Zhang, P. Chen, T. N. Murakami, S. M. Zakeeruddin, M. Grätzel, *Adv. Funct. Mater.* **2008**, 18, 341.
- [154] P. Wang, S. M. Zakeeruddin, J. E. Moser, R. Humphry-Baker, M. Grätzel, *J. Am. Chem. Soc.* **2004**, 126, 7164.
- [155] M. Liberatore, L. Burtone, T. M. Brown, A. Reale, A. Di Carlo, F. Decker, S. Caramori, C. A. Bignozzi, *Appl. Phys. Lett.* **2009**, 94.

- [156] H. Nusbaumer, J. E. Moser, S. M. Zakeeruddin, M. K. Nazeeruddin, M. Grätzel, *J. Phys. Chem. B* **2001**, 105, 10461.
- [157] P. Wang, S. Zakeeruddin, J. Moser, M. Nazeeruddin, T. Sekiguchi, M. Grätzel, *Nat. Mater.* **2003**, 2, 402.
- [158] W. Kubo, S. Kambe, S. Nakade, T. Kitamura, K. Hanabusa, Y. Wada, S. Yanagida, *J. Phys. Chem. B* **2003**, 107, 4374.
- [159] P. Wang, S. M. Zakeeruddin, J. E. Moser, M. Grätzel, *J. Phys. Chem. B* **2003**, 107, 13280.
- [160] P. Wang, S. M. Zakeeruddin, I. Exnar, M. Grätzel, *Chem. Commun.* **2002**, 2972.
- [161] P. Wang, S. M. Zakeeruddin, P. Comte, I. Exnar, M. Grätzel, *J. Am. Chem. Soc.* **2003**, 125, 1166.
- [162] F. Gao, Y. Wang, D. Shi, J. Zhang, M. K. Wang, X. Y. Jing, R. Humphry-Baker, P. Wang, S. M. Zakeeruddin, M. Grätzel, *J. Am. Chem. Soc.* **2008**, 130, 10720.
- [163] P. Wang, B. Wenger, R. Humphry-Baker, J. E. Moser, J. Teuscher, W. Kantelechner, J. Mezger, E. V. Stoyanov, S. M. Zakeeruddin, M. Grätzel, *J. Am. Chem. Soc.* **2005**, 127, 6850.
- [164] P. Wang, S. M. Zakeeruddin, R. Humphry-Baker, M. Grätzel, *Chem. Mater.* **2004**, 16, 2694.
- [165] T. Murakami, S. Ito, Q. Wang, M. Nazeeruddin, T. Bessho, I. Cesar, *J. Electrochem. Soc.* **2006**, 153, A2255.
- [166] E. Ramasamy, W. Lee, D. Lee, J. Song, *Appl. Phys. Lett.* **2007**, 90, 173103.
- [167] G. Veerappan, K. Bojan, S. Rhee, *ACS Appl. Mater. & Interface* **2011**, 3, 857.
- [168] Z. Huang, X. Liu, K. Li, D. Li, Y. Luo, H. Li, *Electrochem. Commun.* **2007**, 9, 596.
- [169] W. Lee, E. Ramasamy, D. Lee, J. Song, *ACS Appl. Mater. & Interface* **2009**, 1, 1145.
- [170] Y. Saito, W. Kubo, T. Kitamura, Y. Wada, S. Yanagida, *J. Photoch. Photobio. A* **2004**, 164, 153.
- [171] M. Biancardo, K. West, F. C. Krebs, *J. Photoch. Photobio. A* **2007**, 187, 395.
- [172] W. J. Hong, Y. X. Xu, G. W. Lu, C. Li, G. Q. Shi, *Electrochem. Commun.* **2008**, 10, 1555.
- [173] M. Grätzel, *Accounts. Chem. Res.* **2009**, 42, 1788.
- [174] F. Hao, H. Lin, J. Zhang, D. Zhuang, Y. Liu, J. Li, *Electrochim. Acta.* **2010**, 55, 7225.
- [175] C. Lin, J. Lin, C. Wan, T. Wei, *Electrochim. Acta.* **2011**, 56, 1941.
- [176] H. Bonnemann, G. Khelashvili, S. Behrens, A. Hinsch, K. Skupien, E. Dinjus, *J. Clust. Sci.* **2007**, 18, 141.
- [177] T. Ma, X. Fang, M. Akiyama, K. Inoue, H. Noma, E. Abe, *J. Electroanal. Chem. Interf. Electrochem.* **2004**, 574, 77.
- [178] T. Hoshikawa, M. Yamada, R. Kikuchi, K. Eguchi, *J. Electroanal. Chem.* **2005**, 577, 339.
- [179] B. Koo, D. Lee, H. Kim, W. Lee, J. Song, *J. Electroceram.* **2006**, 17, 79.
- [180] C. H. Yoon, R. Vittal, J. Lee, W.-S. Chae, K.-J. Kim, *Electrochim. Acta.* **2008**, 53, 2890.
- [181] C. Yang, H. Zhang, Y. Zheng, *Curr. Appl. Phys.* **2011**, 11, S147.
- [182] S. Kim, Y. Nah, Y. Noh, J. Jo, D. Kim, *Electrochim. Acta.* **2006**, 51, 3814.
- [183] P. Li, J. Wu, J. Lin, M. Huang, Z. Lan, Q. Li, *Electrochim. Acta.* **2008**, 53, 4161.
- [184] G. Tsekouras, A. Mozer, G. Wallace, *J. Electrochem. Soc.* **2008**, 155, K124.



- [185] L. Chen, W. Tan, J. Zhang, X. Zhou, X. Zhang, Y. Lin, *Electrochim. Acta.* **2010**, 55, 3721.
- [186] Y.-S. Ko, Y.-U. Kwon, *Electrochim. Acta.* **2010**, 55, 7276.
- [187] H. Han, *Appl. Phys. Lett.* **2009**, 94, 103102.
- [188] J. Chen, H. Wei, K. Ho, *Sol. Energ. Mat. Sol. C.* **2007**, 91, 1472.
- [189] Y. Saito, T. Kitamura, Y. Wada, S. Yanagida, *Chem. Lett.* **2002**, 1060.
- [190] T. Muto, M. Ikegami, T. Miyasaka, *J. Electrochem. Soc.* **2010**, 157, B1195.
- [191] S. Patra, K. Barai, N. Munichandraiah, *Synthetic Met.* **2008**, 158, 430.
- [192] J. Pringle, V. Armel, M. Forsyth, D. MacFarlane, *Aust. J. Chem.* **2009**, 62, 348.
- [193] G. Heywang, F. Jonas, *Adv. Mater.* **1992**, 4, 116.
- [194] L. Groenendaal, F. Jonas, D. Freitag, H. Pielartzik, J. R. Reynolds, *Adv. Mater.* **2000**, 12, 481.
- [195] J. Pringle, V. Armel, D. MacFarlane, *Chem. Commun.* **2010**, **46**, 5367.
- [196] T. Chen, X. Wu, R. Rieke, *J. Am. Chem. Soc.* **1995**, 117, 233.
- [197] E. Nasybulin, S. Wei, M. Cox, I. Kymissis, K. Levon, *J. Phys. Chem. C* **2011**, 115, 4307.
- [198] S. Sakurai, H. Jiang, M. Takahashi, K. Kobayashi, *Electrochim. Acta.* **2009**, 54, 5463.
- [199] J. Kroon, *Prog. Photovoltaics.* **2007**, 15, 1.
- [200] H. Wang, G. Liu, X. Li, P. Xiang, Z. Ku, Y. Rong, M. Xu, L. Liu, M. Hu, Y. Yang, H. Han, *Energ. Environ. Sci.* **2011**, 4, 2025.
- [201] H. Han, U. Bach, Y. Cheng, R. Caruso, *Appl. Phys. Lett.* **2007**, 90.
- [202] S. J. Thompson, N. W. Duffy, U. Bach, Y.-B. Cheng, *J. Phys. Chem. C* **2010**, 114, 2365.
- [203] M. Lammert, R. J., *IEEE T. Electron. Dev.* **1977**, 24, 337.
- [204] N. Fuke, A. Fukui, Y. Chiba, R. Komiya, R. Yamanakay, L. Han, *Jpn. J. appl. Phys.* **2007**, 46, L420.
- [205] N. Fuke, A. Fukui, A. Islam, R. Komiya, R. Yamanaka, L. Han, H. Harima, *J. Appl. Phys.* **2008**, 104.
- [206] N. Fuke, F. Atsushi, K. Ryohichi, I. Ashraful, C. Yasuo, Y. Masatoshi, Y. Ryohsuke, H. Liyuan, *Chem. Mater.* **2008**, 20, 4974.
- [207] Y. Y. Yohei Kashiwa, Shuzi Hayasea, *Appl. Phys. Lett.* **2008**, 92.



## 2 Experimental methodology

### 2.1 *Materials and detergents*

#### 2.1.1 **Materials**

Three types of FTO glass (Table 2.1) were used in this project. The TEC-15 FTO glass was ordered from Pilkington (a NSG group company, United Kindom). The NSG 1 and NSG 2 FTO glass are the two batches of glass samples ordered from Nippon Sheet Glass (Japan). The thickness of these glass sheets were measured using a digital vernier. The sheet resistances (five-point average) were measured using a four-point surface conductivity probe (Jandel Model RM3-AR, UK). To measured the FTO layer thickness, the FTO surface was covered by Kapton sticky tapes (Ted Pellar, USA), leaving approximately 1 mm gaps. Zinc powder was then dispersed on top of the gap. 1 M HCl was applied to dissolve the zinc powder and produce hydrogen atom to chemically reduce and etch FTO. The tapes were removed and the FTO glass was washed. The thickness of the FTO layer was then measured using a DekTak Profilometer (Veeco instrument Inc., USA). The optical transmission of the FTO glass was measured using a Cary 5000 UV-Vis spectrometer (Agilent Technologies, Australia). Over the visible range, the transmission of the three types of FTO glass is generally over 80 %.

The Kapton<sup>®</sup> sheets (500HN grade, 128  $\mu\text{m}$  thickness) were obtained as free samples from Dupont Pty Ltd. The Surlyn<sup>®</sup> sheets (25  $\mu\text{m}$  thickness) were purchased from Solaronix, Aubonne, Switzerland. The titanium foil (0.3 mm thickness, 99.8 % commercial purity) was purchased from Baoye Titanium-nickel Industry Co. Ltd (Baoji, China).

**Table 2.1** The thickness, sheet resistance, FTO layer thickness and transmission of visible light of three FTO glass sheets used in our experiments.

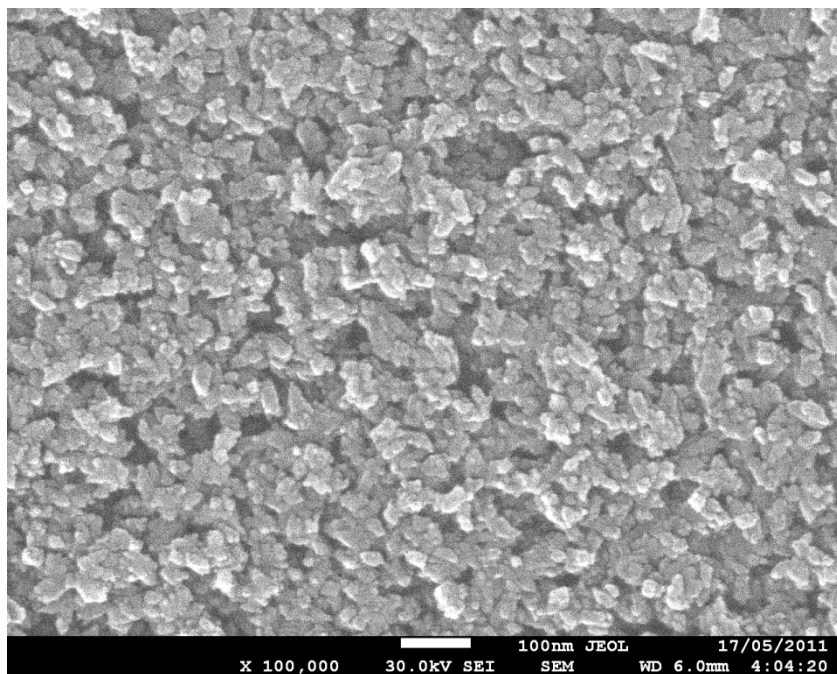
	Glass thickness (mm)	Sheet resistance ( $\Omega/\square$ )	FTO thickness (nm)	Transmission (%)
TEC-15	2.7	15.0	400	> 80 %
NSG 1	3.2	9.7	800	> 80 %
NSG 2	4.0	9.2	600	> 80 %

### 2.1.2 Chemicals and reagents

Unless otherwise stated, all chemicals and reagents used in this project were with the following grades and were purchased from the listed suppliers. All chemicals and reagents were used as received.

Deionized water was produced using ModelLab<sup>®</sup> Type II reagent grade water system (Continental Water System Pty Ltd, Australia). Ethanol (96 %), ethanol absolute (99.7 %), dimethylformamide ( $\geq 99.7$  %) and tert-Butanol ( $\geq 99.5$  %) were purchased from Merck Chemicals (Sydney, Australia). Acetic acid glacial (99.7 %) and hydrochloric acid (32 %) were purchased from Ajax Finechem. Acetonitrile (99.8 %, anhydrous), acetylacetone (99.5 %), 1-butyl-3-methylimidazolium iodide, chloroplatinic acid hexahydrate (powder and chunks), ethyl cellulose, guanidinium thiocyanate (99 %), Hellmanex<sup>™</sup> II (cleaner concentrate for cuvette washing), iodine ( $\geq 99.99$  %), lithium iodide (99.9 %), terpeneol anhydrous ( $\leq 0.5\%$  water), 4-tertbutylpyridine (98 %), tetraethylammonium perchloride ( $\geq 98$  %) and valeronitrile (99.5 %) were purchased from Sigma-Aldrich.

The TiO<sub>2</sub> screen printing pastes PST-18NR (20 nm particles, transparent) and PST-400C (400 nm particles, light scattering) was purchased from JGC Catalysts and Chemicals Ltd. The pastes contain 20 wt% nanoparticles, 10 wt% polymer binders and 70 % terpeneol. A high magnification SEM image of the printed PST-18NR film after sintering is shown in Figure 2.1.



**Figure 2.1** A scanning electron micrograph of the printed PST-18NR film after sintering.

Bis(tetrabutylammonium)[cis-di(thiocyanato)-bis(2,2'-bipyridyl-4-carboxylate-4'-carboxylic acid)-ruthenium(II)] (N719) dye was purchased from Dyesol (Queanbeyan, Australia). The (2,2':6',2' '-terpyridine-4,4',4' '-tricarboxylate)ruthenium(II) tris(tetrabutyl ammonium) tris(isothiocyanate) (N749) dye was synthesized according previously described procedures.<sup>1</sup>

## 2.2 *Standardized DSC fabrication procedures*

### 2.2.1 The preparation of FTO working electrode substrates

To prepare the FTO glass substrates for working electrodes, the received FTO glass sheets (NSG 2, 100 × 100 mm area) were cleaned by ultrasonic agitation in reagents following the order of 5 % Hellmanex solution, deionized water and ethanol (96 %, Merck) each for 10 min. Cleaned glass sheets were dried in air and stored for further use.

### 2.2.2 The deposition of dense TiO<sub>2</sub> blocking layer

Cleaned working electrodes sheets were immersed in 40 mM TiCl<sub>4</sub> aqueous solution and heated at 70 °C in an oven for 30 min. The glass sheets were then rinsed with deionized water and ethanol. The dense blocking layer was formed upon sintering after the screen printing

process. There are two purposes for the dense  $\text{TiO}_2$  blocking layer. Firstly is to strengthen the contact between the  $\text{TiO}_2$  photoelectrode and FTO and second is to reduce dark current caused by back electron transfer from FTO to triiodide ions.<sup>2</sup>

### 2.2.3 The preparation of dye-sensitized $\text{TiO}_2$ working electrodes

The screen-printing experiments were conducted using a Keywell screen-printer (Model KY-600FH, Kangyuan Industrial Co., LTD, Taiwan). Transparent  $\text{TiO}_2$  films with a  $4 \times 4$  mm dimension were printed from the PST-18NR paste using a 32T screen printing mesh with designed patterns. One print results in a  $\text{TiO}_2$  layer with a film thickness of around 6  $\mu\text{m}$ . Two transparent  $\text{TiO}_2$  layers were usually printed to obtain a film thickness of 12  $\mu\text{m}$ . An additional opaque  $\text{TiO}_2$  layer was printed from the PST-400C paste using the same 32T mesh. The sintered scattering layers have a thickness of around 6  $\mu\text{m}$ . For most sandwiched DSC devices,  $\text{TiO}_2$  working electrodes with a "12+6" (12  $\mu\text{m}$  transparent plus 6  $\mu\text{m}$  scattering  $\text{TiO}_2$  films) configuration were used. For back-contact DSCs, 12  $\mu\text{m}$  transparent films were used. After each printing, films were kept in clean petri dishes for 3 min and were then dried for 15 min on a hotplate heated at 125  $^\circ\text{C}$  for 15 min. The films were cooled down to room temperature, and then sintered on a hotplate (using a programmed sintering process as illustrated in Table 2.2).<sup>2</sup>

**Table 2.2** The scheme for the sintering of  $\text{TiO}_2$  mesoporous film.

Steps	(1)	(2)	(3)	(4)	(5)
Ramp time (min)	10	15	5	7	5
Temperature ( $^\circ\text{C}$ )	150	325	375	450	500
Hold time (min)	10	5	5	30	15

$\text{TiCl}_4$  post-treatment of mesoporous  $\text{TiO}_2$  films could effectively improve photocurrent by increasing the active surface area thus dye-loading and by increasing the diffusion coefficient of electrons in the  $\text{TiO}_2$  network.<sup>3</sup> To post-treat the working electrodes, sintered  $\text{TiO}_2$  films were immersed in 40 mM  $\text{TiCl}_4$  aqueous solution and heated at 70  $^\circ\text{C}$  in an oven for 30 min.

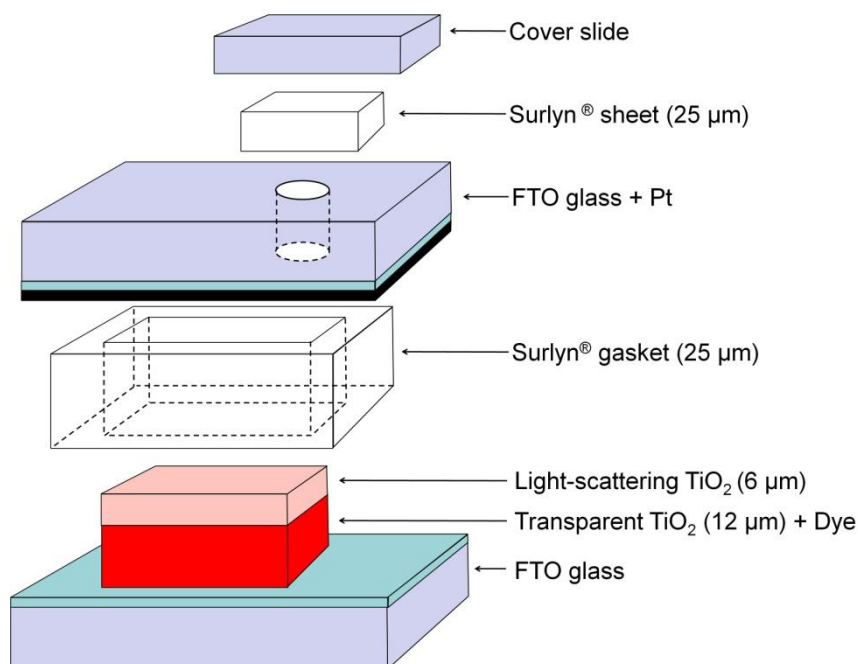
They were then rinsed with deionized water and ethanol, followed by heating with a hot air gun (Leister GH-6056, Leister Process Technologies, Sarnen, Switzerland) at a temperature of 500 °C for 30 min. After cooling to 80 °C, films were immersed in a solution of 0.3 mM N719 dye in a 1:1 (v/v) mixture of acetonitrile and tert-butanol and kept for 24 hours.

#### **2.2.4 The reparation of counter electrodes**

FTO glass sheets (NSG1, 100 × 100 mm area) were drilled to form 1 mm diameter holes. They were then cleaned in 0.1 M HCl by ultrasonic agitation for 10 min. The cleaning is to remove Fe ions which deteriorate the performance of DSCs.<sup>2</sup> They were then cleaned in reagents by ultrasonic agitation as described above. After drying, a drop of H<sub>2</sub>PtCl<sub>6</sub> precursor solution (10 mM in isopropanol) was spread onto the FTO surface followed by heating at 400 °C in a hot air gun.

#### **2.2.5 Cell construction**

The components used to construct a sandwiched DSC are schematically shown in Figure 2.2. Dyed TiO<sub>2</sub> working electrodes were rinsed with acetonitrile and were left to dry. They were then assembled with platinized counter electrodes into a sandwiched architecture. The sandwiched devices were sealed using hot-melt Surlyn<sup>®</sup> gaskets (Solaronix 25 µm thick). Devices were heated to approximately 110 °C and pressed by on a home-made hot-press. The inner frame of the gaskets was 5 × 6 mm and the frame width was 2 mm. Electrolyte containing 0.6 M 1-butyl-3-methylimidazolium iodide, 0.03 M iodine, 0.10 M guanidinium thiocyanate and 0.5 M 4-tertbutylpyridine in a mixture (volume ratio, 85:15) of acetonitrile (99.8%, anhydrous) and valeronitrile was filled into the sealed compartment through the entry ports of the counter electrodes by vacuum back-filling. To finish the cell, the entry ports were covered by small pieces of Surlyn<sup>®</sup> sheet and glass cover slides which were then sealed using a hot soldering iron.



**Figure 2.2** Construction of a sandwiched DSC device, reproduced from reference [2].<sup>2</sup>

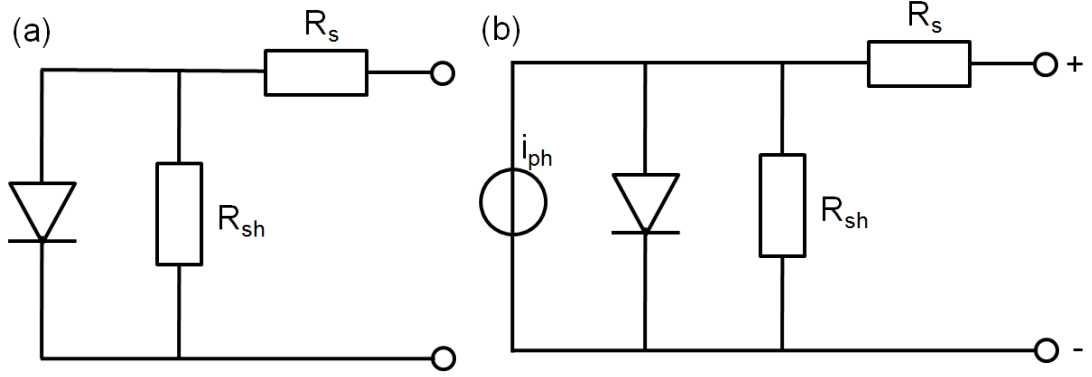
In order to minimize ohmic loss due to bad electrical connections, a solder (PX 2332-70, MBR Electronics, Switzerland) was applied evenly onto the two electrode surfaces using an ultrasonic soldering iron (USS-9200, MBR Electronics, Switzerland). Cables were then soldered onto the contact area.

## 2.3 *Characterization techniques*

### 2.3.1 **Current-voltage (IV) test**

Solar cells, including DSCs, can be simulated by the simple diode equivalent circuits<sup>4</sup> shown in Figure 2.1. Under dark, a solar cell performs similar to a circuit comprising a diode, a shunt resistance ( $R_{sh}$ ) and a series resistance ( $R_s$ ) (Figure 2.3 (a)). When illuminating with light, an additional photocurrent source ( $i_{ph}$ ) is added parallel to the diode to simulate the solar cell under working condition (Figure 2.3 (b)).





**Figure 2.3** Equivalent circuits to simulate DSCs operated under the (a) dark and (b) light illumination conditions.

According to the simple diode model, the output current ( $I_{cell}$ ) of a solar cell can be predicted using Equation 2.1.<sup>5</sup>

$$I_{cell} = I_{ph} - I_d - I_{sh} = I_{ph} - I_0 \left\{ \exp \left[ \frac{-q(V_{cell} + I_{cell}R_s)}{mk_B T} \right] - 1 \right\} - \frac{V_{cell} + I_{cell}R_s}{R_{sh}} \quad 2.1$$

where  $I_{ph}$  is the photocurrent from the current source,  $I_d$  is the dark current,  $I_{sh}$  is the shunt current,  $I_0$  is the reverse saturation current and  $V_{cell}$  is the output voltage of the solar cell.  $m$  is the diode ideality factor,  $k_B$  is the Boltzmann's constant and  $T$  is the absolute temperature.

Under open-circuit condition,  $I_{cell} = 0$  and  $V_{cell} = V_{oc}$ . From Equation 2.1,

$$I_{ph} - I_0 \left\{ \exp \left( \frac{-qV_{oc}}{mk_B T} \right) - 1 \right\} - \frac{V_{oc}}{R_{sh}} = 0 \quad 2.2$$

Since the value of  $R_{sh}$  is usually quite high,  $V_{oc}/R_{sh} \rightarrow 0$ . Equation 2.2 becomes

$$I_{ph} - I_0 \left\{ \exp \left( \frac{-qV_{oc}}{mk_B T} \right) - 1 \right\} = 0 \quad 2.3$$

$$V_{oc} = mV_T \ln \left( \frac{I_{ph}}{I_0} + 1 \right) \cong mV_T \ln \left( \frac{I_{ph}}{I_0} \right) \quad 2.4$$

where  $V_T = \frac{-k_B T}{q} = -0.026V$ . According to Equation 2.4,  $V_{oc}$  increases with photocurrent and accordingly with light intensity.

Under the short-circuit condition,  $V_{cell} = 0$  and

$$I_{cell} = I_{ph} = I_{sc} \quad 2.5$$

According to Equation 2.5, the  $I_{sc}$  of a solar cell is proportional to the light intensity.

The fill factor of the solar cell can be estimated using Equation 2.6. Graphically, the fill factor is the ratio between the solid and the dashed rectangular as shown in Figure 2.4.

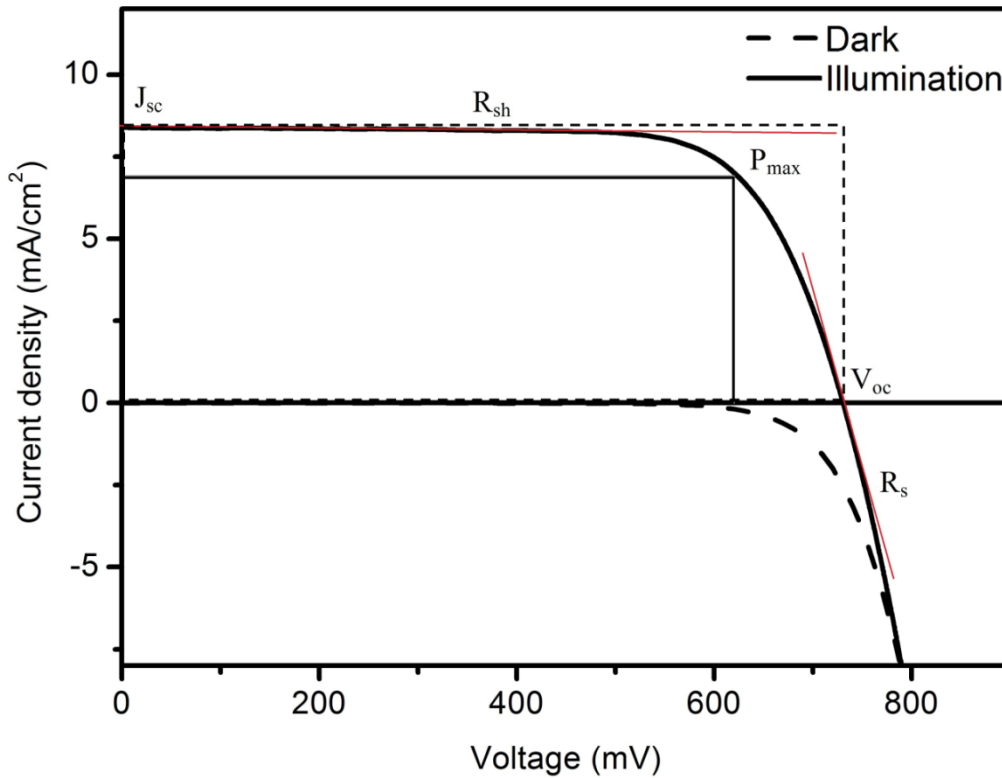
$$FF = \frac{P_{max}}{I_{sc} \times V_{oc}} = \frac{I_m V_m}{I_{sc} \times V_{oc}} \quad 2.6$$

where  $I_m$  and  $V_m$  are the current density and voltage corresponding to the maximum power point.

The solar energy to electricity conversion efficiency ( $\eta$ ) of the solar cells can be calculated using Equation 2.7.

$$\eta = \frac{V_{oc}(V) \times I_{sc}(mA) \times FF}{A(cm^2) \times P_{in}(mW)} \times 100 \% \quad 2.7$$

where  $FF$ ,  $A$  and  $P_{in}$  are the fill factor, testing area of the cell and the incident light power, respectively.



**Figure 2.4** The current-voltage curves measured for a DSC operated under the dark and light illumination condition.

In our experiment, the current-voltage (IV) measurements of DSCs were performed under dark as well as under light illumination conditions. A series of forward voltages, were applied

across the two terminals of the solar cells. The current generated by the devices was measured and converted into current density  $J$  (Figure 2.4).

The points where the illumination curve intersects the vertical and horizontal axes are the short-circuit current density ( $J_{sc}$ ) and the open-circuit voltage ( $V_{oc}$ ) points respectively. The shunt resistance can be estimated from the gradient of the plateau before the current onset, and the series resistance can be estimated from the gradient of the curve when it passes the  $V_{oc}$  point.

The IV testing system consists of a sun simulator (Oriel, USA) equipped with a 1,000 W xenon lamp and a SourceMeter (Keithley, Model 2400). The output of the system was adjusted using a calibrated silicon photodiode cell before each measurement. Devices were tested under simulated AM1.5 sunlight ( $100 \text{ mW/cm}^2$ ). Cells were covered by a  $6 \text{ mm} \times 6 \text{ mm}$  black metal mask during testing. For the IV test under differently light intensities, the output light was filtered by a series of metal grids to achieve 10.3 %, 38.5 %, 68.0 % and 100% light intensities. Devices were scanned with a series of bias voltages across a range of 0 to 1000 mV. The current response was measured using the SourceMeter, and the results were plotted using a custommade testing program.

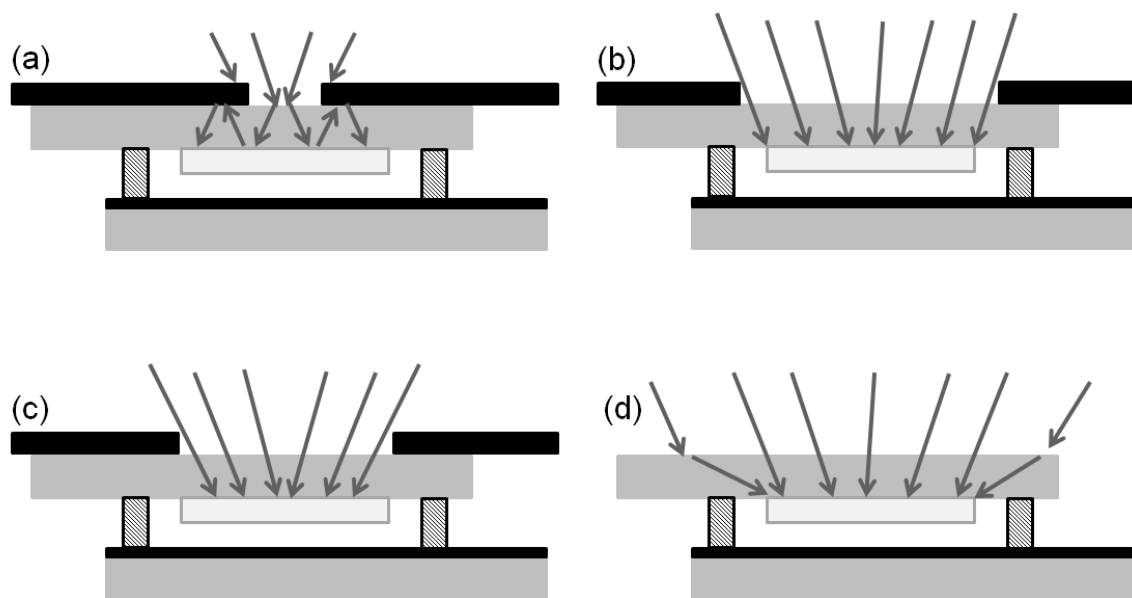
It is worthwhile mentioning that due to the use of diffusive light for the IV test, accuracy of IV results are found to be affected by the aperture size of the mask.<sup>6</sup>

(a) When using mask apertures smaller than the area of the  $\text{TiO}_2$  films (Figure 2.5(a)), there is a significantly drop of  $J_{sc}$  resulted from the shading losses by the aperture. While the shading effect is compensated by the light which is reflected and reabsorbed by the unexposed  $\text{TiO}_2$ , the combined effect makes the results very unreliable. In general, the  $J_{sc}$  values measured using this setup are found to be underestimated.

(b) When using apertures having a similar size with the  $\text{TiO}_2$  films (Figure 2.5(b)), the shading effect still exists. Besides, the alignment of the aperture with the  $\text{TiO}_2$  films is difficult. These factors make the interpretation of results inaccurate.

(c) Reliable IV results can be obtained using the setup schematically shown in Figure 2.5(c). The rectangular aperture side length is approximately 1-3 mm longer than that of the  $\text{TiO}_2$  films. The undesired effects discussed above can be eliminated. The  $J_{sc}$  values are found to be stable when varying the aperture size within this range.

(d) When using masks with much larger apertures or using no masks (Figure 2.5(d)), the  $J_{sc}$  and the efficiencies are overestimated. This is because that the directly illuminated and the deflected light both can reach the  $\text{TiO}_2$  films.



**Figure 2.5** Schematic diagrams showing the effects of aperture size on the light irradiation to the  $\text{TiO}_2$  films, reproduced from reference [6].<sup>6</sup>

The IV measurements performed in this project generally followed the method proposed by Ito et al.<sup>6</sup> However, even under optimized fabrication condition the screen-printed  $\text{TiO}_2$  film can be slightly larger than the expected area ( $4 \times 4$  mm) due to the spreading of paste during the printing process. We therefore realize that the energy conversion efficiency can be overestimated. Furthermore, due to the use of diffused light, light reflection and piping can also cause an overestimation problem, although the factor is minimized by the use of black masks and black testing jigs.

### 2.3.2 Incident Photon-to-Electron Conversion Efficiency (IPCE)

The Incident Photon-to-Electron Conversion Efficiency (IPCE) measurement involves the illumination of a solar cell with monochromatic light at a range of wavelength and the calculation of the quantum conversion efficiency of the solar cell at each wavelength. The

IPCE value (measured in percentage) of a solar cell is given by the number of electrons ( $N_e$ ) divided by the number of incident photons ( $N_p$ ) (Equation 2.8).

$$IPCE = \frac{N_e}{N_p} \quad 2.8$$

The number of electrons can be calculated using Equation 2.9

$$N_e = \frac{Q}{e} = \frac{J \cdot A \cdot t}{e} \quad 2.9$$

where  $Q$  is the total quantity of charge produced in the solar cell,  $e$  is the elementary charge ( $1.6 \times 10^{-19}$  C),  $J$  is the current density generated by the solar cell,  $A$  is the cell area and  $t$  is the total time.

The number of photons can be calculated by the energy of incident light ( $E_{light}$ ) divided by the energy of a photon ( $E_{photon}$ ) (Equation 2.10)

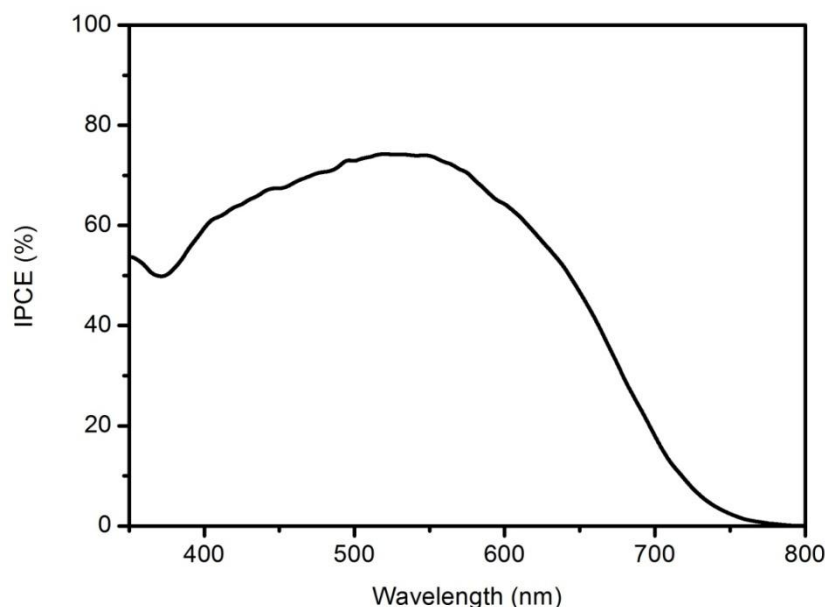
$$N_p = \frac{E_{light}}{E_{photon}} = \frac{P \cdot A \cdot t}{h\nu} = \frac{P \cdot A \cdot t \cdot \lambda}{h \cdot c} \quad 2.10$$

In this equation  $P$  is the power of the incident light,  $\lambda$  is the wavelength of incident light,  $h$  is the Planck's constant ( $6.63 \times 10^{-34}$  m<sup>2</sup> · kg / s) and  $c$  is the speed of light.

From Equation 2.9 and 2.10, the IPCE at each wavelength can be derived into the form as shown in Equation 2.11.

$$IPCE = \frac{N_e}{N_p} = \frac{J \cdot A \cdot t / e}{P \cdot A \cdot t \cdot c / hc} = \frac{J \cdot h \cdot c}{P \cdot e \cdot \lambda} = \frac{J \cdot 1240}{P \cdot \lambda} \quad 2.11$$

In our experiments, the IPCE testing was carried out using a xenon light source (Oriel, USA), a monochromator (Model 74100, Oriel Instruments, USA), a SourceMeter (Keithley, Model 2400) and some essential optical attachments. The wavelength of the monochromatic light was changed by 5 nm between every two data points. The calculated IPCE values were plotted against wavelength. Figure 2.6 shows an IPCE spectrum measured for a sandwiched DSC sensitized by the N719 dye. It is shown in this spectrum that the N719 dye has an absorption maximum at around 550 nm, and a weak absorption of red light. An estimated  $J_{sc}$  can be calculated by the product of IPCE and photon flux.



**Figure 2.6** The Incident Photon-to-Electron Conversion Efficiency (IPCE) results measured for a sandwiched DSC using the N719 dye.

### 2.3.3 Electrochemical Impedance Spectroscopy (EIS)

Electrochemical Impedance Spectroscopy (EIS) involves the examination of electrochemical interfaces using small amplitude AC voltage perturbations at a range of frequencies. It is a versatile technique to determine the kinetics of electrochemical reactions at various interfaces.

The EIS measurement of electrochemical systems, including solar cells, involves the application of small harmonic AC voltage perturbation  $V_{AC}(\omega, t)$  superimposed on a background DC voltage. The resulting AC current  $i_{AC}(\omega, t)$  is measured while the AC voltage is scanned across a certain frequency range  $f = \omega/2\pi$  to determine the impedance  $Z(\omega)$  (Equation 2.12)

$$Z(\omega) = \frac{V_{AC}(\omega, t)}{i_{AC}(\omega, t)} \quad 2.12$$


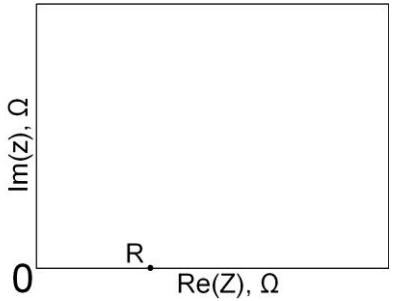
#### *The Electrochemical Impedance Spectroscopy of DSCs*

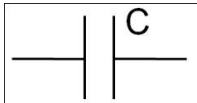
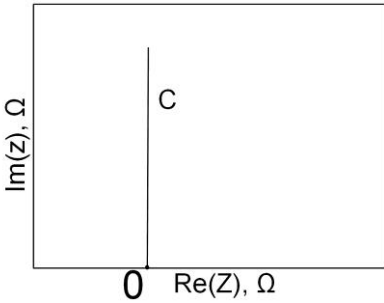
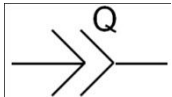
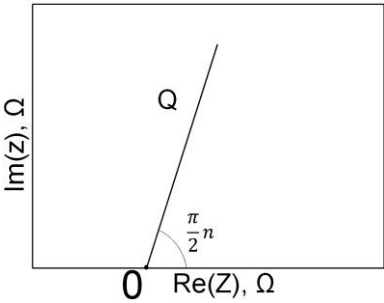

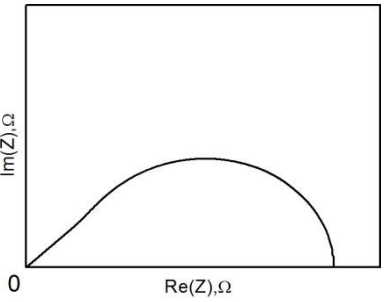
The EIS results for fully assembled solar cells can be interpreted using the Nyquist plot which shows the correlation between the real ( $Z'$ ) and imaginary ( $Z''$ ) parts of impedance elements, and the bode plot which shows the dependency of the impedance magnitude ( $Z$ ) and the phase angle ( $\theta$ ) on frequencies ( $f$ ). EIS results are fitted to equivalent circuits which simulate the electrochemical process at electrochemical interfaces. For DSCs, the commonly used

equivalent elements include resistors ( $R$ ), capacitor ( $C$ ), Constant Phase Element (CPE)), and finite Warburg diffusion element ( $W$ ).

Table 2.3 summarizes the schematic representatives, mathematical equations, and typical Nyquist plots of the equivalent elements commonly used to simulate DSCs. The resistor is a passive frequency-independent element. On the Nyquist plot, it is represented by a point with a real part value but 0 imaginary part value. The capacitance is frequency dependent. On the Nyquist plot, it corresponds to a straight vertical line starting from 0 and extending to infinite with decreasing frequency. A capacitor can only describe the behaviour of ideal parallel-plate capacitors, which are not applicable to any electrochemical interfaces in DSCs. A term of Constant Phase Element (CPE) is usually used to better simulate these interfaces. On the Nyquist plot, a CPE shows a straight line with a phase angle  $< \pi$  against the real axis. Warburg diffusion element is a specific type of constant phase element with a constant phase angle of  $\pi/4$  shown on its Nyquist plot.

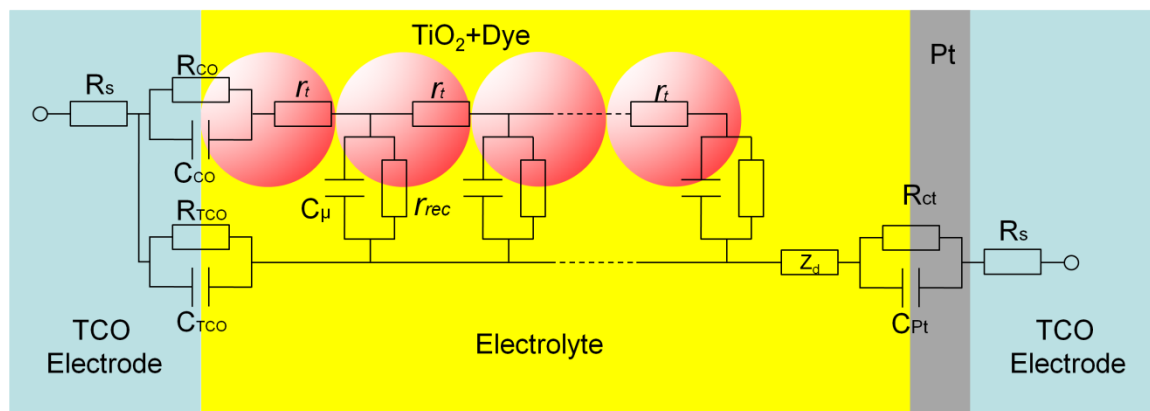
**Table 2.3** Equivalent impedance elements used to simulate electrochemical processes in DSCs. Their representative schemes, mathematical equations and graphs in the Nyquist plot are listed correspondingly.  $f$  is the frequency of applied AC voltage perturbation and  $j = \sqrt{-1}$ .

	Scheme	Equation	Nyquist plot
Resistor ( $R$ )		$Z(f) = R$	

Capacitor (C)		$Z(f) = \frac{1}{2\pi f j C}$	
CPE (Q)		$Z(f) = \frac{1}{Q(2\pi f j)^n}$	
Finite Warburg diffusion element (W)		$Z(f) = R_d \frac{\tanh(j\omega/\omega_d)}{j\omega/\omega_d}$ ( $\omega_d = D/L^2$ , D is the diffusion coefficient of the redox species, L is the effective electrolyte layer thickness)	

The widely accepted model to simulate DSCs in EIS measurements is the transmission line model.<sup>7, 8</sup> Figure 2.7 shows a scheme of the model, in which dyed TiO<sub>2</sub> nanoparticles are connected in a transmission line for electron conduction. A parallel circuit to the TiO<sub>2</sub> transmission line is the ionic diffusion process in electrolyte, which is parallelly connected to the TiO<sub>2</sub> transmission line by the charge recombination process at the TiO<sub>2</sub>/dye/electrolyte interface.





**Figure 2.7** General transmission line model used to describe electrochemical process in liquid state DSCs. On the TCO electrodes,  $R_s$  is the series resistance of the electrode material.  $R_{CO}$  and  $C_{CO}$  are the resistance and capacitance at the TCO/ $\text{TiO}_2$  interface.  $R_{TCO}$  and  $C_{TCO}$  are the charge transfer resistance and the double-layer capacitance at the TCO/electrolyte interface.  $r_t = R_t/L$  is the electron transfer resistance within the  $\text{TiO}_2$  transmission line. The thickness of the  $\text{TiO}_2$  film is  $L$ .  $r_{rec} = R_{rec} \times L$  and  $c_\mu = C_\mu/L$  are the charge transfer resistance at the  $\text{TiO}_2/\text{dye}/\text{electrolyte}$  interface and the chemical capacitance of the  $\text{TiO}_2$  film.  $R_{Pt}$  and  $C_{Pt}$  are the charge transfer resistance and capacitance at the Pt/electrolyte interface.  $Z_d$  is the ionic diffusion resistance within the electrolyte. Please note that in the transmission line model capacitors are usually used instead of CPEs to simplify the fitting during data processing.

In our experiments, the EIS measurements were performed in dark using a VSP2 potentiostat (Biologic Scientific Instruments, USA). A small AC voltage perturbation of 10 mV was superimposed on a series of bias potentials (usually within a range of 400 to 800 mV) while scanning over a frequency range from 500 kHz to 50 mHz. The results, including the real impedance, imaginary impedance and phase angles, were recorded using the EC-Lab software (Version 10.02, Biologic Scientific Instruments, USA). The results were then exported to Zview software and fitted with the transmission line model to determine the value of the individual components.

On a typical Nyquist plot, three arcs can be observed (Figure 2.8(a)). The three arcs from the high to low frequencies are assigned to the charge transfer at the Pt/electrolyte interface, the charge recombination process at the  $\text{TiO}_2/\text{dye}/\text{electrolyte}$  interface and the ionic diffusion within the electrolyte (note that the third semicircles are sometimes merged into the second

one, especially when using iodine/iodide liquid electrolytes with very small diffusion resistance).

From data fitting, the charge transfer resistance ( $R_{ct}$ ) at the Pt/electrolyte interface can be obtained from the high  $f$  arc. The charge recombination resistance ( $R_{rec}$ ) and the chemical capacitance ( $C_\mu$ ) of the  $\text{TiO}_2$  film can be estimated from the medium  $f$  arc (Note that the measured the capacitance only refers to the chemical capacitance ( $C_\mu$ ) of the  $\text{TiO}_2$  film when the applied bias potential is higher than 400 mV.<sup>9</sup> Below this threshold, the measured capacitance is better assigned to the Helmholtz capacitance at the  $\text{TiO}_2$ /dye/electrolyte interface).

The time constant ( $\tau_n$ ) for the charge recombination process, better known as the electron lifetime, can be calculated using Equation 2.13.

$$\tau_n = R_{rec} C_\mu \quad 2.13$$

The diffusion coefficient ( $D_n$ ) of the electrons in  $\text{TiO}_2$  can be obtained from  $R_t$  and  $C_\mu$  using Equation 2.14.

$$D_n = \frac{1}{R_t C_\mu} \quad 2.14$$

The effective diffusion length ( $L_n$ ) of the electrons in  $\text{TiO}_2$  can be calculated using Equation 2.15.

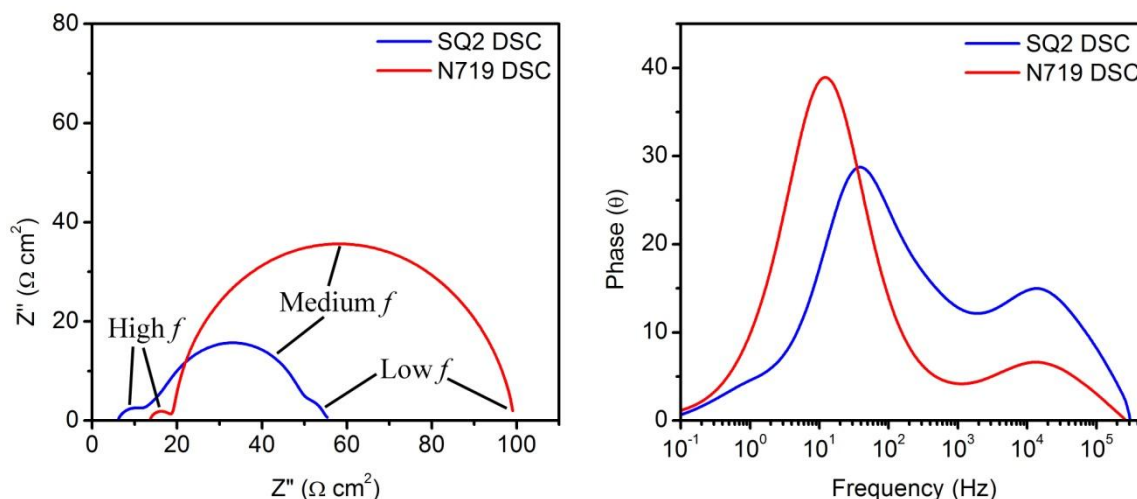
$$L_n = L \sqrt{D_n \tau_n} = L \sqrt{\frac{R_{rec}}{R_t}} \quad 2.15$$

where  $L$  is the thickness of the  $\text{TiO}_2$  film.

The diffusion coefficient ( $D$ ) for the redox species can be calculated from the diffusion resistance ( $Z_d$ ) using Equation 2.16.

$$Z(f) = R_d \frac{\tanh(j\omega/\omega_d)}{j\omega/\omega_d} \quad 2.16$$

where  $\omega_d = D/L^2$  ( $D$  is the diffusion coefficient of the redox species, and  $L$  is the effective electrolyte layer thickness).



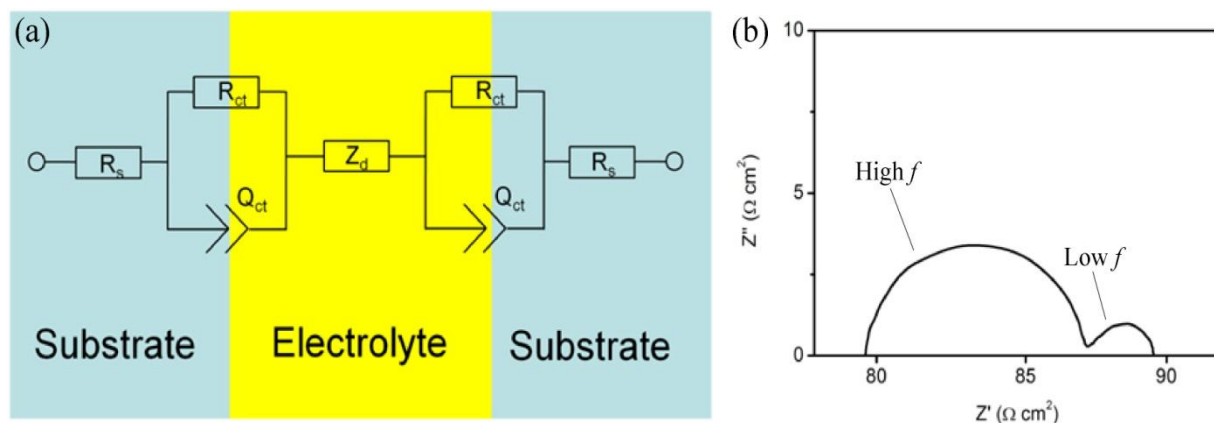
**Figure 2.8 (a)** The Nyquist plot and **(b)** the Bode plot of the EIS results measured for two DSCs using the dyes SQ2 and N719. Both cells were tested in the dark, with a bias voltage of 700 mV applied across the working and counter electrodes.

The Bode plot also provides information about the time constant of the interfaces in DSCs. On a typical Bode plot (Figure 2.8(b)), the two pronounced peaks at high and medium frequencies correspond to the charge transfer at the Pt/electrolyte interface and the  $\text{TiO}_2$ /dye/electrolyte interfaces, respectively. Similar to the observation on the Nyquist plot, the third peak at the low frequency side is not usually shown due to the fast diffusion process within the iodine/iodide electrolyte.

On the Bode plot, a phase peak shift towards the low frequency side indicates an increase in charge transfer. In Figure 2.5(b), the medium frequency peak of the red curve is shifted by almost a decade compared to that of the blue curve, indicating that the charge recombination process at the  $\text{TiO}_2$ /dye/electrolyte interface is much slower in the N719 DSC than in the SQ2 DSC. However, the high frequency peaks on both curves are almost at the same position, which can be explained by the similar charge transfer rate at the counter electrodes.

### ***The Electrochemical Impedance Spectroscopy of symmetrical cells***

The EIS measurements can be applied to symmetrical cells which consist of a thin electrolyte layer sandwiched between two identical electrodes (Figure 2.9). The technique can be used to interpret the charge transfer kinetics at the solid/electrolyte interface and the diffusion process within the electrolyte.



**Figure 2.9** (a) A schematic diagram showing the structure of a symmetrical cell and the equivalent circuit used to simulate the cell in the EIS measurements. (b) A typical Nyquist plot of the results.

In our experiments, symmetrical cells were constructed using certain electrode materials, such as platinized FTO glass, separated by a 25  $\mu\text{m}$  Surlyn<sup>®</sup> gasket. The cell gap was filled with an electrolyte through an entry port on the electrodes by a vacuum back-filling method.<sup>10</sup>

An AC perturbation of 10 mV was applied under the open-circuit condition using the VSP2 potentiostat. On a typical Nyquist plot (Figure 2.9(b)), the high  $f$  arc and low  $f$  arc are assigned to the charge transfer at the solid/electrolyte and the ionic diffusion within electrolyte. The results were fitted with the equivalent circuit shown in Figure 2.9(a) to obtain the values of the interfacial charge transfer resistance ( $R_{ct}$ ), the Helmholtz capacitance ( $Q_{ct}$ ) at the interface and the diffusion resistance ( $Z_d$ ). The diffusion coefficient of the ionic diffusion within electrolyte can be calculated using Equation 2.16.

## 2.4 References to chapter 2

- [1] M. Nazeeruddin, P. Pechy, T. Renouard, S. Zakeeruddin, R. Humphry-Baker, P. Comte, *J. Am. Chem. Soc.* **2001**, 123, 1613.
- [2] S. Ito, T. N. Murakami, P. Comte, P. Liska, C. Grätzel, M. K. Nazeeruddin, M. Grätzel, *Thin Solid Films* **2008**, 516, 4613.
- [3] B. O'Regan, J. Durrant, P. Sommeling, N. Bakker, *J. phys. Chem. C* **2007**, 111, 14001.
- [4] J. Halme, P. Vahermaa, K. Miettunen, P. Lund, *Adv. Mater.* **2010**, 22, E210.
- [5] S. M. Sze, K. K. Ng, *Physics of Semiconductor Devices*, John Wiley & Sons, Inc., Hoboken **2006**.
- [6] S. Ito, M. K. Nazeeruddin, P. Liska, P. Comte, R. Charvet, P. Pechy, M. Jirousek, A. Kay, S. M. Zakeeruddin, M. Grätzel, *Prog. Photovoltaics*. **2006**, 14, 589.
- [7] J. Bisquert, *J. Phys. Chem. B* **2002**, 106, 325.

- [8] Q. Wang, S. Ito, M. Gr äzel, F. Fabregat-Santiago, I. Mora-Sero, J. Bisquert, *J. Phys. Chem. B* **2006**, 110, 25210.
- [9] J. Bisquert, I. n. Mora-Seró, *J. Phys. Chem. Lett.* **2009**, 1, 450.
- [10] H. Han, U. Bach, Y. Cheng, R. Caruso, *Appl. Phys. Lett.* **2007**, 90.



### 3 Laser ablation to produce interdigitated electrodes

#### 3.1 *Background information*

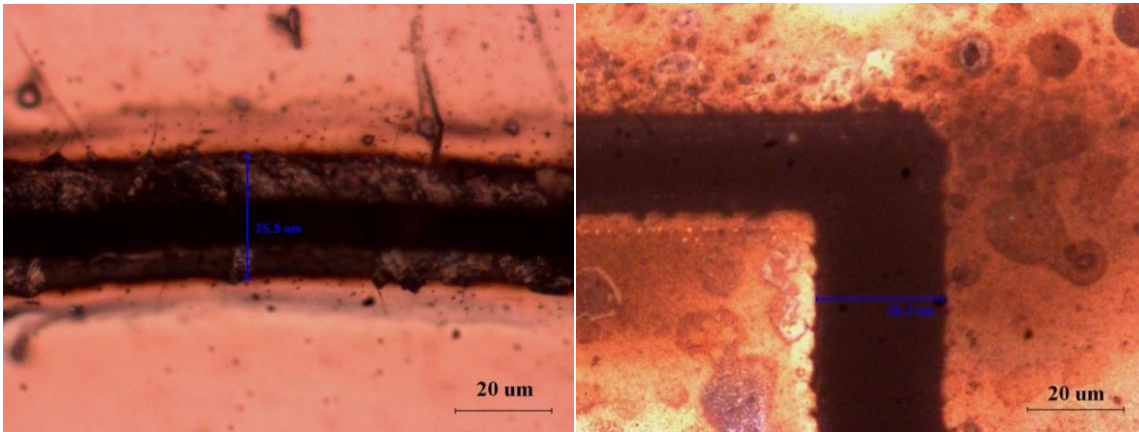
Processing of substrates comprising interdigitated microelectrodes is an essential step before the fabrication of back-contact DSCs. This chapter describes several laser ablation approaches that were used to produce micron-sized interdigitated electrodes for back-contact DSCs. The materials to be processed include FTO glass (NSG 2), Ti coated plain glass and Ti coated polyimide (PI). The ultimate aim of this project is to produce back-contact DSCs on metal coated substrates, especially on flexible substrates such as PI. However, due to the commercial availability and good consistency in properties, FTO glass is always used as a starting material for laser ablation and subsequent experiments. The two laser ablation approaches involved in our experiments are mask-delivered process using a KrF excimer laser (248 nm wavelength) and single beam direct-write process using a ND:YV04 solid-state laser (355 nm wavelength). Both of these two processes employ pulsed laser radiation with nanosecond pulse durations. According to the time scale, pulsed laser radiation could be classified into three categories, namely nanosecond (ns), picosecond (ps) and femtosecond (fs) laser pulses. The interactions of such laser pulses with materials have been intensively studied during the past decades.<sup>1-7</sup> It has been shown that the absorption of laser radiation by materials involves several stages at different time domains. The laser energy is firstly absorbed by free electrons, and then thermalized into electron subsystem followed by heat transfer into lattice and then to bulk material.<sup>2</sup>

Cooling of 'hot' electrons is an extremely fast process. It has been shown that the time  $\tau_e$  involved in this relaxation process is within a range of 1 to 3 ps.<sup>7-9</sup> The later stage involving heat transfer into lattice occurs within  $\tau_i$ , which is much less than a nanosecond.<sup>10</sup> The way that laser pulses interacting with substrate materials is dependent on the length of pulse duration  $\tau_L$  in comparison to  $\tau_e$  and  $\tau_i$ .

For femtosecond laser pulses, condition  $\tau_L < \tau_e$  applies. There is almost no electron-lattice coupling and the ablation leads to a direct solid-to-vapor phase transition.<sup>2</sup> In this case the heat transfer into the bulk material can be neglect, resulting in minimal heat generation in the

substrate. Such advantages allow for precise ablation of materials, producing sharp-edged features with relatively low energy inputs. When using picosecond laser pulses, condition  $\tau_e < \tau_L < \tau_i$  is fulfilled. There is limited heat transfer from the free electrons to the lattice. With a weak coupling between the two, there is still considerable heating of the substrates which leads to melting of materials adjacent to the ablated features. Further increasing laser pulses to the nanosecond regime leads to strong coupling between free electrons and the lattice. Materials are firstly melted and then evaporated. Significant heat transfer can occur depending on the heat diffusion coefficient of the specific materials. This results in enlarged heat affected zones on substrates, which makes precise processing of materials very complicated.<sup>2</sup>

Figure 3.1 compares two micron-sized patterns fabricated on titanium coated PI substrates using nanosecond laser pulses and femtosecond laser pulses. Despite of the difference in wavelength or pulse energy used in these experiments, differences could be noticed in terms of the thermal effects produced by the two types of lasers. Figure 3.1 (a) shows a substantial heat affected zone adjacent to the laser etched groove. Distortion of the PI substrate and cracking of the Ti coating are observed. Figure 3.1 (b) shows a clearly defined etching boundary produced by the femtosecond laser. Heating effects are much less obvious than in Figure 3.1(a), only a small amount of powdery debris is observed adjacent to the micropattern.



**Figure 3.1** Simple line features fabricated by (a) a nanosecond laser pulses at 355 nm with 52 ns pulse duration and (b) femtosecond laser pulses at 800 nm with 50 fs pulse duration. The average single pulse fluences is 11  $\mu\text{J}$  for both experiments.



When fabricating micropatterns, heating of substrate is not desirable, especially for substrates comprising layers of different materials. Rapid heating could result in severe thermal shock thus cracking of substrate materials. For the interdigitated electrodes in this project, melting of electrode materials could result in shorting bridges and lumps of materials deposited on top of electrode surface. These defects could deteriorate the performance of back-contact DSCs. Table 3.1 summarize selected thermal and physical properties of the materials used in the laser ablation experiments. Ti, SnO<sub>2</sub> and soda-lime glass have similar thermal expansion coefficient. However, due to the poor thermal conductivity and low fracture toughness of soda-lime glass, Ti and FTO coated glass substrates are prone to thermal shock if heated rapidly by laser radiation. Ti coated PI substrates are prone to melting and distortion due to the thermal instability of polymeric material.

**Table 3.1** Selected thermal and physical properties of SnO<sub>2</sub>, soda-lime glass, PI and titanium.<sup>11-13</sup>

	Substrate materials		Coating materials	
	Soda-lime glass	PI	SnO <sub>2</sub>	Ti
Coefficient of thermal linear expansion ( $\times 10^6 \text{ K}^{-1}$ )	9.0	20	3.5	8.6
Thermal conductivity ( $\text{W m}^{-1} \text{ K}^{-1}$ )	1.7	0.12	1.0	21.9
Melting point	$T_g = 570 \text{ }^\circ\text{C}$	$T_g = 410 \text{ }^\circ\text{C}$	1630	1668
Boiling point	NA	NA	1800 (sublime)	3287

From this aspect, lasers with very short pulse durations such as femtosecond lasers are best suited for fabricating interdigitated microelectrodes. However, due to limited access to experimental apparatus, most samples in this project were produced by laser pulses with nanosecond durations.

As a general guideline, functioning micropatterns should (at least) fulfill the following three criteria

1. The ablated grooves have to have good insulation over a long distance. This is not a simply target, as for a typical test cell with an area of  $4 \times 4$  mm and 10  $\mu\text{m}$  wide electrodes/gaps, the overall length of insulating grooves is over 800 mm. Any defects in such a long track could result in shorting between electrodes.
2. Cracking of electrodes has to be minimized. Cracks on substrates are acceptable. However, once they propagate onto the micron-sized electrode, the conductivity of single electrode would be reduced dramatically.
3. Delamination of electrode layers has to be suppressed. Once this occurs, the delaminated regions could become dead zones for subsequent cell fabrication procedures.

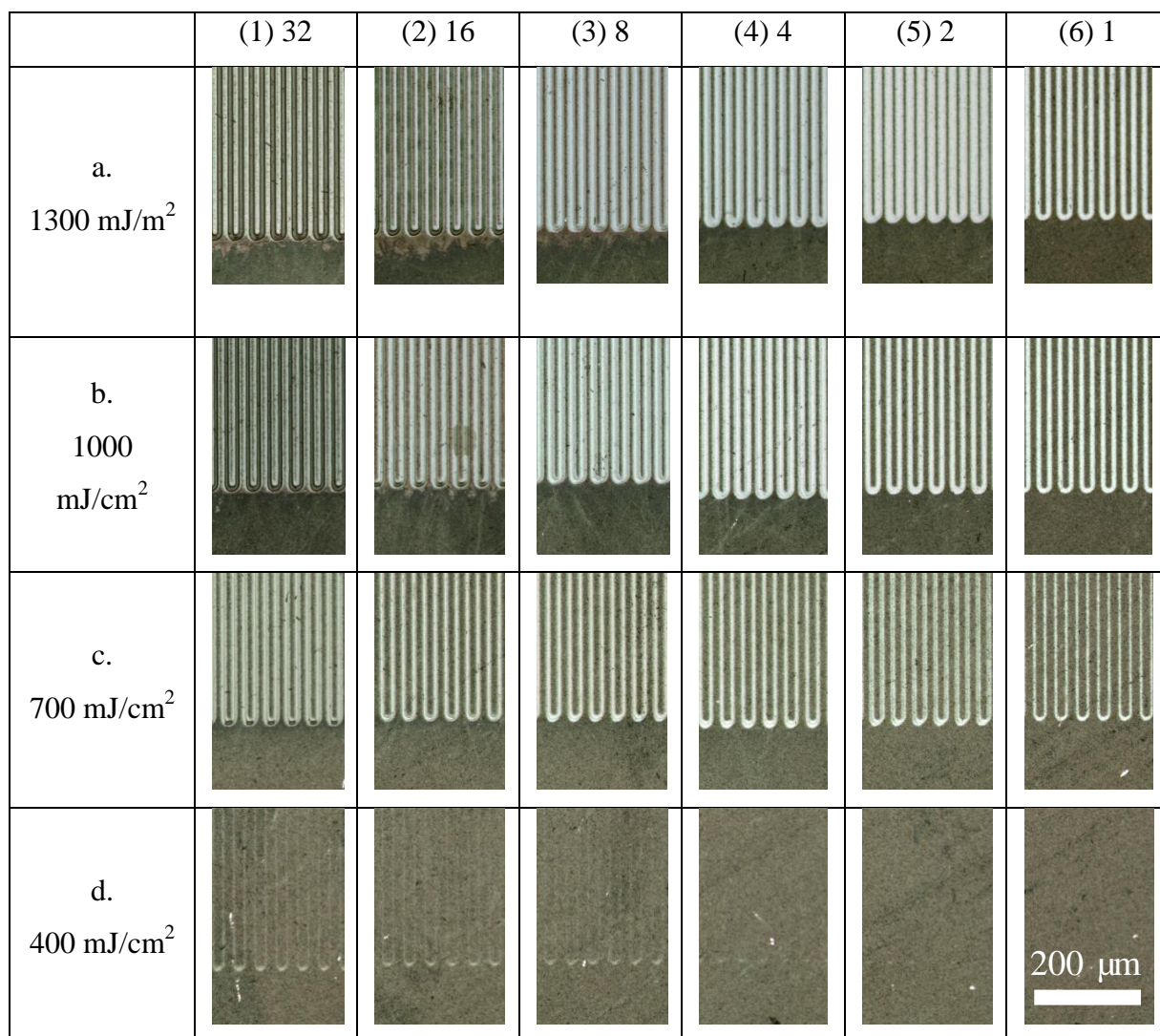
### 3.2 *Mask-delivered process using KrF excimer laser*

The first approach for producing interdigitated electrodes is a mask delivered process. The experiments were performed at MiniFab Pty. Ltd. (Caribbean Gardens, Melbourne, Australia). An Excitech 8000 series excimer laser (248 nm wavelength, 40 ns pulse width and 80 kHz frequency) was used. The output laser beam from the light source has a dimension of  $8000 \times 8000$   $\mu\text{m}$ . It was condensed by a group of lenses (10:1 ratio) to a process laser beam dimension of  $800 \times 800$   $\mu\text{m}$ . In conjunction with a mask dragging system, pulsed laser radiation was delivered through a series chrome-on-quartz masks to produce elementary micropatterns. Processing of large-scale patterns was realized through stitching of a series of elementary micropatterns.

#### 3.2.1 **Evaluation of processing parameters**

Before the actual laser processing, dose tests were conducted to evaluate processing parameters. 248 nm laser pulses were delivered through a mask to ablate  $800 \times 800$   $\mu\text{m}$  micropatterns on FTO glass (NSG 2). Using a beam homogenizer, flat-head laser beams were obtained for homogeneous ablation across each pattern. A matrix of interdigitated patterns was fabricated combining varying laser fluences and pulse numbers as shown in Figure 3.2. Under a low laser fluence of  $400 \text{ mJ}/\text{cm}^2$ , little ablation was observed even at a high pulse number of 32 per area (Figure 3.2 d(6)). Increasing the laser fluences dramatically increases the amount of materials that are removed by a given number of pulses. For samples processed

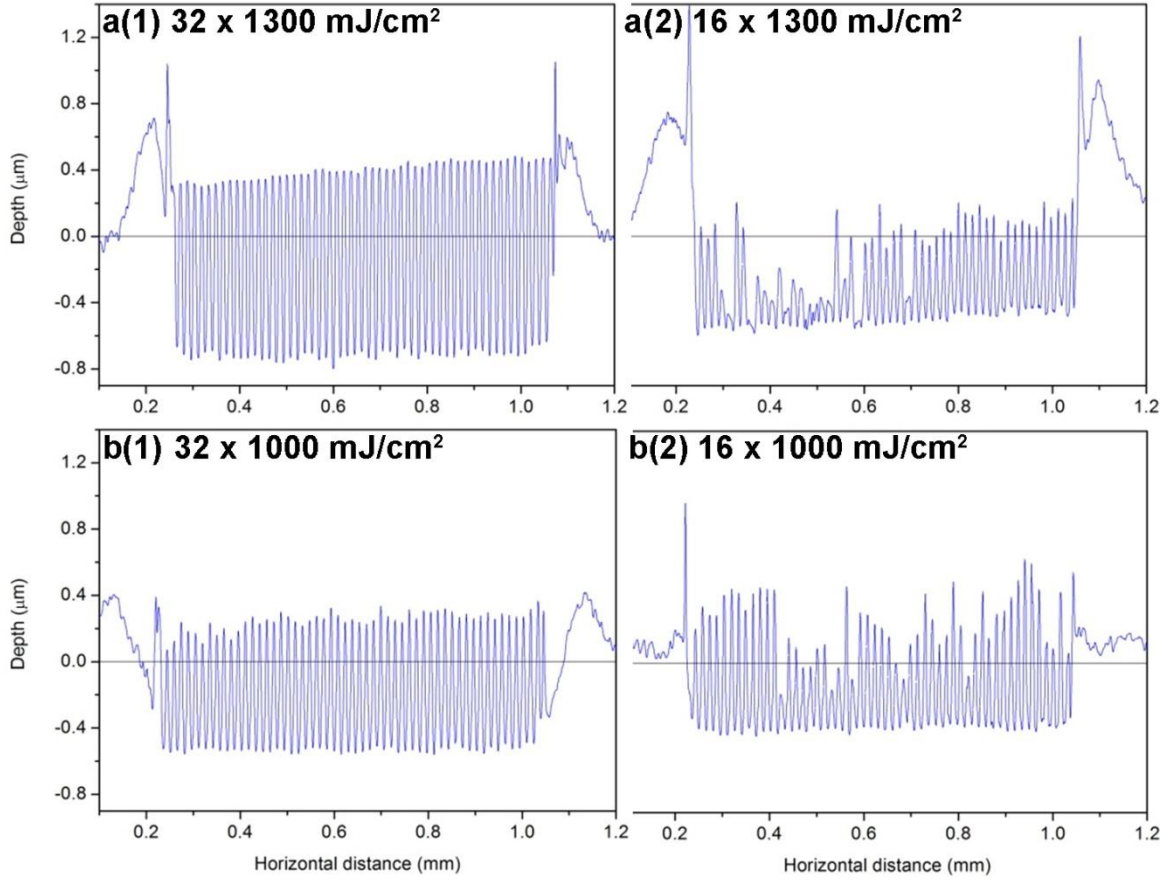
with relatively high fluences and high pulse numbers, debris are observed on electrodes and regions around patterns.



**Figure 3.2** A laser dose test performed on FTO glass substrates by an excimer laser (248 nm wavelength, 20 ns pulse duration). A laser beam was delivered through a mask, producing a  $800 \times 800 \mu\text{m}$  interdigitated micropattern on the substrate. A matrix of micropatterns was produced by 0.4, 0.7, 1.0 and  $1.3 \text{ J/cm}^2$  (row a - d) laser fluences, and 1, 2, 4, 8, 16 and 32 (column (1) - (6)) pulses per area, respectively. The scale bar at the lower right corner is calibrated for all micrographs in this figure.

The surface profile of samples a(1), a(2), b(1) and b(2) are shown in Figure 3.3. The surface profile scan covers regions of unaffected area which defines the zero-line base of the profiles. The contours show accumulation of debris on electrode surface. The effect is mostly

substantial for samples a(1) which was produced by 32 pulses with 1300 mJ/cm<sup>2</sup> single shots fluences. The height of built-up debris is almost comparable to the ablated depth.



**Figure 3.3** Surface profile of dose test samples produced by 248 nm KrF excimerlaser , using parameters of **a(1)** 32 shots and 1300 mJ/cm<sup>2</sup>, **a(2)** 16 shots and 1300 mJ/cm<sup>2</sup>, **b(1)** 32 shots and 1000 mJ/cm<sup>2</sup>, and **b(2)** 16 shots and 1000 mJ/cm<sup>2</sup>, measured with a Dektak optical profilometer.

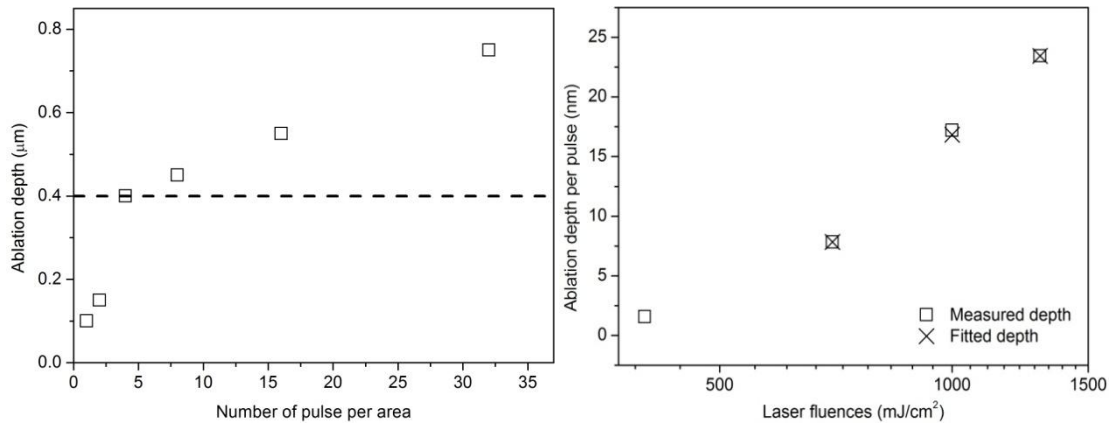
When using 1300 mJ/cm<sup>2</sup> fluence, the ablation depth increases sub-linearly with number of pulses per area (Figure 3.4(a)). On the other hand, when using laser fluences higher than 700 mJ/cm<sup>2</sup>, ablation depth per pulse increases exponentially with increasing laser fluences. Past research has shown dependences of ablation depth per laser pulse  $L$  on laser fluences at lower and higher energy, which could be expressed by the Equation 3.1 and 3.2, <sup>2</sup>

$$L \approx \alpha^{-1} \ln(F/F_{th}^{\alpha}) \quad 3.1$$

$$L \approx l \ln(F/F_{th}^l) \quad 3.2$$

Where  $\alpha^{-1}$  and  $l$  are lower- and higher-energy optical penetration depths.  $F$  is applied laser fluence.  $F_{th}^{\alpha}$  and  $F_{th}^l$  are lower- and higher-ablation fluence thresholds respectively.

Fitting the experimental data Figure 3.4(b) using Equation 3.2, we obtained a higher-energy optical penetration depth of 25 nm and an ablation threshold of 513 mJ/cm<sup>2</sup> for the FTO coating processed by the 266 nm KrF laser used in this experiment. It has been shown that the ablation threshold of a material is increased with increasing laser wavelength, beam waist (for a beam with Gaussian distribution this refers to the beam diameter when intensity drops to 1/e<sup>2</sup> level) and pulse duration.<sup>14, 15</sup> Bovatsek et al.<sup>15</sup> indicated a threshold of 2040 mJ/cm<sup>2</sup> for the ablation of SnO<sub>2</sub> by a 532 nm nanosecond laser (37 ns pulse duration), whereas Raciukaitis et al.<sup>14</sup> estimated a threshold of 210 mJ/cm<sup>2</sup> for the ablation of ITO by a 266 nm picosecond laser (10 ps pulse duration). Although no literature value for the exact same conditions as those used in our experiments are available, an estimated 513 mJ/cm<sup>2</sup> ablation threshold seems to be reasonable for an efficient removal of the FTO coatings.



**Figure 3.4.** Plots of (a) ablation depth vs. number of pulses per area when using a laser fluence of 1300 mJ/cm<sup>2</sup>. The dash line represents the thickness of the FTO layer used in this experiment. (b) average ablation depth per pulse vs. laser fluences calculated from dos test samples produced under a condition of 32 shots per area. Results for higher fluences are fitted with Equation 3.2 to obtain optical penetration depth and ablation threshold for the FTO coating.

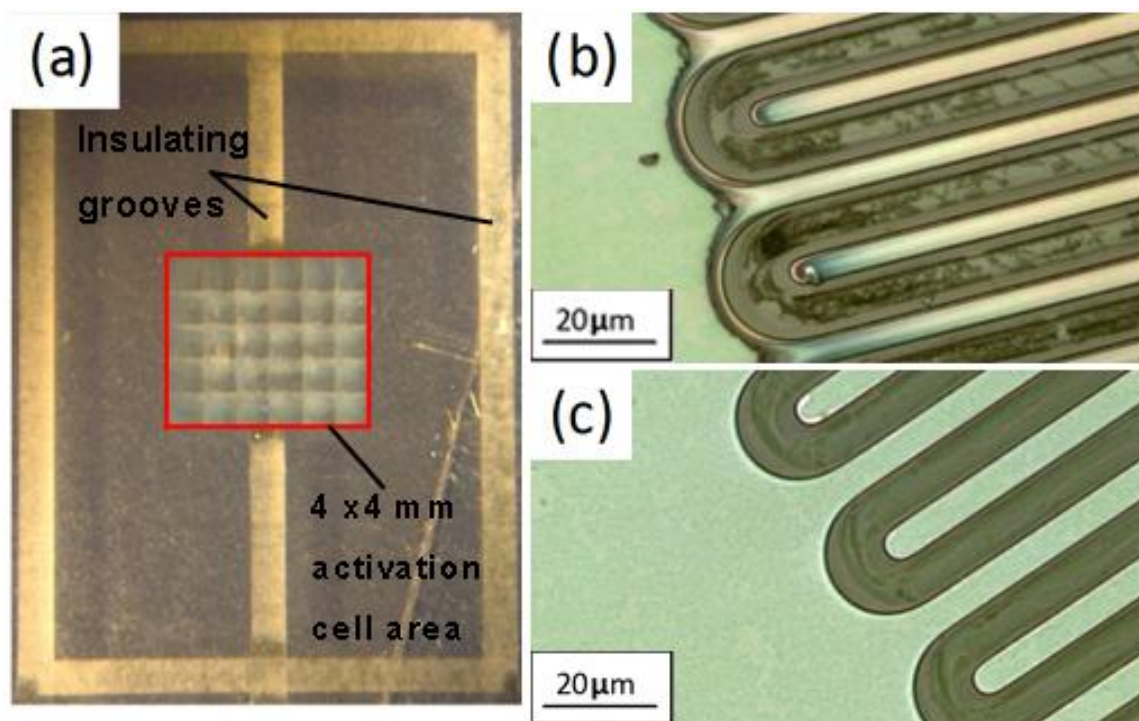
### 3.2.2 Processing of full-size patterns

The actual patterns containing full-size interdigitated electrodes (Figure 3.5(a)) were produced on FTO glass (TEC-15) by stitching elementary units for the left, middle and right features.

Figure 3.5(c) shows a small portion of a typical left feature. The right feature has a mirror pattern to the left feature. The middle feature comprises straight lines that connect the left and right features.  $5 \times 6$  units were combined to produce an overall  $4 \times 4$  mm activation cell area. The patterns were slightly overlapped at the stitching region to obtain continuous micropatterns. The two electrode sets were separated by  $800 \mu\text{m}$  wide insulating grooves.

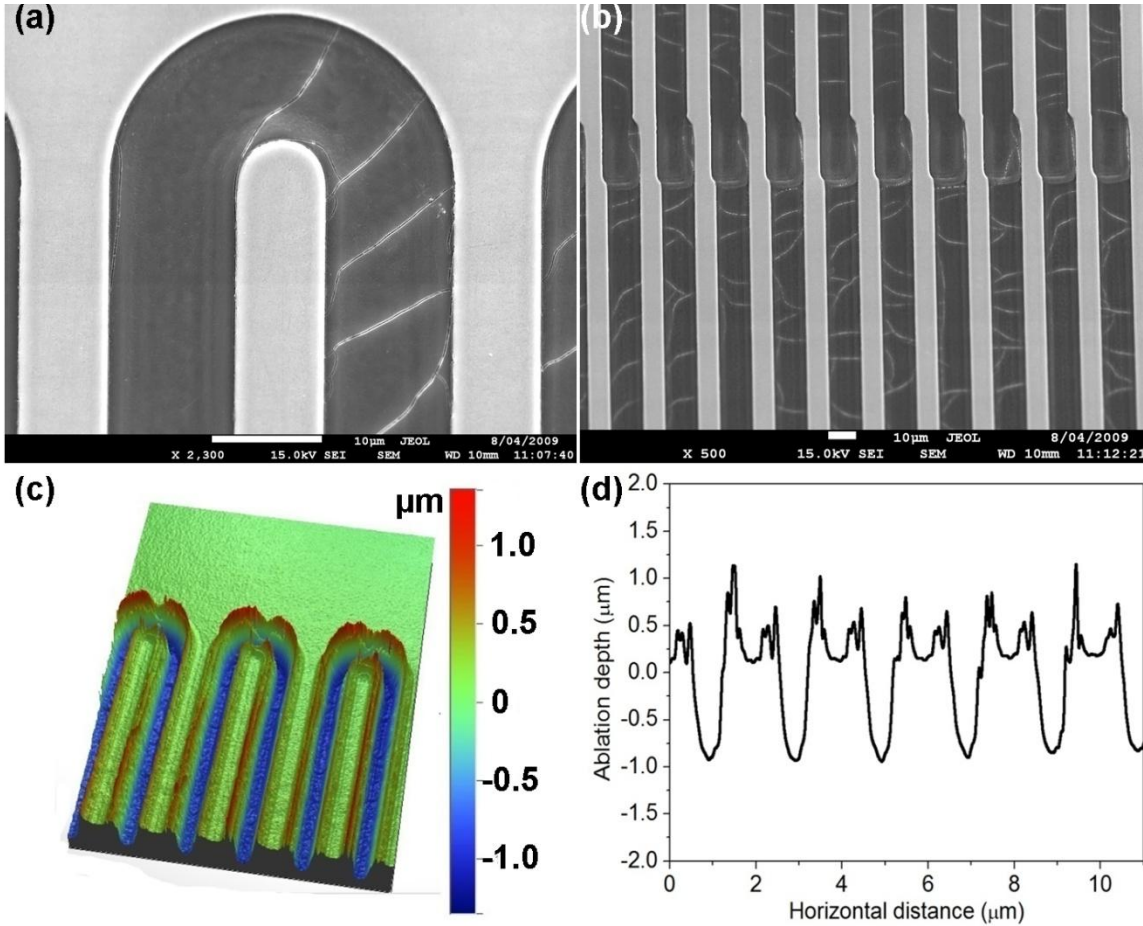
A large amount of debris is observed around ablated area, covering electrodes and adjacent regions (Figure 3.5(b)). The debris has poor electrical conductivity, proved by inefficient electrodeposition onto such surfaces at later experiments. Therefore they are believed to contain mostly glass in molten or powdery form. The strong absorption of 248 nm radiation by glass is a major reason for the observed melting of glass substrates. By polishing and cleaning, clean electrode surfaces (Figure 3.5(c)) could be obtained and prepared for later fabrication stages.





**Figure 3.5** (a) Image of an interdigitated substrate produced by mask delivered KrF excimer laser ablation. The center  $4 \times 4$  mm activation area was produced by stitching  $5 \times 6$  elementary micropatterns. A laser fluence of  $1300 \text{ mJ/cm}^2$  was used for both cell areas and insulating grooves. Pulse numbers per area are 20 and 100 for the two regions respectively. A higher pulse number for the grooves is to ensure perfect electrical insulating between the two electrode sets. After ablation, a large amount of debris is found surrounding ablated areas as shown in (b). Proper polishing and cleaning are essential to obtain a clean surface as shown in (c) in order to prepare for later fabrication stages.

After cleaning, micrographs (Figure 3.6(a)) show features with well-defined edges developed by the mask-delivered process. The depth of the grooves between electrodes is much deeper than the thickness of the FTO coating. This results in complete removal of FTO coating and further etching into the glass substrates. A standard sample produced by such a method could achieve a resistance in the mega-ohm range between the two sets of electrodes. A 3D map and 2D profile of these samples are shown in Figure 3.6(c) and (d) respectively. Build-up of materials could still be measured even after cleaning of electrodes. This results in up to  $1 \text{ } \mu\text{m}$  higher regions on electrode edges than at the middle of the electrodes. It is proven in a later electrodeposition process that the built-up regions have similar electrical conductivity with the rest of the electrodes.



**Figure 3.6** Scanning electron micrographs of (a) interdigitated electrodes and (b) stitching area between two ablated fields. The surface profile of a typical sample was measured by an optical profilometer (Veeco WYKO NT1100 optical profiling system). A 3D mapping result and a 2D profile are shown in (c) and (d) respectively.

Several defects are observed on these patterns.

1. The designed electrode to insulating groove width ratio is 10 μm to 10 μm. However, the actual electrodes and grooves are approximately 8 and 12 μm wide (Figure 3.6(a)). Thinning down of electrodes further reduces electrode surface area thus increasing ohmic resistance of them.
2. Cracks are commonly noticed on the glass substrates at ablated areas, due to thermal shock generated by rapid heating of substrates during ablation. However, the FTO



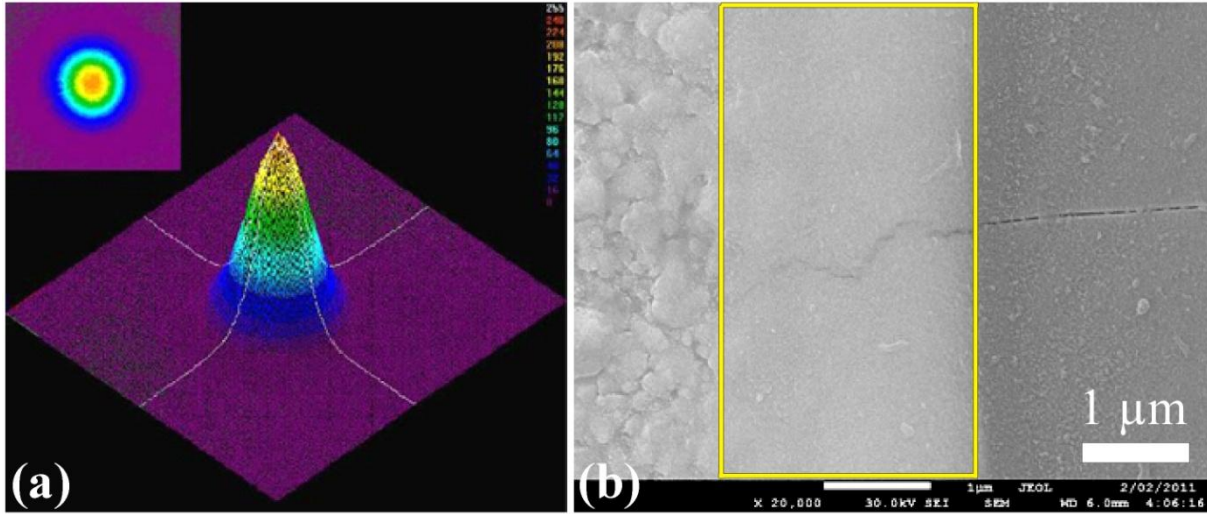
coatings seem to have high thermal-shock resistance, as no crack is found propagating onto the interdigitated electrodes.

3. Stitching boundaries could be easily noticed even in low magnification images (Figure 3.5). At these areas, ablations were conducted twice as a result of overlapped ablation fields. In addition, mechanical moving errors of sample stage result in misalignment between fields. These cause further thinning down of micron-sized electrodes (Figure 3.6 (b)) at stitching areas, which further increase ohmic resistance of individual electrodes.

To conclude the above discussion, there are some intrinsic drawbacks for the processing of interdigitated electrodes using mask-delivered process. A DSC device usually has a dimension of more than  $4 \times 4$  mm. The dimension could be increased to hundreds of  $\text{cm}^2$  for DSC modules. However, it is difficult to use laser beams with comparable sizes. It is almost impossible to process a full-size micropattern in a one-shot process with masks containing full features. Therefore, stitching is almost unavoidable. Stitching errors could always exist, due to the mechanical moving errors of sample stage and even the sample distortion associated with thermal expansion in long term processing. Good coupling between mask changing and sample stage moving also requires high precision control which increases the cost of equipments.

### 3.3 *Direct-write process using ND:YV04 solid-state laser*

In direct-write laser ablation process, focused laser beams with a diameter of typically several microns are used to directly remove materials to produce micropatterns. The direct-write laser ablation experiments were performed in Wuhan National Laboratory for Optoelectronics (WNLO, NO. 1037 Luoyu Road, Wuhan, 430074, P. R. China). The laser source (Aptowave, New York USA) comprises a solid-state ND:YV04 crystal pumped by a laser diode with a pumping wavelength of 1064 nm. An output laser radiation with 355 nm wavelength is produced through a third-harmonic generation. The laser beam is delivered through an oscillating mirror system to achieve x-y scanning on sample surfaces. The laser beam has a Gaussian intensity distribution as shown in Figure 3.7 (a).<sup>16</sup> This results in typically a tapered transition region between unaffected FTO coating and fully exposed substrate as shown in Figure 3.7(b). The width of the tapered region varies from less than 1  $\mu\text{m}$  to several microns depending on the fluences, speed and pulsing frequency of the laser.



**Figure 3.7** (a) Intensity profile of the laser beam used in our experiments.<sup>16</sup> The beam features a typical Gaussian distributed intensity which results in a tapered transition region (the region highlighted by the yellow frame) shown in (b) when processing samples with layered structure.

μm

The direct-write laser ablation process is mask-free and more flexible in fabricating patterns with a large variety of dimensions. Due to the intrinsic differences involved in the two processes, drawbacks associated with stitching in mask-delivered process could be overcome by direct-write process. Large-scale patterns could be produced in a faster continuous process. Since only one stitching is usually required at the end of processing to obtain closed patterns, stitching errors could be easily controlled to the lowest level. Processing rate depends almost exclusively on the moving speed of the laser beam. For laser micromachining facilities at present time, such a speed could be up to thousands of mm per second. This allows for processing interdigitated electrodes in a very high throughput.

### 3.3.1 Evaluation of parameters for the processing of FTO glass

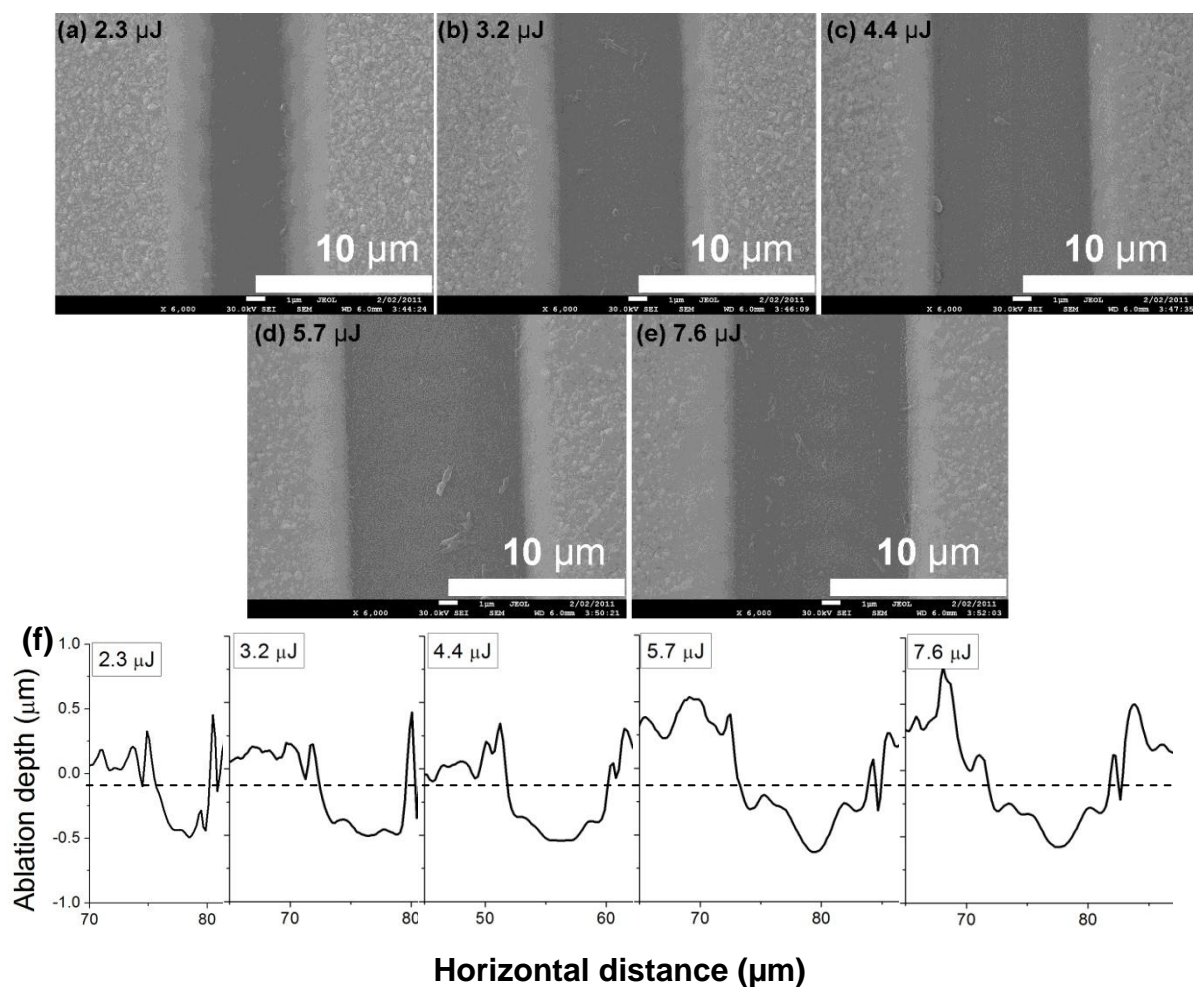
#### The effects of laser fluences

Figure 3.8(a) - (e) shows that the width of completely ablated region (dark grooves in Figure 3.8(a) - (e)) is increased from approximately 3 μm to more than 10 μm when increasing the laser fluences from 2.3 to 5.7 μJ. This is due to the increased effective beam dimension on the samples surfaces. On the other hand, the size of tapered transition regions is slightly reduced, and the dimension of overall ablated feature (completely ablated region plus transition region)

is increased from 10  $\mu\text{m}$  at 2.3  $\mu\text{J}$  to approximately 15  $\mu\text{m}$  at 4.4  $\mu\text{J}$  and remained almost constant after that. This indicates that the effective beam diameter was focused to approximately 15  $\mu\text{m}$  at the surface level of these samples during ablation.

However, increasing laser fluences results in no substantial increment in ablation depth as shown in Figure 3.8(f). The maximum depth of ablation is almost reached at a low fluence of 2.3  $\mu\text{J}$  and only increased by approximately 0.1  $\mu\text{m}$  until a fluence of 7.6  $\mu\text{J}$  is reached. This indicates that the ablation rate of glass substrates is much lower than that of FTO coatings, possibly due to the sublimation of FTO at around 1800  $^{\circ}\text{C}$ . The difference in ablation rate could also attribute to the difference in absorption coefficient of glass and FTO towards the absorption of 355 nm light.

To summarize the results shown in Figure 3.8, too low fluence such as 2.3  $\mu\text{J}$  results in narrow insulating tracks and large tapered region which could result in shorting when producing long distance grooves. While too high fluence such as 5.7  $\mu\text{J}$  results in too wide grooves which reduce effective electrode area. Appropriate laser fluences for the processing of interdigitated micropatterns on FTO are believed to be between 3.2 and 4.4  $\mu\text{J}$ .



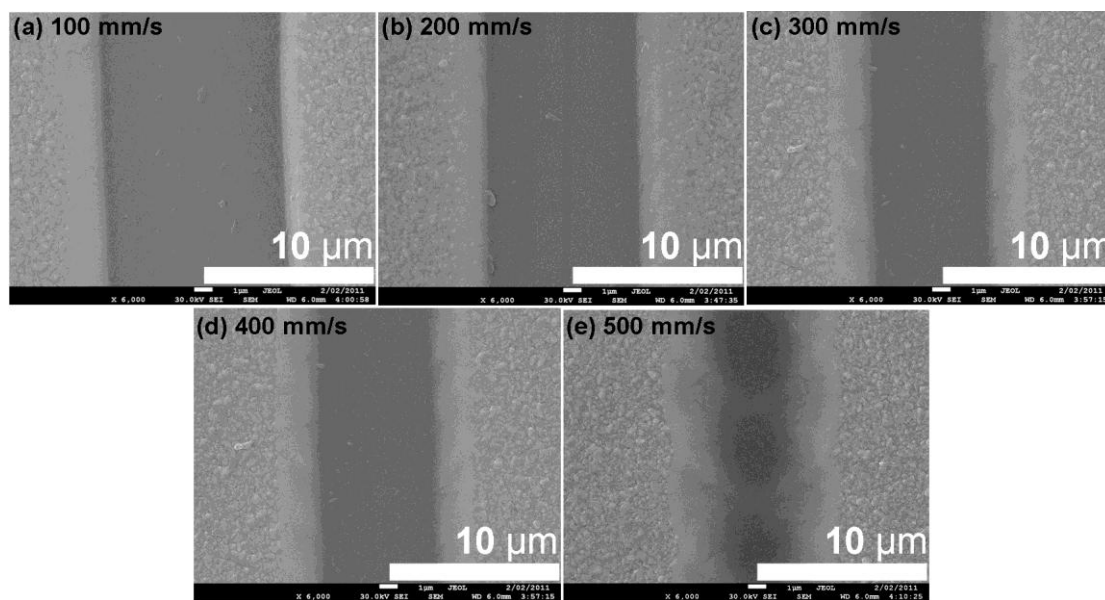
**Figure 3.8** Scanning electron micrographs showing the morphology of micropatterns produced by laser pulses with single pulse energy of (a) 2.3, (b) 3.2, (c) 4.4, (d) 5.7 and (e) 7.6  $\mu\text{J}$ . The beam moving speed and pulsing frequency are 200 mm/s and 90 kHz for all samples. The dark regions in the images are fully exposed glass substrates, while the regions with rough surfaces are unaffected FTO coatings. The surface profiles shown in (f) were measured using an optical profilometer (Veeco WYKO NT1100 optical profiling system).

### The effects of beam travelling speed

Figure 3.9 summarizes surface morphology of substrates ablated by laser beam moving at the speed of (a) 100, (b) 200, (c) 300, (d) 400 and (e) 500 mm/s on FTO glass surface. It is shown that a lower speed generally results in a wider groove with narrower tapered region on FTO coatings.

For all these samples, pulse frequencies were fixed at 90 kHz. For circular beam spots with an effective diameter of 10  $\mu\text{m}$ , the distance that the beam moves between shots has to be less than 10  $\mu\text{m}$  in order to produce a continuous pattern rather than isolated craters. Therefore the maximum beam moving speed at 90 kHz frequency can be calculated by  $90,000 \text{ pulses/s} \times 10^{-2} \text{ mm} = 900 \text{ mm/s}$ .

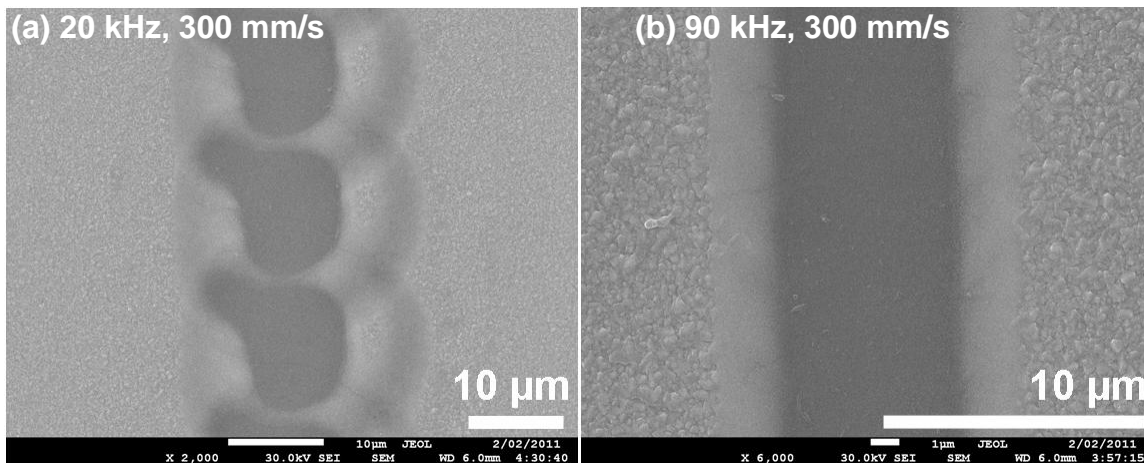
At a speed of 500 mm/s (Figure 3.9 (d)), the distance between every two shots is 5.5  $\mu\text{m}$ . Craters are partially joint with large tapered region at the surrounding area. There are also shorting bridges in-between them, rendering this speed not applicable to produce smooth grooves when using 90 kHz pulsing frequency. Reducing speed to less 300 mm/s (Figure 3.9 (c)) results in reduced distance between shots to 3.3  $\mu\text{m}$ . Such a condition seems to give smooth grooves with relatively small tapered regions. However, further reduce speed to less than 200 mm/s results in greatly widened insulating grooves, which potentially reduce electrode width thus effective electrode areas. A suitable speed for the processing of interdigitated electrodes on FTO glass would be between 200 and 300 mm/s.



**Figure 3.9** Straight groove features produced by laser beams with 4.4  $\mu\text{J}$  fluences and 90 kHz frequency. The beam moving speed on the samples surfaces are varied from 100 to 500 mm/s, corresponding to a distance between every two shots of (a) 1.1 , (b) 2.2 , (c) 3.3 , (d) 4.4 and (e) 5.5  $\mu\text{m}$ , respectively.

### The effects of pulsing frequency

Pulsing frequency, correlated with beam travelling speed, dramatically varies the surface morphology of ablated micropatterns. Figure 3.10(a) and (b) show images of simple straight line features produced by 20 and 90 kHz laser pulses that travel at a speed of 300 mm/s. The beam moving distance between two shots for these two frequencies are 15 and 3.3  $\mu\text{m}$  respectively. The difference in groove width is due mostly to the different laser fluences employed for these two samples. However, by excluding the differences in fluences, we could still notice greatly varied morphologies resulted from the two frequencies. At a speed of 300 mm/s, a higher frequency of 90 kHz results in a 3.3  $\mu\text{m}$  beam moving distance between every two shots, producing smooth grooves. In comparison, 20 kHz results in a 15  $\mu\text{m}$  beam moving distance between every two shots, producing scattered craters. In addition, non circular craters are observed on the 20 kHz sample, indicating a non-homogeneous energy profile of the laser beam. Undoubtedly, a higher frequency of 90 kHz is more suitable for the process of interdigitated electrodes.



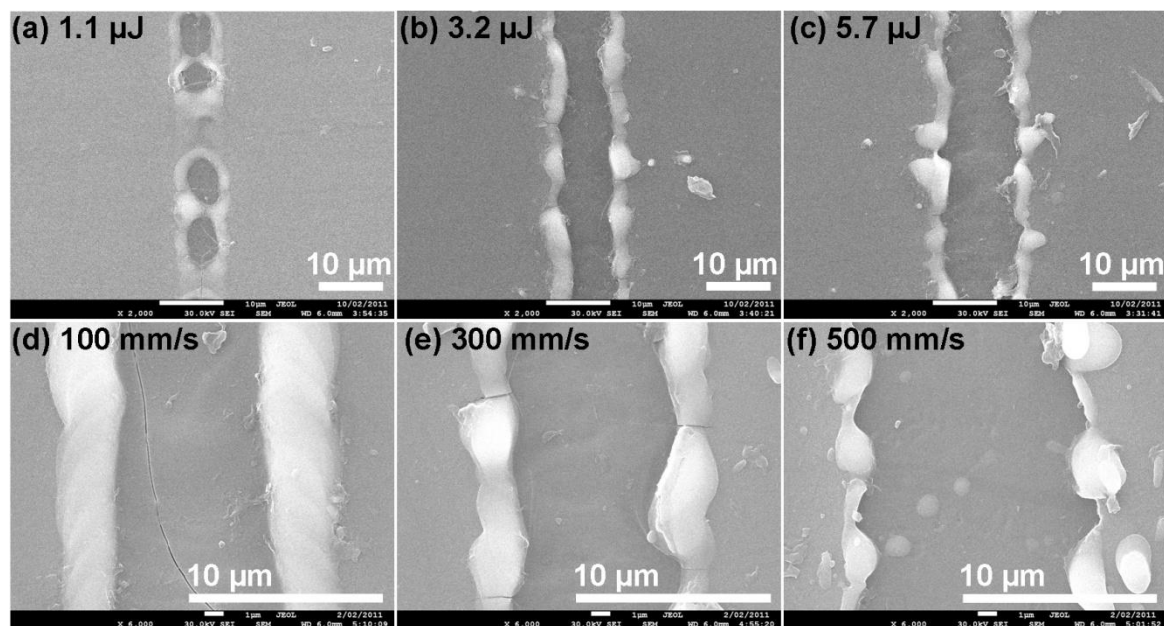
**Figure 3.10** Scanning electron micrographs showing straight groove micropatterns produced by laser pulses with (a) 20 and (b) 90 kHz laser pulses and moving at a speed of 300 mm/s on sample surface. Under these two conditions, the laser beams are moved by a distance of 15 and 3.3  $\mu\text{m}$ , respectively. The fluences for (a) and (b) are 31.0 and 4.4  $\mu\text{J}$  respectively.

### 3.3.2 Evaluation of parameters for the processing of Ti coated glass and PI

Ti coated glass and PI samples were prepared by magnetron sputtering operated at 110 W under an Ar pressure of 3.0 mTorr for 60 minutes. The coatings have a thickness of 300 nm and an average surface conductivity of  $4 \text{ } \Omega/\square$ .

To optimize parameters for the processing of Ti coated glass, laser pulses with a fixed frequency of 90 kHz were operated at fluences ranging from 1.1 to 5.7  $\mu\text{J}$  (Figure 3.11 (a) - (c)), and beam moving speed from 100 to 500 mm/s (Figure 3.11(d) - (e)). It is shown that 1.1  $\mu\text{J}$  is insufficient in producing a continuous groove. The actual output laser power from the laser source was 0.5 W. The instability of the energy output of the laser source at such a low power level is the main reason for the uncontinuous feature. At the other extreme, a 5.7  $\mu\text{J}$  fluence produces a more than 10  $\mu\text{m}$  wide groove, and results in significant melting and particles deposited onto adjacent regions. This fluence is believed to be too high for the ablation of 300 nm Ti coating on glass. An intermediate fluence of 3.2  $\mu\text{J}$  is more appropriate for producing interdigitated electrodes.

Comparing the micropatterns produced by different speeds, 100 mm/s seems to be too low for our purpose. When using 100 mm/s and 90 kHz, the laser beam was only moved by 1.1  $\mu\text{m}$  between every two shots. In this case, the laser energy was concentrated onto a relatively small area. As a result, significant melting was observed at the regions adjacent to the ablated grooves, and substrates were cracked by thermal shock (Figure 3.11(d)). On the other hand, a high speed of 500 mm/s results in splash of molten droplets all around micropattern, which increase the potential of shorting. A medium speed of 300 mm/s seems to be suitable for our purpose.

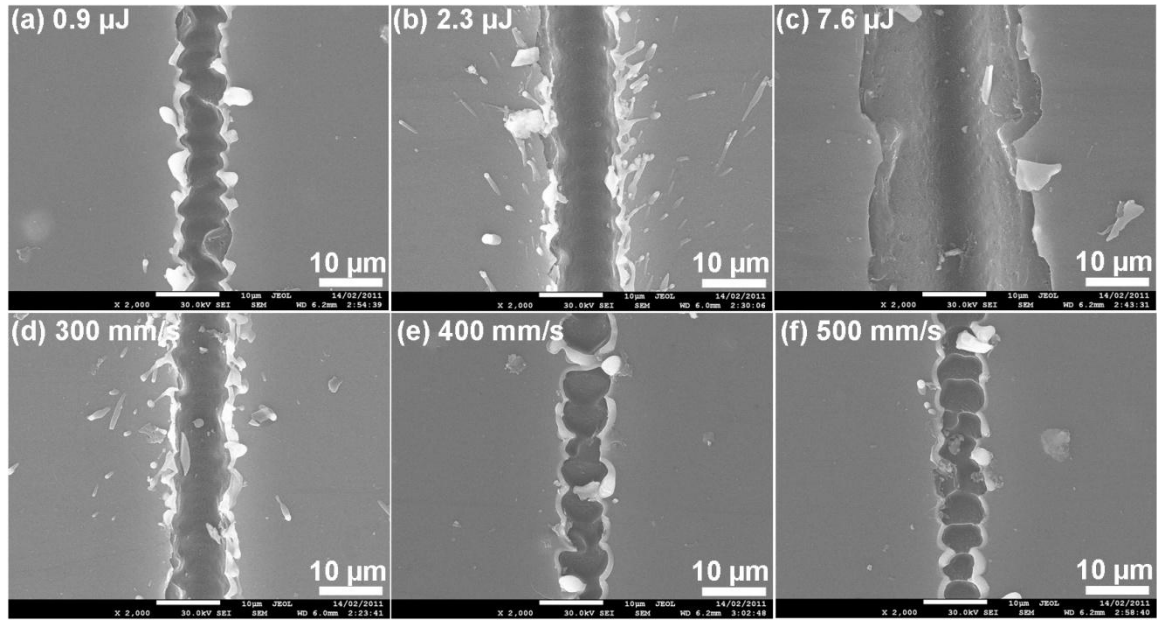


**Figure 3.11** Ablation of Ti coated glass by 355 nm solid-state laser operated at fluences of (a) 1.1, (b) 3.2 and (c) 5.7  $\mu\text{J}$  laser fluences. The laser pulses have a frequency of 90 kHz and were moved at a speed of 300 mm/s on sample surface. The laser beam was moved by a distance of 3.3  $\mu\text{m}$  between every two shots. A comparison of different beam moving speed is shown in (d), (e) and (f) for 90 kHz pulses with a 3.2  $\mu\text{J}$  fluence. The beam moving distances were 1.1, 3.3 and 5.5  $\mu\text{m}$  respectively for the three samples.

Similar trend are observed for the processing of Ti coated PI. For laser beams moving at 300 mm/s, the beam was moved by 3.3  $\mu\text{m}$  between every two shots. Increasing laser fluences from 0.9 to 7.6  $\mu\text{J}$  dramatically change ablated groove width from less than 10  $\mu\text{m}$  to more than 20  $\mu\text{m}$  (Figure 3.12(a) - (c)). 0.9  $\mu\text{J}$  fluence is too low to completely remove the Ti coating, whereas a too high fluence of 7.6  $\mu\text{J}$  causes severe delamination of Ti coatings around the ablated area.

At a laser fluence of 1.6  $\mu\text{J}$ , moving speeds of 300, 400 and 500 mm/s were used. 300 mm/s was the only speed that is applicable for our purpose. Higher speeds generally results in scattered craters, similar to what has been shown for the processing of FTO and Ti coated glass substrates. When using high moving speed such as 400 and 500 mm/s, missing pulse is also noticed.





**Figure 3.12** Ablation of Ti coated PI by 355 nm solid-state laser operated at fluences of (a) 0.9, (b) 2.3 and (c) 7.6  $\mu\text{J}$ . The laser pulses have a frequency of 90 kHz and were moved at a speed of 300 mm/s on sample surface. A comparison of different beam moving speeds is shown in (d), (e) and (f) for 90 kHz pulses with a 1.6  $\mu\text{J}$  fluence. The beam moving distances between every two shots are 3.3, 4.4 and 5.5  $\mu\text{m}$  for the three processing conditions.

### 3.3.1 Comparison of ablation on different materials

Due to the heating effect generated by nanosecond laser pulses, ablation defects such as cracking and melting of materials are almost unavoidable. On FTO glass, cracks are found propagating to tapered region (Figure 3.7(b)), but they are mostly terminated at the boundary of the un-ablated coatings. Clean sample surfaces could be obtained, with little debris or molten materials building up adjacent to features. Some particles are dispersed on the exposed substrates, which could possibly be molten glass attach to the substrates.

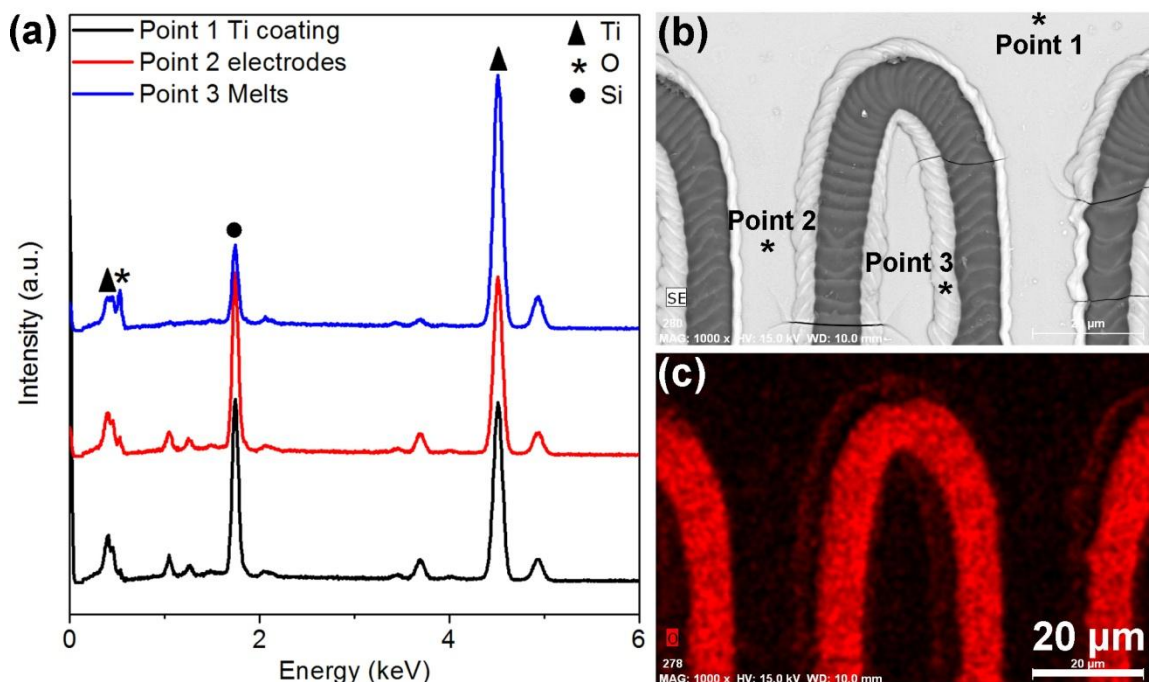
Ablation of Ti coated glass and PI substrates is more complicated than that of FTO glass. One obvious difference is the weaker coating-to-substrate adhesion for Ti coated glass and PI than for FTO glass, which could be explained by the differences in bonding natures between oxide-to-oxide and metal-to-oxide bonds.

The FTO to glass adhesion is essentially a ceramic to ceramic adhesion. On the other hand, the Ti to glass adhesion is a metal to ceramic adhesion, which consists of incoherent interface.

The transition from metallic to ionic bonds results in a large mismatch between different microstructures, and thus much weaker coating adhesion.

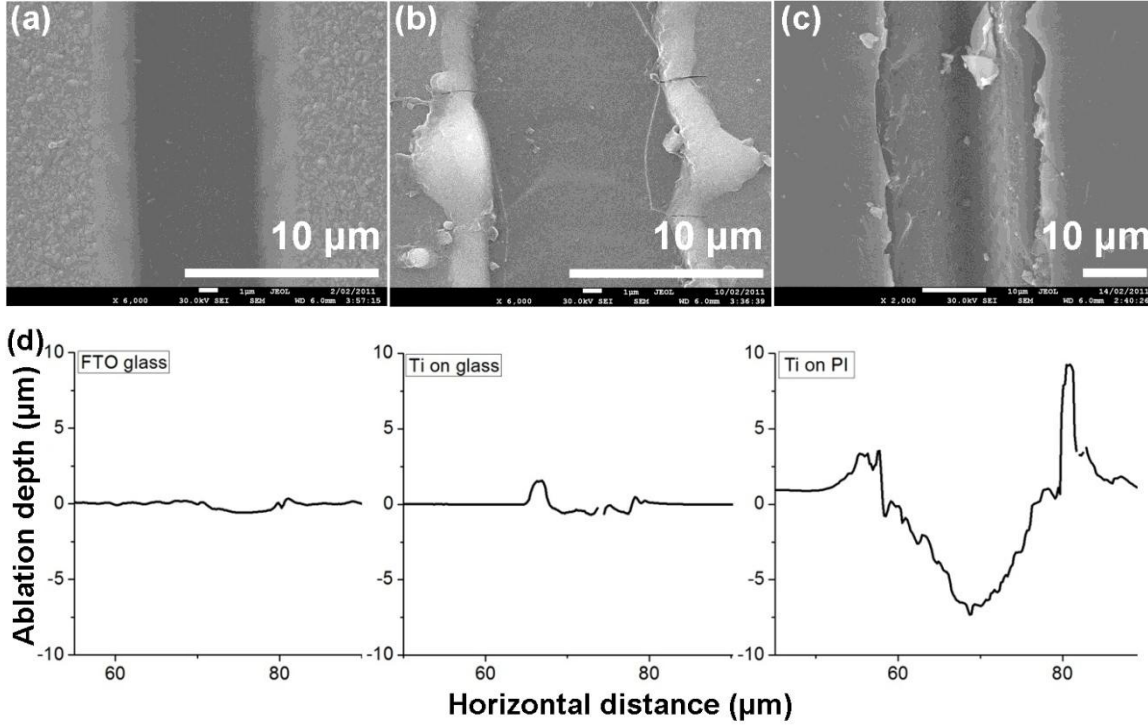
Similar principle can be applied to explain the weak adhesion between Ti and PI. Coating strength in both cases could be improved by annealing at high temperature, this might however cause other issues such as oxidation and thermal shock.

On the other hand, melting and splash of Ti indicates a much higher temperature than the melting point of Ti ( $T_m = 1668\text{ }^{\circ}\text{C}$  as shown in Table 3.1) is reached during the ablation process. At this temperature, it is quite possible that the FTO coating is quickly sublimed (Table 3.1), whereas Ti coatings are firstly melted and then evaporated. The high temperature also results in oxidation of Ti, especially at the regions around the ablated area. This is proved by the EDX results shown in Figure 3.13. From point 1 on Ti coating that is away from micropattern to point 2 at the middle of an electrode and further to point 3 on molten region (Figure 3.13(b)), an increase in oxygen content is observed (Figure 3.13(a)). This indicates an increased level of oxidation. The result is confirmed by the EDX mapping of oxygen distribution as shown in Figure 3.13(c). A brighter colour stands for a higher content of oxygen. At the boundary of micro-electrodes where the melts are formed, a higher oxygen content than on the rest of electrodes is found.



**Figure 3.13** (a) Energy-dispersive x-ray spectroscopy (EDS) results measured using a JEOL 7001F field-emission scanning electron microscope for point 1, 2 and 3 shown in (b) the compositional SEM image of interdigitated electrodes patterned on Ti coated glass. The oxygen distribution for the identical location is shown in (c). The scale bar shown in (c) is calibrated for images in both (b) and (c).

Figure 3.14 compares results for features produced on FTO glass, Ti coated glass and Ti coated PI by an identical laser fluence of 28  $\mu\text{J}$ . Heating seems to have less effect on FTO glass (Figure 3.14(a)) than on Ti coated glass and PI. On Ti coated glass, heating results in melts and cracks, (Figure 3.14(b)) while on Ti coated PI heating results in flaking of the Ti coating. Similar groove depths were produced on FTO and Ti coated glass as shown in Figure 3.14(d). Removal of FTO and Ti coating at such fluences is not difficult. Extra energy is dissipated onto substrate materials, and results in ablation of substrates. A much wider and deeper groove is produced on Ti coated PI. This implies the ablation of such a substrate required much lower energy than the other two, due to the fact that PI has a much lower decomposition temperature (a simple burn off experiment shows that PI starts to be carbonized at  $> 500\text{ }^{\circ}\text{C}$ ) than the evaporation temperature of soda-lime glass.



**Figure 3.14** Comparison of (a) FTO glass, (b) 300 nm Ti coated glass and (c) 300 nm Ti coated PI samples ablated by 355 nm solid-state UV laser operated at 4.4  $\mu\text{J}$  fluence, 300 mm/s beam travelling speed, and 90 kHz pulsing frequency. The surface profiles of these three samples are shown in (d), (e) and (f).

### 3.3.2 Processing of full-size patterns

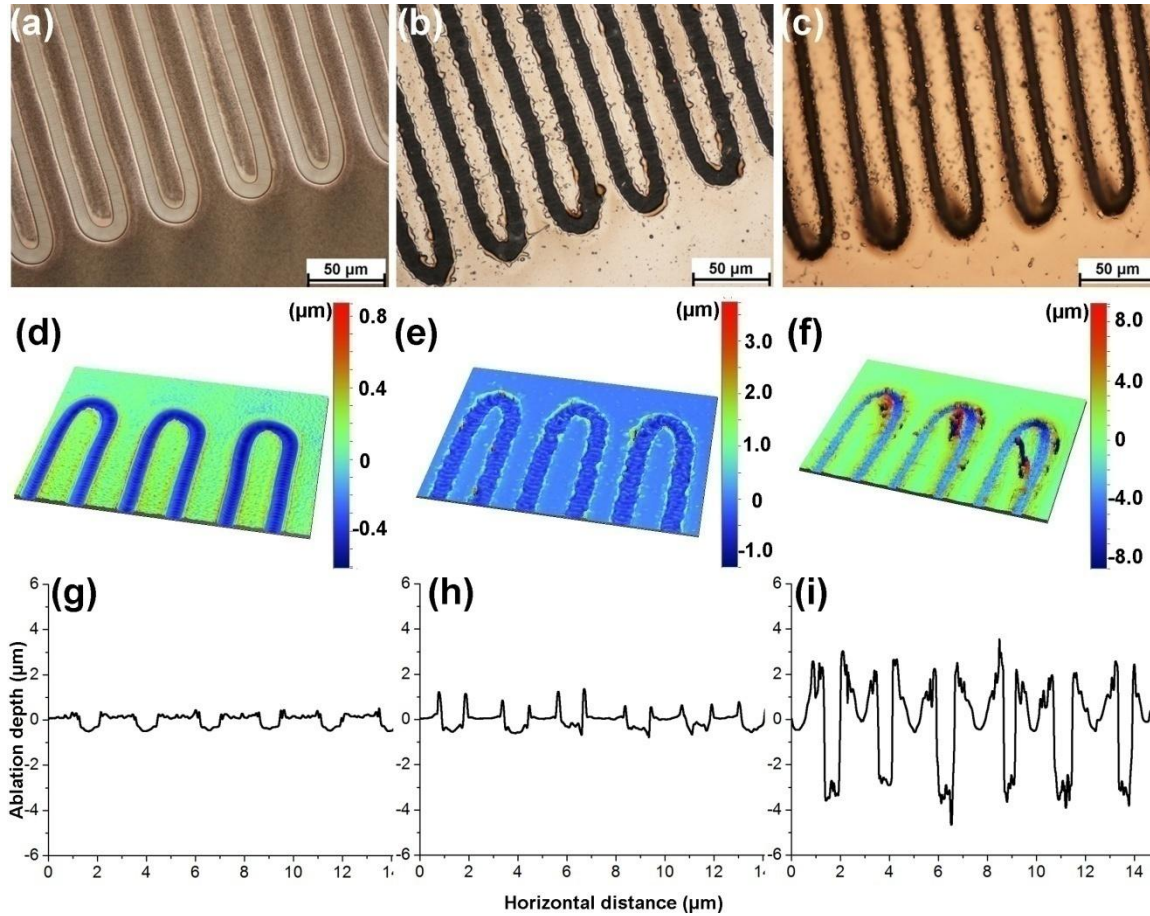
Based on the above discussion, optimized parameters for the processing of the above materials with the Nd:YVO<sub>4</sub> solid-state laser are listed in Table 3.2. Figure 3.15 shows a comparison of samples prepared with these parameters. Micrograph and 3D profile (Figure 3.15 (a) and (d)) show crack-free micro-electrodes with clean surfaces. Slightly distortion of the insulating tracks is due to the vibration of the linear motor within the x-y sample stage, which could be improved by technical adjustments. Average depth of ablation is more than 500 nm (Figure 3.15(g)), which is sufficient to remove FTO and form perfect insulating grooves.

**Table 3.2** Summary of processing parameters for the fabrication of full-size interdigitated electrodes on FTO glass, Ti coated glass and Ti coated PI using a direct-write Nd:YVO<sub>4</sub> solid-state laser. Note that the averages fluences shown in J/cm<sup>2</sup> are calculated based on the assumption that the beam has a homogeneous intensity distribution and has an effective spot size of 10 × 10 μm on sample surfaces.

<b>Solid-state laser</b>	<b>Fluences (J/cm<sup>2</sup>)</b>	<b>Beam moving speed (mm/s)</b>	<b>Pulsing frequency (kHz)</b>
FTO glass	4.4	200	90
Ti coated glass	3.2	300	90
Ti coated PI	2.3	300	90

In contrast, Ti micro-electrodes show a more complicated topography. Micrograph (Figure 3.15(b)) and 3D profile (Figure 3.15(e)) show lumps of melting materials surrounding ablated areas and splashed molten droplets on the electrode surface. An average 500 nm ablation depth ensures good insulation (compared to a 300 nm Ti coating). Shorting bridges are sometimes found on these samples, however this can usually be solved by electrical burn off through the application of a DC voltage across the two electrode sets.

Interdigitated electrodes on Ti coated PI are mostly failed, mostly due to the delamination of the Ti coatings and the thermal distortion of the PI substrate. Micrograph (Figure 3.15(c)) reveals delamination and curling of most micro-electrodes at the tip regions. The major reason is the overheating of substrates by nanosecond laser pulses. Even with a deep etching of 4 μm, <2 kΩ resistances are usually measured between two electrode sets, mostly caused by the curled micro-electrodes.



**Figure 3.15** Comparison of full-size interdigitated electrodes processed on (a) FTO glass (b) Ti coated glass and (c) Ti coated PI using Nd:YVO<sub>4</sub> solid-state UV laser. The surface profiles of these samples were measured using an optical profilometer (Veeco WYKO NT1100 optical profiling system). The 3D mapping and 2D profile results are shown in (d) - (f) and (g) - (i) respectively.

### 3.4 Conclusion

In conclusion, the fabrication of interdigitated electrodes using laser ablation is investigated in this chapter. Mask-delivered KrF excimer laser and direct-write Nd:YVO<sub>4</sub> solid-state laser were employed to process FTO glass, Ti coated glass and Ti coated PI.

Generally, the mask-delivered process is less flexible and requires more sophisticated laser facilities. The major issue for this process is the complexity associated with stitching elementary patterns. There is also the problem with using 248 nm KrF excimer laser radiation. Strong absorption by soda-lime glass at this wavelength results in etching and cracking of substrates.

For direct-write laser ablation, a higher pulsing frequency such as 90 kHz was found desirable for producing smooth microelectrodes. Increasing laser fluence and reducing beam moving speed both result in increased ablated groove width. Ablation on FTO glass was relatively simple. Little delamination or cracking of FTO coating was found, due to the strong adhesion between FTO and glass substrates. However, ablation of Ti coated glass and PI was more problematic, Lumps of molten materials were deposited around ablated grooves, resulted in rough electrode surfaces. For PI substrate further issues of delamination and flaking of Ti coating renders the ablation on this substrate unsuccessful.

Finally, with evaluated processing parameters, patterns with good insulation and acceptable morphology were produced on FTO and Ti coated glass by both laser systems. However, due to the intensive heat generation associated with nanosecond laser pulses, issues of cracking and melting of materials always exist. The processing of micron-sized electrodes using nanosecond laser pulses is proved to be not ideal. Defect-free features with clearly etched edges could be rather easily produced by femtosecond laser pulses. Experiments described in this chapter would be improved upon the availability of femtosecond laser facilities. The prospective successful interdigitated electrodes on Ti coated PI substrates would provide the potential of producing flexible back-contact DSCs on non-transparent substrates.

### 3.5 *References to chapter 3*

- [1] L. Zhigilei, Z. Lin, D. Ivanov, *J. phys. Chem. C* **2009**, 113, 11892.
- [2] B. Chichkov, C. Momma, S. Nolte, F. vonAlvensleben, A. Tunnermann, *Appl. Phys. A-Mater.* **1996**, 63, 109.
- [3] P. Lorazo, L. Lewis, M. Meunier, *Phys. Rev. B* **2006**, 73.
- [4] A. Weck, T. Crawford, D. Wilkinson, H. Haugen, J. Preston, *Appl. Phys. A-Mater.* **2008**, 90, 537.
- [5] X. Liu, *Proc. SPIE.* **2005**, 5713, 372.
- [6] A. Semerok, B. Salle, J. Wagner, G. Petite, O. Gobert, P. Meynadier, *Proc. SPIE.* **2001**, 4423, 153.
- [7] X. Y. Wang, D. M. Riffe, Y. S. Lee, M. C. Downer, *Phys. Rev. B* **1994**, 50, 8016.
- [8] R. W. Schoenlein, W. Z. Lin, J. G. Fujimoto, G. L. Eesley, *Phys. Rev. Lett.* **1987**, 58, 1680.
- [9] W. S. Fann, R. Storz, H. W. K. Tom, J. Bokor, *Phys. Rev. B* **1992**, 46, 13592.
- [10] F. Krasniqi, S. Johnson, P. Beaud, M. Kaiser, D. Grolimund, G. Ingold, *Phys. Rev. B* **2008**, 78.
- [11] Dupont, **2010**.

- [12] D. William, J. Callister, *Materials science and engineering: and introduction*, John Wiley & Sons, Inc., New York **2003**.
- [13] D. R. Lide, W. M. Haynes, *CRC handbook of chemistry and physics*, Boca Raton, Fla. : CRC press, **2009-2010**.
- [14] G. Raciukaitis, M. Brikas, M. Gedvilas, T. Rakickas, *Appl. Surf. Sci.* **2007**, 253, 6570.
- [15] J. Bovatsek, A. Tamhankar, R. Patel, N. Bulgakova, J. Bonse, *Thin Solid Films* **2010**, 518, 2897.
- [16] F. Zhang, J. Duan, X. Zeng, X. Li, *Proc. SPIE.* **2010**, 7584.



## 4 Pulsed-current electrochemical deposition of Pt catalytic coatings

This chapter describes a pulsed-current electrochemical deposition (PEC) technique that is used to produce Pt catalytic coatings for our back-contact DSCs. Furthermore, the technique can be applied at room temperature using simple setup, and is therefore well suited for producing Pt counter electrodes used in conventional DSCs.

As described in Chapter 1, photocurrent generation in DSCs involves a sequence of processes including dye excitation, electron injection into the nanocrystalline  $\text{TiO}_2$ , regeneration of oxidized dye molecules by iodide, ionic diffusion of redox species in the electrolyte and reduction of triiodide at the counter electrode (Equation 4.1).



The reduction of triiodide features a high overpotential on common transparent conductive oxide (TCO) layers such as fluorine-doped tin oxide (FTO) or indium-doped tin oxide (ITO). This necessitates the use of additional catalytic coatings on TCOs in order to afford efficient triiodide regeneration at low overpotentials.

The catalytic coating on CEs is crucial for the performance of DSCs, as the reaction rate relating to the charge transfer at the CE/electrolyte interface, has to be fast enough to cope with a high rate of charge transfer in DSC systems under full sun illumination.

So far the most widely used catalytic material has been Pt<sup>1-4</sup>, owing to its excellent catalytic activity. Alternative materials such as carbon black,<sup>5, 6</sup> carbon nanotubes,<sup>7</sup> poly 3,4-ethylenedioxythiophene (PEDOT)<sup>8, 9</sup>, and graphene/PEDOT composites<sup>10</sup> have also been investigated, yet their catalytic activities are only comparable to that of Pt when their coating thickness approaches a few micrometers<sup>5, 6</sup>.

In Chapter 1, we have discussed the methods used to produce the Pt catalytic coating for DSCs. Most commonly, Pt CEs are produced by thermal decomposition (TD) of Pt precursors,<sup>11</sup> such as hexachloroplatinic acid ( $\text{H}_2\text{PtCl}_6$ ).<sup>3, 4</sup> Alternatively, Pt CEs can be produced by room-temperature processes such as sputtering<sup>7, 12</sup>, chemical reduction<sup>13, 14</sup> and electrochemical deposition (ED).<sup>7, 15-19</sup> Here, we present a systematic study that correlates the pulsed current

deposition conditions with the resulting nanostructure morphology as well as the optical and catalytic properties of the resulting Pt coating. Reducing the amount of electrodeposited Pt per surface area is of great interest in view of the imminent commercialization of DSC technology, allowing to cut fabrication costs while also improving the optical transmission of the catalytic layer. The latter is important for DSC device configurations that operate in back-illumination mode<sup>15</sup> as well as bifacial solar cells.<sup>20</sup> The current study provides an analysis of how catalytic and optical properties are dependent on the deposition conditions, as well as the overall amount of Pt deposited per surface area.

## 4.1 *Experimental methods*

### 4.1.1 **Materials and reagents**

FTO glass substrates (10  $\Omega/\square$ , Nippon Sheet Glass) were cleaned with 5 % Helmanex in water, ultrapure water and ethanol in an ultrasonic bath. TiO<sub>2</sub> paste (JGC Catalysts and Chemicals Ltd, Kitakyushu-Shi (Japan)), N719 dye (Dyesol, Queanbeyan (Australia)) and all other chemical compounds (Sigma-Aldrich (Australia)) were used without further purification.

### 4.1.2 **Pulsed-current electrochemical deposition (PED)**

A purpose-built three electrode electrochemical cell was used for all PED experiments. The aqueous solution contains 2 mM hexachloroplatinic acid (H<sub>2</sub>PtCl<sub>6</sub>). Hydrochloric acid was used as a supporting electrolyte to achieve a pH value of 2.0-2.2. It was reported that the electrolysis of water can be effectively suppressed at this pH range.<sup>21</sup> FTO glass, a Pt plate and Ag/AgCl (3.5 M KCl, 0.197 V vs. SHE) were used as the working, auxiliary and reference electrode, respectively. Current pulses with current densities of  $J_{pulse}$  (measured in mA/cm<sup>2</sup>) were applied for a duration of  $t_{on}$  with an idle period of  $t_{off}$  between every two pulses. Pt deposits were produced by the reduction of PtCl<sub>6</sub> according to Equations 4.2 and 4.3.



The overall deposition process involved a number of pulse cycles and lasted for a total period of  $t_o$ . Assuming a quantitative conversion of electrons to deposited Pt according, the overall Pt

mass loading per unit area ( $m_{Pt}$ ) could be estimated from the number of charges applied to a unit geometrical area of electrode surface Equation 4.4,

$$m_{Pt} = \frac{M_{Pt} \times J_{pulse} \times \frac{t_{pulse}}{t_{pulse} + t_{off}}}{4 \times F} \quad 4.4$$

where  $M_{Pt}$  stands for the molar mass of Pt and  $F$  for the Faraday constant. From the Pt mass loading  $m_{Pt}$  a nominal thickness of the deposited Pt layer was calculated by dividing  $m_{Pt}$  by the bulk density of platinum.

In this study the current density was varied between 3 and 10 mA/cm<sup>2</sup>. Hydrogen evolution at higher deposition potentials could potentially reduce the deposition efficiency and therefore the actual  $m_{Pt}$ . Yet, no substantial gas generation was noticed up to a current density of 10 mA/cm<sup>2</sup>, indicating that high electric charge-to-Pt conversion efficiencies are ensured. The pulse and idle periods of  $t_{on}$  and  $t_{off}$  were kept constant at 100 and 1000 ms respectively. The overall amount of Pt loading (nominal thickness) was adjusted through the overall deposition time  $t_o$  of each deposition experiment. Current densities beyond 10 mA/cm<sup>2</sup> were not tested due to the possibility of significant water electrolysis at these higher current densities. At a current density of 15 mA/cm<sup>2</sup>, bubble formation was observed at the electrode surface.

Three types of CEs were produced using the TD method. For the first and second types, 10 µL of H<sub>2</sub>PtCl<sub>6</sub> solutions (1 and 10 mM in isopropanol) were spread onto a 1.5 cm<sup>2</sup> FTO glass surface. For the third type, 100 µL H<sub>2</sub>PtCl<sub>6</sub> solutions (10 mM in isopropanol) were spread onto the same electrode surface. Samples were dried in air and then sintered with a hot air gun at 400 °C for 15 min. The resulted nominal Pt coating thickness was approximately 0.6, 6.0 and 60 nm, respectively. The 6.0 nm coating is similar to those used in standard cell fabrication as previously described.<sup>2</sup>

#### 4.1.3 Charge transfer resistance ( $R_{ct}$ )

The charge transfer resistance ( $R_{ct}$ ) at the Pt/electrolyte interfaces was measured by electrochemical impedance spectroscopy (EIS) using a VSP2 potentiostat (Biologic Scientific Instruments). A thin layer of electrolyte (0.6 M 1-butyl-3-methylimidazolium iodide, 0.03 M iodine (≥ 99.99%), 0.10 M guanidinium thiocyanate (99%) and 0.5 M 4-tertbutylpyridine (Fluka, 98%) in a mixture of acetonitrile and valeronitrile (volume ratio, 85:15)) were sealed

between two identical platinized CEs to test in symmetrical cells. The cells were biased at 0 V potential with the application of a 10 mV AC voltage perturbation. Frequency of the AC perturbation was varied from 500 kHz to 0.1 Hz. EIS results were fitted to the equivalent circuit of the symmetrical cell to determine  $R_{ct}$ .

#### 4.1.4 Cyclic voltammetry

Cyclic voltammetry experiments were performed using an electrolyte containing 10 mM lithium iodide (99.9%), 1 mM iodine ( $\geq 99.99\%$ ) and 0.1 M lithium perchlorate (99.99%) in an acetonitrile (99.8%, anhydrous) solution. The voltages were scanned between  $-0.4$  V and  $1.0$  V (vs. a Ag/AgCl reference electrode) at a scan rate of  $50 \text{ mV s}^{-1}$  using a VSP2 potentiostat (Biologic Scientific Instruments).

#### 4.1.5 Scanning electron microscopy

SEM images were obtained using a JEOL 6300F (JEOL, Tokyo, Japan) field emission gun electron microscope. Samples were sputter coated with Au-Pd prior to imaging.

#### 4.1.6 UV-Vis spectroscopy

The optical transparency of platinized CEs was measured using a Cary 5000 UV-Vis spectrometer. Baseline correction was conducted without any sample in the optical pathway. Transmission data were taken over a range from 330 to 800 nm. The optical transmission measured at 550 nm was recorded as the optical transparency used for our data plots. The transparency of FTO glass was also measured as a reference.

#### 4.1.7 DSC fabrication

Mesoporous  $\text{TiO}_2$  films were screen-printed using methods previous described.<sup>2</sup> The cell fabrication follows the procedures as described in Chapter 2.

#### 4.1.8 Photocurrent-voltage characterization

The output of a sun simulator (Oriel, USA) equipped with a 1,000 W xenon lamp was adjusted using a calibrated silicon photodiode cell before each measurement. Devices were tested under simulated AM1.5 sunlight ( $100 \text{ mW/cm}^2$ ). Cells were covered by a 6 mm  $\times$  6 mm black mask during testing. The incident photon to electron conversion efficiency (IPCE) was measured

using a xenon light source (Oriel, Model 66901), a monochromator (Oriel, Model 74100), and a SourceMeter (Keithley, Model 2400).

## 4.2 *Results and discussion*

The electrochemical deposition of Pt involves three important fundamental stages, including the ionic adsorption of Pt cations onto the substrate, nucleation and crystal growth to form bulk materials.<sup>22</sup> Electrochemical deposition onto F-doped tin oxide (FTO) surfaces was reported to follow the "Volmer-Weber" mechanism.<sup>22, 23</sup> The binding energy between Pt atoms is greater than that between Pt atoms and the FTO substrate, resulting in the formation of 3D clusters upon the application of an electrical overpotential.

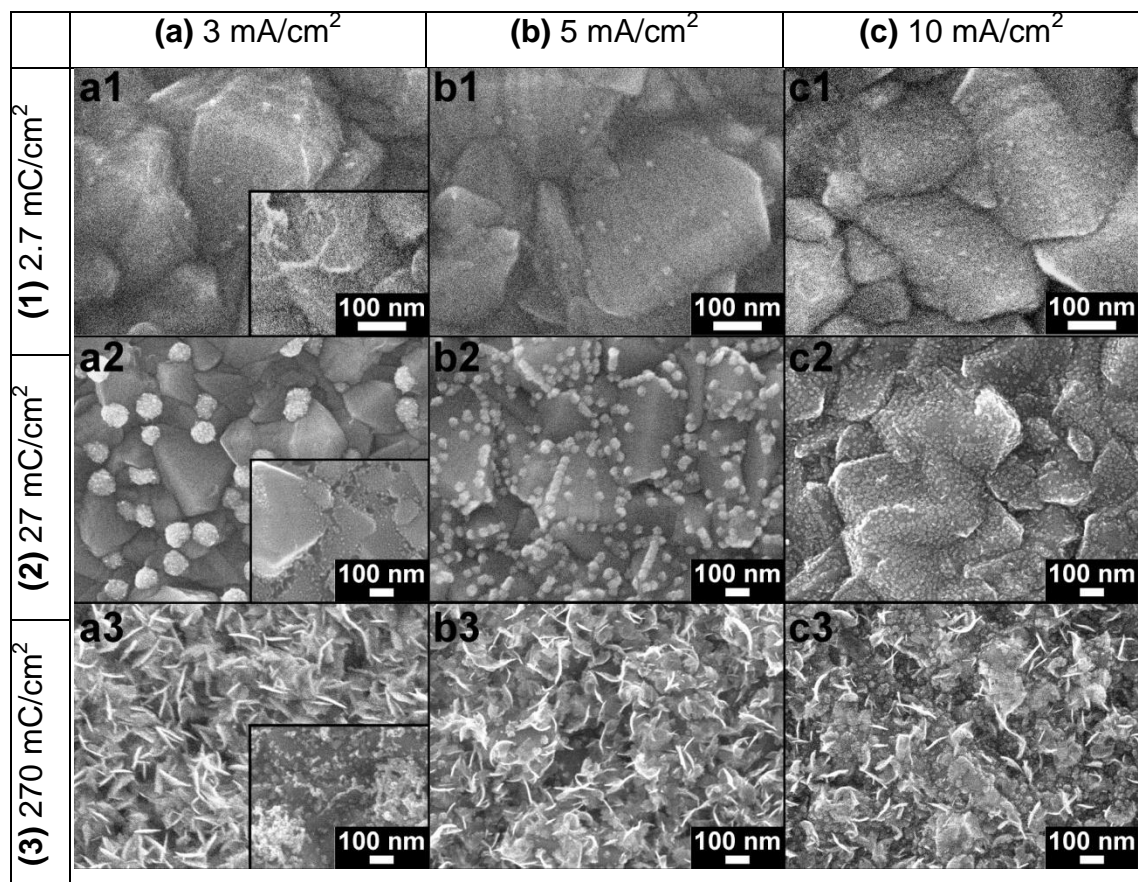
The morphology of Pt coatings significantly affects their catalytic activity.<sup>16, 24</sup> The charge transfer resistance at the CE/electrolyte interface can be reduced through the use of Pt coatings with higher activation surface area. With the same amount of Pt deposits, reducing the Pt particle size while increasing the particle density is a major strategy to reduce  $R_{ct}$  at the interface. This could be achieved by favoring nucleation over crystal growth during the deposition process. We show that while the Pt coating morphology cannot be controlled in the conventional TD method, the morphology, such as particle size and particle density, can be easily manipulated using the PED method described here.

### 4.2.1 **Coating morphology**

The scanning electron microscopic images of Pt coatings on FTO glass produced by PED using pulsed-current densities of 3, 5 and 10 mA/cm<sup>2</sup> are shown in Figure 4.1. Each row shows the morphology of Pt films that result from PED processes with identical integrated electrodeposition currents (total deposition charge) of 2.7, 27 and 270 mC/cm<sup>2</sup> respectively. Assuming a quantitative electrochemical conversion according to Equation 4.2 (see experimental section), these deposition conditions produce dense Pt films with nominal thicknesses of 0.64, 6.4 and 64 nm. Films produced with 2.7 mC/cm<sup>2</sup> show individual Pt nanoparticle deposits of < 10 nm, close to the resolution limit of the SEM. The images provide some indication that the overall size of the visible Pt nanoparticles decreases with increasing current-density whereas the number of visible Pt grains appears to increase with increasing current-density. Films fabricated with 27 mC/cm<sup>2</sup> (nominal Pt deposition thickness of 6.4 nm)

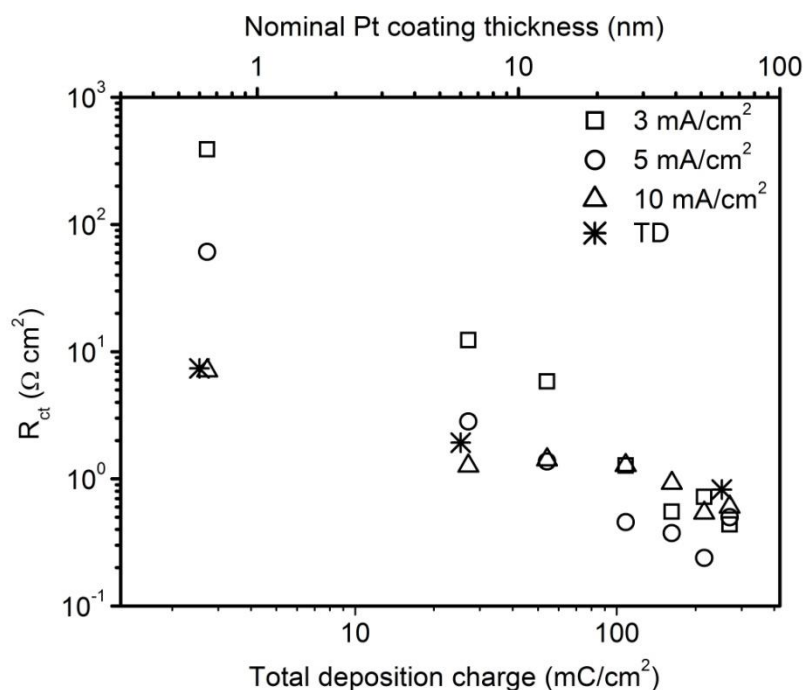
show striking morphology differences as a function of the PED deposition current density. The average Pt particle diameters associated with deposition current densities of 3 and 5 mA/cm<sup>2</sup> are 98 and 40 nm respectively. The density of Pt grains can be calculated accordingly to 26 and 272 NPs/μm<sup>2</sup>. A uniform film with fine particles is observed for the 10 mA/cm<sup>2</sup> sample. The particle size of this film is close to the resolution limit of the SEM, which is around 10 nm. At 5 mA/cm<sup>2</sup> the linear alignment of Pt grains leads to the appearance of some rod-shaped structures. Potentially the energetically favorable independent nucleation of Pt grains alongside FTO crystal grain boundaries, edges or other defects could lead to this effect. At 10 mA/cm<sup>2</sup> a dense coating of sub 10 nm particles can be observed. Further increase of overall galvanic deposition charge to 270 mC/cm<sup>2</sup> (nominal Pt thickness of 64 nm) leads to the formation of Pt films with flake-like as well as nanoparticulate nanostructures for all three current-densities. Flake-like structures with a typical length of around 100 nm form preferably at lower current densities.

Generally, Pt coatings produced by PED are quite uniform across a large area of electrode surface. In comparison, the thermal decomposition method used here (TD; see experimental) can result in coating defects such as large cluster of deposits and uncovered FTO surface (see insert Figure 4.1(a2)). These defects can be explained in terms of the aggregation of H<sub>2</sub>PtCl<sub>6</sub> during the drying of the precursor solution. Aside from these defects the TD method produces Pt films that are composed of small (< 10 nm) nanoparticles, similar to the primary particle size observed for high current density PED.



**Figure 4.1** Scanning electron micrographs of fluorine-doped tin oxide (FTO) glass deposited with Pt by pulsed-current electrochemical deposition using **a1-a3** 3 mA/cm<sup>2</sup>, **b1-b3** 5 mA/cm<sup>2</sup>, and **c1-c3** 10 mA/cm<sup>2</sup> pulsed-current densities to apply total deposition charges of 2.7, 27 and 270 mC/cm<sup>2</sup> (equivalent to Pt coatings with nominal thicknesses of 0.64, 6.4 and 64 nm). The inserted micrograph in **a1-a2** shows the surface morphology of Pt coatings with equivalent nominal thicknesses produced by thermal decomposition on FTO glass.

## 4.2.2 Charge transfer resistance



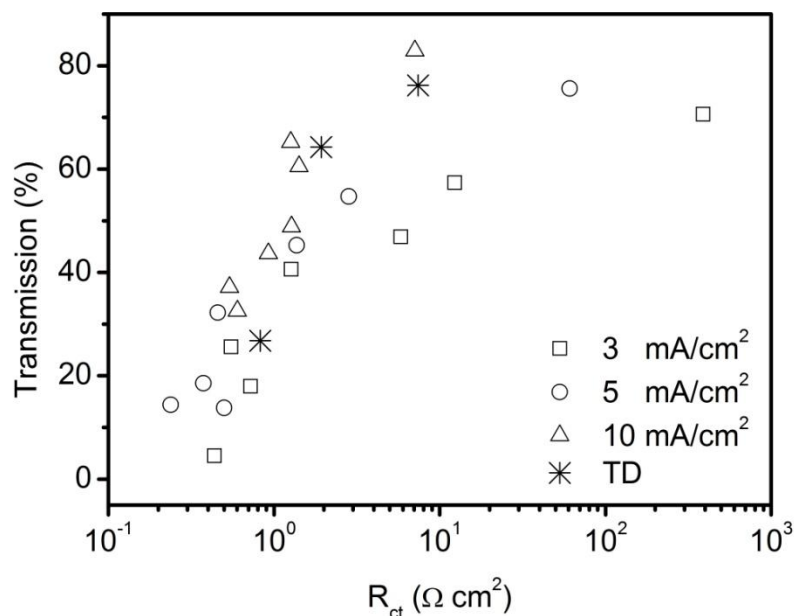
**Figure 4.2** Dependence of charge transfer resistance ( $R_{ct}$ ) on the total deposition charge used to produce Pt coatings by thermal decomposition and pulsed-current electrochemical deposition using 3, 5 and 10 mA/cm<sup>2</sup> pulsed-current densities. Nominal Pt thicknesses are also shown as a reference (see experimental section).

The charge transfer resistance  $R_{ct}$  at the CE/electrolyte interface for the reduction of triiodide to iodide is an important parameter that allows to quantify the activity of catalytic coatings. Figure 4.2 summarizes the measured  $R_{ct}$  values for Pt coatings deposited by PED as a function of the overall galvanic deposition charge and the according nominal Pt thickness. For comparison the  $R_{ct}$  values for Pt coatings deposited by TD are also shown as a function of their nominal Pt thickness, assuming quantitative conversion of  $\text{H}_2\text{PtCl}_6$  to Pt. For the different deposition conditions the data indicates a continuous decrease of  $R_{ct}$  with increasing Pt layer thickness. Generally Pt films produced by PED at high current densities show lower  $R_{ct}$  values than films produced at low current densities. This correlates well with the morphological changes observed in Figure 4.1, as  $R_{ct}$  is expected to decrease with increasing active surface area of the catalyst. Pt films produced via TD methods showed a catalytic activity similar to



films produced at  $10 \text{ mA/cm}^2$  via PED. This again correlates well with the similarities in coating morphology observed for films produced by those two deposition methods.

### 4.2.3 Optical transparency



**Figure 4.3** Correlation between optical transmission and charge transfer resistance ( $R_{ct}$ ) for Pt coatings produced by thermal decomposition (TD) and pulsed-current electrochemical deposition (PED) using 3, 5 and  $10 \text{ mA/cm}^2$  pulsed-current densities. The total deposition charge for the PED samples was varied from 2.7 to  $270 \text{ mC/cm}^2$ . The nominal thicknesses of the three TD samples shown are 0.64, 6.4 and 64 nm.

Optical transparency of CEs is important for DSC devices operating under back illumination mode (i.e. light irradiation from CEs), such as bifacial DSCs<sup>20</sup> and metal foil based flexible devices<sup>15</sup>. Generally, reducing the Pt film thickness will result in a cost reduction as well as an increase in optical transparency of the counter electrode which increases the optical light harvesting capability of those DSCs. At the same time it will result in an increase in  $R_{ct}$  with potentially adverse effects on the overall solar cell performance.

Figure 4.3 plots the measured optical transmission of the films analyzed in Figure 4.2 as a function of their  $R_{ct}$  values, showing decreasing optical transparency with decreasing  $R_{ct}$ . The plot also reveals a trend where films deposited at high current densities generally show better

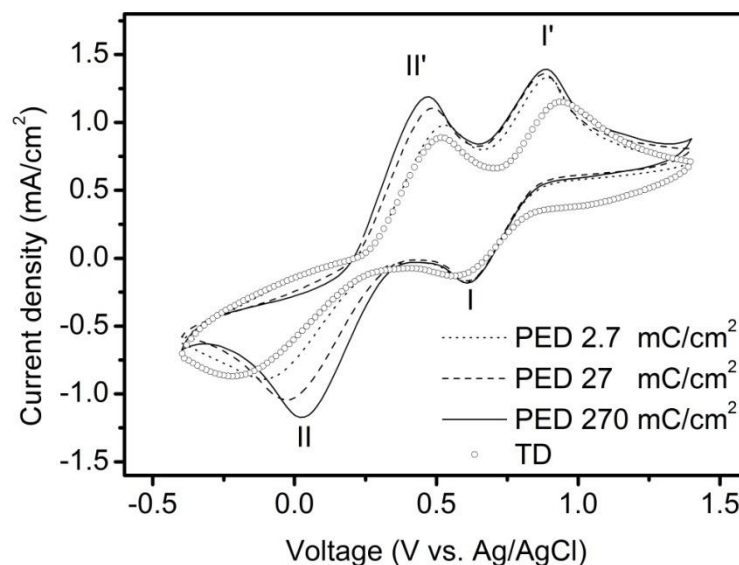
optical transmissions at comparable  $R_{ct}$  values, compared to films produced at lower current densities. The data points for the thermally deposited Pt layers are comparable to those of films made by PED with deposition current densities of 10 mA/cm<sup>2</sup>, with slight advantages of the PED layers over the TD films. Optical transmission values of up to 82 % could be measured for these films with  $R_{ct}$  values of 8  $\Omega$  cm<sup>2</sup>. This is almost identical to the transmission of the uncoated FTO glass (83 %) used as CE substrates in this study. The deposition process for the thinnest Pt coating produced by the 10 mA/cm<sup>2</sup> current density takes only 2.3 seconds. Such a rapid production of the high performance CE can be important for high throughput roll-to-roll fabrication process.

The data representation chosen for Figure 4.3 also allows to compare data sets produced by different deposition techniques, independent of the actual conversion rate of the thermal or electrochemical process, as the data is not plotted as a function of nominal film thickness.

#### 4.2.4 Cyclic voltammetry

The catalytic activity of Pt coatings is further characterized by cyclic voltammetry. In an anodic scan, iodide is oxidized to triiodide (peak II') and then to iodine (peak I') according to the reactions shown in Equation 4.5 and 4.6. In a reverse scan, iodine is reduced to triiodide (peak I) and then to iodide ions (peak II) according to the reactions shown in Equation 4.7 and 4.8.<sup>24</sup>

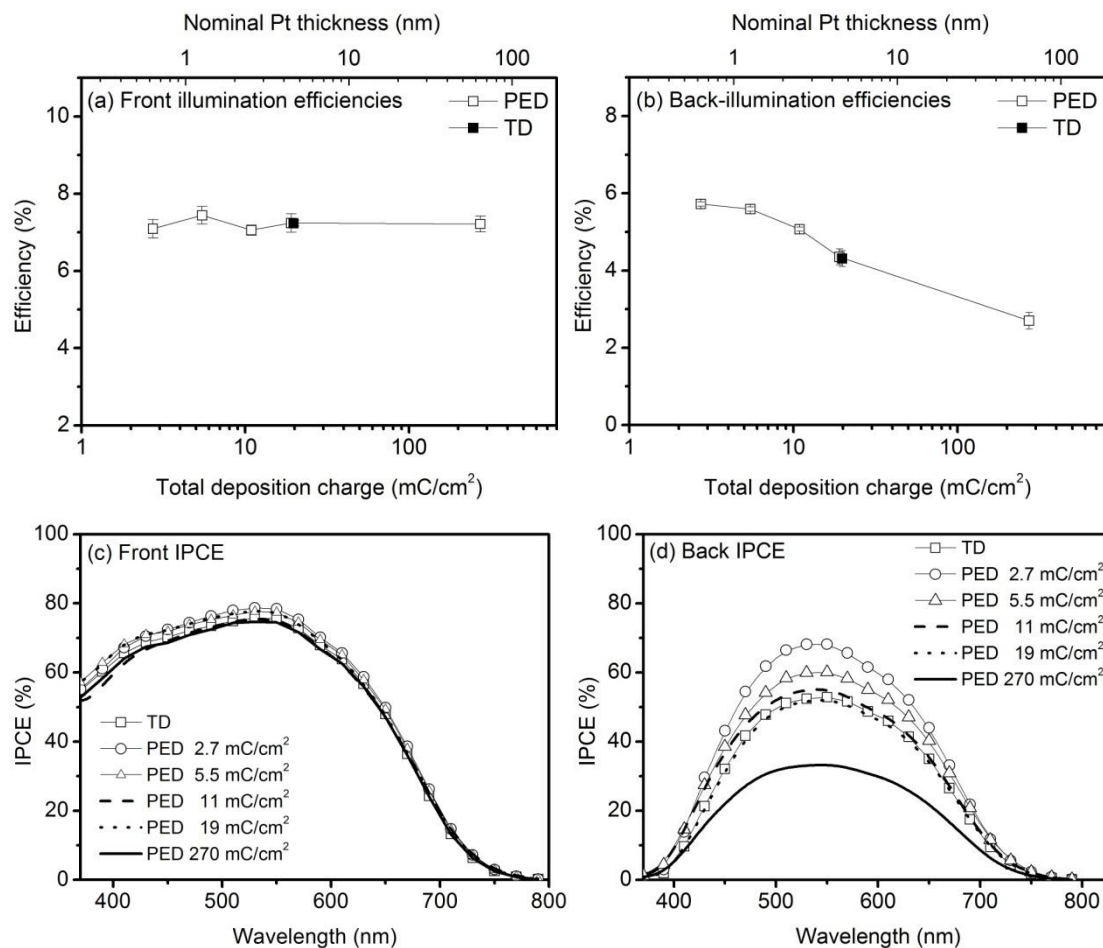




**Figure 4.4** Cyclic voltammetry measured for a Pt coating produced by thermal decomposition (TD) and pulsed-current Electrochemical deposition (PED) in an iodine/iodide electrolyte (10 mM lithium iodide, 1 mM iodine and 0.1 M lithium perchlorate in an acetonitrile solution). The PED samples were produced using a pulsed-current density of 10 mA/cm<sup>2</sup>. The total deposition charges for the three samples are 2.7, 27 and 270 mC/cm<sup>2</sup> (equivalent to Pt coatings with nominal thicknesses of 0.64, 6.4 and 64 nm). The TD sample has a nominal thickness of 6 nm.

The quality of catalytic coatings can be judged from the peak-to-peak separation between peak II and II' as well as the oxidation and reduction current densities. Figure 4.4 shows the cyclic voltammogram of a variety of Pt coatings. The peak-to-peak separation for films produced by PED decreases from 640 to 500 and 440 mV as the galvanic deposition charge increases from 2.7 to 27 and 270 mC/cm<sup>2</sup> respectively. The peak-to-peak separation of a TD Pt film with a nominal Pt thickness of 6 nm was measured to be 740 mV, which is significantly higher than the 640 mV measured for the thinnest PED film (2.7 mC/cm<sup>2</sup>), corresponding to a nominal Pt thickness of 0.64 nm. The oxidation and reduction current densities follow similar trends. Contrary to the results derived from impedance spectroscopic experiments that show similar R<sub>ct</sub> values for PED films produced at high current-density and TD films, cyclovoltammetry indicates that films produced via high-current density PED are superior in catalytic performance over TD Pt films.

### 4.2.5 Photovoltaic performances of DSCs



**Figure 4.5** Solar energy conversion efficiencies of DSCs assembled with CEs platinized by thermal decomposition (TD) and 10 mA/cm<sup>2</sup> pulsed-current electrochemical deposition (PED). For PED samples, the total deposition charge was varied from 2.7 to 270 mC/cm<sup>2</sup>. The TD sample has a nominal Pt thickness of 6 nm. DSCs were measured under (a) front and (b) back illumination conditions. The Pt loadings are measured by charge densities as well as nominal thicknesses. The Incident Photon-to-Electron Conversion Efficiencies (IPCEs) of these DSCs are shown in (c) and (d) for testing under front and back illumination conditions.

#### Efficiencies under front and back illumination

DSCs were assembled with CEs produced by 10 mA/cm<sup>2</sup> PED and TD and their photovoltaic performance under simulated sunlight was characterized with the light incident on the TiO<sub>2</sub> working electrode (front) and Pt counter electrode (back) respectively. The optimized

literature procedure<sup>2</sup> used to fabricate TD counter electrodes yielded Pt films with a nominal film thickness of 6,0 nm. Figure 4.5(a) shows similar solar energy conversion efficiencies under front illumination for all DSCs regardless of fabrication methods or thicknesses. The difference in  $R_{ct}$  previously observed for the different CEs has no obvious effect on the efficiency of the DSCs. The inconsistency among these devices attributed mostly to variations in the general DSC fabrication processes rather than the effect of different CEs. Surprisingly, DSCs employing CEs with a nominal thickness of only 0.64 nm could achieve an efficiency of 7.1 %, which is as high as those with much thicker Pt coatings. Increasing the nominal thickness by 100 fold (to 64 nm) provides negligible benefit towards a higher efficiency. However, under back illumination (Figure 4.5(b)), the DSCs with the lowest nominal Pt thickness (0.64 nm) feature the highest efficiency (5.8%), due to their superior transparency compared to CEs with thicker Pt coating. DSCs made from CEs fabricated via TD feature a conversion efficiency of 4.2%, similar to those assembled from PED CEs with a comparable nominal thickness (19 mC/cm<sup>2</sup>; 4.3 %).

### **Incident photon-to-electron conversion efficiencies**

Under front illumination, similar incident photon-to-electron conversion efficiencies (IPCEs) close to 80 % are measured for all devices (Figure 4.5(c)). This is in good agreement with the trend in efficiencies observed for IV characterizations. Furthermore IPCE measurements are performed under short-circuit at photon fluxes that are significantly lower than at full sun illumination, such that differences in catalytic performance should not affect the IPCE characteristics in front illumination mode. Under back illumination (Figure 4.5(d)) the IPCE performances drop with increasing nominal Pt layer thickness, in accordance with the increasing optical filter effect of the Pt coating. The highest IPCE peak close to 70 % is measured for a DSC with the thinnest Pt coating. All IPCE curves drop dramatically at wavelength below 550 nm due to the absorption of the thin electrolyte layer between the counter electrode and the sensitized TiO<sub>2</sub> film. This drop also explains the difference in energy conversion efficiency when comparing DSCs under front and back-illumination. All solar cells presented in this study were assembled with a standard 25  $\mu$ m thick surlyn spacer between working and counter electrode. Ito et al. have previously demonstrated a strategy to significantly reduce the impact of electrolyte absorption on the device performance under

back-illumination.<sup>20</sup> IPCEs for DSCs featuring thermally deposited Pt CEs show IPCE performances that are very similar to those featuring PED CEs with comparable nominal thickness.

### 4.3 *Conclusions*

In conclusion, Pt catalytic coatings for DSC counter electrodes (CEs) were produced by pulsed-current electrochemical deposition (PED). The morphology of the Pt coating was strongly dependent on the deposition current density and the overall layer thickness. Pt layers deposited by PED at 10 mA/cm<sup>2</sup> with nominal thicknesses of up to 6.4 nm revealed a nanostructured morphology with grain sizes below 10 nm. Pt layers fabricated under these conditions also showed the most favorable relation between catalytic activity and optical transparency. DSCs employing FTO counter electrodes with a nominal Pt thickness of 0.64 nm performed similar (+/-5 %) to DSCs employing CEs with Pt thicknesses that were 10 and 100x as thick, fabricated by PED or alternatively the conventionally employed thermal decomposition of H<sub>2</sub>PtCl<sub>6</sub>. Their optical transparency of 82 % was close to that of uncoated FTO glass. This electrodeposition process is highly compatible with the high-throughput fabrication of DSCs. Following the PED deposition conditions described in this paper Pt-coated high-performance counter electrodes can be produced at room temperature within 2.3 seconds without the need for any thermal post-treatment. The overall amount of Pt used to cover 1 m<sup>2</sup> corresponds to 14 mg. Based on an estimated price of 50 US\$ per g of Pt this corresponds to a cost of 0.7 US\$/m<sup>2</sup> or, when applied in a 8% DSC module, of less than 0.01 US\$/W<sup>peak</sup>. The process described is also compatible with flexible polymer substrates and roll-to-roll fabrication processes.

### 4.4 *References to chapter 4*

- [1] B. O'Regan, M. Grätzel, *Nature* **1991**, 353, 737.
- [2] S. Ito, T. N. Murakami, P. Comte, P. Liska, C. Grätzel, M. K. Nazeeruddin, M. Grätzel, *Thin Solid Films* **2008**, 516, 4613.
- [3] Y. Chiba, A. Islam, Y. Watanabe, R. Komiya, N. Koide, L. Y. Han, *Jpn. J. Appl. Phys.* **2006**, 45, L638.
- [4] T. Bessho, S. M. Zakeeruddin, C. Yeh, E. Diau, M. Grätzel, *Angew. Chem. Int. Edit.* **2010**, 49, 6646.

- [5] T. Murakami, S. Ito, Q. Wang, M. Nazeeruddin, T. Bessho, I. Cesar, *J. Electrochem. Soc.* **2006**, 153, A2255.
- [6] E. Ramasamy, W. Lee, D. Lee, J. Song, *Appl. Phys. Lett.* **2007**, 90, 173103.
- [7] B. Koo, D. Lee, H. Kim, W. Lee, J. Song, *J. Electroceram.* **2006**, 17, 79.
- [8] Y. Saito, W. Kubo, T. Kitamura, Y. Wada, S. Yanagida, *J. Photoch. Photobio. A* **2004**, 164, 153.
- [9] M. Biancardo, K. West, F. C. Krebs, *J. Photoch. Photobio. A* **2007**, 187, 395.
- [10] W. J. Hong, Y. X. Xu, G. W. Lu, C. Li, G. Q. Shi, *Electrochem. Commun.* **2008**, 10, 1555.
- [11] N. Papageorgiou, W. Maier, M. Grätzel, *J. Electrochem. Soc.* **1997**, 144, 876.
- [12] T. Hoshikawa, M. Yamada, R. Kikuchi, K. Eguchi, *J. Electroanal. Chem.* **2005**, 577, 339.
- [13] T. Wei, C. Wan, Y. Wang, *Appl. Phys. Lett.* **2006**, 88, 103122.
- [14] T. Wei, C. Wan, Y. Wang, C. Chen, H. Shiu, *J. Phys. Chem. C* **2007**, 111, 4847.
- [15] S. Ito, N.-L. C. Ha, G. Rothenberger, P. Liska, P. Comte, S. M. Zakeeruddin, P. Pechy, M. K. Nazeeruddin, M. Grätzel, *Chem. Commun.* **2006**, 4004.
- [16] S. Kim, Y. Nah, Y. Noh, J. Jo, D. Kim, *Electrochim. Acta.* **2006**, 51, 3814.
- [17] C. Yang, H. Zhang, Y. Zheng, *Curr. Appl. Phys.* **2011**, 11, S147.
- [18] C. Lin, J. Lin, C. Wan, T. Wei, *Electrochim. Acta.* **2011**, 56, 1941.
- [19] L. Chen, W. Tan, J. Zhang, X. Zhou, X. Zhang, Y. Lin, *Electrochim. Acta.* **2010**, 55, 3721.
- [20] S. Ito, S. M. Zakeeruddin, P. Comte, P. Liska, D. Kuang, M. Grätzel, *Nat. Photonics.* **2008**, 2, 693.
- [21] M. E. Baumgärtner, C. J. Raub, *Plat. Met. Rev.* **1988**, 32, 188.
- [22] E. Budevski, G. Staikov, W. J. Lorenz, *Electrochemical Phase Formation and Growth: An Introduction to the Initial Stages of Metal Deposition*, VCH Verlagsgesellschaft mbH & VCH Publishers, Weinheim & New York **1996**.
- [23] Y.-S. Ko, Y.-U. Kwon, *Electrochim. Acta.* **2010**, 55, 7276.
- [24] C. H. Yoon, R. Vittal, J. Lee, W.-S. Chae, K.-J. Kim, *Electrochim. Acta.* **2008**, 53, 2890.



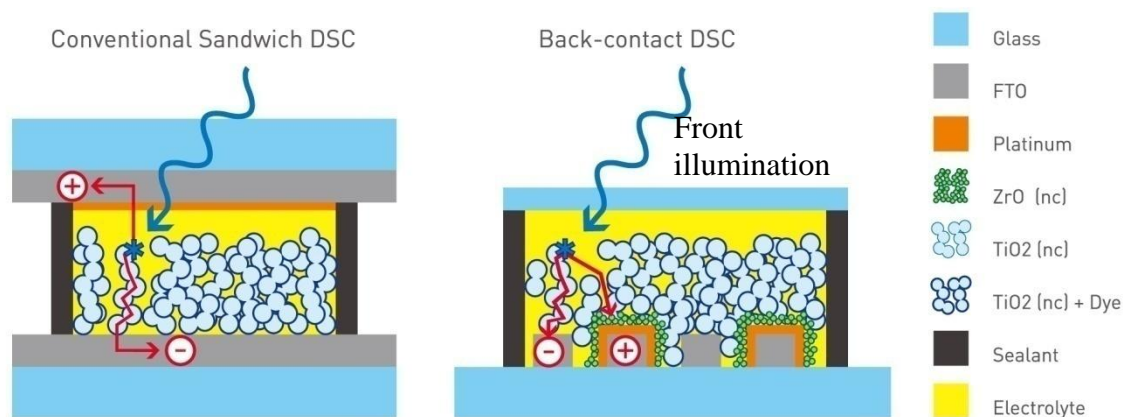


## 5 Interdigitated back-contact DSCs

This chapter describes the fabrication and characterization of interdigitated back-contact dye-sensitized solar cells (IBCDSCs). The DSC architecture differs from the sandwich DSC structure in that the charge collecting electrodes are both located on the same side of the dye-sensitized  $\text{TiO}_2$  film. Compared to previously reported back-contact DSC architectures,<sup>1-3</sup> the architecture described in this chapter is truly monolithic. The interdigitated back-contact architecture has been applied to silicon solar cells to achieve enhanced efficiencies, especially for those used under concentrated sunlight.<sup>4, 5</sup> Yet, this geometry has never been reported previously in the area of dye-sensitized solar cells.

### 5.1 *The structure of interdigitated back-contact DSC*

A comparison between the configuration of a typical IBCDSC and that of the most common DSC device is schematically shown in Figure 5.1. The device configuration of a typical IBCDSC preserves most of the design features common to conventional sandwich DSCs. The device consists of two sets of microelectrodes, namely Working and Counter Electrodes (WEs and CEs). The microelectrodes are conducting fingers fabricated from conductively materials coated substrates by laser ablation. To allow for efficient collection of electrons, the spacing between adjacent collecting electrodes needs to be shorter than the maximum free electron diffusion length.<sup>6</sup> On the other hand, the contacting electrodes need to be charge selective. In our design, the width of the electrodes is typically 10  $\mu\text{m}$ , and the width of the insulating track in between the electrodes is 10-15  $\mu\text{m}$ . The CEs are coated with a Pt catalytic layer and then a protective mesoporous  $\text{ZrO}_2$  film. A  $\text{TiO}_2$  mesoporous film is subsequently printed on top of the entire structure. After staining with dye, the cell is filled with electrolyte, and then sealed by a plain glass piece with a Surlyn<sup>®</sup> gasket.



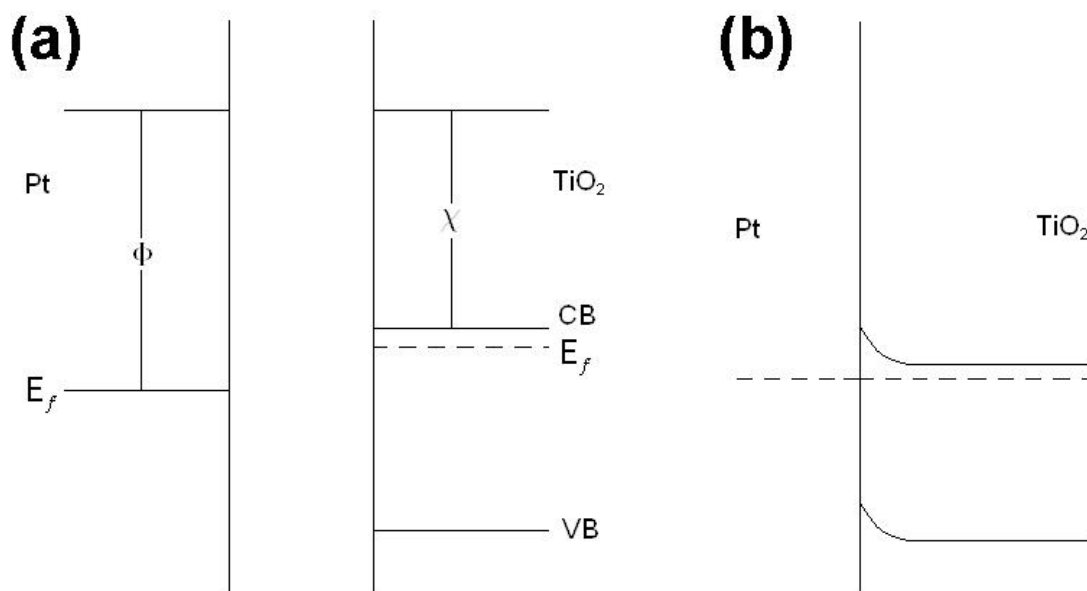
**Figure 5.1** Cross-sectional view of a conventional sandwich DSC and an interdigitated back-contact DSC (IBCDSC). This interdigitated pattern was produced by laser ablation, after which the Counter Electrode set (CE, set 2) was coated by a Pt black layer and a porous insulating ZrO<sub>2</sub> layer. A TiO<sub>2</sub> mesoporous film was printed on top of the entire substrate and stained with dye. The cell was sealed by a plain glass cover slide and filled with an electrolyte containing I/I<sub>3</sub><sup>-</sup> redox mediator. The bare FTO Working Electrode set (WE, set 1) forms an ohmic contact while the Pt-coated counter electrode set (cathode) forms a Schottky contact with the TiO<sub>2</sub> film, so that the electrons and holes are collected by electrode set 1 and 2 respectively. In the following sections, the illumination from the top side through the covering slide is defined as front illumination, whereas the illumination from the back contact electrodes side is defined as back illumination.

The working principle of the IBCDSC is similar to that of the conventional DSCs. When a photon is absorbed, a dye molecule gets excited and injects an electron into the conduction band of the TiO<sub>2</sub> film. The injected electron diffuses in the mesoporous TiO<sub>2</sub> film and is collected by the WEs. On the other hand, the photooxidized dye molecule is regenerated by the redox couple which is then reduced at the CEs.

Earlier work in the area of monolithic<sup>7</sup> and bifacial DSCs<sup>8</sup> has shown that direct contact between the mesoporous TiO<sub>2</sub> film and the counter electrode should be avoided. In IBCDSCs architecture, ZrO<sub>2</sub> nanoparticles were employed to make the protective layer on the CEs. The ZrO<sub>2</sub> is porous to allow the diffusion of redox species through to the Pt electrode.

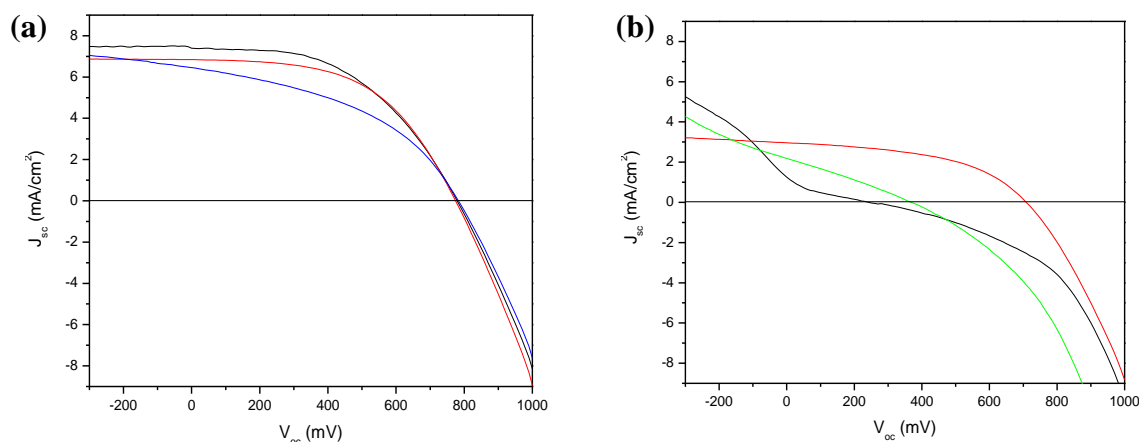
In fact, the ZrO<sub>2</sub> coating is not a necessary component in IBCDSCs. Due to a high work function of 5.6 eV, Pt forms a metal/semiconductor (Schottky) heterojunction with the TiO<sub>2</sub> nanoparticles (Figure 5.2), where electron flow from TiO<sub>2</sub> to Pt can be blocked during the

operation of DSCs.<sup>9, 10</sup> A further  $\text{ZrO}_2$  coating is employed as an insulating layer to shield off any direct contact between  $\text{TiO}_2$  and bare FTO through possible pin holes in the Pt coating.



**Figure 5.2** Band diagram showing the heterojunction formed at the  $\text{TiO}_2$ /platinum interface (a) before and (b) after contact.<sup>9</sup>

We have fabricated IBCDSCs with and without the  $\text{ZrO}_2$  protective layer. Figure 5.3 shows a comparison between the two types of devices. Regardless of other factors that affect cell performances, the use of the  $\text{ZrO}_2$  protective layer has dramatically increased the consistency of the results.



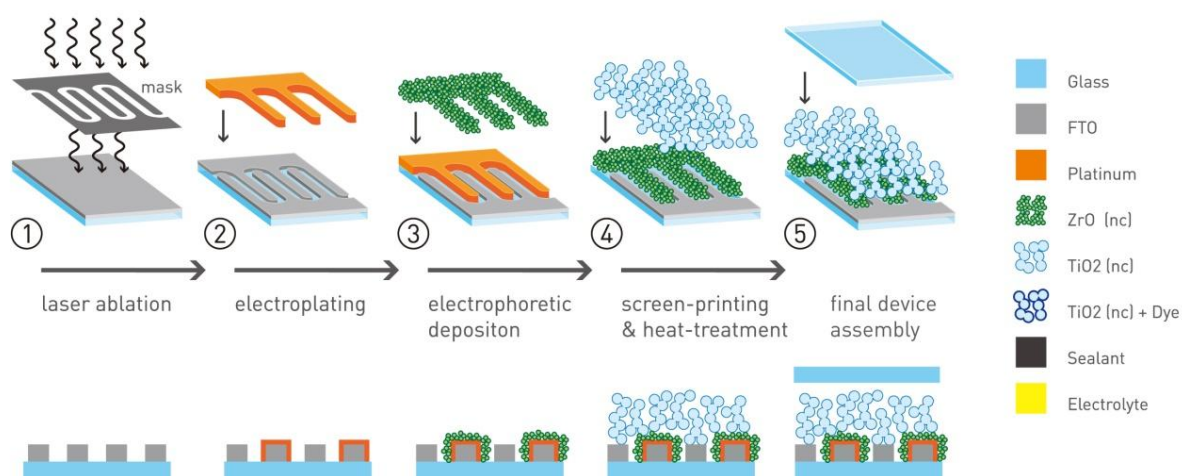
**Figure 5.3** Current-voltage characteristic of interdigitated back-contact DSCs (a) with and (b) without applying the  $ZrO_2$  protective layer. As shown that cell performances are widely scattered for cells without the  $ZrO_2$  layer. Better consistence is shown when using the protective layer.

An obvious advantage of the IBCDSC design is to reduce the use of electrode material. On top of that, the substrate itself is not necessarily transparent like the requirement for conventional DSCs. A great variety of substrate materials, such as metal coated polymer sheets, can be used to replace the expensive FTO glass. Furthermore, light can be irradiated through the front side of the devices (see Figure 5.1 for the definition of front illumination). As such, the transmission loss can be minimized by using a transparent cover slide, such as a plain glass slide or a thin plastic sheet. A pair of two charge selecting electrodes can be fabricated on a common backplate. Printing and drying of  $TiO_2$  is the final step in the assembly of IBCDSCs, so that all structural features necessary for interconnection and current collection can already be implemented into the backplate before the DSC components are deposited. The manufacture of the micron-sized interdigitated electrodes will not be difficult when considering the mass production of large area integrated circuits where electrodes in similar scales are rapidly produced. Laser ablation is not the only option for the fabrication, other techniques such as photolithography etc. could also be employed.

In the following section we firstly describe in general the fabrication of IBCDSCs. We then present results of the devices on FTO and Ti coated substrates.

## 5.2 The fabrication of interdigitated back-contact DSCs

The IBCDSC device fabrication steps are summarized in Figure 5.4. The figure only shows the laser ablation using a mask-delivered process, however the laser ablation can also be conducted using a direct-write process (the laser ablation processes are discussed in detail in Chapter 3). After laser ablation, one set of electrodes are electrochemically coated with a Pt coatings. A protective  $\text{ZrO}_2$  layer is further deposited onto the Pt coating. The  $\text{TiO}_2$  film is printed on the entire backplate. Following the sintering and dying processes, devices are sealed using transparent float glass sheets.



**Figure 5.4** An illustration of the fabrication steps employed for the fabrication of interdigitated back-contact DSCs, comprising (1) the laser ablation of substrates, (2) the electrochemical deposition of platinum, (3) the electrophoretic deposition of  $\text{ZrO}_2$ , (4) the screen-printing and the sintering of a  $\text{TiO}_2$  mesoporous film and (5) the final assembly of the device.

### 5.2.1 The laser ablation process

The fabrication of interdigitated micro-patterns on FTO glass and Ti coated glass has been discussed in Chapter 2. For this chapter, the interdigitated micro-patterns on FTO glass were fabricated using the mask-delivered laser ablation in the MiniFab (Caribbean business park, Melbourne, Australia) and the direct-write laser ablation in the Wuhan National Laboratory of Optoelectronics (WNLO, Wuhan, China). The interdigitated micro-patterns on Ti coated glass

were also fabricated using the direct-write process in WNLO. The materials and processing parameters for the three types of interdigitated backplates are summarized in Table 5.1

**Table 5.1** Summary of the materials and processing parameters used in the laser ablation of three types of conductive layer coated substrates. (\* the spot size/diameter is only an approximation measured from the ablated feature size. The term used here is different from the conventionally defined laser spot size, which refers to the beam diameter at the  $1/e^2$  level of the Gaussian intensity profile)

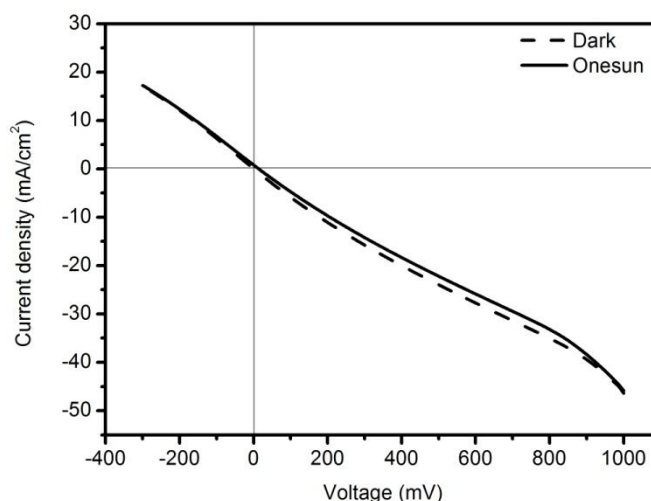
Backplates code	MiniFAB FTO	WNLO FTO	WNLO Ti
Materials	TEC-15 FTO glass	NSG 2 FTO glass	Ti coated glass
Conductive layer	400 nm FTO	600 nm FTO	300 nm Ti
Laser type	Excimer Mask-delivered	Solid-state UV Direct-write	Solid-state UV Direct-write
Wavelength (nm)	248	355	355
Laser fluence (J/cm <sup>2</sup> )	1.3	4.4	3.2
Spot size/ Diameter * (μm)	800	10	10
Sport shape	Square	Round	Round
Pulsing frequency (kHz)	40	90	90
Pulse/field	20		
Spot moving speed (mm/s)		200	300

### 5.2.2 The electrochemical deposition of platinum black

The catalytic coatings for IBCDSCs were produced using the Pulsed-current Electrochemical Deposition (PED) method. The electrochemical deposition method is used instead of the conventional Thermal Decomposition (TD) method mainly because in IBCDSCs a selective deposition is required to produce the non-symmetrical structure on the same substrate. Besides, the electrochemical deposition method has the advantages of room temperature processing and

simple experimental setup. The catalytic coatings produced using the PED method exhibit comparable performances to those produced by the TD method. (For the detailed evaluation of PED conditions, please refer to Chapter 4.)

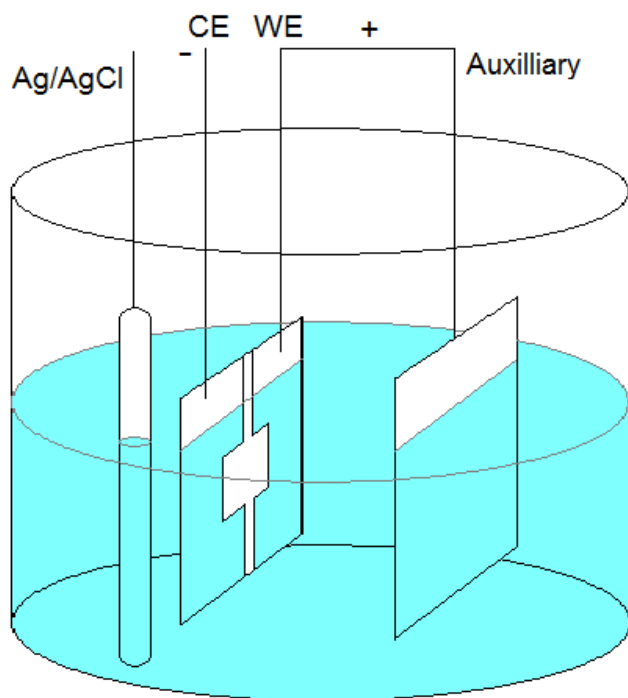
According to the investigation in Chapter 4, Pt coatings with smaller Pt particles would have larger surface area and therefore better catalytic activity towards the reduction of triiodide ions. However, it was found that in the  $\text{ZrO}_2$  electrophoretic deposition process, small Pt particles, such as those with 10-50 nm diameters, could easily drift across the insulating track and contaminate WEs. The Pt contamination makes the WEs active towards triiodide reduction, causing internal shorting in the devices. One example of these unsuccessful devices is shown in Figure 5.5. The current-voltage curves measured under dark and one sun illumination both show a low shunt resistance, indicating internal shorting of the device. This shorting is attribute to the Pt contamination onto the working electrode.



**Figure 5.5** Current-voltage characteristics of an IBCDSC comprising 20 nm Pt particles produced by  $10 \text{ mA/cm}^2$  pulsed current density.

Successful IBSDSC devices employ 100 nm Pt particles produced using  $3 \text{ mA/cm}^2$  current pulses in a total duration of 100 s. The pulsed current on and off time are 0.1 and 1s respectively. The experimental setup of the electrochemical deposition experiment is schematically shown in Figure 5.6. Negative current pulses were applied to the counter electrodes (CEs). The working electrodes (WEs) were connected to the Pt auxiliary electrode to avoid undesired Pt deposition. Here, the CEs and WEs refer to the counter and working

electrodes for the IBCDSC rather than for the electrochemical cell shown in Figure 5.6. After the deposition, samples were immersed in 600 ml of distilled water to remove residual solution from the sample surface. A post sintering at 200 °C for 15 min was used to improve the mechanical stability of the Pt black coating.



**Figure 5.6** Schematic representation of the assembly of the electrochemical cell for the deposition of Pt black. Negative current was applied to the CEs of the backplate. The WEs is shorted with the counter electrode to avoid undesired Pt deposition. A Ag/AgCl standard electrode is served as a reference, and a Pt plate is used as an auxiliary electrode.

### 5.2.3 Electrochemical characterization

The catalytic activity of the platinized CEs was characterized by a cyclic voltammetry (CV) sweep in an electrolyte containing 10mM of lithium iodide, 1mM iodine and 0.1M tetraethylammonium perchloride dissolved in acetonitrile. A DC sweeping potential (50 mV s<sup>-1</sup> scan rate) between -0.4 V and 1.0 V was applied on the platinized CEs against a Ag/AgCl (3.5 M KCl) reference electrode. To prove that there is no contamination on the WEs, the



same measurement was conducted on the plain FTO WEs after the electrodeposition of CEs. A plain FTO glass sample was also measured for comparison.

#### 5.2.4 Electrophoretic deposition (EPD) of $\text{ZrO}_2$ nanoparticles

Zirconium dioxide ( $\text{ZrO}_2$ ) was employed to fabricate the porous insulating layer covering the platinized finger electrodes. The  $\text{ZrO}_2$  suspension was prepared by dispersing 1g of  $\text{ZrO}_2$  nanoparticles (50-100 nm zirconia ZT2, Z-Tech Zirconia) in 100ml mixture of ethanol and acetylacetone (45:55) followed by ball milling for 24 hours.<sup>11</sup> According to reference 12, the  $\text{ZrO}_2$  nanoparticles are positively charged in acetylacetone,<sup>12</sup> and therefore they can be deposited onto the platinized CE set through the application of a negative potential. In our experiment, a constant voltage of -10 V was applied for 100 s to induce the migration and selective deposition of charged  $\text{ZrO}_2$  nanoparticles onto the platinized FTO finger electrodes, leaving the plain FTO fingers uncoated. The coated samples were sintered at 450 °C for 20 min to make the  $\text{ZrO}_2$  coating mechanically stable.

It has been reported that electrophoretic deposition of  $\text{ZrO}_2$  requires the application of relatively high DC voltages (up to 480 V).<sup>13</sup> However, due to the short distance between adjacent electrodes, high electric fields can be obtained even at moderate voltage such as 10 V.

#### 5.2.5 Cell assembly

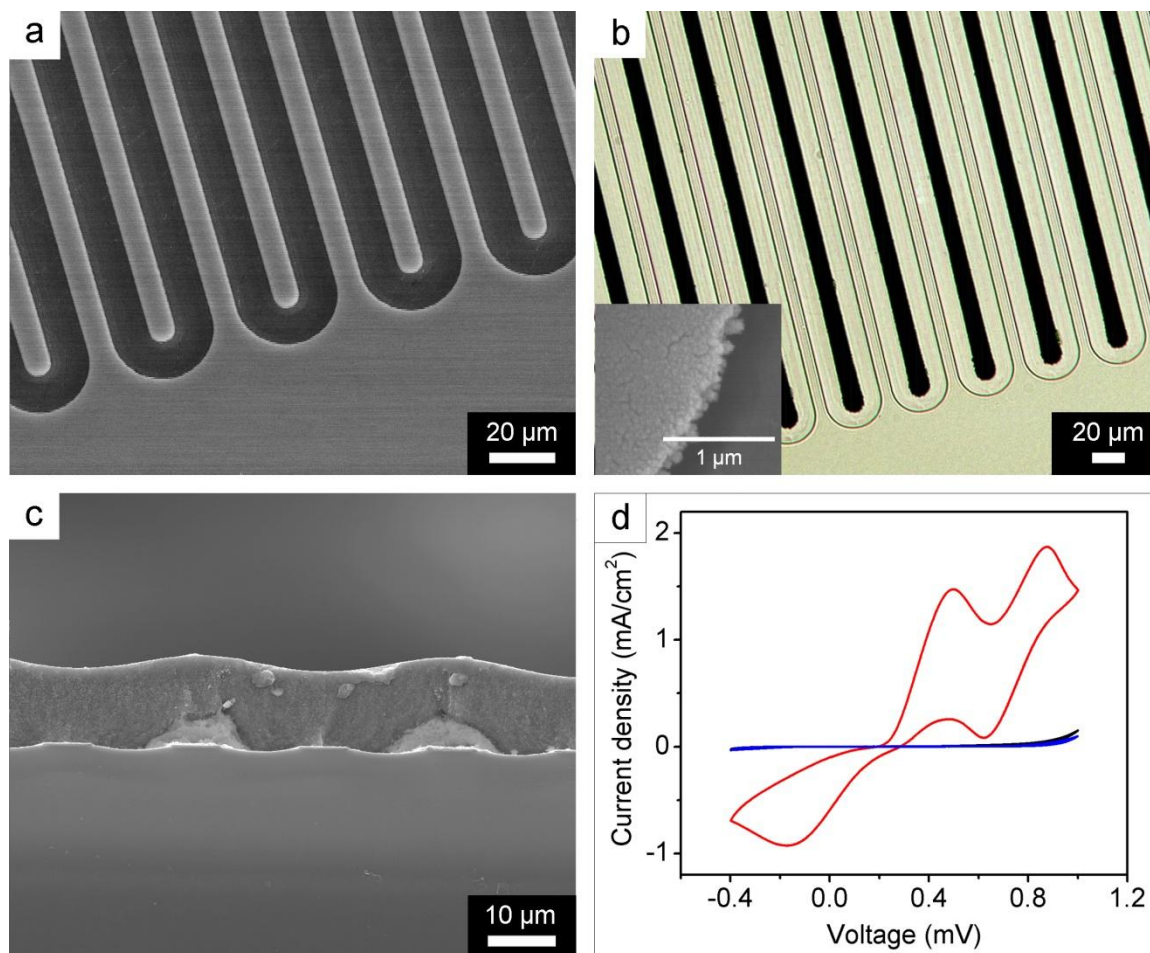
For IBCDSCs, a 12  $\mu\text{m}$   $\text{TiO}_2$  film was screen-printed on the backplates, covering both WEs and CEs. They were then sintered and dyed according to the procedures described in Chapter 2. Devices were assembled using transparent float glass sheets (1 mm thick) and Surlyn<sup>®</sup> gaskets. The electrolyte with the composition described in Section 2.2.5 was filled through an entry port on the window glass sheets.

For comparison, conventional sandwich DSCs (ref-DSCs) with identical device parameters ( $\text{TiO}_2$  film thickness, electrolyte composition,  $\text{TiO}_2$  paste) were fabricated based on identical fabrication protocols ( $\text{TiO}_2$  printing, sintering, dyeing, sealing). Counter electrodes for reference DSCs consisted of platinized FTO glass fabricated by a PED method identical to the one used for IBCDSCs.

### 5.3 *Devices on the MiniFAB FTO backplates*

#### 5.3.1 **The microstructure of backplates**

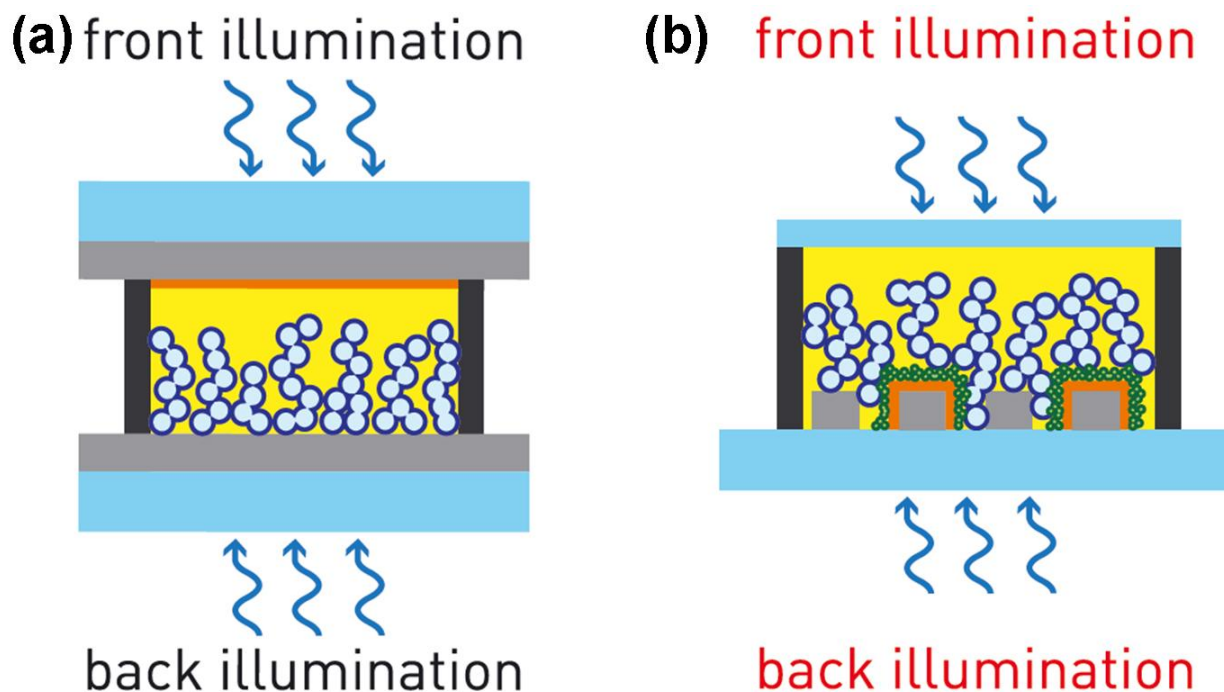
Figure 5.7 shows the microstructure of interdigitated finger electrodes on the TEC-15 glass after each fabrication step. A symmetric set of interdigitated FTO finger electrodes was produced by the mask delivered laser ablation process (Figure 5.7(a)). The active area of each backplate consists of 2x100 interdigitated finger electrodes of 8  $\mu\text{m}$  width and 4 mm length (active electrode area: 4x4 mm). The width of the gap between electrodes is 12  $\mu\text{m}$ . After the electroposition process, a homogeneous dense Pt black coating was selectively deposited onto the CE set, without any obvious pinholes on the coating or any contamination to the WEs (Figure 5.7(b)). The thickness of the Pt layer was measured to be 50-100 nm (profilometry). High magnification SEM picture (insert in Figure 5.7(b)) shows that the Pt coating consists of closely packed Pt nanoparticles with a size of approximately 50-100 nm. Figure 5.7(c) shows that the  $\text{ZrO}_2$  coating has a thickness of around 3  $\mu\text{m}$ , accordingly the  $\text{TiO}_2$  film shows a wave shape following the surface profile of the interdigitated electrodes. The CV result for the platinized CEs (red line in Figure 5.7(d)) shows a typical reduction peaks at 0.62V and -0.18 V, in accordance with previously reported data for non-patterned platinized FTO electrodes.<sup>14</sup> On the contrary, the working electrode fingers that had been positively biased during the electrodeposition step show a similar activity (black line) towards the reduction of triiodide as untreated FTO glass (blue line), confirming that platinum contamination during the electroplating process could be avoided.



**Figure 5.7** Microstructure of interdigitated finger electrodes. (a) Scanning Electron Microscopy (SEM) micrograph of a FTO coated glass plate after laser ablation. (b) Optical micrograph of the IBCDSC backplate after the platinization process. The insert shows the morphology of the Pt coating at the tip of a finger electrode. (c) SEM micrograph of a IBCDSC device cross-section after deposition of the mesoporous  $\text{TiO}_2$  film. The  $\text{ZrO}_2$  layer is visible as a brighter semicircular area of about  $3\ \mu\text{m}$  thickness surrounding each counter electrode. (d) Cyclic voltammograms (CVs) in iodine/triiodide electrolyte, following the platinization process: platinized (cathode, red solid line) and non-platinized (anode, black line) finger electrodes. For comparison the CV of a plain FTO glass sheet (blue line, identical measurement conditions) is also shown.

### 5.3.2 Photovoltaic characteristic

In our photovoltaic measurements, IBCDSCs and ref-DSCs were characterized under both front and back illumination conditions. The two modes of measurement are schematically illustrated in Figure 5.8.

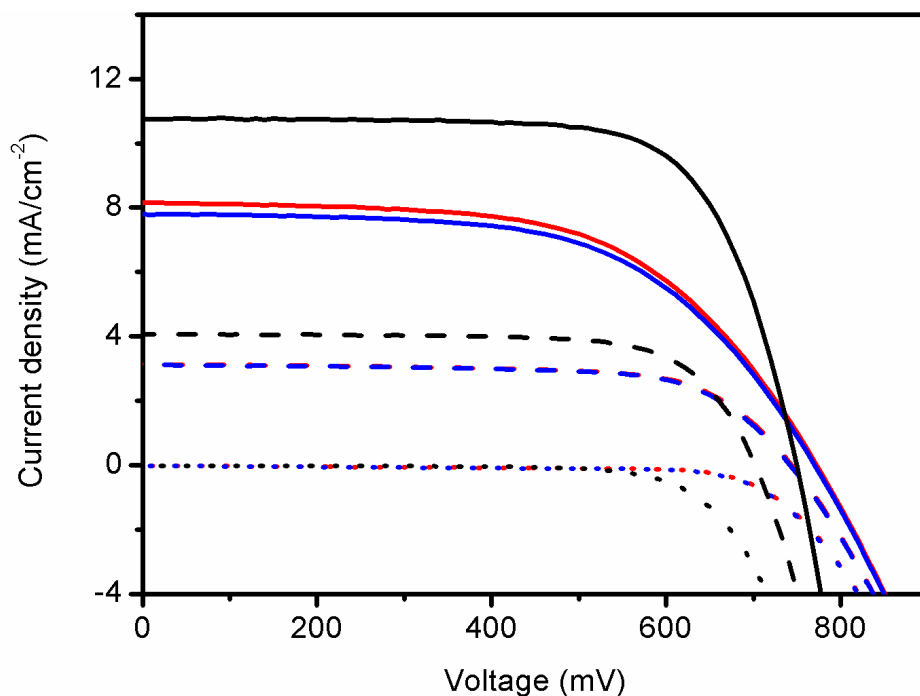


**Figure 5.8** Schemes defining the front and back illumination conditions of (a) a conventional sandwiched DSC and (b) an IBCDSC.

Figure 5.9 and Table 5.2 summarize the current-voltage (I-V) characteristic of IBCDSCs and ref-DSCs under simulated solar irradiation and in the dark. The highest short-circuit current density for IBCDSCs was recorded for front-illumination ( $8.2 \text{ mA cm}^{-2}$ ), compared to  $10.8 \text{ mA cm}^{-2}$  for ref-DSCs, illuminated in back-illumination mode. The highest conversion efficiency for the IBCDSC is 4.2 %, measured under back illumination using 38.5 % light intensity. Unfortunately, the IBCDSC is yet to produce higher current density under front illumination, mostly due to the light transmission loss occurred in the electrolyte layer between the  $\text{TiO}_2$  film and the transparent cover slide.

It is found in our experiment that IBCDSCs generally yielded higher open-circuit voltages than conventional ref-DSCs. Accordingly the dark-current onset for IBCDSCs is shifted to higher voltages, compared to that of ref-DSCs. In part, this can be explained in terms of a reduced FTO working electrode area for IBCDSCs, which is confined to a set of narrow FTO fingers occupying about one fifth of the geometric surface area. Reduced dark currents and increased open-circuit voltages could therefore at least be explained on the basis of reduced

recombination at the FTO/electrolyte interface for BC-DSCs, especially when considering the situation that none of the IBCDSC or ref-DSC substrates were covered by a dense  $\text{TiO}_2$  blocking layer. The higher  $V_{oc}$  could also be explained in terms of the reduced potential of separating positive and negative charges,<sup>15</sup> as in IBCDSCs both charges are transported in the same direction.



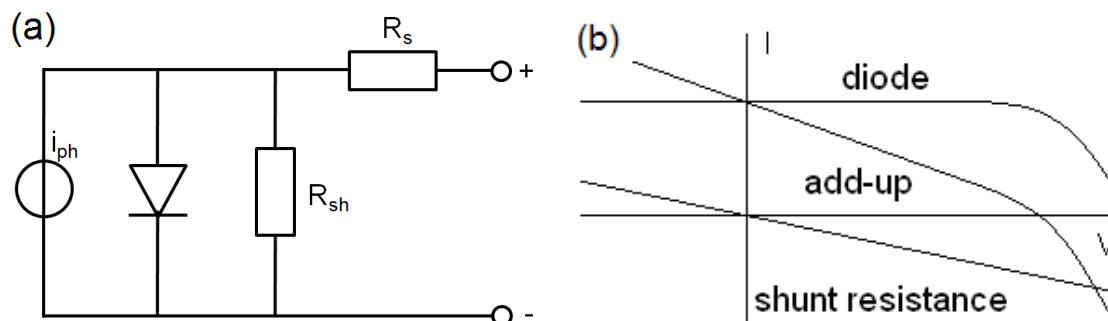
**Figure 5.9** Current-voltage characteristic of an IBCDSC under front (blue) and back (red) illumination compared to a ref-DSC under back-illumination (black). The cells were characterized under 38.5% (dash lines) and 100 % (solid lines) simulated sunlight ( $\text{AM1.5}$ ,  $1000 \text{ W m}^{-2}$ ). Dark currents (dotted lines) are also shown.

Fill factors of IBCDSCs at moderate light illumination ( $\leq 385 \text{ W m}^{-2}$ ) are very similar ( $\pm 3\%$ ) to those of ref-DSCs but are decreased at full sun illumination. The reduced fill factors can be explained by the higher internal resistance and also by the lower shunt resistance (represented by the slope of the IV curves between 0 and 400 mV) of the IBCDSC compared to the ref-DSC. From the slope of the IV curve at the region approaching the  $V_{oc}$  point, the internal resistance for the IBCDSC and ref-DSC are estimated to be  $199 \Omega$  and  $35 \Omega$ , respectively.

**Table 5.2** Current-voltage characteristic of a reference DSC, and an IBCDSC fabricated on interdigitated FTO backplates. Devices are measured in the back and front side illumination mode under 10.3%, 38.5% and 100.0% simulated sun light (AM1.5, 1000 W m<sup>-2</sup>).

	IBCDSC back illumination			IBCDSC front illumination			Ref-DSC back-illumination		
Light	10.3	38.5	100.0	10.3	38.5	100.0	10.3	38.5	100.0
Intensities	%	%	%	%	%	%	%	%	%
V <sub>oc</sub> (mV)	698	743	773	696	742	770	635	702	750
J <sub>sc</sub> (mA cm <sup>-2</sup> )	0.79	3.13	8.16	0.80	3.12	7.79	1.09	4.07	10.76
FF	0.67	0.69	0.58	0.66	0.69	0.58	0.69	0.72	0.72
η (%)	3.59	4.19	3.64	3.59	4.14	3.50	4.65	5.37	5.77

According to the simple diode equivalent circuit shown in Figure 5.10(a) (see also discussion in Section 2.3.1), the shunt resistance is equivalent to a conducting contact between working and counter electrode. In IBCDSCs the shunt is most likely due to the direct contact between TiO<sub>2</sub> and the FTO fingers underneath the Pt&ZrO<sub>2</sub> coatings. According to the trapping-detrapping model for the electron conduction in DSCs<sup>16-19</sup>, the conductivity of TiO<sub>2</sub> film is correlated to the concentration of conduction band electrons and accordingly to the light intensity. Considering the current design, the shorting bridge formed by interconnected TiO<sub>2</sub> nanoparticles would become more conductive with increased illumination. Therefore the shunt resistance is reduced with increased light intensity. An ideal diode combined with a low-resistance shunt resistor would together perform to show a I-V curve with reduced slop when increasing light intensity (Figure 5.10(b)).



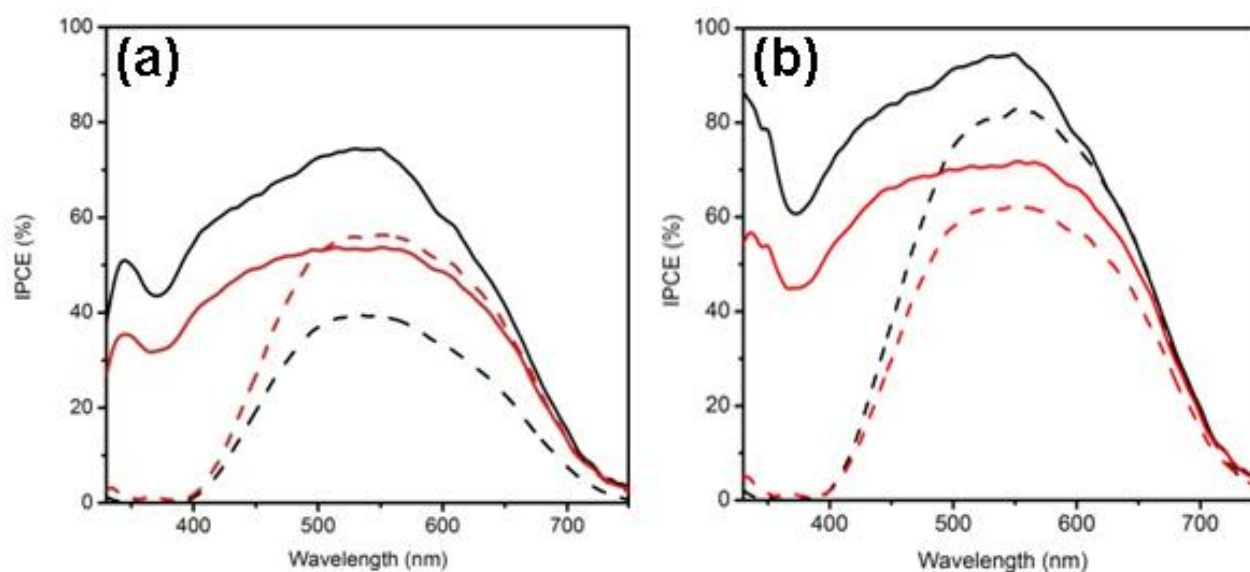
**Figure 5.10** Schematic representations of (a) a simplified equivalent circuit of DSC consisting of a diode component, a shunt resistance and a series resistance, and (b) effect of a shunt resistance to the overall current-voltage characteristics. The add-up curve is the sum of the curves of the diode and the shunt resistance.

The incident photon-to-electron conversion efficiencies (IPCEs) for IBCDSCs and ref-DSCs are shown in Figure 5.11(a). When measured under the front-illumination condition, the IBCDSCs show an increased performance compared to back-illuminated IBCDSCs at wavelengths higher than 500 nm. This is in contrast to the conventional DSCs where front-illumination generally yields lower IPCEs than back-illumination.<sup>8</sup> Below 500 nm the front-illumination IPCE drops dramatically due to the optical absorption of triiodide, which is contained in the electrolyte layer between the front window material and the sensitized  $\text{TiO}_2$  film. The width of this electrolyte spacer layer (13  $\mu\text{m}$ ) can be estimated from the thickness of the Surlyn gasket (25  $\mu\text{m}$ ) and the  $\text{TiO}_2$  film (12  $\mu\text{m}$ ). The 13  $\mu\text{m}$  thick electrolyte layer was used for both IBCDSCs and ref-DSCs. The undesired absorption of the electrolyte layer can be possibly avoided by using thinner Surlyn gaskets or by employing a transparent  $\text{SiO}_2$  layer on top of the  $\text{TiO}_2$  film.<sup>8</sup> Alternative electrolytes absorbing less light could also be used for this purpose.

Under the back-illumination condition, a remarkably high peak IPCE of 54 % was measured for IBCDSCs. The value is lower than that measured for comparable ref-DSCs (75 %). The reduction in peak IPCE under this illumination condition can be explained in terms of the reduced transmission of the respective window materials. In IBCDSCs part of the incident light has to pass through Pt black coated CEs and then dye-coated  $\text{ZrO}_2$  protective layer. On the contrary, in ref-DSCs the incident light is only partially absorbed by the FTO glass substrates. Under front-illumination, IBCDSCs show a peak IPCE of 56 %, compared to 39 %

measured for ref-DSCs. The modest performance of the ref-DSC can be explained in terms of the low transmission of the platinized FTO counter-electrode ( $T=50\%$ ) used here.

IPCE results were corrected from the light absorption of respective window materials (Note that for IBCDSCs measured under back-illumination, only the optical transmission losses occurred at the patterned substrates and the Pt black coating were considered. The transmission loss at the dye-coated  $ZrO_2$  layer was not considered in this case). Under back- and front-illumination conditions, the transmission-corrected peak IPCE values for IBCDSCs are 72 % and 62 %, respectively (Figure 5.11(b)).



**Figure 5.11** (a) Incident photon to electron conversion efficiency (IPCE) of an interdigitated back-contact DSC (IBCDSC, red) and a conventional sandwich DSC (ref-DSC, black) under front (solid lines) and back (dashed lines) illumination. (b) Transmission-corrected IPCE results for the two devices measured under the front- and back-illumination conditions. The illumination directions are schematically illustrated in Figure 5.7. Front-illumination refers to a situation where the light is incident through the top float-glass window (IBCDSC) and counter electrode (ref-DSC) respectively. Back-illumination refers to illumination conditions where the light is incident through the backplate (IBCDSC) and the working electrode (ref-DSC) respectively.

### 5.3.3 Photocurrent mapping

Preliminary work was conducted on the characterization of IBCSCs using a photocurrent mapping method (CSIRO Newcastle, Australia). The method involves the use of 635 nm laser

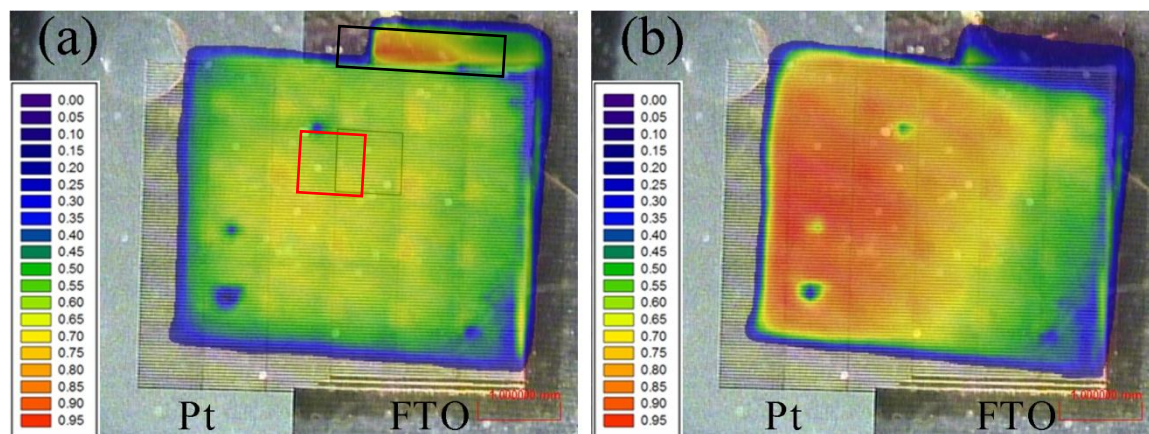


radiation that is focused down to a 10  $\mu\text{m}$  laser spot and is scanned across a solar cell. The light intensity of the laser spot is equivalent to 100 suns ( $10 \text{ W}/\text{cm}^2$ ). The photocurrent at each spot is measured and plotted as a contour map. During the test, the solar cell can be either kept in the dark or biased with a background white light to measure the performance under different conditions.

The photocurrent mapping can be used to probe possible cell defects in our IBCDSCs. In general, the photoelectrode of IBCDSCs is less homogeneous than that of conventional DSCs. Defects, including shorting bridges and contaminations, are more frequently detected in IBCDSCs.

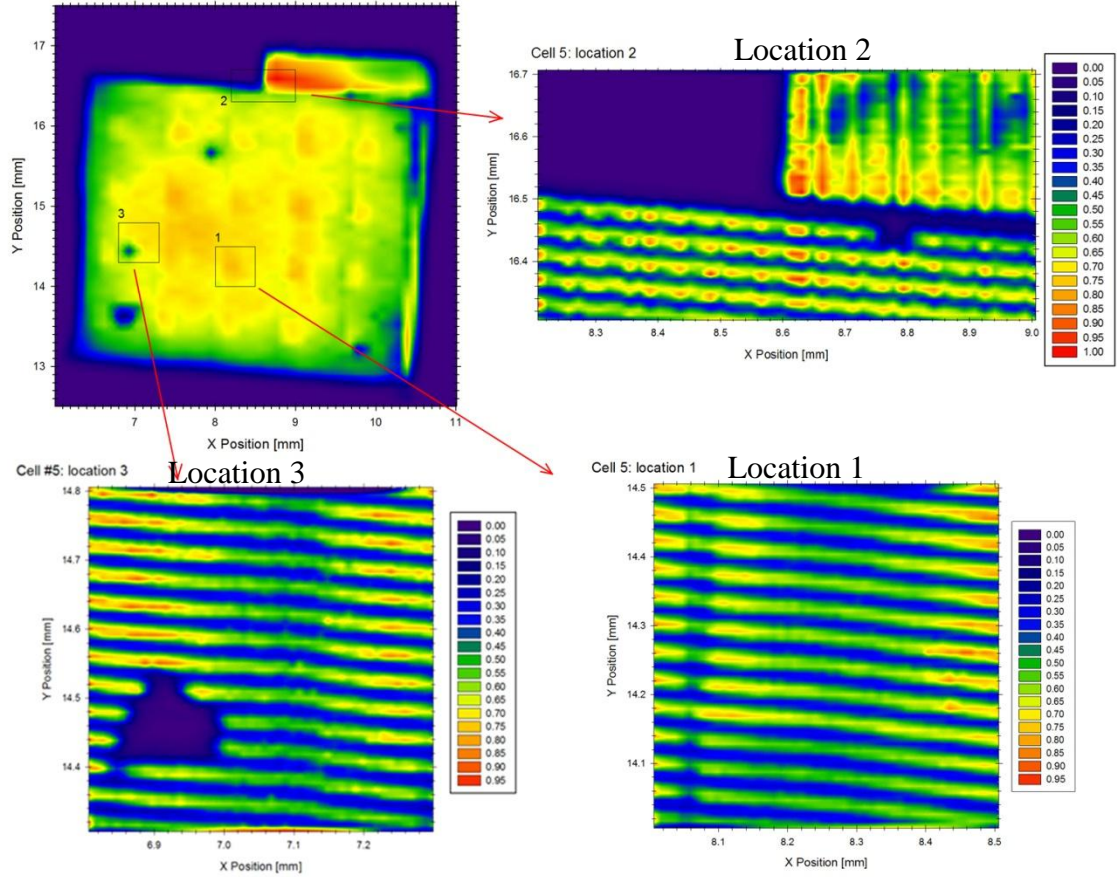
The photocurrent contour map in Figure 5.12 shows the results obtained under the back illumination condition (refer to Figure 5.8 for the definition of back illumination). The Figure shows distinct boundaries between adjacent laser ablated fields on the cell backplate (a sample of these fields is marked with the red square in Figure 5.12(a)). Within each of these fields, the lower left corner produces higher photocurrent than the rest of the area.

Figure 5.12 (a) and (b) compares an identical sample measured without and with the use of a white light bias. Without the white light bias, the upper right corner of the device shows much higher current than the rest of the area (marked by the black frame Figure 5.12(a)). In fact, this is the area with  $\text{TiO}_2$  printed on bare FTO surface. The triiodide ions are generated quite far away from the closest Pt CE. This indicates that the redox species in the electrolyte can effectively diffuse across a distance of 500  $\mu\text{m}$ . However, when the white light bias is applied, the photocurrent generated from the upper right corner is significantly reduced. This could be explained in terms of the iodide deficiency in this region when the entire cell is under the working condition. At the upper right corner where the  $\text{TiO}_2$  film is printed on bare FTO surface, the triiodide ions are quite far from the Pt CEs and it is difficult for them to be reduced by the CEs. This region is therefore deficient in iodide ion which is essential for the generation of photocurrent.



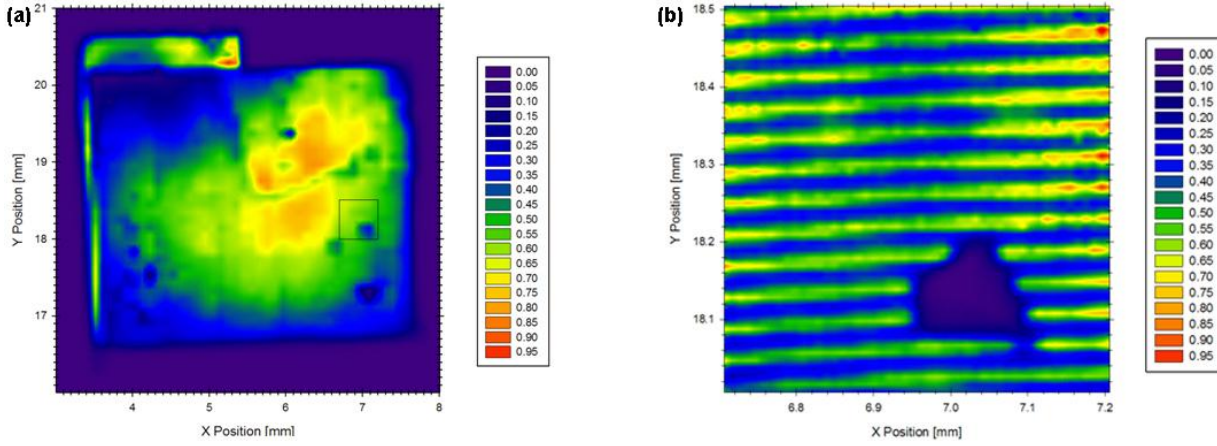
**Figure 5.12** Photocurrent mapping of an IBSDSC under back illumination condition (a) without and (b) with the use of a white light bias. The laser radiation has a wavelength of 635 nm and was scanned across an area of 5×5 mm. The background images in (a) and (b) show the micrograph of an interdigitated back-contact DSC comprising plain FTO electrodes and Pt coated electrodes. The photocurrent maps under the two testing conditions are cropped and superimposed with the TiO<sub>2</sub> film in order to show the current output at different regions of the film. The relative current density values are shown as a false colour image.

Figure 5.13 shows magnified photocurrent maps of the IBCDSC at three specific locations. The photocurrent map of location 1 shows greatly varied cell performances in different regions. The low photocurrent regions (the blue regions) are the locations of the CEs, as this is the part where light illumination is blocked by the Pt coatings. As the device was tested under the back illumination condition, significant shading was caused by the Pt&ZrO<sub>2</sub> coating. Location 2 shows a boundary region of the interdigitated area. The photocurrent pattern measured for the area of interdigitated electrodes is again due to the shading effects. Location 3 is a region with a 'dead spot', which could be due to a delamination of the TiO<sub>2</sub> film or a shorting at this region.



**Figure 5.13** High resolution photocurrent map measured for the IBCDSC at three locations. No white light bias was applied during the test.

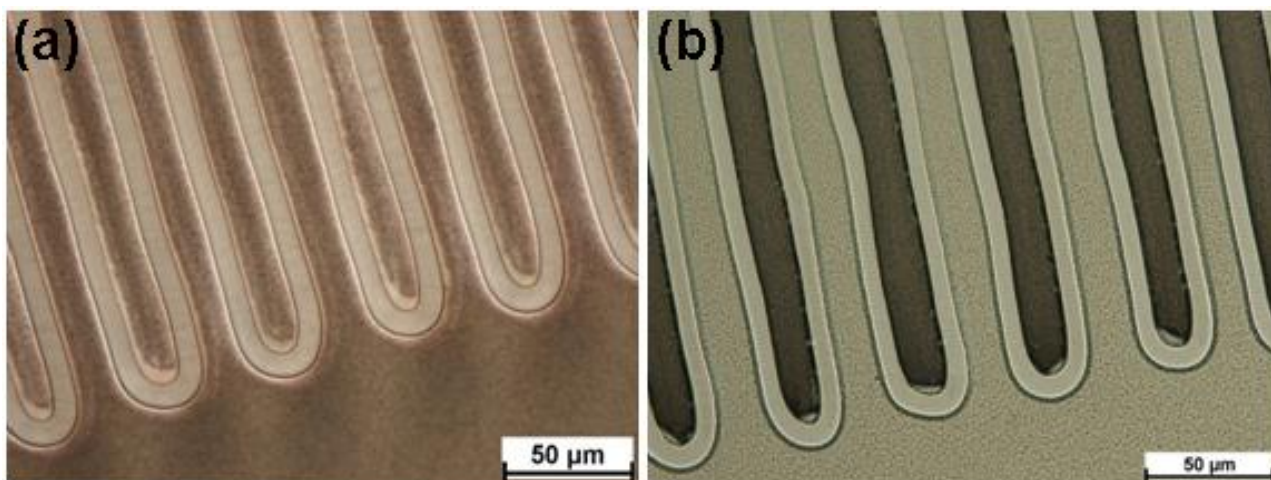
Figure 5.14(a) shows the photocurrent contour map of the IBCDSC measured in dark under the front illumination condition (refer to Figure 5.8 for the definition of the front illumination condition). The high resolution photocurrent map in Figure 5.14(b) shows the distribution of photocurrent densities in a strip pattern. The low-current stripes (dark blue regions) exhibit a periodicity of 40  $\mu\text{m}$ , corresponding to the distance between any adjacent two counter electrodes in the IBCDSC (see Figure 5.7(c) for detailed information). The low current produced at the dark-blue regions is due to the thinner  $\text{TiO}_2$  films printed on top of the  $\text{ZrO}_2$  coatings. The low photocurrent at these regions can also attribute to the longer distance (up to 50  $\mu\text{m}$ ) that electrons generated at the regions need to travel before reaching the working electrodes, however this is believed to be a minor effect compared to the effect of the thinner  $\text{TiO}_2$  films.



**Figure 5.14** (a) Photocurrent mapping of the IBCDSC measured under front illumination condition without the use of white light bias. The probing laser radiation has a wavelength of 635 nm and was scanned across an area of  $5 \times 5$  mm. The high resolution photocurrent map of the highlighted location is shown in (b).

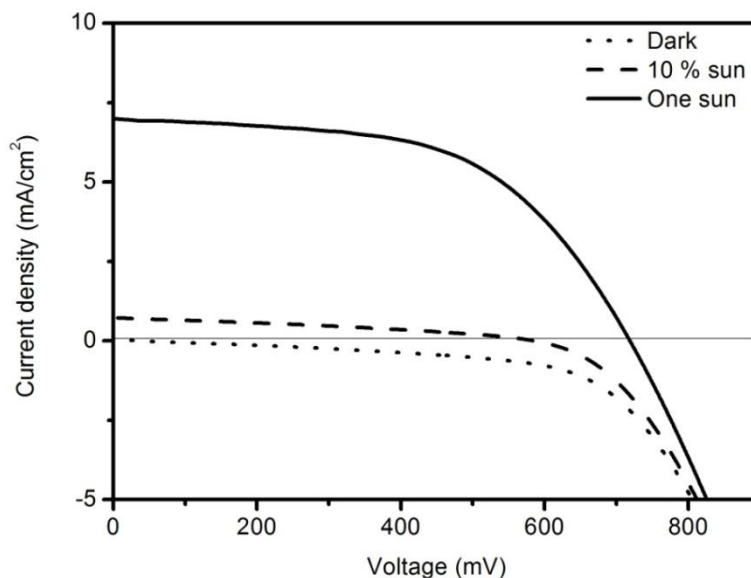
#### 5.4 Interdigitated back-contact DSCs on WNLO FTO backplates

Interdigitated back-contact DSCs (IBCDSCs) were also constructed on FTO backplates ablated using the direct-write laser facility in WNLO. Compared to the mask-delivered process, the direct-write process yields similar micro-patterns in a much higher production rate. Under the current experimental condition, the time frames for the production of a  $4 \times 4$  mm interdigitated area are 2 min and 3 s for the mask delivered and direct-write processes, respectively. The morphologies of the micro-patterns after laser ablation and after platinization are shown in Figure 5.15.



**Figure 5.15** Optical micrographs of FTO finger electrodes (a) after the direct-write laser ablation and (b) after the electrochemical deposition of Pt.

The IV characteristics of the IBCDSCs employing such backplates are shown in Figure 5.16 and Table 5.3. The devices were only measured in the front-illumination mode. Under one sun illumination, a current density of  $6.99 \text{ mA/cm}^2$  was measured, similar to the results of devices using the MiniFAB FTO backplates. However, A low shunt resistance of less than  $1 \text{ k}\Omega$  results in low a low fill factor of the cell. The low shunt resistance is possibly due to the Pt contamination onto the working electrodes.



**Figure 5.16** The current-voltage curves of an IBCDSC fabricated on the WNLO FTO backplates.



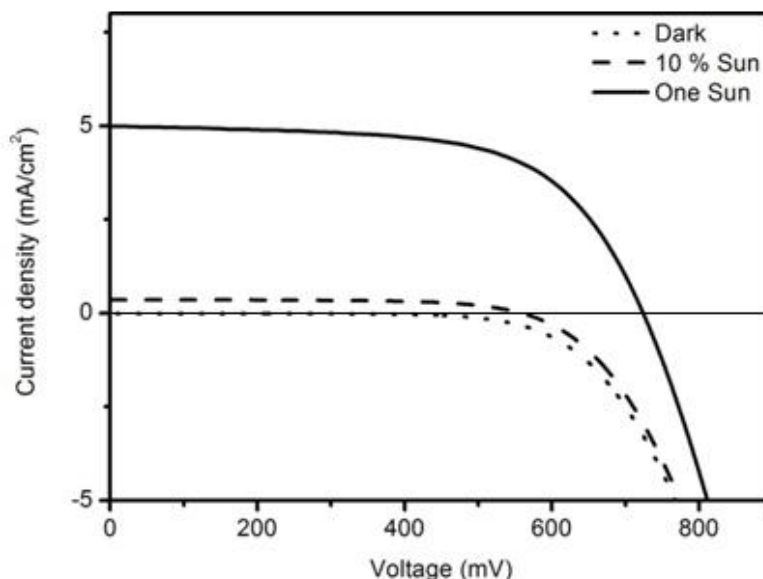
**Table 5.3** Summary of the current-voltage characteristic of an IBCDSC fabricated on the WNLO FTO backplates.

Light Intensity:	10.3% Sun	100.0% Sun
Voc (mV)	586	719
Jsc (mA/cm <sup>2</sup> )	0.73	6.99
Fill Factor	0.336	0.556
Efficiency (%)	1.4	2.79

### 5.5 *Interdigitated back-contact DSCs on WNLO Ti backplates*

The ultimate objective for the research of IBCDSCs is to eliminate the use of TCO materials and to fabricate back-contact DSCs using metal substrates. While the previously reported all-metal-electrode-type DSCs are still based on sandwiched architecture,<sup>1-3</sup> the all-metal-type IBCDSCs developed in this project are truly monolithic. The preparation of backplates containing interdigitated Ti finger electrodes is described in Chapter 3. IBCDSCs on these substrates were fabricated using identical procedures for their FTO analogs.

Figure 5.17 and Table 5.4 summarize the I-V characteristic of an IBCDSC fabricated on Ti finger electrodes. Due to the use of opaque substrates, the devices were only measured in the front-illumination mode. Under one-sun illumination, a modest current density is observed for the device. The low performance can be partially attributes to the cracking on Ti fingers (see section 3.3.3 for details) that restricts an efficient charge collection.



**Figure 5.17** The current-voltage (I-V) characteristic of an IBCDSC fabricated on a Ti finger electrodes.

**Table 5.4** Current-voltage characteristic of an IBCDSC fabricated on the WNLO Ti backplates.

Light Intensity:	10.3% Sun	100.0% Sun
Voc (mV)	558	724
Jsc (mA/cm <sup>2</sup> )	0.35	4.99
Fill Factor	0.642	0.622
Efficiency (%)	1.23	2.25

## 5.6 Conclusion

In conclusion, interdigitated back-contact DSCs (IBCDSCs) were fabricated on backplates comprising laser patterned interdigitated finger electrodes selectively coated with platinum black and ZrO<sub>2</sub> protective coating. The performances of IBCDSCs are limited by shunt resistance and light transmission loss at the electrolyte layer on top of the TiO<sub>2</sub> films. However, no obvious reduction in the charge collection efficiency was found on the IBCDSCs, indicating that better cell performances can be achieved on the novel device through improved fabrication procedures.

Beyond FTO glass, Ti coated glass was also implemented as the substrate materials for IBCDSCs. To the best of our knowledge, this is the first time report of back-contact DSCs based on interdigitated electrodes with a monolithic device structure. Although the device

performances were not promising at this early stage of development, better conversion efficiencies can be expected upon the availability of better processed finger electrodes. Further developments of the IBCDSC architecture could be focused on the refinement of fabrication conditions as well as the implementation of devices on flexible metal coated polymer substrates.

## 5.7 References to chapter 5

- [1] N. Fuke, F. Atsushi, K. Ryohichi, I. Ashraful, C. Yasuo, Y. Masatoshi, Y. Ryohsuke, H. Liyuan, *Chem. Mater.* **2008**, 20, 4974.
- [2] N. Fuke, A. Fukui, Y. Chiba, R. Komiya, R. Yamanakay, L. Han, *Jpn. J. appl. Phys.* **2007**, 46, L420.
- [3] Y. Y. Yohei Kashiwa, Shuzi Hayasea, *Appl. Phys. Lett.* **2008**, 92.
- [4] V. K. Emmanuel, G. Beaucarne, *Prog. Photovolt: Res. Appl.* **2006**, 14, 107.
- [5] M. A. Green, K. Emery, Y. Hishikawa, W. Warta, *Prog. Photovoltaics.* **2011**, 19, 84.
- [6] L. Peter, *J. Phys. Chem. C* **2007**, 111, 6601.
- [7] A. Kay, M. Gr äzel, *Sol. Energ. Mat. Sol. C.* **1996**, 44, 99.
- [8] S. Ito, S. M. Zakeeruddin, P. Comte, P. Liska, D. Kuang, M. Gr äzel, *Nat. Photonics.* **2008**, 2, 693.
- [9] S. M. Sze, K. K. Ng, *Physics of Semiconductor Devices*, John Wiley & Sons, Inc., Hoboken **2006**.
- [10] G. Hope, *J. Phys. Chem-US* **1983**, 87, 1979.
- [11] Z. Xu, G. Rajaram, J. Sankar, D. Pai, *Surf. Coat. Tech.* **2006**, 201, 4484.
- [12] C. Ji, W. Lan, P. Xiao, *J. Am. Ceram. Soc.* **2008**, 91, 1102.
- [13] H. Chen, A. D. Pasquier, G. Saraf, J. Zhong, Y. Lu, *Semicond. Sci. Technol.* **2008**, 23, 045004.
- [14] C. H. Yoon, R. Vittal, J. Lee, W.-S. Chae, K.-J. Kim, *Electrochim. Acta.* **2008**, 53, 2890.
- [15] F. Fabregat-Santiago, I. Mora-Sero, G. Garcia-Belmonte, S. Gimenez, J. Bisquert, *J. Phys. Chem. C* **2009**, 113, 17278.
- [16] J. Bisquert, I. n. Mora-Seró, *J. Phys. Chem. Lett.* **2009**, 1, 450.
- [17] Q. Wang, S. Ito, M. Gr äzel, F. Fabregat-Santiago, I. Mora-Sero, J. Bisquert, *J. Phys. Chem. B* **2006**, 110, 25210.
- [18] J. Bisquert, *J. Phys. Chem. B* **2002**, 106, 325.
- [19] J. Halme, P. Vahermaa, K. Miettunen, P. Lund, *Adv. Mater.* **2010**, 22, E210.



## 6 Coplanar back-contact DSCs

This chapter describes the second DSC configuration invented in this PhD project. It is defined as 'Coplanar Back-contact DSCs (CBCDSCs)', which essentially comprise a pair of isolated working and a counter electrodes (WE and CE) located on a common side of the dye-sensitized  $\text{TiO}_2$  photoelectrode. For all these devices, N719 dye and standard electrolyte containing the iodine/iodide redox couple were used.

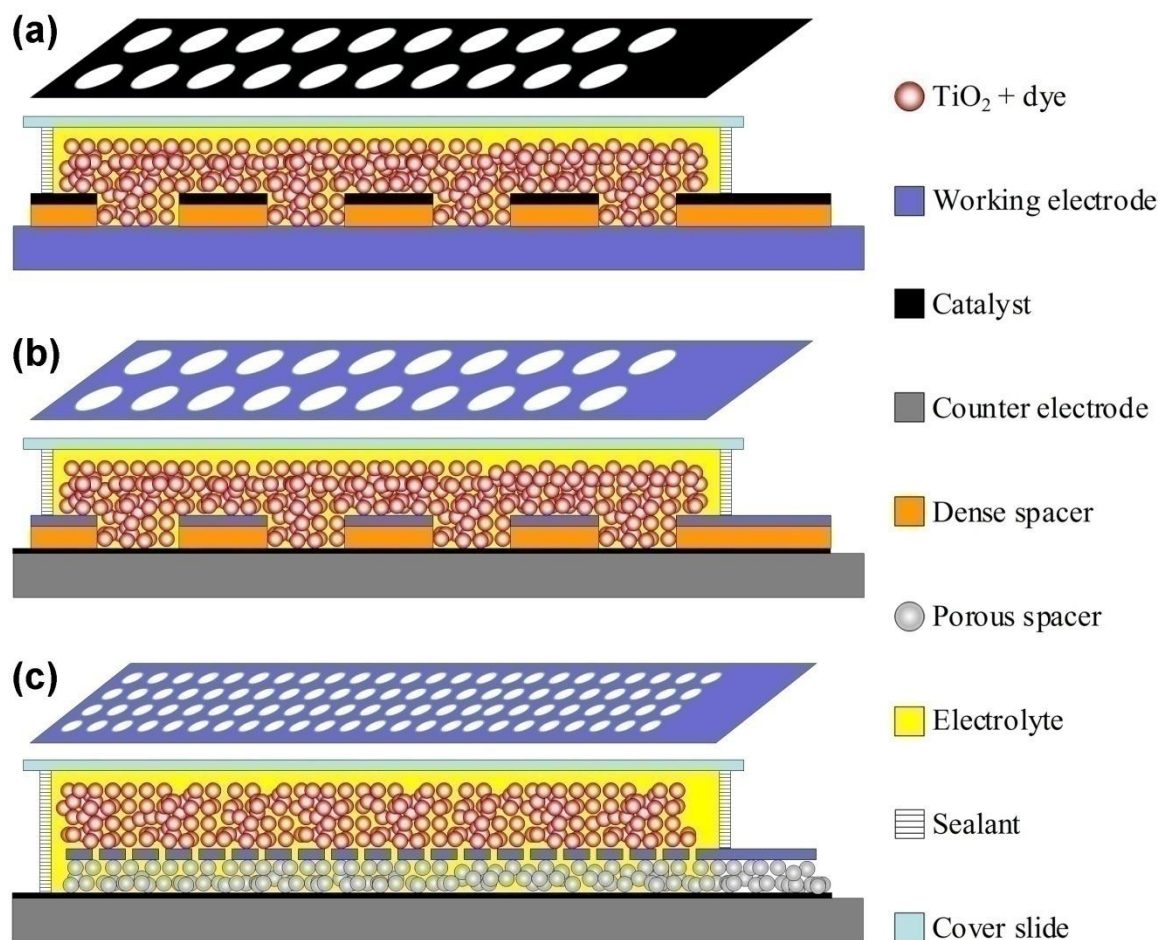
### 6.1 *Configurations of coplanar back-contact DSCs*

Three possible configurations are proposed. Their cross-sectional structures are schematically shown in Figure 6.1. Configuration 1 and 2 (Figure 6.1(a) and (b)) both comprise a dense insulating spacer layer in between the WE and CE. However, the location of them is inverted in the two configurations.

In configuration 1, the working electrode is located at the bottom as the supporting substrate of the device. The counter electrode on top of the spacer layer could be made from a metal layer coated with a catalyst or a conductive catalytic layer. Micron-sized holes are fabricated on the top electrode and the spacer layer to allow for a direct contact between printed  $\text{TiO}_2$  photoelectrode and the bottom working electrode.

In configuration 2, the bottom electrode is used as the counter electrode with a catalytic coating for redox couple reduction. The working electrode is deposited on top of the spacer layer to directly contact the  $\text{TiO}_2$  photoelectrode. Penetrating holes are also fabricated in this configuration to allow for a contact between the redox couple and the catalytic coating.

Configuration 3 (Figure 6.1(c)) is evolved from configuration 2. In this architecture the dense spacer layer and the top working electrode are replaced by a porous spacer layer coated with a porous working electrode. Similar to the penetrating holes in architecture 2, the pores on these two layers allow for a direct contact between the redox couple and the bottom catalytic coating.



**Figure 6.1** Schematic diagram of coplanar back-contact DSCs (CBCDSCs) showing the three possible configurations (a), (b) and (c). From bottom to top, the electrode structures for (a) is working electrode, dense insulating spacer, catalytic counter electrode and  $\text{TiO}_2$  photoelectrode. The electrode structure for (b) is counter electrode, catalytic coating, dense insulating spacer, working electrode and  $\text{TiO}_2$  photoelectrode. The electrode structure for (c) is counter electrode, catalytic coating, porous insulator, porous working electrode and  $\text{TiO}_2$  photoelectrode. In (a) and (b), the top electrodes and the spacer layers are perforated. The purpose of the perforation in (a) and (b) are to allow for a  $\text{TiO}_2$ /working electrode and a electrolyte/counter electrode contacts respectively. In (c) porous top electrode and porous spacer layer are used. The purpose of the pores is to allow for a electrolyte/counter electrode contact. Components in the scheme are colour-coded with an illustration on the right. The 3D drawings on top of each device represent the structure of the top electrodes with micro- and nano- sized penetrating holes.

In a brief summary, the common features for these CBCDSCs and their advantages over conventional DSCs are listed as follow,

1. Both working and counter electrodes are located on a common side of the dye-sensitized photoelectrode. Therefore none of these two electrodes need to be transparent. The light transmission loss typically occurred on the TCO electrodes could be avoided. Highly conductive metal electrodes could be used to make DSC modules.
2. There is an insulating spacer layer to electrically separate the working and counter electrodes. A substrate comprising laminated working electrode-spacer layer-counter electrode is defined as a 'backplate', which could be fabricated by simply printing methods.
3. The top electrode and spacer layer are either perforated or porous by themselves. In configuration 1, this is designed to allow for a direct attachment of photoelectrode to working electrode (Figure 6.1(a)) In configuration 2 and 3, this is to allow for a direct contact between the redox mediators and the counter electrode (Figure 6.1(b) and (c)).
4. CBCDSCs could be sealed with transparent cover slides. No electrical conduction property is required for this cover.

## 6.2 *Materials selection*

The coplanar back-contact design eliminates the requirement of transparency for electrode materials, and therefore enables us to select materials in a much wider range. However, materials used in these devices need to have long term stability in the selected electrolyte system. In our experiments, iodine/iodide electrolyte is used. The electrode materials are required to be stable in such an electrolyte. Less corrosive electrolytes, such as those containing cobalt (II/III)<sup>1</sup> and those comprising ionic liquids<sup>2</sup>, could also be used in the CBCDSC system, although these alternative materials were yet implement in the current work. Other than the requirement of being corrosion resistive, there are further requirements for the properties of the two electrodes and spacer layers.

### **For working electrodes**

1. The material forms an ohmic contact with TiO<sub>2</sub> nanoparticles.
2. The material has negligible catalytic activity towards triiodide reduction under a bias voltage within the operational voltage range of DSCs (up to 1 V for most cells). This is to ensure a high shunt resistance and thus a low leakage current under cell operation condition.

**For counter electrodes**

1. In configuration 1 and 2,  $\text{TiO}_2$  paste is directly printed onto the counter electrodes. The catalytic materials should form a Schottky contact with  $\text{TiO}_2$  nanoparticles to avoid direct electron transfer from  $\text{TiO}_2$  to counter electrodes. Alternatively, a porous insulating coating could be applied to physically separate the  $\text{TiO}_2$  nanoparticles from the counter electrode.
2. The counter electrodes/catalyst should be active towards triiodide reduction. A low charge transfer resistance at counter electrode/electrolyte interface is important for the efficiency of solar cells.

Table 6.1 summarizes selected physical properties of some metals. It is shown that Ti is a superior material to make working electrodes, due to its good stability in iodine/iodide electrolytes and its low catalytic activity towards triiodide reduction (a low dark current of  $4 \times 10^{-2} \text{ mA/cm}^2$  at 500 mV bias).<sup>3</sup> With an intrinsic oxidation layer, Ti makes a perfect ohmic contact with  $\text{TiO}_2$  nanoparticles. The electrical conductivity of Ti is lower than other materials listed in Table 6.1. However, a theoretical sheet resistance as low as  $0.42 \text{ } \Omega/\square$  could be obtained with even a  $1 \text{ } \mu\text{m}$  thick Ti film. Pt forms a Schottky contact with  $\text{TiO}_2$  due to its high work function, therefore it could be used as counter electrode to directly contact with the  $\text{TiO}_2$  photoelectrode. However, when using Pt as catalyst coated on other counter electrode materials, a pin-hole free coating is essential to avoid a direct contact between  $\text{TiO}_2$  and the electrode material underneath.

**Table 6.1** Work function, electrical conductivity, catalytic activity and stability in  $I_3^-/3I^-$  electrolyte of selected metals according to reference 7-9.<sup>3-5</sup> Note that the resistivity of FTO is calculated from the sheet resistance of FTO glass (NSG) based on the assumption that FTO forms a planer thin film on glass substrates.

	Work function (eV)	Resistivity ( $\times 10^{-9}$ $\Omega$ m)	Dark current at 500 mV bias (mA/cm <sup>2</sup> )	Time for complete dissolving in electrolyte (hr)
Ti	4.3	420	$4 \times 10^{-2}$	>1600
FTO		$\approx 5000$	$1.5 \times 10^{-1}$	
Ni	5.2	69.3	$4 \times 10^{-4}$	>1600
Cr	4.5	125	$2 \times 10^{-2}$	
Al	4.3	28.2	$5 \times 10^{-3}$	100
Pt	5.6	105	20	>1600

### For insulating spacer layer

Generally any insulating material stable in  $I_3^-/3I^-$  electrolyte could be selected for this application. From this point of view, most ceramic materials are applicable. Polymeric materials, however, are mostly not heat resist, thus only applicable if  $TiO_2$  photoelectrode could be fabricated through low temperature processes. Heat-resist polymers that could be used for our purpose include polyimide (PI) and polytetrafluoroethylene (PTFE).

## 6.3 Experimental procedures

Configuration 2 and 3 were implemented in this project. Devices were firstly built on FTO glass before transferring the technology onto Ti foils.

### 6.3.1 Fabrication of insulating spacer

#### Dense ceramic spacer

The sol-gel method was employed to produce  $SiO_2$  dense ceramic spacer layers on FTO glass.<sup>6, 7</sup> To prepare the silica sol, two solutions were prepared. For the first one, 2.38 ml tetraethyl orthosilicate (>99 %, Aldrich) was mixed with 2.33 ml absolute ethonal (99.95 % Merck). For the second, 1.23 ml distilled water was mixed with 0.06 ml  $HNO_3$  (70% Univar). Solution 2 was then added into solution 1 drop-wise under vigorous stirring. The sol was then applied onto FTO glass by doctor-blading and left in air to dry.

Spray pyrolysis was employed to produce  $\text{Al}_2\text{O}_3$  coatings on FTO glass.<sup>8</sup> A 0.35 mol N,N-dimethylformamide (>99 %, Sigma) solution of aluminum acetylacetonate (99 %, Aldrich) was sprayed onto the FTO glass substrates preheated to 500 °C on a hotplate. The spray was conducted for up to 500 times with a 2 s interval between every two sprays. The sample was then left on the hotplate for 5 min and cooled down in air. A thin layer of gold was sputter coated onto such coatings to check the insulating property of the  $\text{Al}_2\text{O}_3$  coatings.

### Dense polyimide spacer

Several materials were used to produce dense spacer layers on FTO glass substrates for configuration 2. Polyimide were firstly tried to produce polymeric spacer layers. PI coatings were produced on FTO glass by spin coating a polyamic acid based precursor (PI2545, HD Microsystems) at various spin rates (Laurell spin coater, Model WS-400BZ-6NPP/LITE). Excess amount of precursor was dispensed on static samples, which were then spun using the program shown in Table 6.2. Coated films were dried at 140 °C for 5 min and then baked on a hot plate in air using the baking program shown in Table 6.3.

**Table 6.2** Programs for the spin coating of PI2545 polyamic acid based precursor to produce dense PI insulating spacer layers.

Steps	1	2
Starting speed (rpm)	0	500
Acceleration (rpm/s)	3240	108
Final speed (rpm)	500	Various final speed
Time (s)	5	60

**Table 6.3** Baking program for PI insulating spacer layer produced by spin coating of PI2545 polyamic acid based precursor.

Steps	1	2	3
Ramp time (min)	45	30	70
Temperature ( °C)	200	350	80
Hold time (min)	30	60	0

**Porous spacer layer**

For configuration 3, ZrO<sub>2</sub> nanoparticles (Zirconia ZT2, Z-Tech Zirconia) were used to make porous spacer layers. FTO glass and Ti foil substrates were firstly coated with Pt catalyst by thermal decomposition of an isopropanol (anhydrous, Sigma-Aldrich) precursor solution containing 10 mM H<sub>2</sub>PtCl<sub>6</sub> (38 % Pt basis, Aldrich). Porous insulating spacer layers were deposited by doctor-blading of a slurry containing ZrO<sub>2</sub> nanoparticles. To prepare the slurry, 4.5 g ZrO<sub>2</sub> nanoparticles were mixed with 2.7 g ethyl cellulose (Elthoxyl content 49 %, Aldrich) and 20.8 g terpinol (Anhydrous, Fluka). The mixture was then dissolved in 40 ml of absolute ethanol (99.95 %, Merck) with the addition of 2 g acetic acid (anhydrous, Univar). The slurry was ball milled for 8h to break down aggregation of nanoparticles. 6 and 10 µm thick spacer layers were prepared by doctor blading for 3 and 5 times. Films were dried at 125 °C in between each two printings. After printing, films were sintering at 450 °C for 30 min.

**6.3.2 Fabrication of top electrodes by magnetron sputtering**

For both configuration 1 and 2, a secondary electrode on top of the spacer layers was prepared by magnetron sputtering. Samples were loaded into the chamber of a sputtering system (LBS5000 sputtering/evaporation system), which were pumped down to a vacuum level of lower than  $4 \times 10^{-6}$  Torr. To sputter coat samples, Ar was purged into the chamber to achieve a pressure of  $2 \times 10^{-3}$  Torr and 100 W DC input power was applied to a 3 inch Ti target for required time durations.

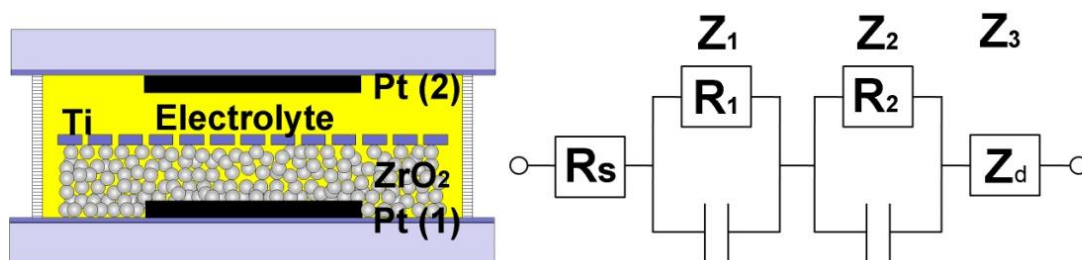
**6.3.3 Laser ablation for configuration 1**

Preliminary laser ablation experiments were conducted using a CO<sub>2</sub> IR laser system (Versa laser VLS 3.50, 25 µm wavelength). A matrix of dots was produced on substrates comprising of a FTO/PI/Ti layered structure. The designed diameter of dots is 100 µm. The spacing between each two holes is 100 µm.

**6.3.4 Measurement of diffusion resistance**

The diffusion resistance within electrolyte was quantitatively measured by EIS<sup>9-11</sup> using the electrochemical cell setup shown in Figure 6.2(a). The equivalent circuit for such a setup is

show in Figure 6.2(b). EIS experiments were performed using a potentiostat (VSP, BioLogic Science Instruments). Cells were biased at 0 V potential with the application of a 10 mV AC voltage perturbation. Frequency of the AC perturbation was varied from 500 kHz to 0.1 Hz. EIS data was fitted with the Z-fit function of EC-lab software (Version 10.02, Biologic Science Instruments).



**Figure 6.2 (a)** Schematic diagram of a cell used to measure the diffusion resistance of  $I_3^-/3I^-$  redox through porous spacer layer and porous Ti electrodes. Pt coatings with  $5 \times 5$  mm dimension were produced by thermal decomposition onto FTO glass substrates. One electrode in the cell was coated with  $ZrO_2$  porous spacer layer which was subsequently sputter coated with Ti. The area of  $ZrO_2$  coatings is much larger than that of Pt coatings to achieve complete coverage. An equivalent circuit used to fit experimental data for such cells is shown in **(b)**.  $Z_1$ ,  $Z_2$  and  $Z_3$  are assigned to Pt/electrolyte interface (1) and (2), and ionic diffusion within electrolyte, respectively.  $R_1$  and  $R_2$  are assigned to the real parts of  $Z_1$  and  $Z_2$ , respectively.

### 6.3.5 Cell fabrication

$TiO_2$  photoelectrodes were screen printed and dried using the standard procedure described previously in Chapter 3. For sintering, the standard program was modified to avoid cracking of coatings. The most significant change here is the extension of time spent on the burning off of polymer binders at temperature ranging from 325 to 375 °C (Table 6.4). The final sintering temperature was reduced to 450 °C to avoid oxidation of sputter coated Ti coatings. Sintered  $TiO_2$  films were then soaked in 0.3 mM N719 dye solution for 24 hrs and sealed with plain glass cover slides. An iodine/iodide electrolyte was back-filled into the sealed compartment through an entry port on the glass cover slide.



CBCDSCs were also fabricated on Ti foils. However, due to the complexity in sealing these devices, they are only tested under open conditions. Electrolyte was applied before test, and cells were covered with glass cover slides.

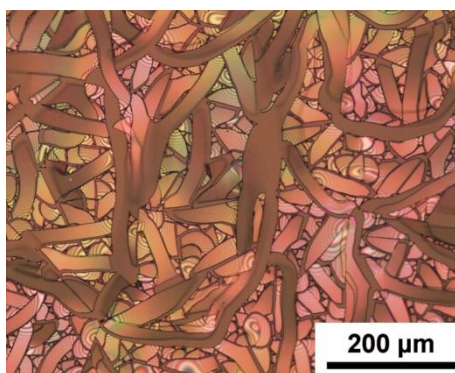
**Table 6.4** Modified sintering program for TiO<sub>2</sub> photoelectrodes printed on sputter coated Ti coatings. The ramping time from 325 to 375 °C was change from 5 min (standard procedure described in Chapter 3) to 30 min.

Step	1	2	3	4	5
Ramp time (min)	10	15	30	7	5
Temperature ( °C)	150	325	375	450	500
Holding time (min)	10	5	5	30	15

## 6.4 Results and discussion

### 6.4.1 Configuration 2 - dense ceramic spacer layer

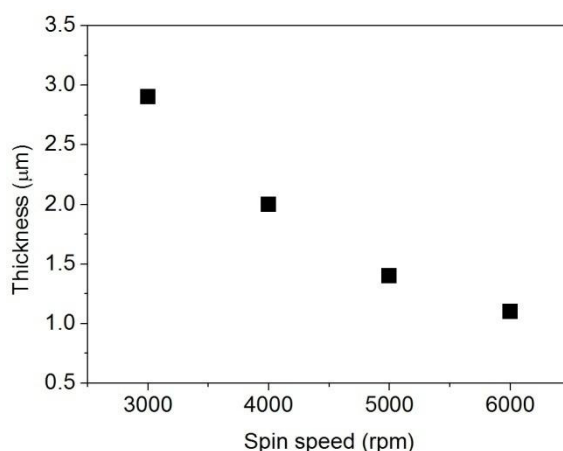
Fabrication of dense ceramic spacer layers was generally not successful. SiO<sub>2</sub> coatings produced by sol-gel methods were mostly cracked (Figure 6.3) due to the volume shrinkage that occurred during the gelation process. For Al<sub>2</sub>O<sub>3</sub> spacer layers produced by spray pyrolysis, <100 Ω resistances were measured for most samples, even on the ones that were spray coated for 500 times. It is difficult to make pin-hole free Al<sub>2</sub>O<sub>3</sub> coatings with the manual spray process used in our experiment.



**Figure 6.3** Optical micrograph of the SiO<sub>2</sub> coating produced by sol-gel method on FTO glass substrate. Coatings were mostly cracked due to the volume shrinkage that occurred during the gelation process.

### 6.4.2 Configuration 2 - dense polyimide spacer layer

A plot of average film thickness versus spin speed is shown in Figure 6.4. For safety reasons, the final spin speeds for most samples were restricted to below 5000 rpm. At 4000 rpm, 2  $\mu\text{m}$  films were obtained. However,  $<100\ \Omega$  resistances were usually measured between top and bottom electrodes, indicating pin-holes on these coatings. Good insulation was obtained by applying three coatings using 4000 rpm spin speed. The final thickness of the three coatings is approximately 6  $\mu\text{m}$  measured by a profilometer.



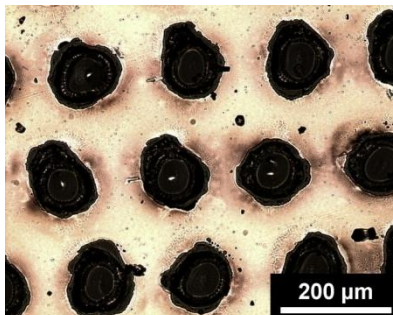
**Figure 6.4** Plot of average thickness vs. spin speed for spin coated PI spacer layer after baking. Thickness were measured using a profilometer.

### 6.4.3 Configuration 2 - Preliminary laser ablation tests

Circular holes with 100  $\mu\text{m}$  diameter were produced on FTO-PI-Ti substrates by laser ablation (Figure 6.5). However, all samples were shorted after laser ablation, possibly due to conductive debris connecting top and bottom electrodes after laser ablation. Damage of bottom FTO electrodes was also noticed on optical micrographs.

In this preliminary laser experiment, around 400 holes were produced on a  $4 \times 4\ \text{mm}$  standard cell testing area. However, the  $>100\ \mu\text{m}$  feature size would results in long pathlengths for electrons to travel before they are collected. As a result the electron collection would be inefficient if these samples are used to make solar cells.<sup>12</sup> To ensure efficient charge collection, the feature size would be reduced to sub 50  $\mu\text{m}$ , and correspondingly the number of holes

would exceed 1600 in a  $4 \times 4$  mm area. Such substrates would easily fail, with the presence of a very small percentage of shorted holes.

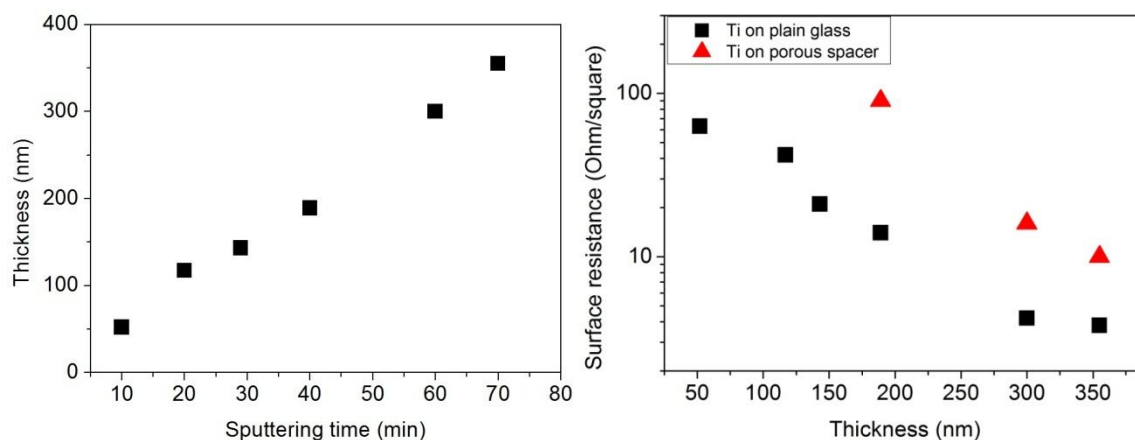


**Figure 6.5** A typical pattern comprising perforated top electrode and PI spacer layer produced by laser ablation. Thermal degradation of bottom electrode could be noticed from the image.

#### 6.4.4 Configuration 3 - magnetron sputtering of Ti porous electrodes

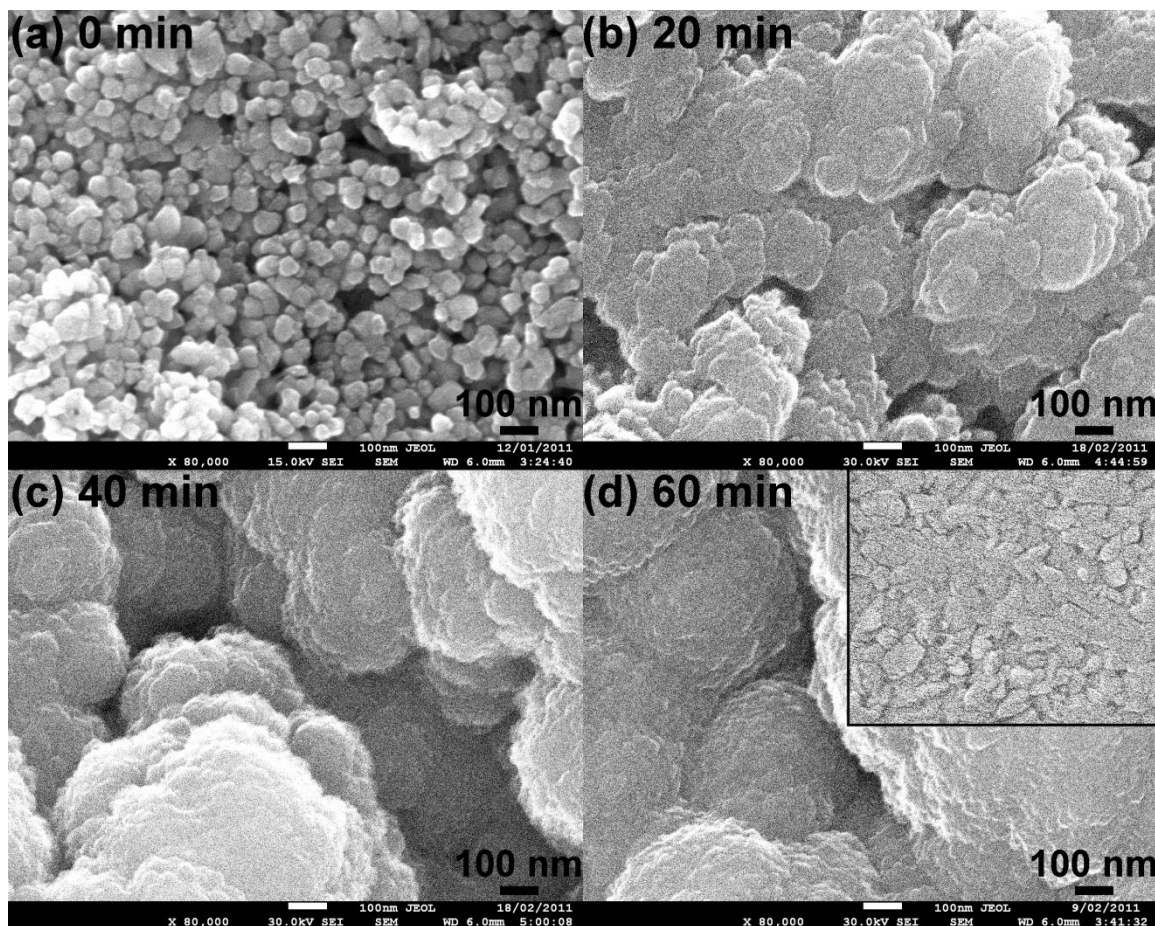
Figure 6.6 shows that the Ti coating thickness depends linearly on the sputtering time, while the sheet resistance of such coatings on both glass and porous spacer layers depend logarithmically on coating thickness. 300 nm thick Ti coating on glass gives a sheet resistance of approximately  $4 \text{ } \Omega/\square$ , which could correspond to a resistivity of  $1.2 \times 10^{-6} \text{ } \Omega \cdot \text{m}$  (Equation 6.1). This is higher than the bulk value of  $4.2 \times 10^{-7} \text{ } \Omega \cdot \text{m}$ . The increase in resistivity could be associated with the formation of grain boundaries, coating defects, and oxides related to the magnetron sputtering process.<sup>13, 14</sup> The sheet resistance of coatings produced under identical condition but on porous spacer layers is approximately  $11 \text{ } \Omega/\square$ , which is comparable to the sheet resistance of the FTO glass used in our experiment. The sheet resistance of porous electrodes could be further reduced by increasing the coating thickness while retaining their porosity.<sup>15</sup>

$$\rho = R \cdot t = 4 \times 300 \times 10^{-9} \text{ m} = 1.2 \times 10^{-6} \text{ } \Omega \cdot \text{m} \quad 6.1$$



**Figure 6.6** (a) Thickness of sputter coated Ti on plain glass substrates measured by a profilometer. (b) Sheet resistance of these coatings on plain glass and porous spacer layer plotted against coating thickness.

Figure 6.7 shows the morphology of a porous  $\text{ZrO}_2$  spacer layer (Figure 6.7(a)) coated on FTO glass, and the evolution in microstructure with increasing Ti thickness (Figure 6.7(b), (c) and (d)). Figure 6.7(a) shows that 50 nm  $\text{ZrO}_2$  nanoparticles are uniformly dispersed and are interconnected. When sputter coating for 20 min (125 nm coating on plain glass), Ti deposits are coated on  $\text{ZrO}_2$  particles and are joint to form larger aggregates. When sputter for 40 and further to 60 min, micron-sized Ti particles are formed. The final coating at 60 min has an equivalent thickness of 350 nm on plain glass, the size of particles , and a sheet resistance of  $11 \Omega/\square$  on porous spacer layer compared to a value of  $4 \Omega/\square$  on glass substrates. The porosity of the coating is sufficient at this stage to ensure effective ionic diffusion through these coatings in fully assembled cells.



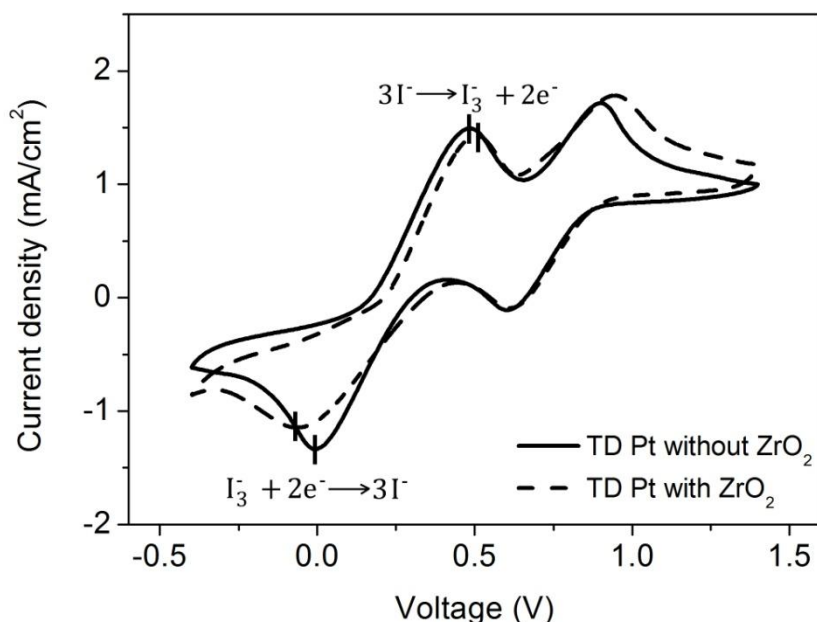
**Figure 6.7** Scanning electron micrographs showing the morphology of (a) a porous insulating spacer layer made of  $\text{ZrO}_2$  nanoparticles, and the same layer coated with Ti by DC magnetron sputtering performed at 100 W for (b) 20, (c) 40 and (d) 60 min (equivalent to 125, 170 and 350 nm Ti coatings measured on glass substrates). The inserted image in (d) shows an identical Ti coating on plain glass coated for 60 min.

#### 6.4.5 Configuration 3 - electrochemical activity of covered Pt catalytic coatings

In CBCDSC configuration 3, the Pt catalytic layers are covered by a porous  $\text{ZrO}_2$  spacer layer and a porous Ti electrode. The covering of Pt by these coatings might result in the reduction in activation surface area for triiodide reduction. It is therefore essential to evaluate the catalytic activity of the Pt catalytic layer after the coverage by the  $\text{ZrO}_2$  and the Ti coatings.

A Pt layer was deposited by the thermal decomposition of  $\text{H}_2\text{PtCl}_6$  at 400 °C. The catalytic activities of  $\text{ZrO}_2$  covered Pt catalyst were characterized by cyclic voltammetry (CV). As shown in Figure 6.8, no obvious change in the height of both oxidation and reduction peak is

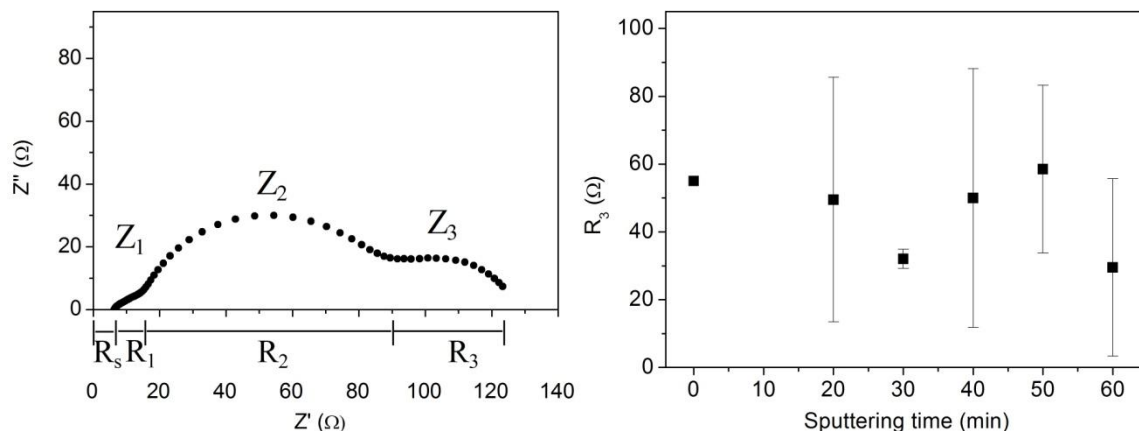
observed for Pt with and without  $\text{ZrO}_2$ . The peak positions also remain unaltered, indicating sufficient catalytic activity of the Pt catalyst after the coverage by the  $\text{ZrO}_2$  coating.



**Figure 6.8** Cyclic voltammetry (CV) results showing a comparison between the electrochemical activity of Pt coatings with and without the coverage of porous  $\text{ZrO}_2$  spacer layers. The Pt coating is produced by the thermal decomposition (TD) of  $\text{H}_2\text{PtCl}_6$ .

The electrochemical activities of substrates comprising Pt/ $\text{ZrO}_2$ /Ti are further characterized by EIS measurements. Figure 6.9(a) shows a typical Nyquist plot of the EIS results measured for the electrochemical cell (Pt coating covered by  $\text{ZrO}_2$ ) shown in Figure 6.2(a).  $R_s$  is the series resistance of the electrode material. Three semicircles are assigned to three impedance components  $Z_1$ ,  $Z_2$  and  $Z_3$ . Their real parts are  $R_1$ ,  $R_2$  and  $R_3$  respectively. The smaller  $R_1$  at high frequency refers to the charge transfer resistance at the uncovered Pt/electrolyte interface, while the larger resistance  $R_2$  at medium frequency refers to the charge transfer resistance at the covered Pt/electrolyte interface. The coverage of the Pt coatings by porous  $\text{ZrO}_2$  layers results in a reduced Pt/electrolyte contact area therefore higher charge transfer resistance for triiodide reduction.  $R_3$  at low frequency is the diffusion resistance within the electrolyte.<sup>9, 16</sup> For cells with different sputtered Ti coatings, no real trend in  $R_3$  could be observed (Figure 6.9(b)). This indicates that increasing Ti coating thickness has no effects on the diffusion within the electrolyte. The finding further confirms the observation from the micrographs in

Figure 6.7, which show pores of over 100 nm size for samples with 300 nm thick Ti coatings (Figure 6.7(d)).



**Figure 6.9 (a)** Nyquist plot of EIS results measured for the electrochemical cell shown in Figure 6.2.  $R_s$  is the series resistance in the cell,  $R_1$ ,  $R_2$  and  $R_3$  are the real parts of impedance components  $Z_1$ ,  $Z_2$ , and  $Z_3$ , respectively. **(b)** Plot of  $R_3$  vs. sputtering time for electrochemical cells (Figure 6.2(a)) comprising porous Ti layer sputtered coated for 0, 20, 30, 50, and 60 mins.

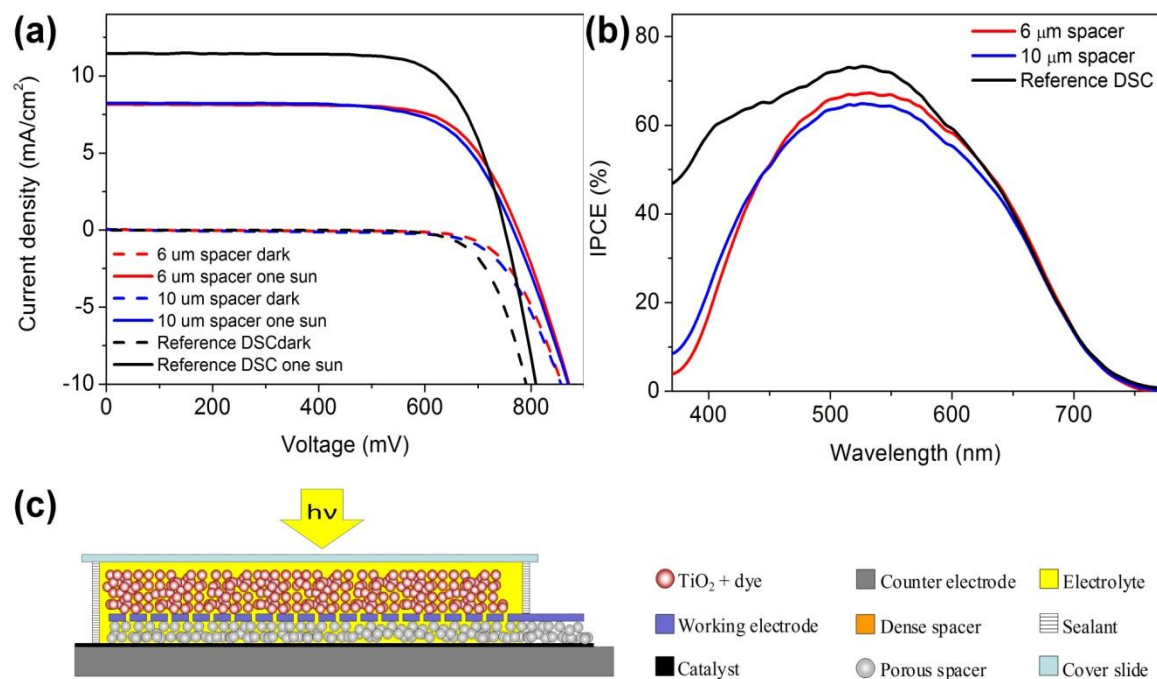
#### 6.4.6 Configuration 3 - Characterization of fully assembled cells

Figure 6.10 and Table 6.5 compares photovoltaic performances of CBCDSCs to a reference DSC using identical  $\text{TiO}_2$  layers, dye, and electrolyte. It is noticed that the performance of our reference DSC is not as good as what usually could be obtained for a typical DSC employing identical materials.<sup>17</sup> This is due to the absent of a light scattering layer as well as the elimination of some critical fabrication steps, such as  $\text{TiCl}_4$  post-treatment of  $\text{TiO}_2$  electrode.<sup>18</sup> However, it is fair to use the reference cell fabricated here to compare to our coplanar back-contact devices.

Under dark and one-sun illumination ( $\text{AM1.5}$ ,  $100 \text{ mW/cm}^2$ ), the I-V curves (Figure 6.10 (a)) of the two CBCDSCs show typical diode and photodiode behaviour. No obvious shunting is observed, indicating an effective isolation between working and counter electrodes by the  $\text{ZrO}_2$  spacer layers. However, slightly lower fill factors are measured for CBCDSCs than standard reference DSC, mostly due to higher internal resistances. Similar I-V characteristic are measured for the two CBCDSCs, indicating that the thickness of spacer layers has no



significant effect on the performance of solar cells. The current densities at one sun illumination for both coplanar back-contact cells are 8.2 mA/cm<sup>2</sup>, compared to 11.5 mA/cm<sup>2</sup> for the reference cell. This comes mostly from the light transmission loss due to the absorption by an electrolyte layer between top cover slide and TiO<sub>2</sub> film.



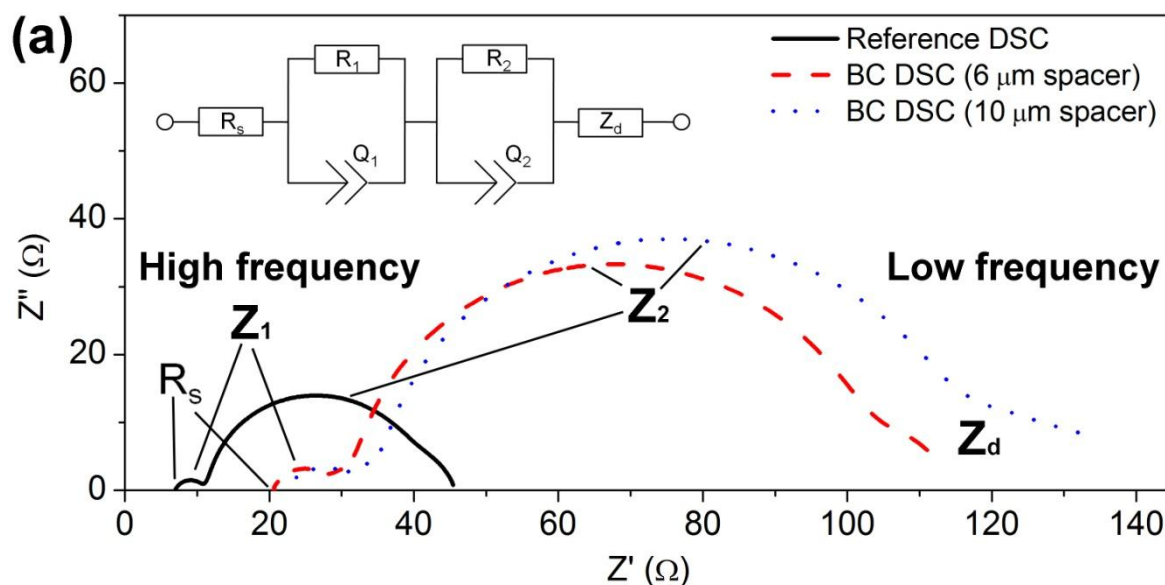
**Figure 6.10** (a) Current density-voltage (I-V) characteristic of coplanar back-contact DSCs (CBCDSCs) with 6 and 10 μm insulating spacer layers in comparison to a standard reference DSC using identical TiO<sub>2</sub>, dye and electrolyte. A schematic diagram of the architecture of the CBCDSCs is shown in (c). All cells are measured under dark and one sun illumination (AM1.5, 100 mW/cm<sup>2</sup>) conditions. The CBCDSCs and the reference DSC are measured with light illuminating from the transparent cover slide and the TiO<sub>2</sub> photoelectrode respectively. (b) Incident Photon-to-Electron Conversion Efficiency (IPCE) of the three solar cells.



**Table 6.5** Photovoltaic characteristics of coplanar back-contact DSCs (CBCDSCs) comprising 6 and 10  $\mu\text{m}$  insulating spacer layers in comparison to a standard reference DSC using identical  $\text{TiO}_2$ , dye and electrolyte.  $V_{oc}$ ,  $J_{sc}$ ,  $FF$  and  $\eta$  refers to open-circuit voltage, short-circuit current density, fill factor and efficiency, respectively

	BC DSC (6 $\mu\text{m}$ spacer)	BC DSC (10 $\mu\text{m}$ spacer)	Reference DSC
$V_{oc}$ (mV)	776	766	751
$J_{sc}$ ( $\text{mA}/\text{cm}^2$ )	8.2	8.2	11.5
$FF$	0.72	0.70	0.74
$\eta$ (%)	4.57	4.40	6.34

The IPCE spectra (Figure 6.10(b)) of the three devices show photocurrent peaks at around 550 nm, corresponding roughly to the absorption peak (534 nm)<sup>20</sup> of the standard ruthenium dye N719. The IPCE spectra also show 67 % and 65 % IPCE peak values measured for the coplanar back-contact cells with 6 and 10  $\mu\text{m}$  spacer layers, compared to a 72% peak measured for the reference DSC. At wavelength above 600 nm, similar IPCEs are measured for both types of devices, indicating similar photocurrent generation at these wavelengths. Below 550 nm, there is a drop in IPCE of coplanar back-contact cells, mostly due to the strong absorption by iodine electrolyte at this regime of the solar spectrum. This further proves the lower photocurrent densities measured for coplanar back-contact cells in I-V characterization.



**(b)**

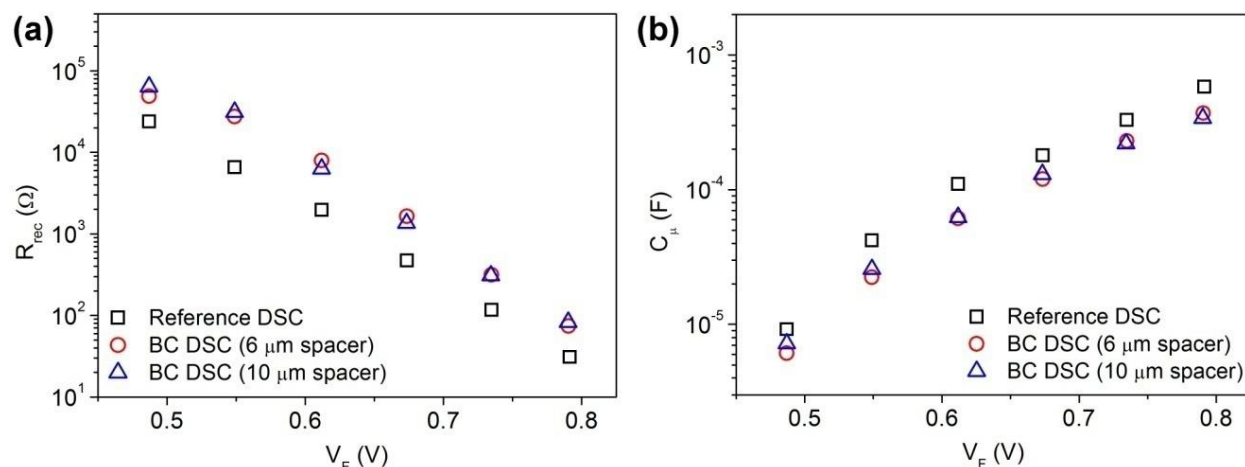
	BC DSC (6 $\mu\text{m}$ spacer)	BC DSC (10 $\mu\text{m}$ spacer)	Reference DSC
$R_s$	20.4	22.0	7.0
$R_1$	9.6	11.6	4.0
$R_2$ ( $R_{\text{rec}}$ )	74.7	83.8	31.2
$Q_2$ ( $C_\mu$ )	$0.38 \times 10^{-3}$	$0.35 \times 10^{-3}$	$0.62 \times 10^{-3}$
$R_3$	33.3	28.0	17.4
$R_{\text{tot}}$	63.3	61.6	28.4

**Figure 6.11** Nyquist plot of Electrochemical Impedance Spectroscopy (EIS) results measured for coplanar back-contact DSCs (with 6 and 10  $\mu\text{m}$  spacer layers) and a reference DSC biased at 0.8 V under dark. The impedance components  $R_s$ ,  $Z_1$ ,  $Z_2$  and  $Z_d$  are assigned to series resistance, Pt/electrolyte interface,  $\text{TiO}_2$ /dye/electrolyte interface and diffusion of redox species in a DSC. The inserted image shows a simplified equivalent of these solar cells based on the transmission-line model.<sup>21-23</sup>  $R_1$ ,  $R_2$ ,  $R_3$  are resistance components of  $Z_1$ ,  $Z_2$  and  $Z_d$ , respectively. **(b)** Summary of important parameters obtained from EIS measurements through fitting data with equivalent circuit. The resistances and capacitances are measured in  $\Omega$  and  $F$ , respectively.  $R_{\text{tot}}$  refers to total internal resistance.

Figure 6.11(a) shows Nyquist plots of EIS results measured for the three DSCs. Three typical semi-circles are identified on each curve. From high frequency to low frequency, they are assigned to three impedance components measured for Pt/electrolyte interface,  $\text{TiO}_2/\text{dye}/\text{electrolyte}$  interface and diffusion of redox species in a DSC. The result could be fitted by the inserted equivalent circuit in Figure 6.11 according to the transmission-line model proposed in previous studies.<sup>21-23</sup> Internal resistances  $R_{\text{tot}}$  are calculated by  $R_s + R_1 + R_3$ , which is the sum of series resistance, charge transfer resistance at Pt/electrolyte interface and diffusion resistance within electrolyte.<sup>16</sup>

Figure 6.11(b) summarizes parameters obtained from fitting EIS measurements. It is shown that higher  $R_s$ ,  $R_1$  and  $R_3$  result in higher  $R_{\text{tot}}$  for CBCDSCs. The increased series resistance  $R_s$  is due to oxidation of porous Ti electrodes during sintering of  $\text{TiO}_2$  electrodes. Higher charge transfer resistance  $R_1$  at the Pt/electrolyte interface and slightly higher diffusion resistances within electrolyte are due to the partial coverage of Pt catalyst by  $\text{ZrO}_2$  spacer layers. As a result, higher  $R_{\text{tot}}$  of 63.3  $\Omega$  and 61.6  $\Omega$  are measured for the two CBCDSCs compared to 28.4  $\Omega$  for the reference DSC. This results in a shallower gradient at potentials close to the open-circuit voltage point on I-V curves. Fill factors of these devices are therefore lower for coplanar back-contact devices.

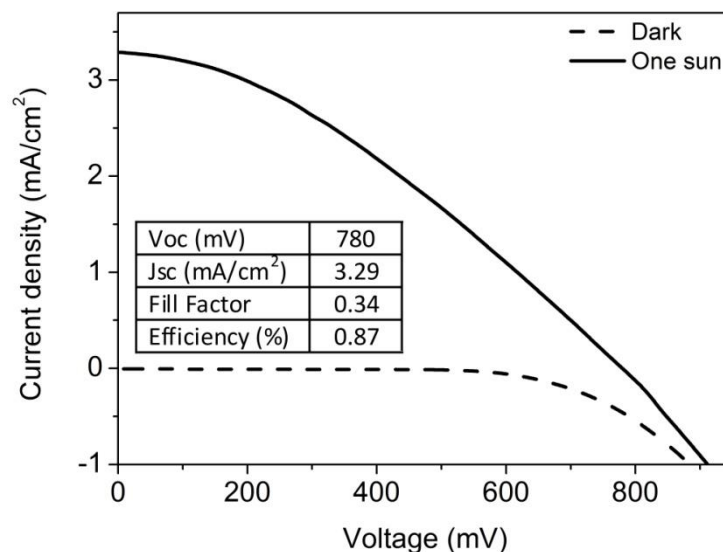
However, higher recombination resistances  $R_{\text{rec}}$  of 74.7 and 83.8  $\Omega$  are measured for the two CBCDSCs, in agreement with later dark current on-sets as well as higher open circuit voltages under one-sun illumination. Recombination resistance  $R_{\text{rec}}$  at the  $\text{TiO}_2/\text{dye}/\text{electrolyte}$  interface and chemical capacitance  $C_\mu$  of mesoporous  $\text{TiO}_2$  film are further plotted against Fermi level voltage  $V_F$  (Figure 6.12(a) and (b)). This voltage can be calculated by subtracting ohmic drop component from the applied bias voltage across cells.<sup>24, 25</sup> It is shown that both  $R_{\text{rec}}$  and  $C_\mu$  show exponential dependence on  $V_F$ .<sup>24</sup> Similar  $R_{\text{rec}}$  and  $C_\mu$  are measured for the two CBCDSCs. Compared to the reference DSC, higher  $R_{\text{rec}}$  and lower  $C_\mu$  are measured for coplanar back-contact cells at bias voltage ranging from 0.5 to 0.8 V. This can be explained in terms of a shift in the conduction band edge of  $\text{TiO}_2$  towards a higher position.<sup>23</sup> Given that identical fabrication condition for  $\text{TiO}_2$  photoelectrodes and identical dye and electrolyte are used for both coplanar back-contact and reference cells, one reason for the reduced recombination is believed to be the reduced dark current at Ti electrodes than FTO electrodes.



**Figure 6.12** (a) Recombination resistance  $R_{rec}$  and (b) chemical capacitance  $C_\mu$  of a reference DSC and coplanar back-contact DSCs with 6 and 10  $\mu\text{m}$  spacer layers measured in dark at various wavelength.  $V_F$  refers to 'Fermi level voltage'.<sup>24</sup> It is defined as a voltage upon which a change in Fermi level of  $\text{TiO}_2$  is occurred, and could be calculated by subtracting the ohmic voltage drops from the applied bias voltages.

#### 6.4.7 Preliminary results of coplanar back-contact DSCs on Ti substrates

Under on-sun illumination, the I-V curve of the cell shows a triangular characteristic. This indicates a very high internal resistance due to the cracking of sputter coated Ti working electrode during sintering. A Low current of  $3.3 \text{ mA/cm}^2$  were measured for CBCDSCs on Ti foils, possibly due to the evaporation of electrolyte from open cells during testing.



**Figure 6.13** Current density-voltage characteristics of a coplanar back-contact DSC fabricated on Ti foil substrate. The cell was measured under dark and on-sun illumination (AM1.5, 100 mW/cm<sup>2</sup>). The inserted table shows open-circuit voltage, short-circuit current density, fill factor and efficiency of the solar cell.

## 6.5 Conclusion

In conclusion, we have invented a novel DSC configuration which we refer to as coplanar back-contact DSCs (CBCDSCs). A typical device of this configuration comprises a laminated working electrode-insulator-counter electrode backplate located on a common side of a dye-sensitized TiO<sub>2</sub> photoelectrode.

Three possible configuration configurations were proposed, whereas only configuration 2 and 3 were fabricated. For configuration 2, several dense spacer layers, including PI, SiO<sub>2</sub> and Al<sub>2</sub>O<sub>3</sub> layers were produced. However, all electrodes were shorted either before or after laser ablation process. Due to the difficulties in making functional coplanar back-contact substrates, no successful device has been made for configuration 2. For configuration 3, a porous ZrO<sub>2</sub> spacer layer was fabricated to effectively isolate coplanar working and counter electrodes while allowing for ionic diffusion between the counter electrode and the TiO<sub>2</sub> photoelectrode. Working devices have been successfully produced by simple fabrication methods. Due to the good commercial availability and geometrical flatness, FTO glass was used as starting materials for CBCDSCs. A solar energy conversion efficiency of 4.57 % (one-sun illumination,

AM1.5 100 mW/cm<sup>2</sup>) has been achieved, compared to an efficiency of 6.34 % for a reference DSC comprising of identical TiO<sub>2</sub> layer, dye and electrolyte. The lower efficiency is mostly due to the absorption of light below 550 nm by iodine electrolyte, which could be solved by using a transparent SiO<sub>2</sub> coating<sup>26</sup>. Higher internal resistances of CBCDSCs measured by EIS also contribute to low fill factors and therefore lower cell efficiencies. EIS results also reveal higher  $R_{\text{rec}}$  for coplanar back-contact devices, which could be due to lower recombination on Ti electrodes than on FTO electrodes. This is in agreement with the later dark current on-set in dark measurement and higher  $V_{\text{oc}}$  under one-sun illumination.

Finally, CBCDSCs were fabricated on Ti foil. Due to technical difficulties during the cell fabrication process, the cell performance was not promising. A solar energy conversion efficiency of 0.87 % was measured under one-sun illumination. However, this is so far the first coplanar DSC employing exclusively metal based electrodes. To our best knowledge, the CBCDSCs invented in this project is the only type of coplanar DSCs that could employ non-transparent materials for both working and counter electrodes. Such advantages enable the production of low-cost coplanar DSC modules on highly conductive metal-based substrates.

## 6.6 References to chapter 6

- [1] A. Yella, H. W. Lee, H. N. Tsao, C. Y. Yi, A. K. Chandiran, M. K. Nazeeruddin, E. W. G. Diau, C. Y. Yeh, S. M. Zakeeruddin, M. Grätzel, *Science* **2011**, 334, 629.
- [2] Y. Cao, J. Zhang, Y. Bai, R. Li, S. M. Zakeeruddin, M. Grätzel, P. Wang, *J. Phys. Chem. C* **2008**, 112, 13775.
- [3] K. Okada, H. Matsui, T. Kawashima, T. Ezure, N. Tanabe, *J. Photoch. Photobio. A* **2004**, 164, 193.
- [4] S. M. Sze, K. K. Ng, *Physics of Semiconductor Devices*, John Wiley & Sons, Inc., Hoboken **2006**.
- [5] D. William, J. Callister, *Materials science and engineering: and introduction*, John Wiley & Sons, Inc., New York **2003**.
- [6] C. Brinker, G. W. Scherer, *Sol-gel science: the physics and chemistry of sol-gel processing*, Academic Press, Boston **1990**.
- [7] Y. Castro, A. Duran, R. Moreno, B. Ferrari, *Adv. Mater.* **2002**, 14, 505.
- [8] J. Guzman-Mendoza, M. Garcia-Hipolito, M. Aguilar-Frutis, C. Falcony-Guajardo, *J. Phys.: Condens. Matter* **2001**, 13, L955.
- [9] L. Han, N. Koide, Y. Chiba, A. Islam, T. Mitate, *C. R. Chimie* **2006**, 9, 645.
- [10] L. Han, N. Koide, Y. Chiba, T. Mitate, *Appl. Phys. Lett.* **2004**, 84, 2433.
- [11] T. Hoshikawa, M. Yamada, R. Kikuchi, K. Eguchi, *J. Electroanal. Chem.* **2005**, 577, 339.

- 
- [12] J. Jennings, A. Ghicov, L. Peter, P. Schmuki, A. Walker, *J. Am. Chem. Soc.* **2008**, 130, 13364.
  - [13] M. Day, M. Delfino, J. Fair, W. Tsai, *Thin Solid Films* **1995**, 254, 285.
  - [14] K. Chan, B. Teo, *IET Sci. Meas. Technol.* **2007**, 1, 87.
  - [15] N. Fuke, A. Fukui, R. Komiya, A. Islam, Y. Chiba, M. Yanagida, R. Yamanaka, L. Han, *Chem. Mater.* **2008**, 20, 4974.
  - [16] L. Han, N. Koide, Y. Chiba, A. Islam, R. Komiya, N. Fuke, A. Fukui, R. Yamanaka, *Appl. Phys. Lett.* **2005**, 86, 1.
  - [17] S. Ito, T. N. Murakami, P. Comte, P. Liska, C. Grätzel, M. K. Nazeeruddin, M. Grätzel, *Thin Solid Films* **2008**, 516, 4613.
  - [18] P. Sommeling, B. O'Regan, R. Haswell, H. Smit, N. Bakker, J. Smits, *J. Phys. Chem. B* **2006**, 110, 19191.
  - [19] B. O'Regan, J. Durrant, P. Sommeling, N. Bakker, *J. phys. Chem. C* **2007**, 111, 14001.
  - [20] M. Nazeeruddin, A. Kay, I. Rodicio, R. Humphrybaker, E. Muller, P. Liska, *J. Am. Chem. Soc.* **1993**, 115, 6382.
  - [21] J. Bisquert, *J. Phys. Chem. B* **2002**, 106, 325.
  - [22] J. Bisquert, A. Compte, *J. Electroanal. Chem.* **2001**, 499, 112.
  - [23] Q. Wang, S. Ito, M. Grätzel, F. Fabregat-Santiago, I. Mora-Sero, J. Bisquert, *J. Phys. Chem. B* **2006**, 110, 25210.
  - [24] J. Bisquert, *Phys. Chem. Chem. Phys.* **2003**, 5, 5360.
  - [25] E. M. Barea, C. Zafer, B. Gultekin, B. Aydin, S. Koyuncu, S. Icli, F. F. Santiago, J. Bisquert, *J. Phys. Chem. C* **2010**, 114, 19840.
  - [26] S. Ito, S. M. Zakeeruddin, P. Comte, P. Liska, D. Kuang, M. Grätzel, *Nat. Photonics.* **2008**, 2, 693.





## 7 Three-terminal tandem DSCs

### 7.1 *Introduction*

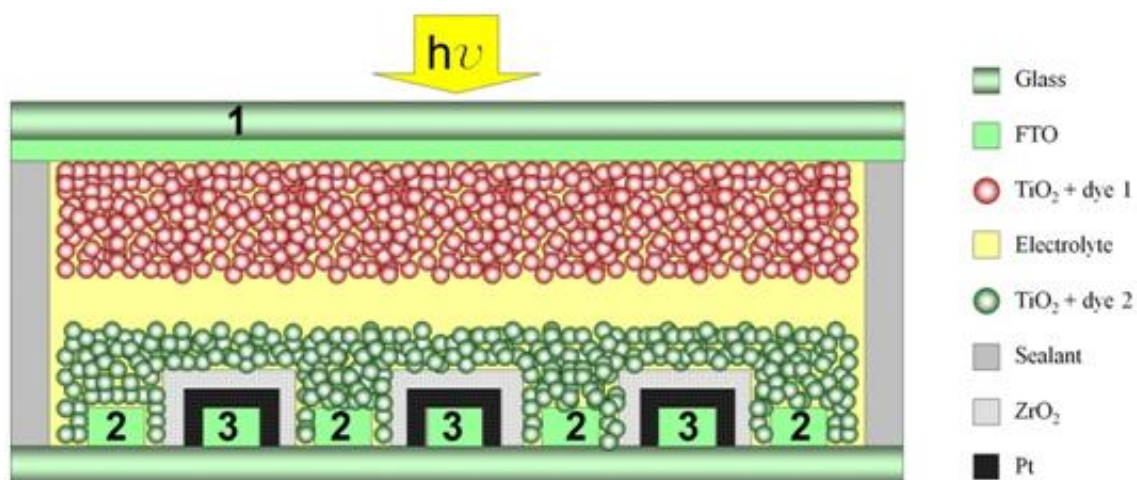
Making use of tandem solar cells is one of the strategies to improve solar energy conversion efficiencies,<sup>1-7</sup> as multiple-junction photovoltaic devices have higher theoretical conversion efficiencies than single-junction solar cells. A theoretical efficiency of 41.9 % is expected with two cells connected in series, while over 50 % efficiency can be exceeded with more cells.<sup>8</sup> Tandem solar cells can be fabricated through stacking two or more subcells with complementary absorption spectrums. These subcells cooperate to absorb sunlight in an extended range of wavelengths.

Subcells in tandem photovoltaic could be connected in parallel or in series, resulting either in enhanced photocurrent or photovoltage. Matching of photovoltage or photocurrent is essential when connecting multiple subcells in these configurations, as the overall device performance is limited by the worst performing component. In previous studies, tandem solar cells with three terminals are commonly adopted as the architecture to produce tandem silicon solar cells, thin film solar cells as well as polymer solar cells<sup>6, 9-11</sup>. These devices usually have subcells sharing either the common cathode or common anode. As the two subcells in these devices produce different photovoltages, the subcells are measured individually, and the overall device efficiencies are calculated by mathematical addition of the efficiencies of individual cells.

In the field of DSC research, tandem devices with a photoanode-photocathode two-terminal setup were produced to extend the absorption spectrum into the red regime.<sup>12</sup> In these tandem devices, the conventionally platinized cathodes were replaced by photocathodes which transfer electrons to triiodide ions. Photoanode and photocathode are connected in series, providing enhanced photovoltage. Although with theoretically predicted higher efficiencies, cell performances up to now are far from ideal. A critical limiting factor is the lower current generated by photocathode than by photoanode. This limits the overall current of the tandem solar cells. There are also difficulties in matching the energy levels of different dyes with the redox potential of the electrolyte.

In this chapter, we propose a three-terminal tandem DSC architecture. We utilize the features of back-contact DSCs whose dye-sensitized  $\text{TiO}_2$  photoelectrodes are located on the same side of working and counter electrodes. The transparent cover slide in the back-contact DSCs are replaced by conventional  $\text{TiO}_2$  photoelectrodes. Both interdigitated and coplanar back-contact DSCs can be used to construct tandem DSCs, however only the interdigitated devices are implemented in our experiment.

The device configuration of a three-terminal tandem DSC is schematically shown in Figure 7.1. The cell consists of a mesoporous  $\text{TiO}_2$  photoelectrode sitting on top of an interdigitated back-contact DSC. Light irradiation is applied from the top side of the tandem cell. As described in Chapter 4, the back-contact DSC comprises a pair of charge-collecting electrodes. In the tandem device, electrode 1 and 2 are two Working Electrodes (WEs) connected in parallel. Electrode 3 is used as a common Counter Electrode (CE) for triiodide reduction.

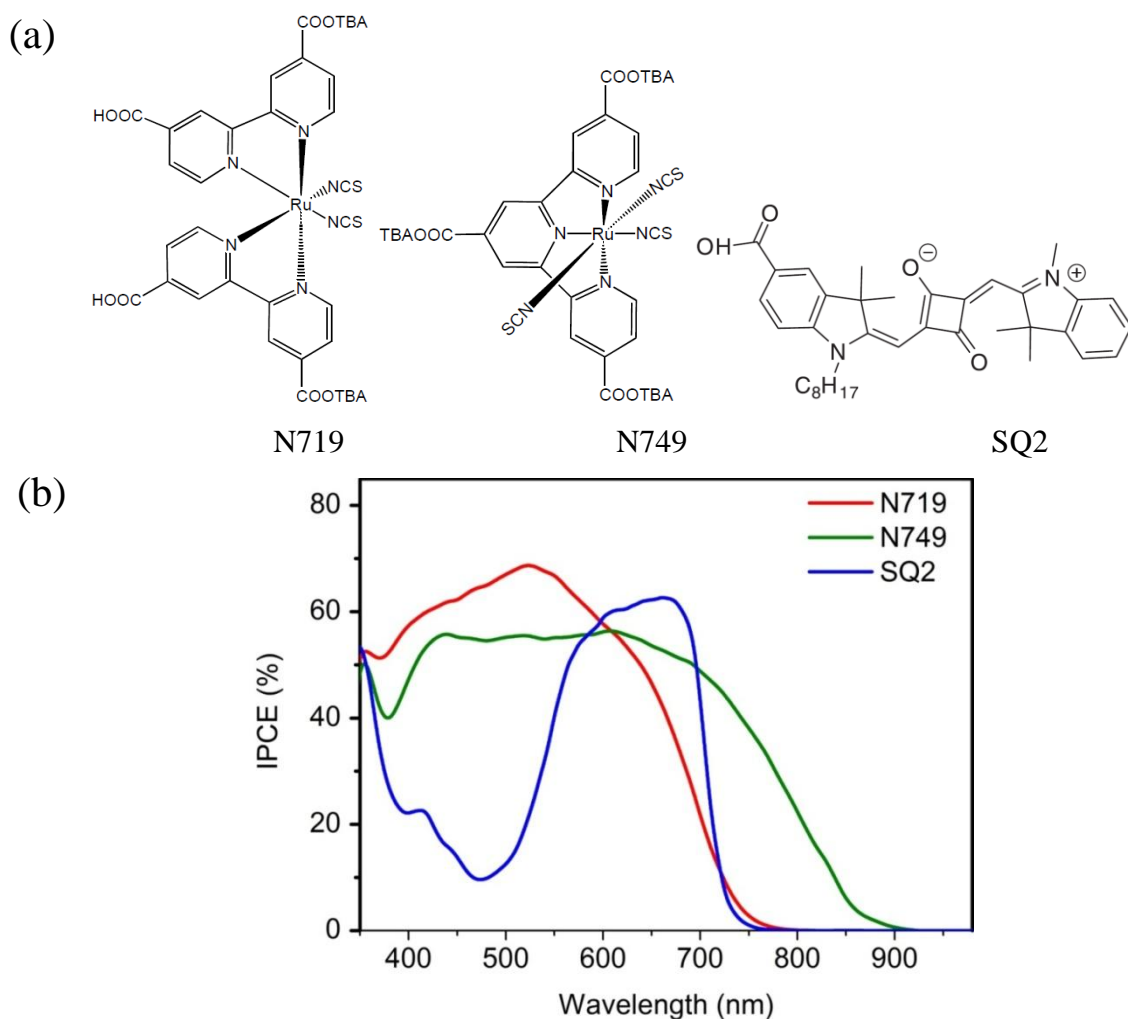


**Figure 7.1** Scheme of a three-terminal tandem DSC comprising a conventional DSC working electrode at front and an interdigitated back-contact DSC on the backside of light irradiation. Electrode 1 and 2 are two working electrodes connected in parallel, while electrode 3 performs as a common counter electrode in the system.

In order to achieve substantially enhanced photovoltaic performance, the two dyes used in the three-terminal tandem DSCs should have supplementary absorption spectra. However, the work described in this chapter are mostly for proof-of-principle purpose. Only three dyes are implemented in our experiments to make functioning tandem devices. For all devices, the

N719 dye <sup>13</sup> is used as dye 1 for the front TiO<sub>2</sub> photoanode. The N749 dye (black dye) <sup>14</sup> or the SQ2 <sup>15, 16</sup> are used as dye 2 for back-contact electrodes.

The chemical structures of the three dye molecules are shown in Figure 7.2(a). The IPCE spectrums measured for standard DSCs (see Section 2.2 for details) using these dyes are shown in Figure 7.2(b). Both N749 and SQ2 dye contribute to higher IPCE than N719 dye at wavelength higher than 600 nm. Both dyes are suited for the back-contact cells in the tandem devices, although they compete with the N719 dye for the absorption of visible light.



**Figure 7.2** (a) Structures of the N719, N749 and SQ2 dyes. (TBA refers to tetrabutylammonium). (b) The IPCE spectra measured for standard DSCs using the three dyes.

## 7.2 *Three-terminal tandem DSCs using N719 and N749 dyes*

Tandem devices combining N719 and N749 dyes were firstly investigated. Before fabricating tandem devices, N749 dye was investigated as the sensitizer in standard DSCs to optimize fabrication conditions.

### 7.2.1 **The effects of mixing light scattering particles in TiO<sub>2</sub> films**

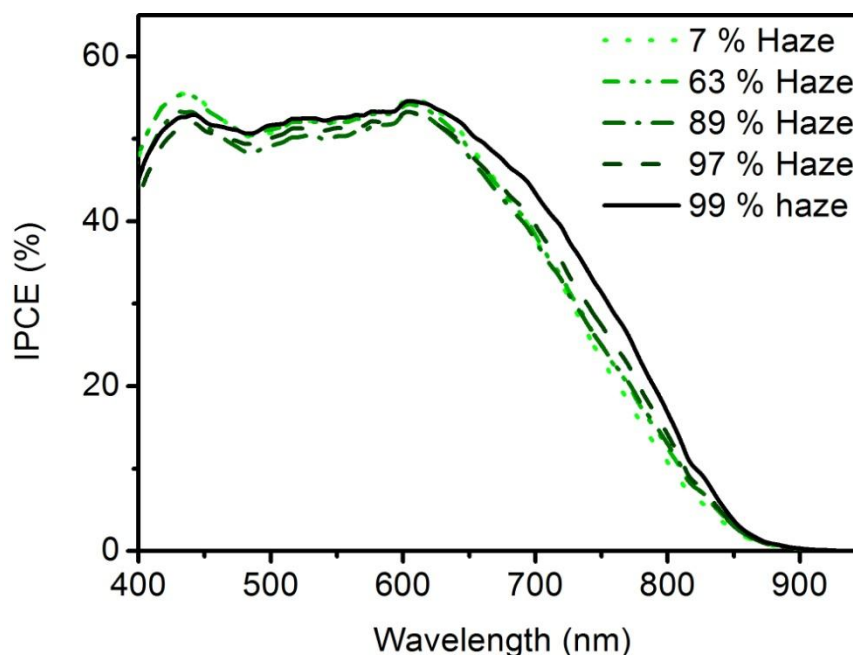
DSCs sensitized with the panchromatic N749 dye can achieve high conversion efficiencies of up to 11.1 %.<sup>17</sup> However, the dye has a limited extinction coefficient of  $12,200 \text{ M}^{-1} \text{ cm}^{-1}$  at the absorption peak.<sup>14</sup> TiO<sub>2</sub> photoelectrodes with good light scattering properties are essential to enhance the response to red light.<sup>17</sup> In standard DSCs we could use scattering layers comprising large TiO<sub>2</sub> on the backside of transparent film to enhance light scattering. However, this is not applicable to back-contact DSCs. The other strategy proposed in previous study is to use TiO<sub>2</sub> films mixing small and large TiO<sub>2</sub> particles to obtain enhanced haze.<sup>17</sup>

**Table 7.1** Weight ratio between 400 nm and 20 nm particles in screen printing pastes A to E and the corresponding haze ratio resulted from the addition of 400 nm light scattering particles.

	Weight ratio 400 nm : 20 nm particles (%)	Haze (%)
A	0	7
B	5	63
C	10	89
D	16	97
E	20	99

In our experiment, two TiO<sub>2</sub> screen-printing pastes comprising 20 and 400 nm TiO<sub>2</sub> particles were mixed. The overall weight percentages of nanoparticles in pastes were kept consistent, whereas the ratio between 20 nm and 400 nm nanoparticles were varied according to the values shown in Table 7.1. Table 7.1 also shows the resulted haze which is calculated by the ratio between the diffusive transmitted light to the overall light transmitted through TiO<sub>2</sub> films (the diffusive and overall light transmission were measured using a UV-vis spectrometer equipped with an integrating sphere).

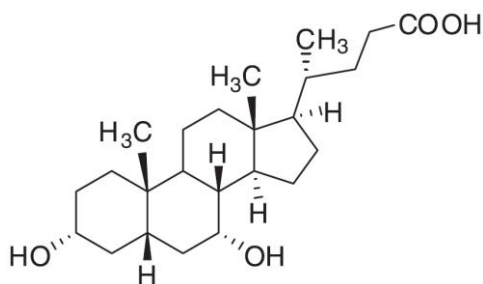
Standard DSCs comprising  $\text{TiO}_2$  film with various haze were tested. Enhanced IPCE results (Figure 7.3) are measured, mostly towards the absorption of red light. The sample with 99 % haze shows an increased IPCE of 20 % at 800 nm compared to the 10 % IPCE measured for the sample with 7 % haze. However, the enhancement is less than those shown in previous studies.<sup>17</sup> Besides, the IPCE peaks are only around 55 %, less than the 80 % IPCE shown in literature.<sup>17</sup>



**Figure 7.3** IPCE of DSCs using  $\text{TiO}_2$  mesoporous films with different levels of haze. The  $\text{TiO}_2$  films have a thickness of 12  $\mu\text{m}$  and are sensitized with the N749 dye.

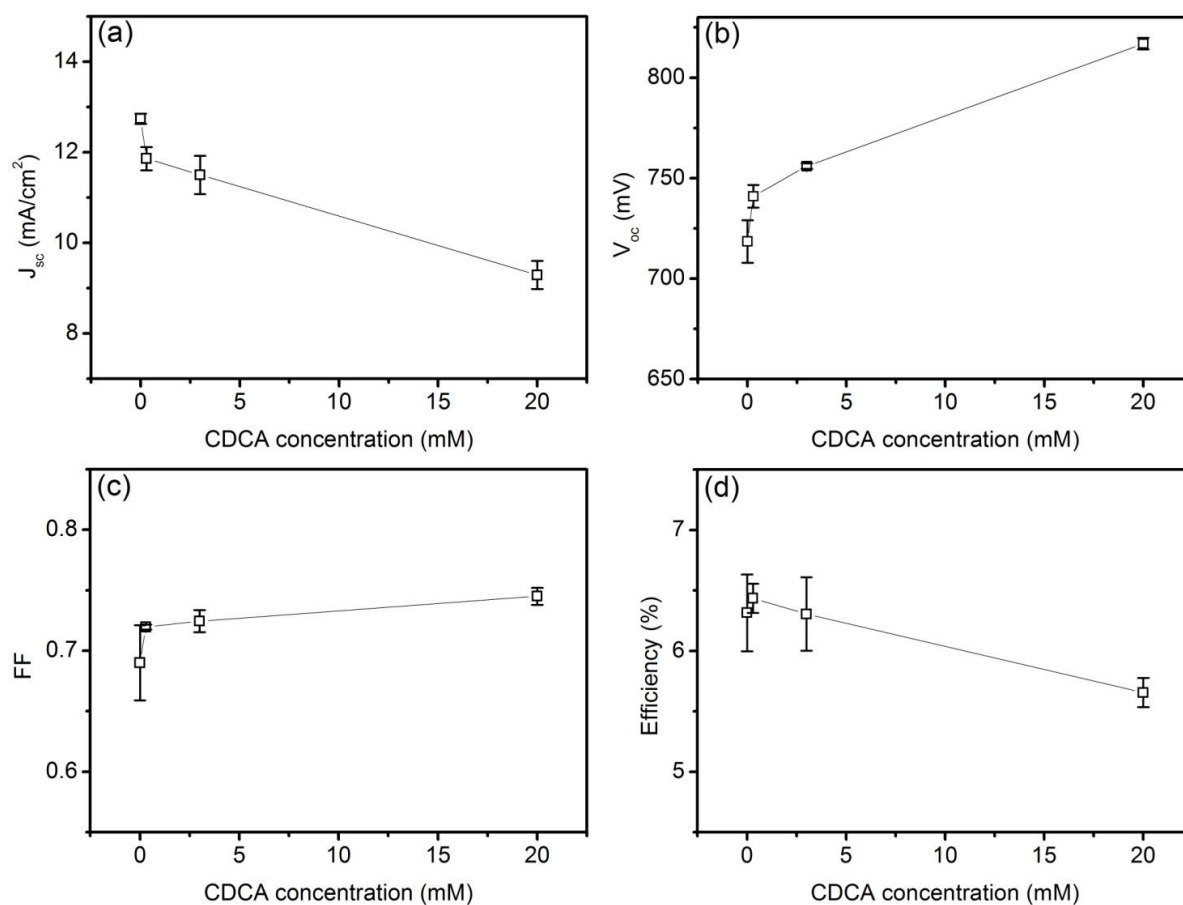
### 7.2.2 The effects of using coadsorbent in the N749 dye solution

Sensitization of  $\text{TiO}_2$  in the N749 solution requires the presence of the coadsorbent to achieve optimized results. This is due to the fact that the N749 dye molecules form aggregations on  $\text{TiO}_2$  surface without the use of coadsorbent.<sup>18</sup> Chenodeoxycholic Acid (CDCA) is a coadsorbent widely used to breakdown dye aggregations and to passivate uncovered  $\text{TiO}_2$  surface.<sup>19, 20</sup> The chemical structure of CDCA is shown in Figure 7.4.



**Figure 7.4** Chemical structure of chenodeoxycholic acid (CDCA)

The effects of CDCA as a coadsorbent in N749 dye solution were investigated in our experiment. The TiO<sub>2</sub> films with 99 % haze were soaked in 0.3 mM N749 dye solution containing 0, 0.3, 3 and 20 mM CDCA coadsorbent. Figure 7.5 shows that increasing CDCA concentration results in reduced  $J_{sc}$  and increased  $V_{oc}$ . The increased  $V_{oc}$  (Figure 7.5(b)) can be explained by the reduced back electron transfer from TiO<sub>2</sub> to triiodide attributing to the passivation of TiO<sub>2</sub> surface by CDCA. At the same time, CDCA molecules compete with the N749 dye molecules to attach onto the TiO<sub>2</sub> surface.<sup>19</sup> Increasing CDCA concentration therefore results in reduced dye adsorption, which explains the reduction in  $J_{sc}$  shown in Figure 7.5(a). On the other hand,  $FF$  of the cells are found increasing with increasing CDCA concentration. The overall cell efficiencies is increased when increasing the CDCA concentration from 0 to 0.3 mM, and decreased when further increasing the CDCA concentration to 3 and 20 mM. The reduction in efficiency is mostly due to the suppressed  $J_{sc}$ .



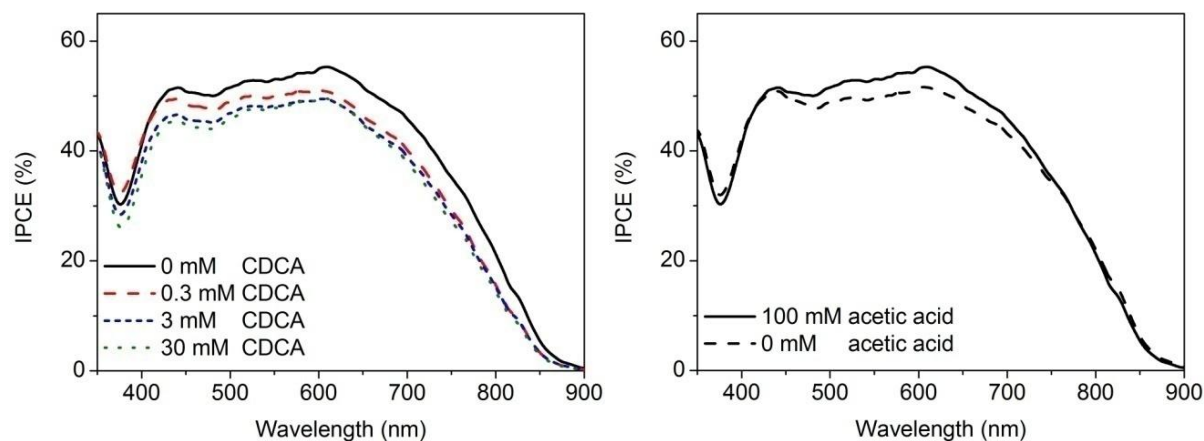
**Figure 7.5** The effects of chenodeoxycholic acid (CDCA) as a coadsorbent in 0.3 mM N749 dye solution on (a) the short-circuit current densities  $J_{sc}$ , (b) the open-circuit voltages  $V_{oc}$ , (c) the fill factors  $FF$  and (d) the efficiencies of DSCs using the  $TiO_2$  films with 99 % haze. Two cells were measured for each data point.

Other than CDCA, acetic acid is also implemented as a coadsorbent in our experiment. Table 7.2 shows that the addition of 100 mM acetic acid in 0.3 mM N749 dye solution results in increased  $V_{oc}$  and  $FF$ , whereas no substantial change could be noticed for  $J_{sc}$ . As a result, cell efficiency is improved when using 100 mM acetic acid as a coadsorbent.

**Table 7.2** Effect of acetic acid as a coadsorbent to the photovoltaic performance of DSCs comprising 12  $\mu\text{m}$   $\text{TiO}_2$  transparent films sensitized in 0.3 mM N749 dye with and without the addition of 100 mM acetic acid as a coadsorbent. Two cells were measured for each data point.

	$J_{sc}$ ( $\text{mA}/\text{cm}^2$ )	$V_{oc}$ (mV)	$FF$	$\eta$ (%)
0.3 mM N749	$12.7 \pm 0.1$	$718 \pm 10$	$0.69 \pm 0.03$	$6.31 \pm 0.32$
0.3 mM N749 + 100 mM acetic acid	$12.7 \pm 0.3$	$748 \pm 4$	$0.73 \pm 0.01$	$6.98 \pm 0.05$

Similar trends can be observed from IPCE results (Figure 7.6(a)), which show suppressed IPCE when increasing the concentration of CDCA. Over the entire absorption spectrum, the IPCE is much higher for the cells without the using of CDCA. For such a cell, the IPCE at 800 nm is slightly higher than 20 %, which is comparable to the result shown in literature.<sup>17</sup> Further addition of CDCA to 3 and 20 mM reduces the IPCE, and this is in good agreement with the  $J_{sc}$  drop measured in the IV characteristics. Figure 7.6(b) shows that the addition of 100 mM acetic acid results in slightly enhanced IPCE at wavelengths ranging from 500 to 750 nm.



**Figure 7.6** Incident photon-to-electron conversion efficiencies (IPCEs) measured for (a) DSCs sensitized in 0.3 mM N749 dye solution containing 0, 0.3, 3 and 20 mM of chenodeoxycholic acid as a coadsorbent, and (b) DSCs sensitized in 0.3 mM N749 with and without the addition of 100 mM acetic acid.



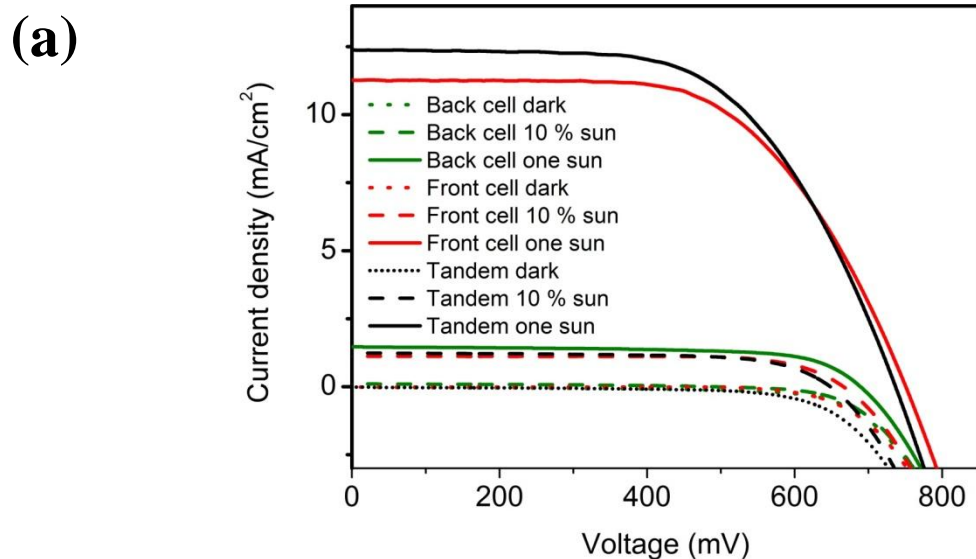
### 7.2.3 The assembly of tandem devices

To assemble three-terminal tandem DSCs, 12  $\mu\text{m}$  transparent  $\text{TiO}_2$  films were printed and sintered on FTO glass electrodes and were soaked in 0.3 mM N719 dye for 24 hours.  $\text{TiO}_2$  films with 99% haze were prepared on interdigitated backplates and soaked in solution containing 0.3 mM N749 dye and 100 mM acetic acid for 24 hours.

Figure 7.7(a) shows that better photovoltaic performance is observed for the tandem device compared to individual subcells. The front and back subcells show one-sun efficiency of 5.12 % and 0.69 % respectively, while the overall tandem efficiency is 5.43 %. An even higher tandem efficiency of 5.81 % can be calculated by mathematical summation of individual efficiencies.<sup>7</sup> The  $J_{sc}$  of front and back subcells are 1.47 and 11.27  $\text{mA}/\text{cm}^2$ , respectively. When shorting the two working electrodes, the tandem device produces an overall  $J_{sc}$  of 12.39  $\text{mA}/\text{cm}^2$ , slightly lower than the sum (12.74  $\text{mA}/\text{cm}^2$ ) of two  $J_{sc}$  measured for two subcells.  $V_{oc}$  of tandem device is 736.4 mV, lower than a front  $V_{oc}$  of 750.4 mV. In a parallel connection, the overall tandem  $V_{oc}$  is compromised by the lower value contributed by the back subcell. Precise matching between photovoltages of the two subcells is essentially required to avoid this drawback.

Under 10 % sun,  $V_{oc}$  of front and back subcells are 666.1 mV and 491.0 mV respectively, while the tandem  $V_{oc}$  is 648.4 mV, more close to the  $V_{oc}$  of front subcell. Tandem  $J_{sc}$  under this light intensity is 1.24  $\text{mA}/\text{cm}^2$ , similar to the summation of the two individual  $J_{sc}$  (1.23  $\text{mA}/\text{cm}^2$ ).

Under dark similar  $J_{sc}$  onsets are observed for back and front subcells, however both are later than that of tandem device. The change in the dark current onset can be explained by the differences in charge recombination on cells with different FTO electrode areas.



**(b)**

	Front subcell 10 % sun	Front subcell one sun	Back subcell 10 % sun	Back subcell one sun	Tandem 10 % sun	Tandem one sun
$V_{oc}$ (mV)	666	750	491	689	648	736
$J_{sc}$ (mA/cm <sup>2</sup> )	1.12	11.27	0.105	1.47	1.24	12.4
FF	0.75	0.61	0.38	0.68	0.68	0.60
$\eta$ (%)	5.4	5.1	0.19	0.69	5.3	5.4

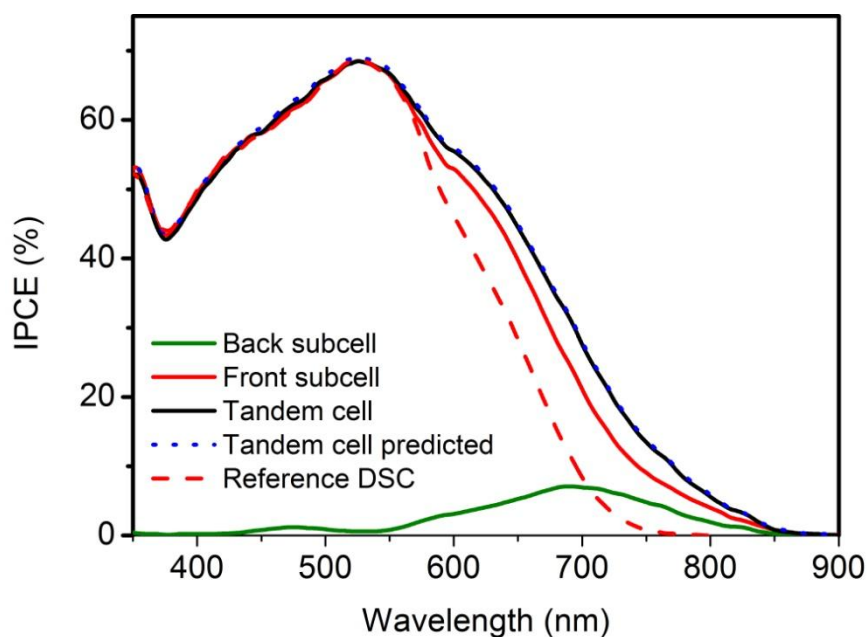
**Figure 7.7 (a)** Current density-voltage characteristics of a three-terminal tandem DSCs measured under dark (dotted lines), 10 % (dashed lines) and 100 % (solid lines) simulated AM1.5 sunlight. The tandem DSCs consist of front electrodes with 12  $\mu\text{m}$   $\text{TiO}_2$  films sensitized with the N719 dye and interdigitated back-contact DSCs with 12  $\mu\text{m}$   $\text{TiO}_2$  films (with 99 % haze) sensitized with the N749 dye. The front and back working electrodes were firstly measured separately against a common counter electrode, and then shorted to measure under a two-terminal setup. **(b)** Summarized photovoltaic performance of back, front and tandem cell under 10 % and 100 % simulated sunlight.

An enhanced IPCE is also observed for the tandem device compared to individual subcells (Figure 7.8). This is in good agreement with the trend of  $J_{sc}$  observed from the IV characteristics. A predicted IPCE was calculated by mathematically adding the IPCEs of two subcells. It is shown that the predicted IPCE perfectly superimposes the experimentally measured tandem IPCE. Unfortunately, due to the competing absorption spectrum between the two sensitizers, only modest performance increases were observed for the tandem device.

The IPCE peak of the tandem cell (around 70 %) is almost identical to those measured for the front subcells. Below 550 nm, most light is absorbed by the front subcell or otherwise by the

electrolyte, leaving the back subcell with almost no illumination at this region. The IPCE onset of the back subcell starts from 500 nm and reaches a peak of around 8 % at 700 nm.

Figure 7.8 also compares the IPCE of the front subcell to a standard reference DSC using identical  $\text{TiO}_2$  film, dye and electrolyte. It is shown that the IPCE of the reference cell starts its onset from 750 nm, corresponding to the absorption threshold of N719 the sensitizer. In comparison, the IPCE onset of the front subcell is red-shifted to 850 nm. Such an extended IPCE towards the IR region is believed to be due to partial dissolving of N749 dye molecules and further adsorption onto the front  $\text{TiO}_2$  film. It could also be estimated that the dissolved dye molecules in the electrolyte could result in a filtering effect that reduce light irradiation onto the back subcell.



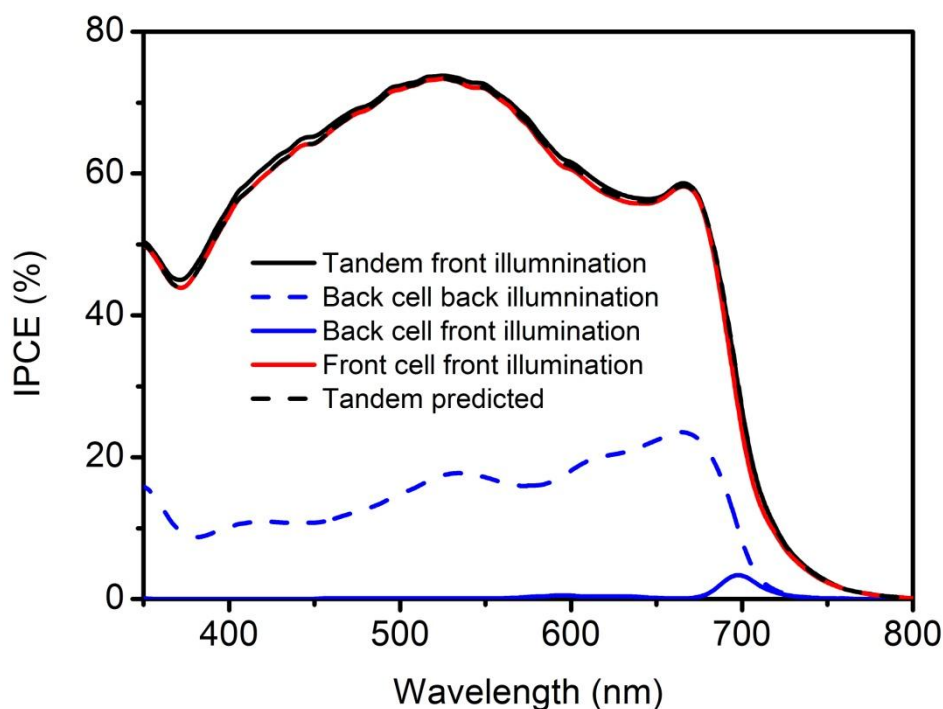
**Figure 7.8** IPCE of tandem DSC using N719 on front conventional DSC photoanode and N749 dye on back-contact cell. Two subcells were characterized separately and then in a two-terminal tandem setup. The dotted line shows the IPCE predicted by summation of the IPCEs of the individual subcells.

### 7.3 Tandem DSCs using N719 and SQ2 dyes

Dye contamination is also observed, when using N719 dye on the front subcell and SQ2 dye on the back subcell. As shown in Figure 7.9, IPCE of the front subcell nearly superposes that of the tandem device, whereas the IPCE of the back subcell is almost negligible. For the IPCE of the front subcell using N719 dye, an IPCE peak at around 540 nm is observed. Other than

that, an additional peak at around 675 nm is also noticed, corresponding to the absorption peak of SQ2 dye at this wavelength. This IPCE peak is quite pronounced, indicating a considerable co-sensitization effect. These observations imply considerable dissolving and re-adsorption of physically or chemically bound SQ2 dye molecules. The dissolving of dye molecules could attribute to the molecular exchange of dye molecules with pyridine molecules in the electrolyte. Dissolved dye molecules results in strong filtering effect which causes a negligible IPCE measured for the back subcell.

The back subcell was further characterized in back illumination mode (i.e. illuminate through the back-contact electrode). An IPCE peak at 675 nm is observed, corresponding to the absorption peak of SQ2 dye at this wavelength. Besides, an additional peak is noticed at around 545 nm, resulted from the absorption by N719 dye. This suggests that N719 dye molecules are partially dissolved and contaminate onto the back subcell, even though the dye molecules are believed to strongly bind to the  $\text{TiO}_2$  surface due to the formation of multiple carboxylate bonds.<sup>21</sup>



**Figure 7.9.** IPCE of a three-terminal tandem DSC using N719 dye as front sensitizer and SQ2 dye as back sensitizer. 12  $\mu\text{m}$   $\text{TiO}_2$  films were used on both the front and back subcells. The two subcells were characterized separately, and then shorted to measure in a two-terminal setup. The back subcell was also measured under back side illumination (i.e. illuminate through back-contact substrate) to show the IPCE without filtering effect from dissolved dye molecules.

#### 7.4 Conclusion

In conclusion, we have successfully fabricated a novel type of three-terminal tandem DSCs. Interdigitated back-contact DSCs are located on the backside of conventional DSC photoelectrodes to construct tandem devices with extended absorption range. The performances of sandwiched DSCs using N749 dye were optimized through the use of  $\text{TiO}_2$  films with haze and the addition of a coadsorbent into the dye solution.

After that, tandem devices combining N719 and N749 sensitizers were constructed. Over 10 % improvements in photocurrent and conversion efficiency were observed on tandem devices compared to the front subcells. However, drawbacks were also noticed for the tandem devices.

N749 dye was found to desorb from the back subcells and re-adsorbed onto the front TiO<sub>2</sub> films. This results in a filtering effect that limits the performance of the back subcells.

The dye contamination is more substantial in tandem device using N719 and SQ2 sensitizers. The absorption peak of the SQ2 dye at 675 nm can be clearly observed on the front subcells. Besides, the N719 dye molecules were also found to contaminate to the back subcells. Dissolved and re-adsorbed dye molecules in the N719 and SQ2 tandems devices result in a strong filtering effect that deteriorates the performance of the back subcells. The combination of the N719 and SQ2 dyes is not suitable for the three-terminal tandem DSCs,

Overall, tandem devices fabricated in our experiments are mostly for proof-of-principle purpose. Dye contamination is a critical issue that limits the performance of the back-contact cells. Other than that, the dyes used for the front and back subcells have almost identical absorption spectra, resulting in limited contribution from back subcells to the overall performance of tandem devices. The performances of three-terminal tandem devices can be improved using dye molecules that have strong absorption of IR light.

## 7.5 References to chapter 7

- [1] J. Kim, K. Lee, N. Coates, D. Moses, T. Nguyen, M. Dante, *Science* **2007**, 317, 222.
- [2] J. Xue, S. Uchida, B. Rand, S. Forrest, *Appl. Phys. Lett.* **2004**, 85, 5757.
- [3] K. Bertness, S. Kurtz, D. Friedman, A. Kibbler, C. Kramer, J. Olson, *Appl. Phys. Lett.* **1994**, 65, 989.
- [4] M. W. Wanlass, J. S. Ward, K. A. Emery, T. A. Gessert, C. R. Osterwald, T. J. Coutts, *Sol. Cells* **1991**, 30, 363.
- [5] K. Bertness, D. Friedman, S. Kurtz, A. Kibbler, C. Kramer, J. Olson, *J. Propul. Power* **1996**, 12, 842.
- [6] T. Soga, M. Yang, T. Jimbo, M. Umeno, *Jpn. J. appl. Phys.* **1996**, 35, 1401.
- [7] S. Sista, Z. Hong, M.-H. Park, Z. Xu, Y. Yang, *Adv. Mater.* **2010**, 22, E77.
- [8] A. Goetzberger, C. Hebling, H.-W. Schock, *Mat. Sci. Eng. R-Rept.* **2003**, 40, 1.
- [9] S. Sista, Z. R. Hong, M. H. Park, Z. Xu, Y. Yang, *Adv. Mater.* **2010**, 22, E77.
- [10] M. A. Steiner, M. W. Wanlass, J. J. Carapella, A. Duda, J. S. Ward, T. E. Moriarty, K. A. Emery, *Prog. Photovoltaics* **2009**, 17, 587.
- [11] T. Nagashima, K. Okumura, K. Murata, Y. Kimura, Ieee, in *Conference Record of the Twenty-Eighth Ieee Photovoltaic Specialists Conference - 2000*, **2000**, 1193.
- [12] A. Nattestad, A. J. Mozer, M. K. R. Fischer, Y. B. Cheng, A. Mishra, P. Bauerle, U. Bach, *Nat. Mater.* **2010**, 9, 31.
- [13] M. Nazeeruddin, A. Kay, I. Rodicio, R. Humphrybaker, E. Muller, P. Liska, *J. Am. Chem. Soc.* **1993**, 115, 6382.

- [14] M. Nazeeruddin, P. Pechy, T. Renouard, S. Zakeeruddin, R. Humphry-Baker, P. Comte, *J. Am. Chem. Soc.* **2001**, 123, 1613.
- [15] S. Alex, U. Santhosh, S. Das, *J. Photoch. Photobio. A* **2005**, 172, 63.
- [16] J. Yum, P. Walter, S. Huber, D. Rentsch, T. Geiger, F. Nuesch, *J. Am. Chem. Soc.* **2007**, 129, 10320.
- [17] Y. Chiba, A. Islam, Y. Watanabe, R. Komiya, N. Koide, L. Y. Han, *Jpn. J. Appl. Phys.* **2006**, 45, L638.
- [18] M. Ikeda, N. Koide, L. Han, A. Sasahara, H. Onishi, *Langmuir* **2008**, 24, 8056.
- [19] J. Yum, S. Moon, R. Humphry-Baker, P. Walter, T. Geiger, F. Nuesch, *Nanotechnology* **2008**, 19.
- [20] T. Daeneke, T. Kwon, A. Holmes, N. Duffy, U. Bach, L. Spiccia, *Nat. Chem.* **2011**, 3, 211.
- [21] A. Kay, Vol. PhD, Ecole Polytechnique Fédérale de Lausanne, Lausanne, Switzerland **1994**.





## 8 General conclusions and outlook

### 8.1 *General conclusions*

The objective of this PhD project is to develop TCO free back-contact DSCs with both anode and cathode are located on a common side of dye-sensitized TiO<sub>2</sub> films. In the back-contact designs, light transmission losses commonly occurred at TCO electrodes can be reduced. On top of that, such devices enable the use of flexible metal substrates to fabricate DSC electrodes with much lower series resistances and therefore enhanced charge collection efficiencies.

Two types of back-contact DSC architectures were developed. The first type comprises interdigitated finger electrodes which were prepared using laser ablation techniques. Single beam direct-write technique was found superior to mask-deliver process for high throughput production of interdigitated electrodes. However, both of the two techniques used in our experiment employ nanosecond laser pulses which result in substantial heating and thus cracking and distortion of substrate materials. The nanosecond laser pulses are therefore proved to be not well suited for producing finger electrodes with 10  $\mu\text{m}$  dimension. The heating of substrate materials can be significantly reduced using femtosecond laser pulses, which were not implemented in this project.

Systematical studies were carried out on the electrochemical deposition of Pt catalytic coating used for interdigitated back-contact DSCs. The correlation of deposition parameters, coating morphologies and the electrochemical activities of Pt coatings were summarized. Improved catalytic activities were measured for coatings with smaller Pt particles produced by higher pulsed-current densities such as 10 mA/cm<sup>2</sup>.

Working interdigitated back-contact DSC devices were successfully fabricated on both FTO and Ti coated glass substrates. The highest solar energy to electricity conversion efficiency measured for these devices were close to 4 %, this is compared to around 6 % efficiencies measured for sandwiched DSCs employing identical TiO<sub>2</sub>, dye and electrolyte. To a large extent, the reduced efficiencies are due to the light transmission losses occurred at the electrolyte layer on top of TiO<sub>2</sub> films. This issue can be solved by using thinner Surlyn gaskets, or using a transparent SiO<sub>2</sub> film on top of the TiO<sub>2</sub> films. On the other hand, defects on finger

electrodes as a result of imperfect laser ablation process also contribute to the reduced efficiencies.

The second back-contact architecture comprises coplanar electrodes. Compared to the first type, this architecture omits the requirement of microfabrication processes, and therefore can be more easily fabricated. Working devices were successfully fabricated on FTO glass as well as on Ti foils. The highest efficiencies of 4.6 % were measured for the coplanar back-contact DSCs compared to a 6.3 % efficiency measured for sandwiched DSCs using identical  $\text{TiO}_2$ , dye and electrolyte. Similar internal resistances were measured for the back-contact and the sandwiched DSCs using electrochemical impedance spectroscopy. The lower conversion efficiency for the coplanar back-contact DSCs is mostly due to the light transmission loss occurred at the electrolyte layer on top of  $\text{TiO}_2$  films.

Further, tandem DSCs were constructed using interdigitated back-contact DSCs on the back side of conventional  $\text{TiO}_2$  photoelectrodes. These devices feature three terminals. The counter electrode of the interdigitated back subcell is shared by the two working electrodes on the front and back subcells. The N749 and SQ2 dyes were implemented on the back subcells to extend the absorption spectra of the tandem cells into red light region. However, cross contamination of dye molecules between the two subcells was generally found. Dissolving of dye molecules into electrolyte and re-adsorption onto the front subcells result in substantial filtering effects that limit the performance of the back subcells. In the three-terminal tandem DSCs using the N719 and N749 dyes, around 10 % improvements in the photocurrent and the efficiency were measured when compare the performance of the tandem DSC to that of the front subcells. Better performed three-terminal DSCs can be fabricated using better designed IR dyes.

## 8.2 *Outlook*

Although back-contact solar cells are known for many years, the back-contact architectures are only recently exploited to produce DSCs.

Back-contact DSCs open up a way to produce TCO-free DSCs, which have potentially reduced cost and increased the device efficiencies. While our back-contact architectures are different from those shown in literature, the device efficiency shall be further improved to catch up with the performance of other back-contact DSCs as well as conventional DSCs. This

requires the further optimization of the fabrication techniques for our back-contact DSCs. One important issue regarding the light transmission loss occurring on iodine/iodide electrolyte can be solved by using thinner sealing gaskets, by using a transparent spacer layer on top of the  $\text{TiO}_2$  film, or by using alternative electrolytes with reduced light absorption.

The electron transport characteristics in our back-contact DSCs will be comprehensively studied to understand the effect of alternative device architectures on the device performance. An interesting finding in the project is the commonly higher open-circuit voltages measured on our back-contact DSCs than on reference DSCs. With the present data, we attribute the high open-circuit voltage to the reduced recombination on the working electrodes of our back-contact DSCs. However, the higher voltage could also attribute to the different charge transport characteristics in the back-contact DSCs. In these devices, electrons and triiodide move towards the same direction. There can be a reduced voltage consumption on pulling apart the negative and positive charges. Further experiments will be conducted to further understand the mechanisms behind this finding.

Furthermore, our back-contact designs will be applied to produce efficient all-metal-type DSC modules. The use of metal electrodes can potentially reduce the series resistance in modules, and therefore increase the module efficiencies.

Three-terminal tandem DSCs comprising back-contact DSCs will be further investigated. The novel tandem DSCs use two dyes on separated photoelectrodes. With better designed IR dyes and complementary dye absorption, the novel devices can potentially surpass the best efficiency of the present DSCs.



## Appendix: Curriculum Vitae

Name: Dongchuan Fu

Email:

### Education

Mar. 2008 to date	Ph.D study under the supervision of A/Prof. Udo Bach Department of materials engineering, Monash University, Clayton Campus.
Sep. 2003 to Dec. 2007	Monash University and Wuhan University of Technology (2+2 undergraduate program) Bachelor of Engineering (with First Class A Honours) in the field of Materials Engineering from Monash University Bachelor of Engineering in the field of Materials Engineering from Wuhan University of Technology
Jul. to Nov. 2011	Graduate Certificate in Commercializing Research from Monash University

### Awards during PhD studies

2010	Chinese government award for outstanding self-financed students abroad
2011	Monash university Commercialisation Training Scheme (CTS) Award

## Publications and patent during PhD studies

Publications	<p><b>D. Fu</b>, X.L. Zhang, R. Barber and U. Bach, Dye-Sensitized Back-Contact Solar Cells, <i>Advanced Materials</i>, 2010, 38, 4270. (Highlighted in Nature Photonics and NPG Asia Materials. Technology Focus, Dye-sensitized Cell Redesign, Nature Photonics, Vol 4, Sept. 2010, p 597 Nature Publishing Group, Research Highlights, Solar Cells: Things are getting clearer, doi:10.1038/asiamat.2010.141)</p> <p>X.L. Zhang, F. Huang, A. Nattestad, K. Wang, <b>D. Fu</b>, A. Mishra, P. Buerle, U. Bach and Y.-B. Cheng. Enhanced Open-circuit Voltage of P-type DSC with Highly Crystalline NiO Nanoparticles, <i>Chemical Communications</i>, 2011, 47, 4808.</p>
Patent	U. Bach and D. Fu, Photovoltaic Devices, WO2010060154A1

## Conferences and presentations

- Poster presentation at the MRS 2011 fall conference, Boston, November 2011
- Poster presentation at the 18th International Conference on Photochemical Conversion and Storage of Solar Energy (IPS 18th), Seoul, July 2010
- Presentation at the 2009 Department of Materials Engineering Postgraduate Conference
- Presentation at the 2010 Department of Materials Engineering Postgraduate Conference